frontiers | Research Topics

Measuring and modeling the ground deformation of geological disasters using modern geodesy

Edited by
Xinjian Shan, Jeffrey Todd Freymueller, Caijun Xu and Zhenjie Wang

Published in
Frontiers in Earth Science

ISSN 1664-8714
ISBN 978-2-8325-2988-1
DOI 10.3389/978-2-8325-2988-1

About Frontiers

Frontiers is more than just an open access publisher of scholarly articles: it is a pioneering approach to the world of academia, radically improving the way scholarly research is managed. The grand vision of Frontiers is a world where all people have an equal opportunity to seek, share and generate knowledge. Frontiers provides immediate and permanent online open access to all its publications, but this alone is not enough to realize our grand goals.

Frontiers journal series

The Frontiers journal series is a multi-tier and interdisciplinary set of open-access, online journals, promising a paradigm shift from the current review, selection and dissemination processes in academic publishing. All Frontiers journals are driven by researchers for researchers; therefore, they constitute a service to the scholarly community. At the same time, the *Frontiers journal series* operates on a revolutionary invention, the tiered publishing system, initially addressing specific communities of scholars, and gradually climbing up to broader public understanding, thus serving the interests of the lay society, too.

Dedication to quality

Each Frontiers article is a landmark of the highest quality, thanks to genuinely collaborative interactions between authors and review editors, who include some of the world's best academicians. Research must be certified by peers before entering a stream of knowledge that may eventually reach the public - and shape society; therefore, Frontiers only applies the most rigorous and unbiased reviews. Frontiers revolutionizes research publishing by freely delivering the most outstanding research, evaluated with no bias from both the academic and social point of view. By applying the most advanced information technologies, Frontiers is catapulting scholarly publishing into a new generation.

What are Frontiers Research Topics?

Frontiers Research Topics are very popular trademarks of the *Frontiers journals series*: they are collections of at least ten articles, all centered on a particular subject. With their unique mix of varied contributions from Original Research to Review Articles, Frontiers Research Topics unify the most influential researchers, the latest key findings and historical advances in a hot research area.

Find out more on how to host your own Frontiers Research Topic or contribute to one as an author by contacting the Frontiers editorial office: frontiersin.org/about/contact

Measuring and modeling the ground deformation of geological disasters using modern geodesy

Topic editors

Xinjian Shan — Institute of Geology, China Earthquake Administration, China
Jeffrey Todd Freymueller — Michigan State University, United States
Caijun Xu — Wuhan University, China
Zhenjie Wang — China University of Petroleum (Huadong), China

Citation

Shan, X., Freymueller, J. T., Xu, C., Wang, Z., eds. (2023). *Measuring and modeling the ground deformation of geological disasters using modern geodesy*. Lausanne: Frontiers Media SA. doi: 10.3389/978-2-8325-2988-1

Table of contents

frontiers | Frontiers in Earth Science

TYPE Original Research
PUBLISHED 12 September 2022
DOI 10.3389/feart.2022.970493

OPEN ACCESS

EDITED BY
Gang Rao,
Southwest Petroleum University, China

REVIEWED BY
Wanpeng Feng,
School of Earth Sciences and Engineering, Sun Yat-sen University, Zhuhai Campus, China
Yongsheng Li,
Ministry of Emergency Management, China

*CORRESPONDENCE
Caijun Xu,
cjxu@sgg.whu.edu.cn

SPECIALTY SECTION
This article was submitted to Structural Geology and Tectonics, a section of the journal Frontiers in Earth Science

RECEIVED 16 June 2022
ACCEPTED 26 July 2022
PUBLISHED 12 September 2022

CITATION
Xiong L, Xu C, Liu Y, Zhao Y, Geng J and Ortega-Culaciati F (2022), Three-dimensional displacement field of the 2010 Mw 8.8 Maule earthquake from GPS and InSAR data with the improved ESISTEM-VCE method.
Front. Earth Sci. 10:970493.
doi: 10.3389/feart.2022.970493

Three-dimensional displacement field of the 2010 Mw 8.8 Maule earthquake from GPS and InSAR data with the improved ESISTEM-VCE method

Luyun Xiong[1], Caijun Xu[1,2,3]*, Yang Liu[1,2,3], Yingwen Zhao[1], Jianghui Geng[4,5] and Francisco Ortega-Culaciati[6]

[1]School of Geodesy and Geomatics, Wuhan University, Wuhan, Hubei, China, [2]Key Laboratory of Geospace Environment and Geodesy, Ministry of Education, Wuhan University, Wuhan, Hubei, China, [3]Key Laboratory of Geophysical Geodesy, Ministry of Natural Resources, Wuhan, Hubei, China, [4]GNSS Research Center, Wuhan University, Wuhan, Hubei, China, [5]Hubei Luojia Laboratory, Wuhan, Hubei, China, [6]Department of Geophysics, Faculty of Physical and Mathematical Sciences, University of Chile, Santiago, Chile

The 2010 Mw 8.8 Maule earthquake occurred offshore central Chile and ruptured ~500 km along the megathrust fault resulting from the oceanic Nazca plate subducting beneath the continental South American plate. The Maule earthquake produced remnant crustal displacements captured by a vast set of geodetic observations. However, given the nature of the observational techniques, it is challenging to extract its accurate three-dimensional coseismic deformation field with high spatial resolution. In this study, we modified the extended simultaneous and integrated strain tensor estimation from geodetic and satellite deformation measurements (ESISTEM) method with variance component estimation algorithm (ESISTEM-VCE) to retrieve the three-dimensional surface displacement field of this event by integrating the interferometric synthetic aperture radar (InSAR) and global positioning system (GPS) measurements. The ESISTEM-VCE method accounts for the spatial correlation of surface displacement among the adjacent points and determine the accurate weight ratios for different data sets, but also uses the uncertainties of GPS data and considers the different spatial scales from the different datasets. In the simulation experiments, the RMSEs of the ESISTEM-VCE method are smaller than those of the ESISTEM and ESISTEM-VCE (same *d0*) methods, and the improvements of 97.1%, 3.9%, and 84% are achieved in the east-west, north-south, and vertical components, respectively. Then, we apply the proposed methodology to the 2010 Mw 8.8 Maule earthquake, to obtain a three-dimensional displacement field that could provide fine deformation information. In the east-west component, the significant deformation is in the north of the epicenter, closed to the Constitución, with a maximum westward displacement of 495.5 cm. The displacement in the north-south component is relatively small compared to that in the east-west component. The maximum uplift reaches 211.8 cm, located at the southwest of the Concepción. Finally, the derived vertical displacements are also compared with field investigations, indicating that the ESISTEM-VCE method can obtain

more accurate weight of different datasets and perform better than the ESISTEM method. The results highlight that the earthquake ruptured along the NE-SW direction, with a dominant thrust and a relatively small component of right-lateral strike-slip, coinciding with the characteristics of subduction and right-lateral shear. The experiments with the simulated and real data suggest that the improved ESISTEM-VCE method in this study is feasible and effective.

KEYWORDS

The 2010 Mw 8.8 Maule earthquake, three-dimensional displacement field, ESISTEM-VCE method, GPS, InSAR

Introduction

On 27 February 2010, an Mw 8.8 earthquake struck the coast of Chile's Maule region. It is the fifth-largest earthquake since the beginning of the modern recording, and the largest megathrust earthquake in this zone since the 1960 Mw 9.5 Chile earthquake (Tong et al., 2010; Lorito et al., 2011). The earthquake occurred along the interface between the Nazca and South American plates with a convergence rate of ~6.5 cm/yr (Kendrick et al., 2003; Ruegg et al., 2009; Vigny et al., 2009; Pollitz et al., 2011). Subsequently, the surface deformation caused by this event was observed by global positioning system (GPS) stations and interferometric synthetic aperture radar (InSAR) images. The horizontal displacement from the GPS stations (Figure 1) shows a strong seaward motion, with a small southward motion, being consistent with oblique convergence in the subduction margin. Meanwhile, the vertical displacements along the coastal exhibit surface uplift consisted with a rupture on the megathrust, with a maximum uplift of 188.7 cm at the south of the epicenter. Inland, the GPS measurements show the subsidence due to the effect of coseismic slip (Vigny et al., 2011), with a maximum of 72.8 cm.

The InSAR technique is powerful to detect ground surface displacement, such as earthquakes (Massonnet et al., 1993; Xu et al., 2020; Yang et al., 2020a, 2020b), volcanoes (Guo et al., 2019; Wang L. et al., 2021), and mining collapses (Yang et al., 2016). For the Maule event, the Japan Aerospace Exploration Agency (JAXA) imaged the deformation areas with the Advanced Land Observatory Satellite (ALOS) Phased Array type L-band Synthetic Aperture Radar (PALSAR) images (Tong et al., 2010; Pollitz et al., 2011; Zhang et al., 2021). Besides, this event induced some geohazards such as the tsunami with a maximum runup of 29 m, resulting in 156 casualties and economic losses of about 30000 million dollars (http://www.ngdc.noaa.gov/hazard/tsu.shtml; https://www.ngdc.noaa.gov/hazel/view/hazards/tsunami/event-more-info/4682).

Following the event, different data sources have been used in several studies to investigate the Maule earthquake rupture process and the mechanics of the subduction environment. Tong et al. (2010) quantitatively derived the coseismic slip distribution based on the elastic dislocation model with a combination of GPS and ALOS data. Lay et al. (2010) inferred the finite-fault slip distribution using the teleseismic P, SH, and Rayleigh wave data. Delouis et al. (2010) presented the slip distribution based on the static and High-Rate GPS, teleseismic, and InSAR data. Lorito et al. (2011) derived the slip distribution with a robust model using a combination of tsunami, GPS, InSAR data, and land-level changes (Farías et al., 2010). Luttrell et al. (2011) estimated the stress drop and crustal tectonic stress of the Maule earthquake. However, there is still no research on the coseismic three-dimensional surface displacement field related to this event. Although InSAR has played a significant role in measuring surface deformation, it is confined to one-dimensional line of sight (LOS) displacement of the geohazards such as earthquakes and volcanic eruptions (Jung and Hong, 2017; He et al., 2018; Xiong et al., 2020). The LOS results cannot fully reflect the real deformation in most cases (Song et al., 2017). However, the three-dimensional displacement field can assist us to comprehensively understand the characteristics of the seismogenic fault and provide enlightenment of the earthquake rupture (Fialko et al., 2001; He et al., 2018, 2019; Zhou et al., 2018; Liu et al., 2019; Xiong et al., 2020).

It is well known that GPS data offer high precision in measuring surface deformation, but provide sparse three-dimensional displacement caused by an earthquake. Moreover, the sites of the network of GPS stations registering the Maule earthquake are unevenly distributed, being denser near the coast and more scattered at the epicentral or far-field areas (Hill et al., 2012; Jiang, 2014; Elliott et al., 2016). Therefore, compared to one-dimensional LOS displacement or sparse GPS observations, the large-scale three-dimensional displacement field can provide exhaustive information that helps to produce a straightforward geological interpretation (Jung and Hong, 2017; He et al., 2019). Generally, GPS and InSAR data are fused to estimate three-dimensional surface displacement. As a first step in previous studies (Gudmundsson et al., 2002; Samsonov and Tiampo, 2006; Hu et al., 2012), sparse GPS measurements are interpolated to fill in the LOS grid. To avoid GPS interpolation and consider the spatial correlation of surface displacements among the adjacent points, Guglielmino et al. (2011) proposed the SISTEM method. Based on the elastic theory, SISTEM method can provide the solutions of the strain tensor, the displacement field, and the rigid body rotation tensor. Luo and Chen (2016) proposed the ESISTEM approach that both surrounding InSAR and GPS

measurements available were used to constrain the derived displacements, while the SISTEM approach only used the surrounding GPS measurements. Furthermore, neither the SISTEM nor ESISTEM methods account for the relative weight between GPS and InSAR measurements needed to compensate for the highly larger amount of InSAR observations. With the spatial correlation of the adjacent points' displacements taken into consideration in the SISTEM/ESISTEM methods, more measurements are involved to estimate displacements and strain at the points of interest. Thus, providing a chance to use the variance component estimation (VCE) algorithm to determine accurate relative weights between GPS, ascending, and descending InSAR data in the SISTEM/ESISTEM methods. In previous research, Hu et al. (2012) introduced the VCE algorithm to estimate the relative weight between InSAR and GPS measurements for inferring the three-dimensional surface displacements. However, their method does not consider the spatial correlation of neighboring surface displacements. Liu et al. (2018, 2019) and Hu et al. (2021) incorporated the VCE algorithm into the strain model based on the elastic theory, using only InSAR measurements. Nevertheless, they calculated displacements/strain in a given spatial window, without determining the distance-decaying constant. However, the spatial distribution characteristics and resolutions (spatial scales) of GPS and InSAR data are quite different. For instance, while InSAR observations are homogenously distributed over a broad area, the spatial distribution of the GPS stations is highly heterogeneous in the large-scale deformation area of the 2010 Maule earthquake. Therefore, Liu et al. (2018), Liu et al. (2019) and Hu et al. (2021) approaches are not suitable when integrating GPS and InSAR data to derive the three-dimensional displacement field. In addition, Wang Y. et al. (2021) integrated the VCE and the SISTEM methods to derive three-dimensional surface displacement. However, they defined the relative weight between horizontal and vertical components of GPS data without acknowledging their uncertainties. Moreover, they defined the same distance–decaying constants to multi-source data, which is also not appropriate for GPS and InSAR data with intrinsically different spatial distributions. As a example, for the 2010 Maule earthquake, the spatial scale of GPS data is larger than that of InSAR observations.

To overcome the shortcomings mentioned above, we propose the improved ESISTEM method combined with VCE algorithm (ESISTEM-VCE). We also called this method tight integration of GPS/InSAR data, which is similar to the integration of GPS/INS in navigation. The main objectives of this method are: 1) to avoid the interpolation of sparse GPS data and construct a functional model with physical meaning that takes into account the spatial correlation among adjacent points based on elastic theory; 2) to utilize the uncertainties of horizontal and vertical directions from GPS data, and fully consider the differences of the spatial scales intrinsic to data from GPS networks and InSAR scenery; 3) to make a posteriori estimation of the adjustment stochastic model and determine the accurate weights of GPS, ascending, and descending InSAR data by applying the VCE algorithm. Thus, exploit the intrinsic complementarity of GPS and InSAR data to determine surface displacements. For validation, the improved ESISTEM-VCE method is used to derive the three-dimensional displacements with a simulated experiment. Then, as a novelty, we apply our proposed methodology to the case study of the 2010 Mw 8.8 Maule earthquake.

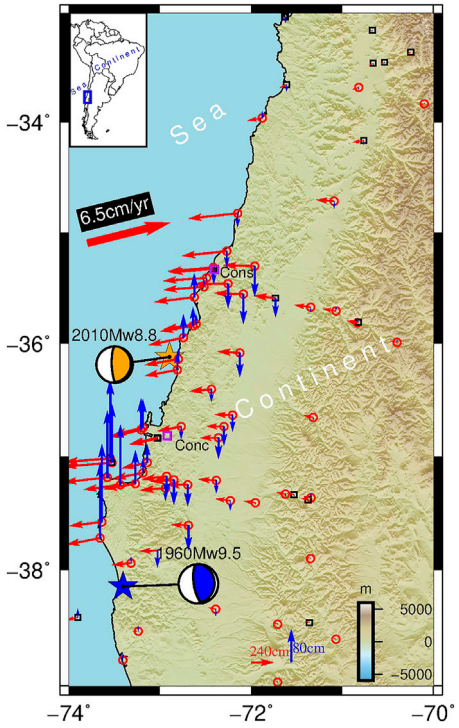

FIGURE 1
The tectonic setting of the 2010 Maule earthquake. The black rectangle represents the continuous GPS stations, and the red circles are campaign stations. The red and blue vectors represent the horizontal and vertical displacements of GPS, respectively. The orange and blue stars are the epicenters of 2010 and 1960 earthquakes, respectively. The orange beach ball is the United States Geological Survey (USGS) centroid moment tensor. The focal mechanism of the blue beach ball is from Fujii and Satake (2013). The bold red arrow shows the interseismic convergence vector between the Nazca plate and the South American plate. The purple rectangles represent the locations of surrounding cities; Cons, Constitución; Conc, Concepción.

ESISTEM-VCE method

For an arbitrary point P^0, whose position and three-dimensional displacements are $x^0 = (x_e^0, x_n^0, x_u^0)$ and $d^0 = (d_e^0, d_n^0, d_u^0)$, respectively. There are N reference points (RPs) surrounding the

P^0 with the positions and displacements are $x^i = (x_e^i, x_n^i, x_u^i)$ and $d^i = (d_e^i, d_n^i, d_u^i)$, respectively, where $i = 1, 2, \cdots N$. The subscripts e, n and u represent the east-west (E-W), north-south (N-S), and vertical (U) components, respectively. Based on the elastic theory (Guglielmino et al., 2011), the relationship between the displacements d^0 and d^i can be expressed as

$$d^i = \boldsymbol{H}\Delta x + d^0 \tag{1}$$

where $\Delta x = x^i - x^0 = [\,\Delta x_e^i \quad \Delta x_n^i \quad \Delta x_u^i\,]^{\mathrm{T}}$ denotes the vector distance between the *ith* RP and the arbitrary point P^0, $\boldsymbol{H} = \partial d^i/\partial x^i$ denotes the elements of the displacement gradient tensor. In the SISTEM method, Guglielmino et al. (2011) only used surrounding GPS measurements. Thus, Luo and Chen (2016) proposed the ESISTEM method, where both surrounding GPS and InSAR measurements can be used in deriving displacements. The linear equation for the ESISTEM method can be expressed as

$$\boldsymbol{d} = \boldsymbol{A}\boldsymbol{X} + \boldsymbol{e} \tag{2}$$

where $\boldsymbol{d}$ is the column observation vector, $\boldsymbol{A}$ is the design matrix, $\boldsymbol{X}$ is the column vector of unknown parameters, and $\boldsymbol{e}$ is the observation error vector. The expressions of the vectors or matrices are shown in the Appendix A. The detailed information about formula derivation can be referred to Luo and Chen (2016).

For the 2010 Mw 8.8 Maule earthquake, the GPS, ascending, and descending InSAR measurements can be together used to extract the three-dimensional surface deformation field. Therefore, the data sets are divided into three groups based on their properties. Their observations are $\boldsymbol{d}_1$, $\boldsymbol{d}_2$, and $\boldsymbol{d}_3$ for GPS, ascending, and descending InSAR measurements, respectively. The corresponding coefficient matrices are $\boldsymbol{A}_1$, $\boldsymbol{A}_2$, and $\boldsymbol{A}_3$, respectively.

The weight matrices $\boldsymbol{W}_j$ $(j = 1, 2, 3)$ is determined by $1/\delta_j^2$, and δ_j denote the standard deviations of the measurements, with their uncertainties of the GPS as well as InSAR data are utilized, respectively, which is different from Wang Y. et al. (2021). Meanwhile, the estimation for any point of interest can be performed over the RPs with a suitable weighting strategy to automatically lower the contribution of points distant from the point of interest (Pesci and Teza, 2007). Hence, the weighted $\mathbf{W}_j^{'}$ is given as (Shen et al., 1996; Guglielmino et al., 2011)

$$\boldsymbol{W}_j^{'} = \boldsymbol{W}_j \exp\left(-d_n/d_j\right) \tag{3}$$

where d_n is the distance between the *ith* RP and the point of interest P^0, and d_j are distance–decaying constants for GPS, ascending, and descending InSAR measurements, respectively (Guglielmino et al., 2011), which is evaluated with the following empirical formula:

$$d_j = \frac{1}{PQ}\sum_{p=1}^{P}\sum_{q\in K_i} d_{pq} \tag{4}$$

which takes into account the obvious spatial scale differences among different data sets and shows the other main difference from Wang Y. et al. (2021). As Guglielmino et al. (2011) described in the paper, P is the number of the RPs of the network, K_i is the set of Q nearest stations in the circle centered at the i station for different data sets. In our study, we also refer to it that Q ranges between four and six.

Let $\boldsymbol{N}_j = \boldsymbol{A}_j^T\boldsymbol{W}_j^{'}\boldsymbol{A}_j$, $\boldsymbol{L}_j = \boldsymbol{A}_j^T\boldsymbol{W}_j^{'}\boldsymbol{d}_j$ and $\boldsymbol{N} = \sum_1^3 \boldsymbol{N}_j$, $\boldsymbol{L} = \sum_1^3 \boldsymbol{L}_j$. With the weighted least square method (WLS) (He et al., 2018; Wang and Gu, 2020), the estimated unknown vector $\hat{\boldsymbol{X}}$ can be solved, as shown in Eq. 5.

$$\hat{\boldsymbol{X}} = \boldsymbol{N}^{-1}\boldsymbol{L} \tag{5}$$

In this paper, we assumed the initial variances for the data sets are σ_{01}^2, σ_{02}^2, and σ_{03}^2, respectively. The relationship between the estimates and the residuals sum of squares (RSS) of observations is (Cui et al., 2001; Xu et al., 2009)

$$\boldsymbol{S}\boldsymbol{\theta} = \boldsymbol{W}_{\boldsymbol{\theta}} \tag{6}$$

and

$$\mathbf{S} = \begin{bmatrix} 3{*}n1 - 2tr(\boldsymbol{N}^{-1}\boldsymbol{N}_1) + tr(\boldsymbol{N}^{-1}\boldsymbol{N}_1)^2 & tr(\boldsymbol{N}^{-1}\boldsymbol{N}_1\boldsymbol{N}^{-1}\boldsymbol{N}_2) & tr(\boldsymbol{N}^{-1}\boldsymbol{N}_1\boldsymbol{N}^{-1}\boldsymbol{N}_3) \\ tr(\boldsymbol{N}^{-1}\boldsymbol{N}_1\boldsymbol{N}^{-1}\boldsymbol{N}_2) & n2 - 2tr(\boldsymbol{N}^{-1}\boldsymbol{N}_2) + tr(\boldsymbol{N}^{-1}\boldsymbol{N}_2)^2 & tr(\boldsymbol{N}^{-1}\boldsymbol{N}_2\boldsymbol{N}^{-1}\boldsymbol{N}_3) \\ tr(\boldsymbol{N}^{-1}\boldsymbol{N}_1\boldsymbol{N}^{-1}\boldsymbol{N}_3) & tr(\boldsymbol{N}^{-1}\boldsymbol{N}_2\boldsymbol{N}^{-1}\boldsymbol{N}_3) & n3 - 2tr(\boldsymbol{N}^{-1}\boldsymbol{N}_3) + tr(\boldsymbol{N}^{-1}\boldsymbol{N}_3)^2 \end{bmatrix}$$

$\hat{\boldsymbol{\theta}} = [\,\hat{\sigma}_{01}^2 \quad \hat{\sigma}_{02}^2 \quad \hat{\sigma}_{03}^2\,]^T$,
$\boldsymbol{W}_{\boldsymbol{\theta}} = [\,\boldsymbol{V}_1^T\boldsymbol{W}_1^{'}\boldsymbol{V}_1 \quad \boldsymbol{V}_2^T\boldsymbol{W}_2^{'}\boldsymbol{V}_2 \quad \boldsymbol{V}_3^T\boldsymbol{W}_3^{'}\boldsymbol{V}_3\,]^T$, where n_1, n_2, and n_3 are the numbers of the GPS measurements, ascending, and descending ALOS InSAR results. The solution of Eq. 6 can be expressed as

$$\hat{\boldsymbol{\theta}} = \boldsymbol{S}^{-1}\boldsymbol{W}_{\theta} \tag{7}$$

In a real application, iteration is needed to obtain an accurate solution by adjusting the weight as follows:

$$\boldsymbol{W}_j^{'\,k} = \frac{c}{\hat{\sigma}_{0j}^2}\boldsymbol{W}_j^{'\,k-1},\ (j = 1, 2, 3) \tag{8}$$

where c is an arbitrary positive constant, which usually can be assumed to be $\hat{\sigma}_{01}^2$. The iteration will not stop until the variance components are almost identical, i.e. $\hat{\sigma}_{01}^2 \approx \hat{\sigma}_{02}^2 \approx \hat{\sigma}_{03}^2$. In the final, the weights from the last iteration are used to determine the optimal three-dimensional surface displacement field with Eq. 5.

Figure 2 shows the flowchart of the ESISTEM-VCE method. The main steps of the proposed method are as follows. S0: Give the studied region that the three-dimensional surface displacement field needs to be solved. S1: Give the GPS, ascending, and descending InSAR measurements, and divide them into three groups. S2: Determine the d_j according to formula in Guglielmino et al. (2011) with Eq. 4, and compute the $\boldsymbol{W}_j$ $(j = 1, 2, 3)$ according to their standard deviations. S3: Use Eq. 3 to compute the weighted $\boldsymbol{W}_j^{'}$ of the RPs. S4: Compute the estimated unknown vector with Eq. 5. S5: Compute the variance components $\hat{\sigma}_{0j}^2$, $(j = 1, 2, 3)$ with Eq. 7. S6: Use Eq. 8 to update the weight matrix $\boldsymbol{W}_j^{'}$, $(j = 1, 2, 3)$ and go to S4. If $\hat{\sigma}_{01}^2 \approx \hat{\sigma}_{02}^2 \approx \hat{\sigma}_{03}^2$, terminate the iteration. S7: Determine the optimal three-dimensional surface displacement with Eq. 5. S8: Go to S0 until the points in the studied area are all solved.

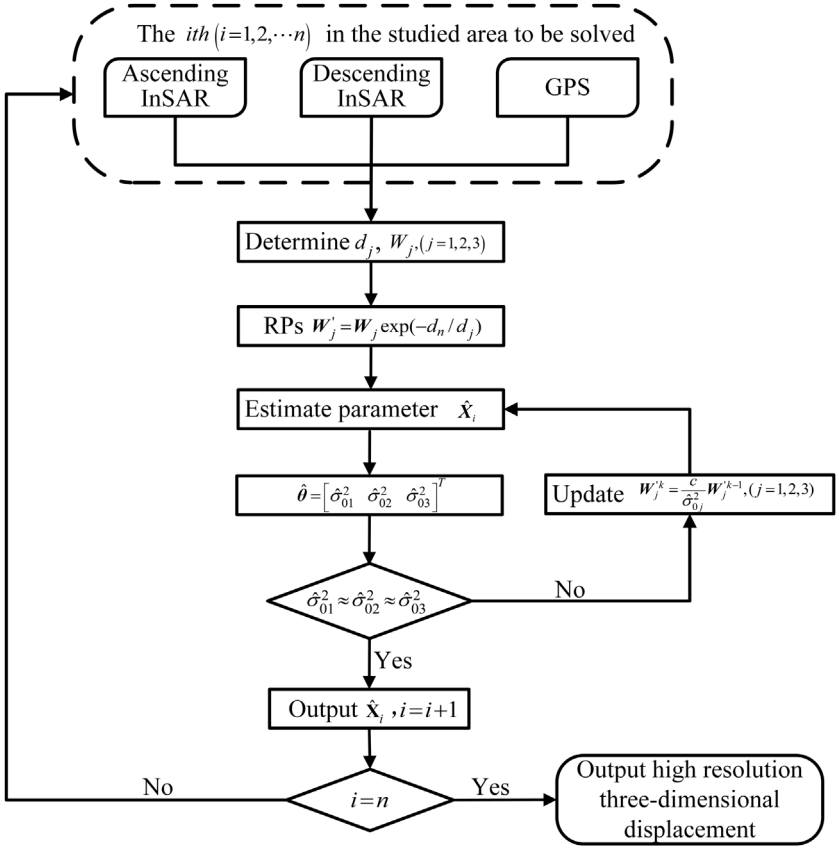

FIGURE 2
The flowchart of the ESISTEM-VCE method.

Simulation experiments

The ESISTEM-VCE method is tested and compared with the ESISTEM method by simulation experiments. The simulated LOS and GPS displacements are obtained from the three-dimensional surface displacement under a given fault slip based on the elastic half-space dislocation theory (Okada, 1985). The model parameters are shown in Table 1, and the slip distribution is shown in Figure 3A. Figures 3B–D show the three-dimensional surface displacement with a cell size of 5 km × 5 km. Two InSAR LOS displacements are calculated from the simulated three-dimensional displacement field with mean unit vectors, [−0.6058, −0.1776, 0.7753] and [0.5855, −0.1697, 0.7919] for ascending and descending ALOS LOS measurements, respectively, based on the InSAR data for the 2010 earthquake (Figures 3E,F). The spatially correlated noises with 1 cm standard deviation on a scale length of 10 km are added to the LOS displacements (Lohman and Simons, 2005; Luo and Chen, 2016). The black dots in Figure 3B are the selected points that are assumed to be GPS stations, and unbiassed Gaussian noises with standard deviations of 3 and 5 mm are added to the horizontal and vertical displacements, respectively.

Figure 4 shows the average three-dimensional displacement fields of 400 tests, which are obtained by Monte Carlo simulation using the ESISTEM-VCE and ESISTEM methods, respectively. It can be found that the derived displacements are both consistent with the simulated ones. However, the displacements of E-W and U components from the ESISTEM method are underestimated. The results from the ESISTEM-VCE method are closer to the simulated values and smoother than those from ESISTEM method in three components.

To quantitatively evaluate the performance of both methods, we use the root mean square error (RMSE)

$$RMSE=\sqrt{\left[X_{sub}-\hat{X}_{sub}\right]^2/num}\,(sub=e,n,u) \tag{9}$$

where num is the total number of points, X_{sub} are the simulated displacements in three components, and $\hat{X}_{sub}$ are the derived ones from the ESISTEM-VCE and ESISTEM methods.

Table 2 shows the average RMSEs in three components from different methods. Meanwhile, Figure 5 displays the RMSEs for

TABLE 1 Model parameters in the experiments.

Length(km)	Width (km)	Strike(°)	Dip(°)	Rake(°)
660	260	16.8	15	116

400 tests. As expected, the RMSEs of the three-dimensional displacements from the ESISTEM-VCE method are lower than those from the ESISTEM method. Compared with the ESISTEM method, the ESISTEM-VCE method achieves 97.1%, 3.9%, and 84% improvements in three components, respectively. It is obvious that the RMSE of the N-S component is larger than those of the E-W and U components, and the accuracy and improvement are worse than the other two components. This is mainly because the LOS displacement is not sensitive to the north-south direction, and the N-S displacement is mainly constrained by the GPS data.

Furthermore, we assumed that the distance–decaying constants for the ascending and descending InSAR measurements are the same as that of GPS measurements in the ESISTEM-VCE method, which is named ESISTEM-VCE (same *d0*) method. This method is used to compare and verify the significance of the different *d0* for different data sets that differ in their spatial scales. The RMSEs are also listed in Table 2, and the improvements are slightly lower than those of ESISTEM-VCE method, which shows that the ESISTEM-VCE performs best. Since the spatial scales of GPS, ascending, and descending InSAR data are different, it is critical to give them different distance–decaying constants, which can be supported by the improvements.

For the ESISTEM-VCE method, the number of RPs is vital for the accuracy of the method. A random Monte Carlo simulation with RPs ranging from 10 to 150 was carried out to assess the performances of the ESISTEM-VCE method. The behavior of the RMSEs versus the number of RPs is reported in

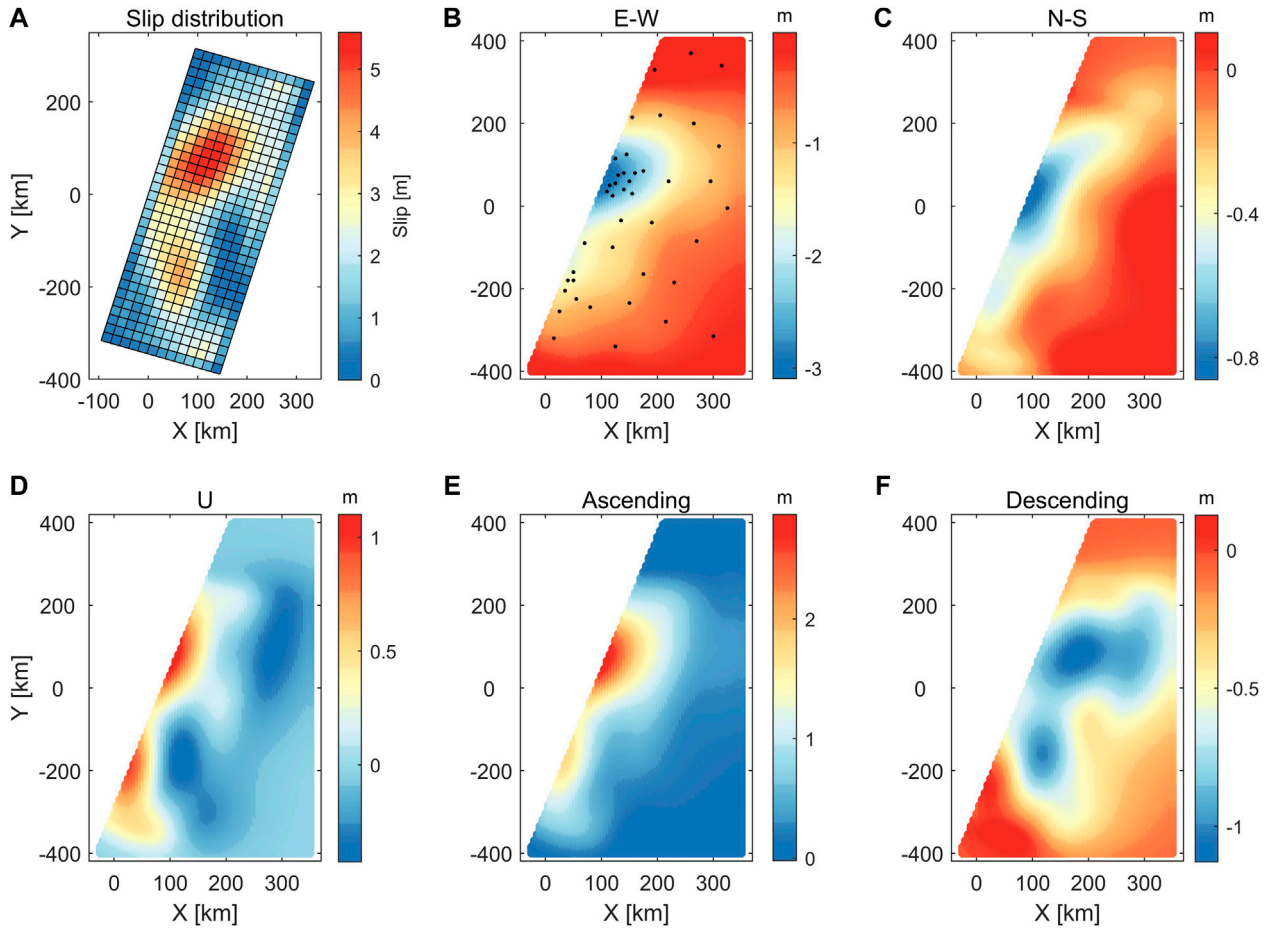

FIGURE 3
The simulated data used in the simulation experiments. **(A)** The slip distribution. **(B–D)** The simulated three-dimensional displacement field according to the elastic half-space dislocation theory. **(E,F)** The simulated ascending and descending InSAR displacements.

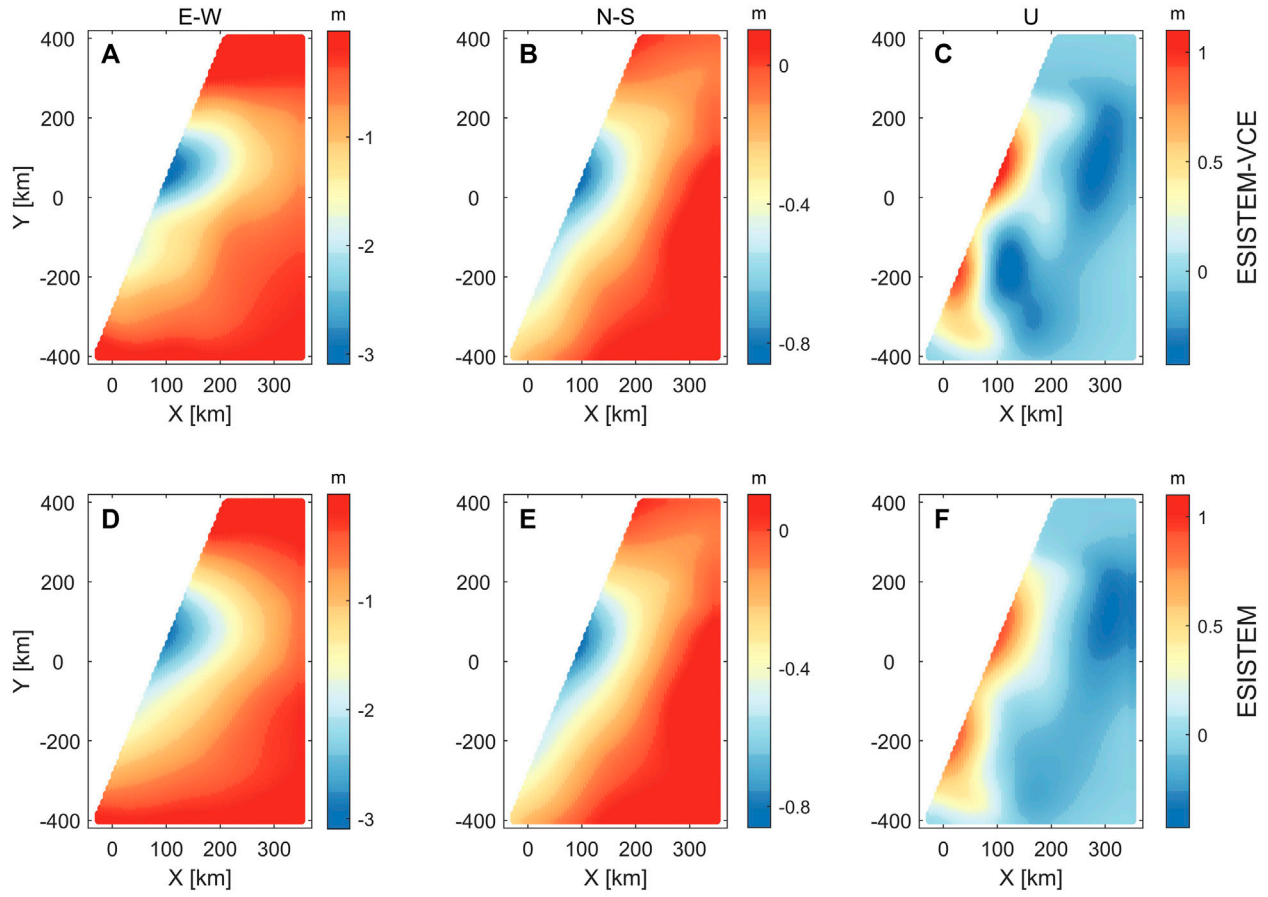

FIGURE 4
Solutions of ESISTEM-VCE and ESISTEM methods for simulation example. The upper row **(A-C)** is from the ESISTEM-VCE method, the low row **(D-F)**is from the ESISTEM method.

TABLE 2 The RMSEs for the EISISTEM-VCE and ESISTEM methods.

Method	E-W (m)	N-S (m)	U (m)
ESISTEM	0.103	0.064	0.100
ESISTEM-VCE (same *d0*)	0.010	0.061	0.020
ESISTEM-VCE	0.003	0.061	0.016
Improvements	97.1%/90.3%[a]	3.9%/3.9%[a]	84%/80%[a]

[a]Improvements calculated by ESISTEM-VCE, ESISTEM-VCE (same *d0*) relative to ESISTEM, respectively.

Figure 6. As expected, it is possible to see that the RMSEs of all three components decrease (the accuracies of the methods increase) with the increase of RPs and tend to be flat. The RMSEs of the N-S component are also greater than the other two components, which is consistent with the performance of Figure 5. Additionally, Figure 6 suggests that, in our simulation experiments, a good tradeoff between the accuracies and the number of RPs can be obtained with 50–60 RPs.

Three-Dimensional displacement field of the 2010Mw 8.8 Maule earthquake

GPS and InSAR data

We assembled a database of GPS and InSAR observations to extract the three-dimensional displacement field of the 2010 Mw

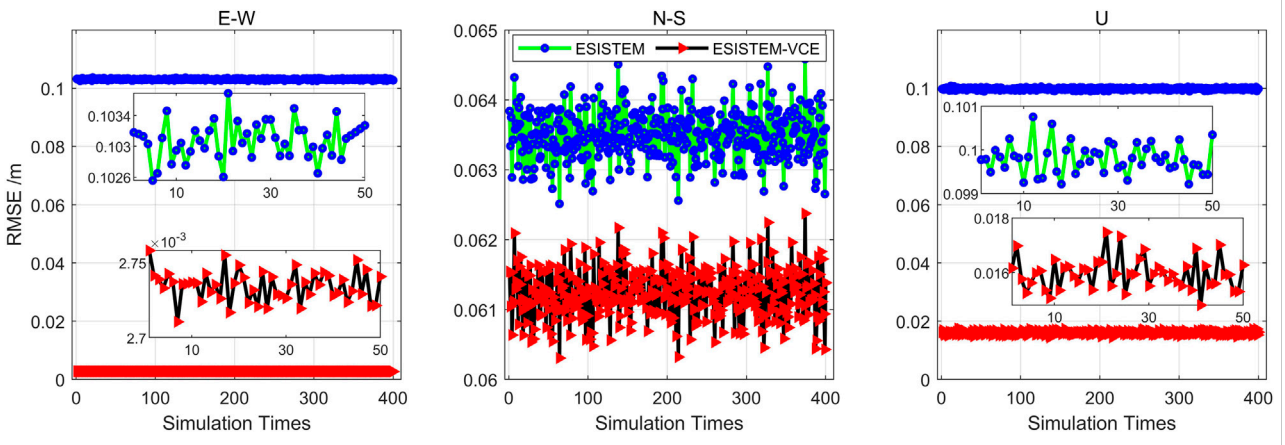

FIGURE 5
The RMSEs for three components from ESISTEM-VCE and ESISTEM methods with 400 Monte Carlo simulations. The black and green lines represent the RMSEs of the ESISTEM-VCE and ESISTEM methods, respectively. The subfigures in E-W and U components are partial enlarged view, respectively.

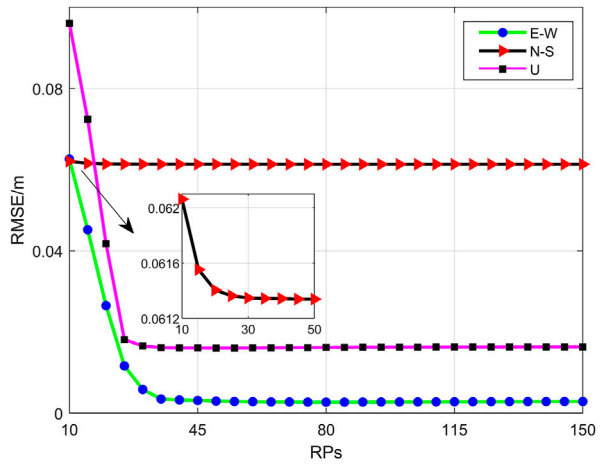

FIGURE 6
The accuracies (RMSEs) versu the RPs.

8.8 Maule earthquake (Figure 7). The GPS data were obtained from Tong et al. (2010), Delouis et al. (2010), Vigny et al. (2011), Moreno et al. (2012), and Melnick et al. (2013). There are 77 stations in total (Figure 7A). The GPS data available prior to the 27th February 2010 Maule earthquake were collected at different times before and re-observed within a few days to months after the event. They were observed on existing benchmarks installed in the framework of the South American Geodynamic Activities (SAGA) project, Central Andes GPS Project (CAP), Concepción Geodetic Activities (COGA) project (Bevis et al., 2001; Klotz et al., 2001; Moreno et al., 2011). These GPS data were processed with the GAMIT/GLOCK software (King and Bock, 2000; Herring et al., 2009) and Bernese GPS software V5.0 (Dach et al., 2007) to estimate the coseismic displacement at each station affected by the Maule earthquake. Detailed information on data acquisition and processing can be found in the references above.

The ALOS data were from Tong et al. (2010). Nine tracks (T111-T119) of ascending InSAR data were obtained with the Fine Beam Single Polarization (FBS) strip-mode (Figure 7B). Two tracks of descending data were obtained with two subswaths (T422-subswaths 3–4) of Scanning Synthetic Aperture Radar (ScanSAR) mode and ScanSAR-FBS mode, and one track (T420) of FBS-FBS mode (Tong et al., 2010) (Figure 7C). The various mode SAR data were processed by using the FBS to ScanSAR software and ScanSAR-ScanSAR processor (Tong et al., 2010) of GMTSAR software (Sandwell et al., 2008). The unwrapped interferograms were converted into LOS displacements composed of 820 and 1112 data points for ascending (the maximum displacement is 418 cm) and descending InSAR observations (the maximum negative displacement is 374 cm), respectively, which are available at ftp://topex.ucsd.edu/pub/chile_eq/. The more detailed information can be referred to Tong et al. (2010).

Results and discussions

Figures 8A–F show the three-dimensional surface displacement fields for the Maule earthquake with GPS and InSAR data derived from ESISTEM-VCE and ESISTEM methods. The derived displacement field is in the hanging wall of the ruptured fault that occurs on the subduction

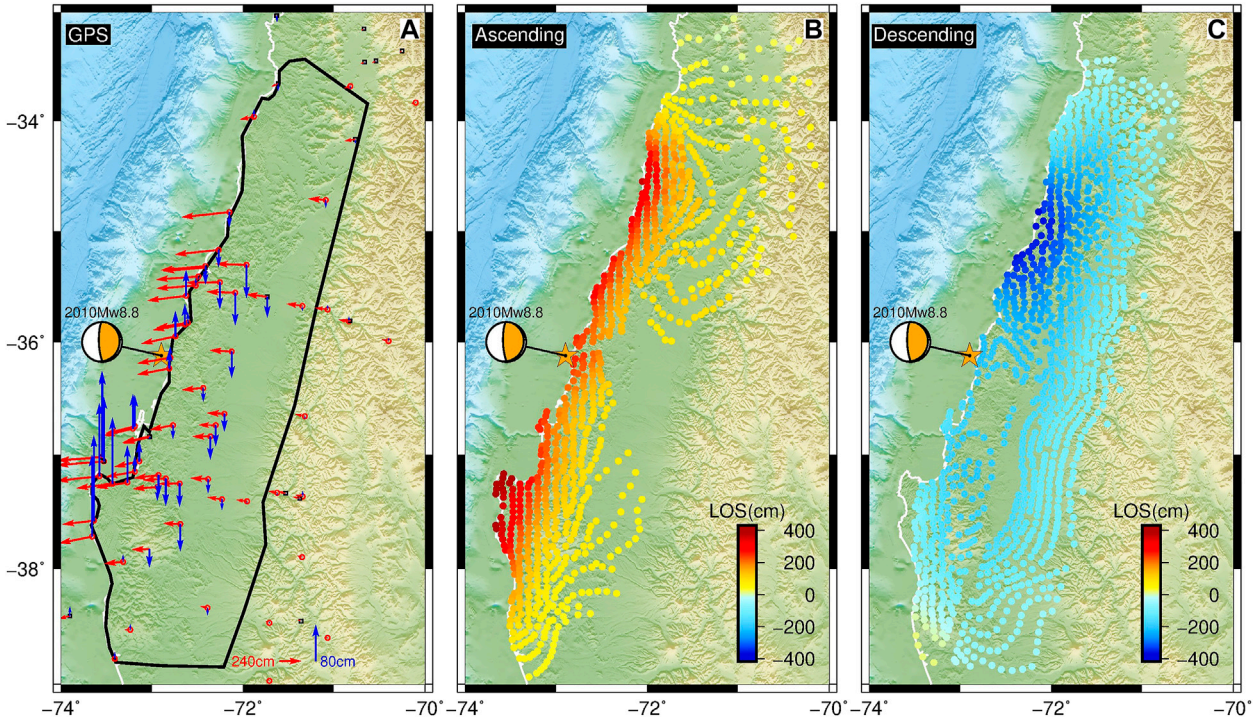

FIGURE 7
The distribution of the data set used in this study. **(A)** The GPS data; the black line denotes the area of three-dimensional displacement to be estimated. **(B)** The ascending ALOS LOS displacements. **(C)** The descending ALOS LOS displacements.

interface, whose strike angle is N16.8°E according to Tong et al. (2010).

Figure 8A shows that the E-W displacement is dominated by the seaward movement. The most intense deformation zone is located to the north of the epicenter, with a maximum value of 495.5 cm near the city of Constitución. The other significant deformation zone is located to the south of the epicenter, with a maximum value of 396.2 cm. These two locations are generally consistent with the large LOS displacements of the corresponding regions in Figures 7B,C. Meanwhile, these maximum value areas display that this event ruptured along the north and south directions, which are consistent with the significant coseismic slip areas in published slip models (e.g., Tong et al., 2010; Vigny et al., 2011; Lin et al., 2013).

Compared to the E-W deformation, the magnitude of the N-S deformation (Figure 8B) is significantly small, and the spatial distribution is different from the E-W component. For example, the most significant deformation of N-S is located around the epicenter, while that of E-W is at the north of the epicenter. The displacement along the coastline moves southward, with a maximum displacement of 72.5 cm, while that away from the coastline moves northward.

The vertical displacement (Figure 8C) demonstrates that the overall magnitude of displacement is smaller than that in the E-W component. The displacement ranges from −103.8 to 211.8 cm, and the maximum surface uplift is located south of the epicenter. Along the coastline, the displacement can be roughly divided into three areas, the areas corresponding to the black, red, and blue lines, which is consistent with the results of Vigny et al. (2011). The north (corresponding to the black line) and south (corresponding to the blue line) areas show the surface uplift. The zone of the epicenter reveals the uplift with displacement lower than 50 cm, which can not be reflected from the sparse GPS or InSAR observations alone. Vigny et al. (2011) described that the data near the epicenter of blue lines (−36.7° to −35.8°) are scarce or lacking. Combined with the GPS data, InSAR observations could detect more deformation information that can not be obtained by a single data source. This implies that the InSAR data can better complement the GPS data in the extraction of three-dimensional displacement.

Figures 8D–F present the three-dimensional surface displacement field from the ESISTEM method. It is noticeable that the deformation characteristics are similar to those of the ESISTEM-VCE method. However, the magnitude of the vertical displacements is underestimated especially in the north or south of the epicenter, which is consistent with the situation in the simulation examples. This should be attributed to the inaccurate weight ratio among the GPS, ascending, and descending ALOS InSAR data.

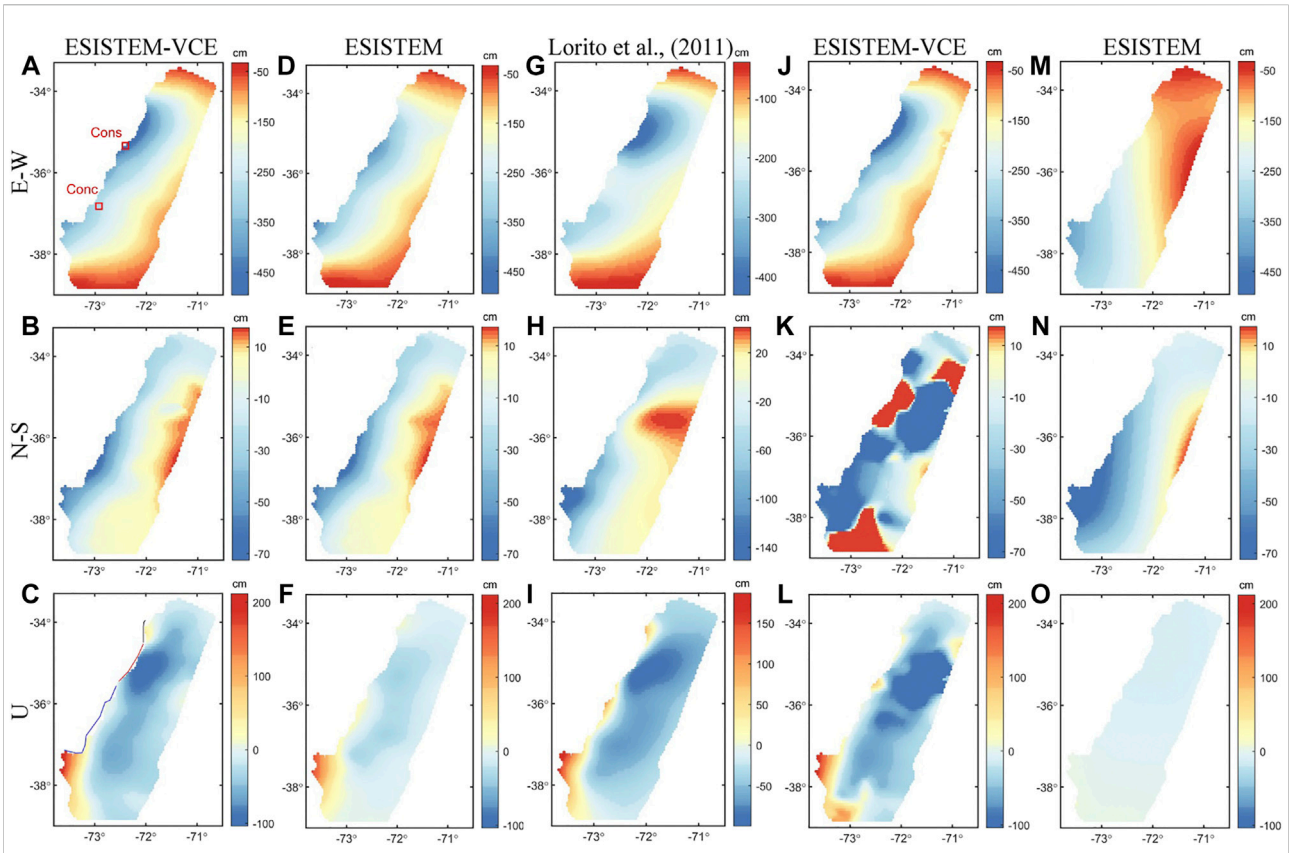

FIGURE 8
Three-dimensional surface displacement field derived from different data sources. **(A–C)** Three-dimensional surface displacement field derived from the ESISTEM-VCE method with all data. In **(A)**, the red rectangles denote the locations of surrounding cities. **(D–F)** Three-dimensional surface displacement field derived from the ESISTEM method with all data. **(G–I)** Three-dimensional displacement field from forward modeling with the slip distribution model from Lorito et al. (2011). **(J–L)** Three-dimensional displacement field derived from the continuous GPS and LOS data with the ESISTEM-VCE method. **(M–O)** Three-dimensional displacement field derived from the continuous GPS and LOS data with the ESISTEM method.

To verify that the vertical displacement is underestimated and to assess the accuracy of our methods quantitatively, we compared the derived displacements to the land-level changes estimated through observations of bleached lithothamnioids crustose coralline algae, submerged quays and piers and flooded beaches, flooded river bars with submerged and flooded trees, and swampy vegetation (Vargas et al., 2011). Figure 9 shows the comparison among the vertical displacements from the field investigation, the ESISTEM-VCE, and the ESISTEM methods, with their corresponding uncertainties also given. It shows that the displacements from the ESISTEM-VCE method are closer to the field investigations than those from ESISTEM method. The overall uncertainties of the ESISTEM-VCE method are smaller than those of ESISTEM method. We obtained the RMSEs between the derived vertical displacements and field investigations, and they are 32.1 and 44.5 cm for ESISTEM-VCE and ESISTEM methods, respectively. Compared to the ESISTEM method, an improvement of 27.9% is achieved by the ESISTEM-VCE method, which should be attributed to the more accurate variance and weight estimations of the InSAR and GPS measurements.

The reliability of the three-dimensional displacement field obtained by the ESISTEM-VCE method is further verified. The slip distribution model given by Lorito et al. (2011) is used to obtain the three-dimensional displacement field from forward modeling (Figures 8G–I). Compared to Figures 8A–C, we found that the deformation patterns are consistent with each other near the epicenter and along the coastline. Whereas, in the area distant from the coastline, they show some differences, especially in the N-S component. These differences may be due to different data constraints and methods used. The results of Figures 8G–I are derived from the forward modeling with the slip distribution based on the elastic dislocation theory, in which the fault plane is divided into 200 subfaults of 25 × 25 km with a large scale. Nevertheless, the similar deformation patterns suggest that the derived results from GPS and InSAR data using the ESISTEM-VCE method are reasonable.

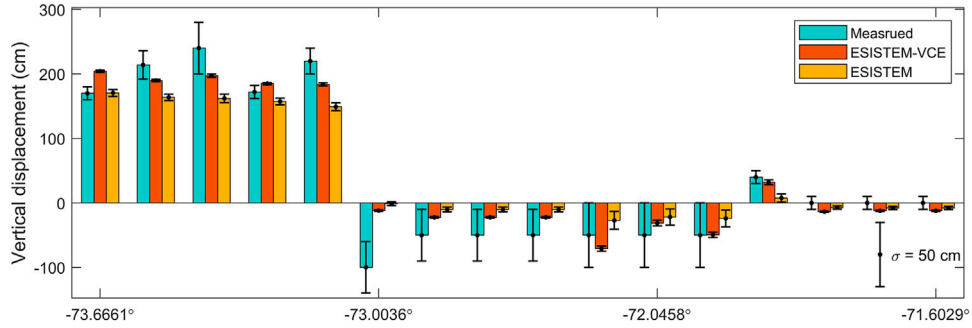

FIGURE 9
Comparison among the vertical displacements measured from field investigation, derived from the ESISTEM-VCE and the ESISTEM methods. The error bars denote the 2σ uncertainties.

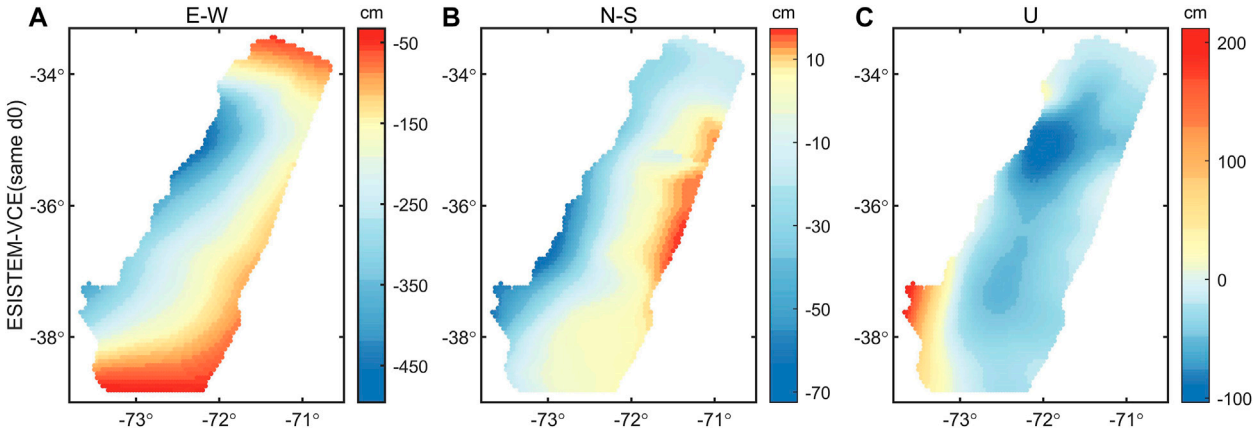

FIGURE 10
Three-dimensional surface displacement field derived from the ESISTEM-VCE method with the same distance–decaying constants for GPS and InSAR data. **(A)** The east-west displacement. **(B)** The north-south displacement. **(C)** The vertical displacement.

The abundant independent observations are helpful to extract the accurate and detailed three-dimensional deformation field. We collected the continuous and campaign GPS data in this study. As is known to us that the precision of the continuous GPS data is higher than the campaign ones. To highlight the importance of campaign GPS data, we retrieved the three-dimensional deformations only with the continuous GPS data and LOS measurements using the ESISTEM-VCE (Figures 8J–L) and ESISTEM (Figures 8M–O) methods. Figures 8A–F,J–O show that the magnitudes and characteristics of deformation are quite different, especially in the N-S components. This should be related to that a few continuous GPS stations can not sufficiently provide constraints on the magnitude and trend of deformation and cannot make up for the insensitivity of LOS measurements to the north-south component. However, it is observed that the magnitudes of displacements in Figures 8J,L are closer to Figures 8A,C than those in Figures 8M,O. This demonstrates that the VCE method is still capable of determining the accurate relative weights between GPS and ALOS data sets. It also manifests that the N-S displacement is mostly constrained by the GPS observations, and the campaign GPS observations play a dominant role in the reconstruction of precise three-dimensional surface deformation.

In addition, the three-dimensional displacement field derived from the ESISTEM-VCE (same *d0*) method is shown in Figure 10, with the distance-decaying constants for ascending and descending InSAR measurements are same as that of GPS data. Figure 10 shows a deformation pattern similar to Figures 8A–C. The RMSE between the vertical displacements from ESISTEM-VCE (same *d0*) and the field investigations is also obtained, which is 35.2 cm. Compared with ESISTEM method, 20.9% improvement is achieved. The comparisons of 27.9 and 20.9% show that

the distance–decaying constants of different data sets should be considered. This also implies that the ESISTEM-VCE method is effective.

The predominantly westward horizontal motion reveals that there existed the right-lateral strike-slip component in the main rupture region, with the east-west extrusion and north-south dextral shear. Meanwhile, it shows that the rupture of this event was bilateral, and propagated to north and south from the epicenter (Lay et al., 2010; Koper et al., 2012; Yue et al., 2014). The case of predominantly east-west displacement could also occur in large subduction zones, such as South America, Japan, or Cascadia (Grandin et al., 2016). A few minutes after the Maule earthquake, large tsunami waves hit the coast ranging from about −39° to −33° (Figure 1). The localized maximum runup of 29 m is located at Constitución, and the runup distribution exhibited almost a decaying trend along the north with runup heights typically of 5–10 m (Fritz et al., 2011; Vargas et al., 2011). The magnitude of displacement decreases from Constitución to the north in the E-W component, showing a similar trend. The predominant deformation in the vertical component along the coastline shows an uplift pattern. These characteristics are coherent with the observations from bleached lithothamnioids crustose coralline algae (Vargas et al., 2011) (Figure 9). The three-dimensional displacement could provide insights into the motion of the tsunami from the similar decaying trend, and be used to make up for insufficient spatial resolution of the coastal uplift measured from bleached lithothamnioids crustose coralline algae or GPS stations.

Conclusion

The three-dimensional displacement field is significant for understanding the characteristics of the seismogenic fault by providing enlightenment of the earthquake rupture. This study develops an improved ESISTEM-VCE method, which is a tight integration of GPS and InSAR data, to derive the three-dimensional displacement field. On one hand, the ESISTEM-VCE method can exploit the spatial correlation of the displacement among adjacent points and determine accurate relative weights between different data sets. On the other hand, the ESISTEM-VCE method can take full advantage of the information about the precision of the GPS measurements and the differences of the spatial scales for different data sets. Thus, the ESISTEM-VCE method can be applied to derive the three-dimensional displacement associated with a transient event such as an earthquake. Simulated experiments are firstly carried out to validate the method. Then, the accurate coseismic three-dimensional displacement field of the 2010 Mw 8.8 Maule earthquake is successfully retrieved for the first time by a combination of GPS and InSAR data. The comparison with the land-level changes from the field investigation also validates that the ESISTEM-VCE method is feasible and valid.

Data availability statement

The original contributions presented in the study are included in the article/Supplementary Material, further inquiries can be directed to the corresponding author.

Author contributions

LX: Investigation, writing-original draft, writing-review and editing, final approval of the version to be submitted. CX: Conceptualization, methodology, supervision, writing-review and editing, funding acquisition, final approval of the version to be submitted. YL: Conceptualization, formal analysis, writing-review and editing, funding acquisition, final approval of the version to be submitted. YZ: Writing-review and editing, final approval of the version to be submitted. JG: Writing-review and editing, final approval of the version to be submitted. FO-C: Writing-review and editing, final approval of the version to be submitted.

Funding

This work is co-supported by the National Natural Science Foundation of China (No. 41721003, No. 41861134009, and No. 41874011), the National Key Research Development Program of China (Grant No. 2018YFC1503603), and PCI PII-180003 ANID-Chile.

Conflict of interest

The authors declare that the research was conducted in the absence of any commercial or financial relationships that could be construed as a potential conflict of interest.

Publisher's note

References

Bevis, M., Kendrick, E., Smalley, R., Jr., Brooks, B., Allmendinger, R., and Isacks, B. (2001). On the Strength of Interplate Coupling and the Rate of Back Arc Convergence in the Central Andes: an Analysis of the Interseismic Velocity Field. *Geochem. Geophys. Geosyst.* 2 (11). doi:10.1029/2001gc000198

Cui, X., Yu, Z., Tao, B., Liu, D., Yu, D., Sun, H., et al. (2001). *Generalized Surveying Adjustment*. 2nd ed Wuhan, China: Wuhan Univ. Press, 102–114.

Dach, R., Hugentobler, U., Fridez, P., and Meindl, M. (2007). *Bernese GPS Software 5.0*. Berne, Switzerland: Astron. Inst. Univ. of Berne. available at http://www.bernese.unibe. ch/docs/DOCU50draft.pdf.

Delouis, B., Nocquet, J. M., and Vallée, M. (2010). Slip Distribution of the February 27, 2010 Mw = 8.8 Maule Earthquake, Central Chile, from Static and High-Rate GPS, InSAR, and Broadband Teleseismic Data. *Geophys. Res. Lett.* 37, L17305. doi:10.1029/2010GL043899

Elliott, J., Jolivet, R., González, P., Avouac, J., Hollingsworth, J., Searle, M., et al. (2016). Himalayan Megathrust Geometry and Relation to Topography Revealed by the Gorkha Earthquake. *Nat. Geosci.* 9, 174–180. doi:10.1038/ngeo2623

Farías, M., Vargas, G., Tassara, A., Carretier, S., Baize, S., Melnick, D., et al. (2010). Land-level Changes Produced by the Mw 8.8 2010 Chilean Earthquake. *Science* 329 (5994), 916. doi:10.1126/science.1192094

Fialko, Y., Simons, M., and Agnew, D. (2001). The Complete (3-D) Surface Displacement Field in the Epicentral Area of the 1999M_W7.1 Hector Mine Earthquake, California, from Space Geodetic Observations. *Geophys. Res. Lett.* 28 (16), 3063–3066. doi:10.1029/2001gl013174

Fritz, H. M., Petroff, C. M., Catalán, P. A., Cienfuegos, R., Winckler, P., Kalligeris, N., et al. (2011). Field Survey of the 27 February 2010 Chile Tsunami. *Pure Appl. Geophys.* 168 (11), 1989–2010. doi:10.1007/s00024-011-0283-5

Fujii, Y., and Satake, K. (2013). Slip Distribution and Seismic Moment of the 2010 and 1960 Chilean Earthquakes Inferred from Tsunami Waveforms and Coastal Geodetic Data. *Pure Appl. Geophys.* 170 (9–10), 1493–1509. doi:10.1007/s00024-012-0524-2

Grandin, R., Klein, E., Métois, M., and Vigny, C. (2016). Three-dimensional Displacement Field of the 2015M_w8.3 Illapel Earthquake (Chile) from across- and Along-track Sentinel-1 TOPS Interferometry. *Geophys. Res. Lett.* 43, 2552–2561. doi:10.1002/2016GL067954

Gudmundsson, S., Sigmundsson, M., and Carstensen, J. (2002). Three-dimensional Surface Motion Maps Estimated from Combined Interferometric Synthetic Aperture Radar and GPS Data. *J. Geophys. Res.* 107 (B10), 2250. doi:10.1029/2001JB000283

Guglielmino, F., Nunnari, G., Puglisi, G., and Spata, A. (2011). Simultaneous and Integrated Strain Tensor Estimation from Geodetic and Satellite Deformation Measurements to Obtain Three-Dimensional Displacement Maps. *IEEE Trans. Geosci. Remote Sens.* 49 (6), 1815–1826. doi:10.1109/tgrs.2010.2103078

Guo, Q., Xu, C., Wen, Y., Liu, Y., and Xu, G. (2019). The 2017 Noneruptive Unrest at the Caldera of Cerro Azul Volcano (Galapagos Islands) Revealed by InSAR Observations and Geodetic Modelling. *Remote Sens.* 11 (17), 1992. doi:10.3390/rs11171992

He, P., Wen, Y., Xu, C., and Chen, Y. (2019). Complete Three-Dimensional Near-Field Surface Displacements from Imaging Geodesy Techniques Applied to the 2016 Kumamoto Earthquake. *Remote Sens. Environ.* 232, 111321. doi:10.1016/j.rse.2019.111321

He, P., Wen, Y., Xu, C., and Chen, Y. (2018). High-quality Three-Dimensional Displacement Fields from New-Generation SAR Imagery: Application to the 2017 Ezgeleh, Iran, Earthquake. *J. Geod.* 93, 573–591. doi:10.1007/s00190-018-1183-6

Herring, T. A., King, R. W., and McClusky, S. C. (2009). *Documentation of the MIT GPS Analysis Software: GAMIT V 10.35, Mass*. Cambridge: Inst. of Technol.

Hill, E., Borrero, J., Huang, Z., Qiu, Q., Banerjee, P., Natawidjaja, D., et al. (2012). The 2010 Mw 7.8 Mentawai Earthquake: Very Shallow Source of a Rare Tsunami Earthquake Determined from Tsunami Field Survey and Near-Field GPS Data. *J. Geophys. Res.* 117, B06402. doi:10.1029/2012jb009159

Hu, J., Li, Z., Sun, Q., Zhu, J., and Ding, X. (2012). Three-dimensional Surface Displacements from InSAR and GPS Measurements with Variance Component Estimation. *IEEE Geosci. Remote Sens. Lett.* 9 (4), 754–758. doi:10.1109/LGRS.2011.2181154

Hu, J., Liu, J., Li, Z., Zhu, J., Wu, L., Sun, Q., et al. (2021). Estimating Three-Dimensional Coseismic Deformations with the SM-VCE Method Based on Heterogeneous SAR Observations: Selection of Homogeneous Points and Analysis of Observation Combinations. *Remote Sens. Environ.* 255, 112298. doi:10.1016/j.rse.2021.112298

Jiang, Z., Wang, M., Wang, Y., Wu, Y., Che, S., Shen, Z. K., et al. (2014). GPS Constrained Coseismic Source and Slip Distribution of the 2013 Mw 6.6 Lushan, China, Earthquake and its Tectonic Implications. *Geophys. Res. Lett.* 41, 407–413. doi:10.1002/2013GL058812

Jung, H. S., and Hong, S. M. (2017). Mapping Three-Dimensional Surface Deformation Caused by the 2010 Haiti Earthquake Using Advanced Satellite Radar Interferometry. *PLoS ONE* 12 (11), e0188286. doi:10.1371/journal.pone.0188286

Kendrick, E., Bevis, M., Smalley, R., Brooks, B., Vargasc, R., Lauría, E., et al. (2003). The Nazca–South America Euler Vector and its Rate of Change. *J. South Am. Earth Sci.* 16 (2), 125–131. doi:10.1016/S0895-9811(03)00028-2

King, R., and Bock, Y. (2000). *Documentation for the GAMIT GPS Analysis Software*. Massachusetts Institute of Technology and Scripps Institute of Oceanography Cambridge.

Klotz, J., Khazaradze, G., Angermann, D., Reigber, C., Perdomo, R., and Cifuentes, O. (2001). Earthquake Cycle Dominates Contemporary Crustal Deformation in Central and Southern Andes. *Earth Planet. Sci. Lett.* 193, 437–446. doi:10.1016/S0012-821X(01)00532-5

Koper, K. D., Hutko, A. R., Lay, T., and Surfi, O. (2012). Imaging Short-Period Seismic Radiation from the 27 February 2010 Chile (M_W8.8) Earthquake by Back-Projection of*P*, *PP*, and*PKIKP*waves. *J. Geophys. Res.* 117, B02308. doi:10.1029/2011JB008576

Lay, T., Ammon, C. J., Kanamori, H., Koper, K. D., Sufri, O., and Hutko, A. R. (2010). Teleseismic Inversion for Rupture Process of the 27 February 2010 Chile (Mw 8.8) Earthquake. *Geophys. Res. Lett.* 37, L13301. doi:10.1029/2010GL043379

Lin, Y. N., Sladen, A., Ortega-Culaciati, F., Simons, M., Avouac, J., Feilding, E., et al. (2013). Coseismic and Postseismic Slip Associated with the 2010 Maule Earthquake, Chile: Characterizing the Arauco Peninsula Barrier Effect. *J. Geophys. Res. Solid Earth* 118, 3142–3159. doi:10.1002/jgrb.50207

Liu, J., Hu, J., Li, Z., Zhu, J., Sun, Q., and Gan, J. (2018). A Method for Measuring 3-D Surface Deformations with InSAR Based on Strain Model and Variance Component Estimation. *IEEE Trans. Geosci. Remote Sens.* 56 (1), 239–250. doi:10.1109/TGRS.2017.2745576

Liu, J., Hu, J., Xu, W., Li, Z., Zhu, J., Ding, X., et al. (2019). Complete Three-Dimensional Coseismic Deformation Field of the 2016 Central Tottori Earthquake by Integrating Left- and Right-Looking InSAR Observations with the Improved SM-VCE Method. *J. Geophys. Res. Solid Earth* 124 (11), 12099–12115. doi:10.1029/2018jb017159

Lohman, R. B., and Simons, M. (2005). Some Thoughts on the Use of InSAR Data to Constrain Models of Surface Deformation: Noise Structure and Data Downsampling. *Geochem. Geophys. Geosyst.* 6 (1). doi:10.1029/2004GC000841

Lorito, S., Romano, F., Atzori, S., Tong, X., Avallone, A., McCloskey, J., et al. (2011). Limited Overlap between the Seismic Gap and Coseismic Slip of the Great 2010 Chile Earthquake. *Nat. Geosci.* 4 (3), 173–177. doi:10.1038/ngeo1073

Luo, H., and Chen, T. (2016). Three-dimensional Surface Displacement Field Associated with the 25 April 2015 Gorkha, Nepal, Earthquake: Solution from Integrated InSAR and GPS Measurements with an Extended SISTEM Approach. *Remote Sens.* 8 (7), 559. doi:10.3390/rs8070559

Luttrell, K., Tong, X., Sandwell, D., Brooks, B., and Bevis, M. (2011). Estimates of stress drop and crustal tectonic stress from the 27 February 2010 maule, chile, earthquake: Implications for fault strength. *J. Geophys. Res. Solid Earth* 116, B11401. doi:10.1029/2011jb008509

Massonnet, D., Rossi, M., Carmona, C., Adragna, F., Peltzer, G., Feigl, K., et al. (1993). The Displacement Field of the Landers Earthquake Mapped by Radar Interferometry. *Nature* 364 (6433), 138–142. doi:10.1038/364138a0

Melnick, D., Moreno, M., Motagh, M., Cisternas, M., and Wesson, R. L. (2013). Splay Fault Slip during the Mw 8.8 2010 Maule Chile Earthquake: REPLY. *Geology* 41 (12), e310. doi:10.1130/G34825Y.1

Moreno, M., Melnick, D., Rosenau, M., Baez, J., Klotz, J., Tassara, A., et al. (2012). Toward Understanding Tectonic Control on the Mw 8.8 2010 Maule Chile Earthquake. *Earth Planet. Sci. Lett.* 321, 152–165. doi:10.1016/j.epsl.2012.01.006

Moreno, M., Melnick, D., Rosenau, M., Bolte, J., Klotz, J., Echtler, H., et al. (2011). Heterogeneous Plate Locking in the South–Central Chile Subduction Zone: Building up the Next Great Earthquake. *Earth Planet. Sci. Lett.* 305 (3-4), 413–424. doi:10.1016/j.epsl.2011.03.025

Okada, Y. (1985). Surface Deformation Due to Shear and Tensile Faults in a Half-Space. *Bull. Seismol. Soc. Am.* 75, 1135–1154. doi:10.1785/bssa0750041135

Pesci, A., and Teza, G. (2007). Strain Rate Analysis over the Central Apennines from GPS Velocities: The Development of a New Free Software. *Boll. Geod. Sci. Affifini* 56 (2), 69–88.

Pollitz, F. F., Brooks, B., Tong, X., Bevis, M. G., Foster, J. H., Bürgmann, R., et al. (2011). Coseismic Slip Distribution of the February 27, 2010 Mw 8.8 Maule, Chile Earthquake. *Geophys. Res. Lett.* 38, 2011GL047065. doi:10.1029/2011GL047065

Ruegg, J. C., Rudloff, A., Vigny, C., Madariaga, R., Chabalier, J., Campos, J., et al. (2009). Interseismic Strain Accumulation Measured by GPS in the Seismic Gap between Constitución and Concepción in Chile. *Phys. Earth Planet. Interiors* 175, 78–85. doi:10.1016/j.pepi.2008.02.015

Samsonov, S., and Tiampo, K. (2006). Analytical Optimization of a DInSAR and GPS Dataset for Derivation of Three-Dimensional Surface Motion. *IEEE Geosci. Remote Sens. Lett.* 3, 107–111. doi:10.1109/LGRS.2005.858483

Sandwell, D. T., Myer, D., Mellors, R., Shimada, M., Brooks, B., and Foster, J. (2008). Accuracy and Resolution of ALOS Interferometry: Vector Deformation Maps of the Father's Day Intrusion at Kilauea. *IEEE Trans. Geosci. Remote Sens.* 46 (11), 3524–3534. doi:10.1109/TGRS.2008.2000634

Shen, Z., Jackson, D., and Ge, B. (1996). Crustal Deformation across and beyond the Los Angeles Basin from Geodetic Measurements. *J. Geophys. Res.* 101, 27957–27980. doi:10.1029/96jb02544

Song, X., Jiang, Y., Shan, X., and Qu, C. (2017). Deriving 3D Coseismic Deformation Field by Combining GPS and InSAR Data Based on the Elastic Dislocation Model. *Int. J. Appl. Earth Obs. Geoinf.* 57, 104–112. doi:10.1016/j.jag.2016.12.019

Tong, X., Sandwell, D., Luttrell, K., Brooks, B., Bevis, M., Shimada, M., et al. (2010). The 2010 Maule, Chile Earthquake: Downdip Rupture Limit Revealed by Space Geodesy. *Geophys. Res. Lett.* 37, L24311. doi:10.1029/2010GL045805

Vargas, G., Farías, M., Carretier, S., Tassara, A., Baize, S., and Melnick, D. (2011). Coastal Uplift and Tsunami Effects Associated to the 2010 Mw 8.8 Maule Earthquake in Central Chile. *Andean Geol.* 38 (1), 219–238.

Vigny, C., Rudloff, A., Ruegg, J. C., Madariaga, R., Campos, J., and Alvarez, M. (2009). Upper Plate Deformation Measured by GPS in the Coquimbo Gap, Chile. *Phys. Earth Planet* 175 (1-2), 86–95. doi:10.1016/j.pepi.2008.02.013

Vigny, C., Socquet, A., Peyrat, S., Ruegg, J., Métois, M., Madariaga, R., et al. (2011). The 2010 Mw 8.8 Maule Megathrust Earthquake of Central Chile, Monitored by GPS. *Science* 332 (6036), 1417–1421. doi:10.1126/science.1204132

Wang, L., and Gu, W. (2020). A-Optimal Design Method to Determine the Regularization Parameter of Coseismic Slip Distribution Inversion. *Geophys. J. Int.* 221 (1), 440–450. doi:10.1093/gji/ggaa030

Wang, L., Jin, Xi., Xu, W., and Xu, G. (2021). A Black Hole Particle Swarm Optimization Method for the Source Parameters Inversion: Application to the 2015 Calbuco Eruption, Chile. *J. Geodyn.* 146, 101849. doi:10.1016/j.jog.2021.101849

Wang, Y., Hu, J., Liu, J., and Sun, Q. (2021). Measurements of Three-Dimensional Deformations by Integrating InSAR and GNSS: An Improved SISTEM Method Based on Variance Component Estimation. *Geomatics Inf. Sci. Wuhan Univ.* 46 (10), 1598–1608. doi:10.13203/j.whugis20210113

Xiong, L., Xu, C., Liu, Y., Wen, Y., and Fang, J. (2020). 3D Displacement Field of Wenchuan Earthquake Based on Iterative Least Squares for Virtual Observation and GPS/InSAR Observations. *Remote Sens.* 12 (6), 977. doi:10.3390/rs12060977

Xu, C., Ding, K., Cai, J., and Grafarend, E. (2009). Methods of Determining Weight Scaling Factors for Geodetic-Geophysical Joint Inversion. *J. Geodyn.* 47 (1), 39–46. doi:10.1016/j.jog.2008.06.005

Xu, G., Xu, C., Wen, Y., Xiong, W., and Valkaniotis, S. (2020). The Complexity of the 2018 Kaktovik Earthquake Sequence in the Northeast of the Brooks Range, Alaska. *Geophys. Res. Lett.* 47 (19), e2020GL088012. doi:10.1029/2020GL088012

Yang, J., Xu, C., Wang, S., and Wang, X. (2020a). Sentinel-1 Observation of 2019 Mw 5.7 Acipayam Earthquake: A Blind Normal-Faulting Event in the Acipayam Basin, Southwestern Turkey. *J. Geodyn.* 135, 101707. doi:10.1016/j.jog.2020.101707

Yang, J., Xu, C., and Wen, Y. (2020b). The 2019 Mw 5.9 Torkaman Chay Earthquake in Bozgush Mountain, NW Iran: A Buried Strike-Slip Event Related to the Sinistral Shalgun-Yelimsi Fault Revealed by InSAR. *J. Geodyn.* 141-142, 101798. doi:10.1016/j.jog.2020.101798

Yang, Z., Li, Z., Zhu, J., Hu, J., Wang, Y., and Chen, G. (2016). InSAR-based Model Parameter Estimation of Probability Integral Method and its Application for Predicting Mining-Induced Horizontal and Vertical Displacements. *IEEE Trans. Geosci. Remote Sens.* 54 (8), 4818–4832. doi:10.1109/tgrs.2016.2551779

Yue, H., Lay, T., Rivera, L., An, C., Vigny, C., Tong, X., et al. (2014). Localized Fault Slip to the Trench in the 2010 Maule, ChileM_w= 8.8 Earthquake from Joint Inversion of High-Rate GPS, Teleseismic Body Waves, InSAR, Campaign GPS, and Tsunami Observations. *J. Geophys. Res. Solid Earth* 119, 7786–7804. doi:10.1002/2014JB011340

Zhang, B., Ding, X., Amelung, F., Wang, C., Xu, W., Zhu, W., et al. (2021). Impact of Ionosphere on InSAR Observation and Coseismic Slip Inversion: Improved Slip Model for the 2010 Maule, Chile, Earthquake. *Remote Sens. Environ.* 267, 112733. doi:10.1016/j.rse.2021.112733

Zhou, Y., Parsons, B. E., and Walker, R. T. (2018). Characterizing Complex Surface Ruptures in the 2013 M_w 7.7 Balochistan Earthquake Using Three-Dimensional Displacements. *J. Geophys. Res. Solid Earth* 123 (11), 10191–10211. doi:10.1029/2018jb016043

Appendix A: The ESISTEM method

The linear equation for the ESISTEM method is

$$\boldsymbol{d} = \boldsymbol{AX} + \boldsymbol{e}$$

where $\boldsymbol{d}$ is the observation vector

$$\boldsymbol{d} = \begin{bmatrix} \boldsymbol{d}_1 \\ \boldsymbol{d}_2 \\ \boldsymbol{d}_3 \end{bmatrix} = \begin{bmatrix} \boldsymbol{d}_{GPS} \\ \boldsymbol{d}_{ASC} \\ \boldsymbol{d}_{DES} \end{bmatrix}$$

and $\boldsymbol{A}$ is the design matrix

$$\boldsymbol{A} = \begin{bmatrix} \boldsymbol{A}_1 \\ \boldsymbol{A}_2 \\ \boldsymbol{A}_3 \end{bmatrix} = \begin{bmatrix} \boldsymbol{A}_{GPS} \\ \boldsymbol{S}_{ASC}\boldsymbol{A}_{ASC} \\ \boldsymbol{S}_{DES}\boldsymbol{A}_{DES} \end{bmatrix}$$

the matrices forms of the $\boldsymbol{A}_{GPS}$, $\boldsymbol{A}_{ASC}$, and $\boldsymbol{A}_{DES}$ are

$$\boldsymbol{A}_j = \begin{bmatrix} 1 & 0 & 0 & \Delta x_e^1 & \Delta x_n^1 & \Delta x_u^1 & 0 & 0 & 0 & 0 & \Delta x_u^1 & -\Delta x_n^1 \\ 0 & 1 & 0 & 0 & \Delta x_e^1 & 0 & \Delta x_n^1 & \Delta x_u^1 & 0 & -\Delta x_u^1 & 0 & \Delta x_e^1 \\ 0 & 0 & 1 & 0 & 0 & \Delta x_e^1 & 0 & \Delta x_n^1 & \Delta x_u^1 & \Delta x_n^1 & -\Delta x_e^1 & 0 \\ \vdots & \vdots & \vdots & \vdots & \vdots & \vdots & \vdots & \vdots & \vdots & \vdots & \vdots & \vdots \\ 1 & 0 & 0 & \Delta x_e^N & \Delta x_n^N & \Delta x_u^N & 0 & 0 & 0 & 0 & \Delta x_u^N & -\Delta x_n^N \\ 0 & 1 & 0 & 0 & \Delta x_e^N & 0 & \Delta x_n^N & \Delta x_u^N & 0 & -\Delta x_u^N & 0 & \Delta x_e^N \\ 0 & 0 & 1 & 0 & 0 & \Delta x_e^N & 0 & \Delta x_n^N & \Delta x_u^N & \Delta x_n^N & -\Delta x_e^N & 0 \end{bmatrix}, (j = GPS/ASC/DES)$$

the $\boldsymbol{S}_m\,(m = ASC/DES)$ in the matrix $\boldsymbol{A}$ is composed of the projection coefficients that for the ascending/descending InSAR measurements from E-W, N-S, and U components to LOS displacement.

And $\boldsymbol{X}$ is the parameter vector

$$\boldsymbol{X} = \begin{bmatrix} d_e^0 & d_n^0 & d_u^0 & \varepsilon_{11} & \varepsilon_{12} & \varepsilon_{13} & \varepsilon_{22} & \varepsilon_{23} & \varepsilon_{33} & \omega_1 & \omega_2 & \omega_3 \end{bmatrix}^{\mathrm{T}}$$

where ε and ω representing strain tensor and rigid body rotation tensor, respectively.

frontiers | Frontiers in Earth Science

TYPE Original Research
PUBLISHED 15 September 2022
DOI 10.3389/feart.2022.976380

OPEN ACCESS

EDITED BY
Caijun Xu,
Wuhan University, China

REVIEWED BY
Kaihua Ding,
China University of Geosciences
Wuhan, China
Xuhua Shi,
Zhejiang University, China
Ming Hao,
The Second Monitoring and Application
Center, China Earthquake
Administration, China

*CORRESPONDENCE
Kaiying Wang,
wangky@ies.ac.cn

SPECIALTY SECTION
This article was submitted to Structural Geology and Tectonics,
a section of the journal
Frontiers in Earth Science

RECEIVED 23 June 2022
ACCEPTED 24 August 2022
PUBLISHED 15 September 2022

CITATION
Wang K and Feng X (2022), Crustal deformation and dynamics of the south-eastern tibetan plateau from stress fields and geodesy.
Front. Earth Sci. 10:976380.
doi: 10.3389/feart.2022.976380

Crustal deformation and dynamics of the south-eastern tibetan plateau from stress fields and geodesy

Kaiying Wang[1]* and Xiangdong Feng[2]

[1]State Key Laboratory of Earthquake Dynamics, Institute of Geology, Beijing, China, [2]Hebei Earthquake Agency, Shijiazhuang, China

South-eastern Tibet rotates clockwise around the eastern Himalayan syntaxis due to the eastward extrusion of the eastern Tibetan lithosphere and it attracts much attention as a window for studying the dynamics of continental collision between India and Eurasia. Competing geodynamic models to describe the deformation of the eastern Tibet have been the debating subject and the dynamic processes responsible for plateau evolution remain poorly understood, partly because the mechanical state at depth and its relationship with surficial deformation are unclear. In this context, a continuous east-west oriented tensional zone was identified at the south-eastern edge of the Tibetan Plateau based on seismogenic stress field and global positioning system data. The profiles of surficial velocity field reveal a relatively speedy motion belt parallel to the Xianshuihe fault extending from north to south in the rotating region east of the tensional zone. Segmented features of the profiles around the extensional zone indicate its close relation with flow channels delineated from magnetotelluric images. Therefore, the deformation at the south-eastern edge of the Tibetan Plateau is mechanically coupled within the crustal depth. We propose a complex regional kinematics with a localised speedy belt and a continuously extensional zone, where material coupling and deformation compatibility were revealed within the crustal depth.

KEYWORDS

south-eastern Tibetan plateau, focal mechanism, stress field, global positioning system, surface velocity field

Introduction

The India-Eurasia collision has been well established to provide a critical control on the present-day crustal stress field and tectonic deformation in the Tibetan Plateau and its surrounding region. As a result of post-collisional convergence, south-eastern Tibet rotates clockwise around the eastern Himalayan syntaxis (Burchfiel et al., 1995; Chen et al., 2000; England and Houseman, 1986; Royden et al., 1997; Tapponnier and Molnar, 1976; Tapponnier et al., 1982; Wang et al., 1998; Wang and Shen, 2020) due to the eastward extrusion of the lower crustal materials from the plateau, obstruction by the

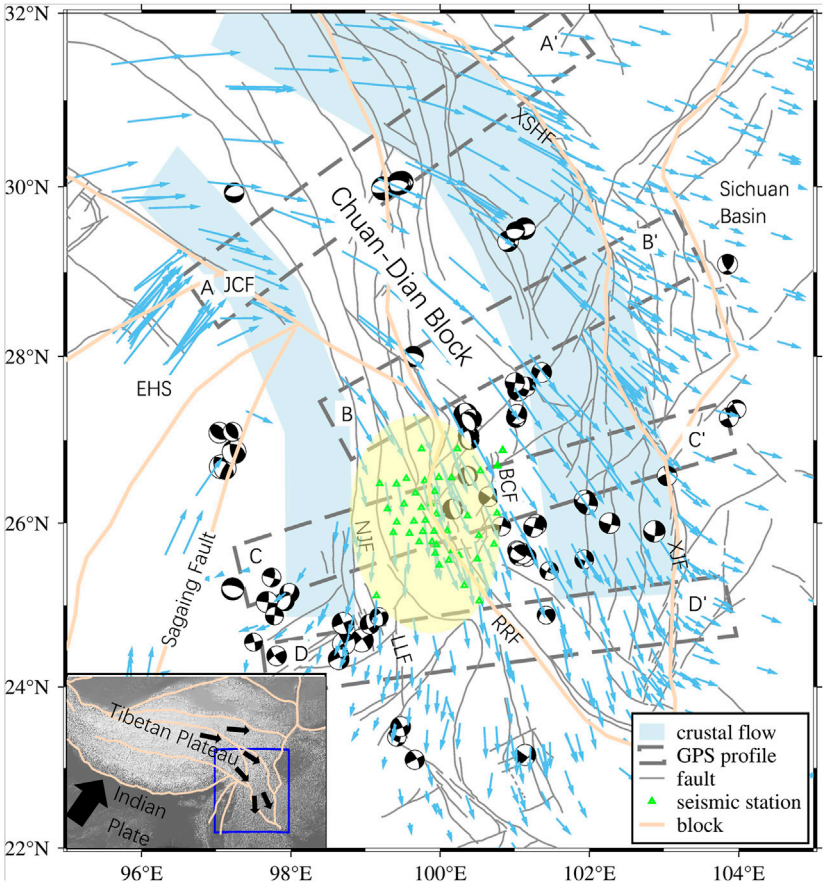

FIGURE 1
Topographic map of south-eastern Tibet. Focal mechanism (1976–2010): from the global CMT catalogue; blue arrows: GPS velocity field relative to Eurasian Plate (Wang and Shen, 2020); Light blue polygons represent crustal flow channels delineated using magnetotelluric data (Bai et al., 2010). The yellow area represents the extensional zone based on focal mechanism and GPS analysis; Black arrows show regional crustal motions. NJF = Nujiang Fault; LLF = Longling Fault; BCF = Binchuan Fault; RRF = Red-River Fault; XSHF = Xianshuihe Fault; XJF = Xiaojiang Fault; JCF = Jiali–Chayu Fault; and EHS = eastern Himalayan syntaxis.

Sichuan Basin (which appears to be deeply rooted and mechanically strong), and certain materials turning southward. The clockwise rotation can be deduced from the distribution of global positioning system (GPS) movement rates (Zhang et al., 2004; Wang and Shen, 2020), major fault slip rates, such as 9–12 mm sinistral slip rates along the Xianshuihe-Xiaojiang fault system (Xu et al., 2003; Wang et al., 2009; Gan et al., 2021), and sinistral coseismic rupture of large earthquakes along the major fault (Figure 1).

The deformation and dynamics of the south-eastern edge of the Tibetan Plateau are important for understanding continent collision where a part of the plateau material is extruded. Several geophysical observation studies in south-eastern Tibet have suggested that low-velocity or mechanically weak zones exist in the mid-lower crust and indicate the possibility of crustal flow (Bai et al., 2010; Bao et al., 2015; Chen et al., 2016; Fu et al., 2010; Li et al., 2008; Liu et al., 2014; Xu and Song, 2010; Yao et al., 2010; Zhao et al., 2013). Although the existence of weak lower crust and probable crustal flow in south-east (SE) Tibet has attracted significant attention, the mechanism remains enigmatic in determining how the crustal material structure, including a weak lower crust, influences the crustal deformation and how the tectonic stress field links dynamics between the surficial and deep deformations. Mid-crustal deformation is not directly constrained by surficial measurements, and the motion may be different from that observed at the surface, considering the coupling of crustal materials at different depths.

In 2018, our dense digital seismic network (30 stations) with a sampling rate of 100 Hz, was deployed within a $2^{\circ} \times 2^{\circ}$ area near the middle of the Sichuan-Yunnan block, which is bounded by

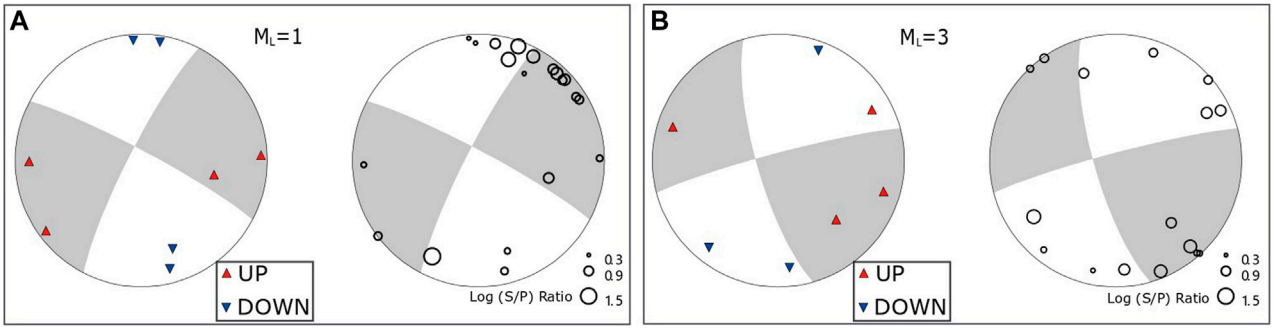

FIGURE 2
Two focal mechanism cases based on P-wave polarities and S/P ratios.

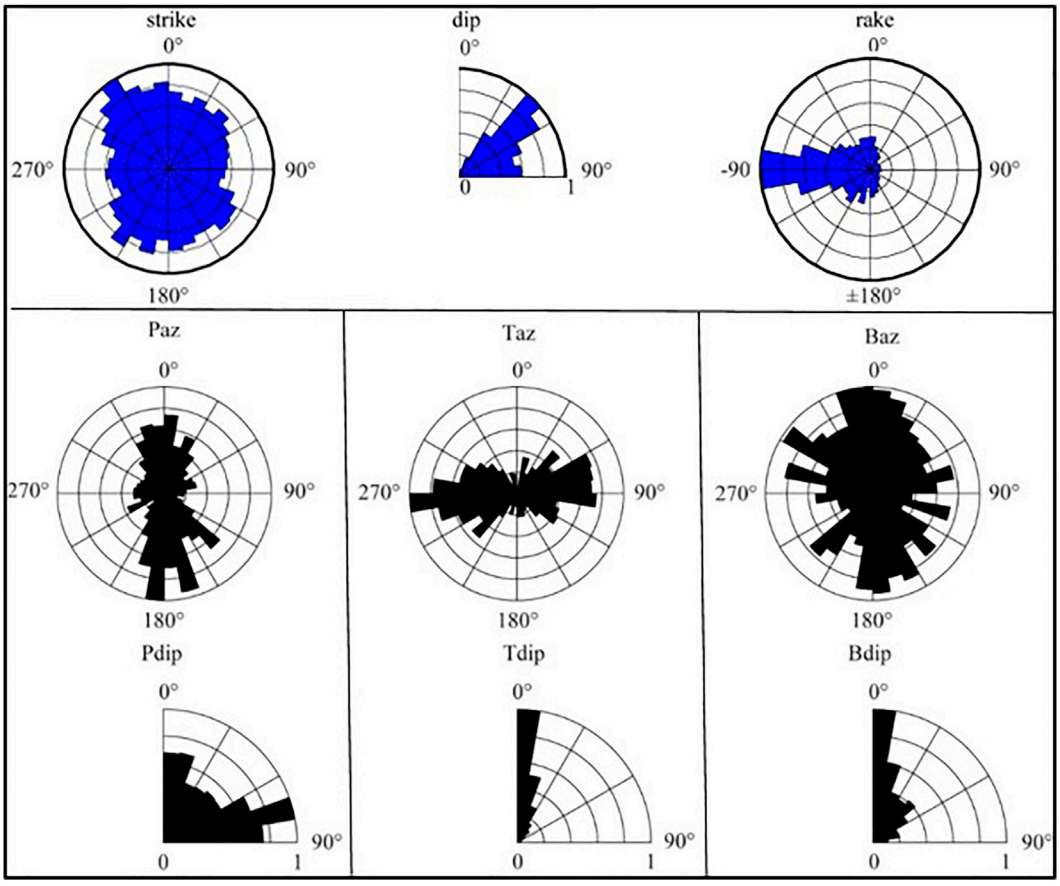

FIGURE 3
Wind rose map showing nodal planes and three focal mechanism axes. The top line shows strikes, dip angles and rakes of the focal mechanisms, and three columns below show azimuths and dip angles for three axes including P, T and B.

the Red-River and Xianshuihe-Xiaojiang faults. Adding some regional permanent stations, the network (Figure 1) recorded over 20,000 earthquakes with M_L 1.3–4.6 between April 2018 and December 2020. In this study, we examined the deep stresses after determining focal mechanisms based on these events and investigated surficial deformation using GPS velocity data.

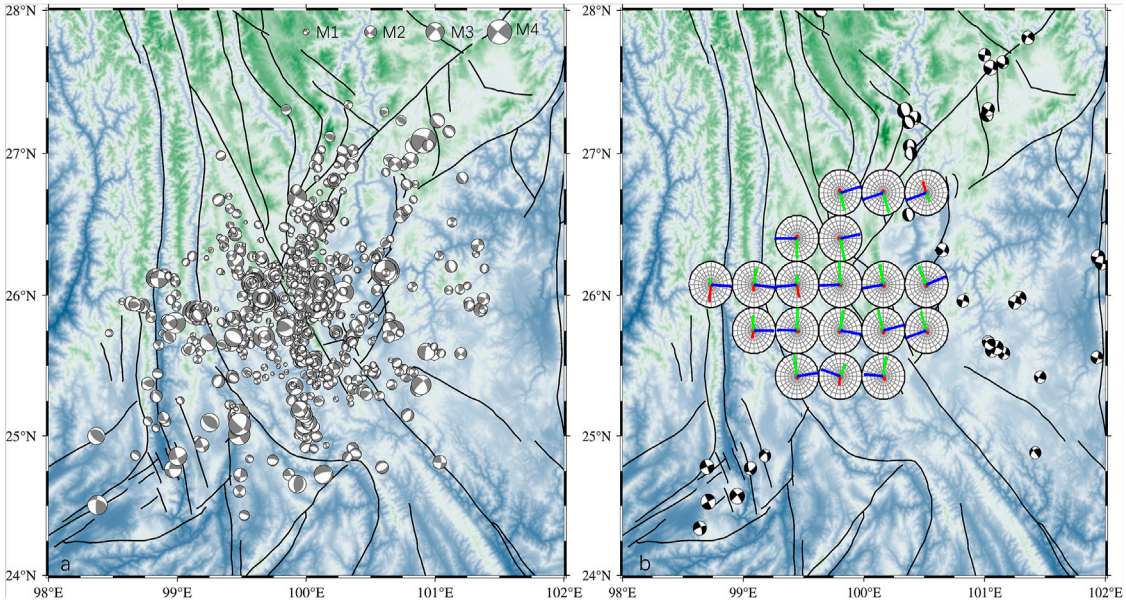

FIGURE 4
(A) Distribution of focal mechanisms based on seismic events recorded by the digital stations shown in Figure 1. **(B)** Projections on the horizontal plane of the three principal stress axes inverted from the focal mechanisms displayed in **(A)**, including the maximum principal stress axes σ_1 (red), medium principal stress axes σ_2 (green), and minimum principal stress axes σ_3 (blue). The background focal mechanisms are from the global CMT catalogue for events with magnitudes above 5.

Focal mechanisms and stress field

The estimation of the stress field by focal mechanisms is an effective tool for understanding crustal mechanics. Focal mechanisms of small earthquakes are generally determined from P-wave first-motion polarities, and the solutions are extremely sensitive to various errors, including inadequate knowledge about the seismic velocity structure. Many studies added S/P amplitude ratios to constrain focal mechanisms as P-wave amplitudes are larger near the P and T axes of the focal mechanism and smaller near the nodal planes (Kisslinger, 1980; Ruey-Juin Rau et al., 1996; Snoke, 2003). In this study, we used the HASH method (Hardebeck, 2002; Hardebeck and Shearer, 2003), which was developed to produce stable focal mechanisms considering the various sources of uncertainty based on P-wave first-motion polarities combining S/P amplitude ratios.

After manually measuring P-wave first-motion polarities and S/P amplitude ratios and using the regional three-dimensional velocity structure data (Yang et al., 2020), we obtained 1,500 focal mechanism solutions for events with a quality grade above C from the five classes of acceptable mechanisms using the quality criteria based on the solution stability (Figure 2; Supplementary Table S1).

We performed a statistical analysis of relevant parameters for the focal mechanism solutions (Figure 3). The wind rose maps of two groups of nodal planes depict an even distribution for strikes and normal faulting with high dip angles. North-south (NS)-oriented P axes with high dip angles and horizontal east-west (EW)-oriented T axes are dominant for these focal mechanisms.

Subsequently, we used the mature software package MSATSI (Hardebeck and Michael, 2006; Martinez-Garzon et al., 2014) to invert the stress orientations from the focal mechanisms. The data were divided into 30 grid points that vary by latitude and longitude over the study area. Each grid containing at least 15 focal mechanisms was allowed to invert three principal stress axes (Figure 4).

The principal stress axes (Figure 4B) are depicted as projections onto the horizontal plane; therefore, large dip angles corresponded to short axes. The stress field distribution shows that the maximum principal stress axes σ_1 are consistently vertical, the intermediate principal stress axes σ_2 are N-S oriented, and the minimum principal stress axes σ_3 are approximately horizontal with an EW-orientation, demonstrating that the covering area is under a continuously EW-oriented extensional crustal stress environment. Focal mechanisms of mid-large earthquakes from the United States Geological Survey around the area also show normal faulting primarily along a series of NS-oriented arc faults near the east boundary of our study area, such as the Binchuan Fault. The extensional deformation of the area was noticed previously and ~3×10^{-8} yr^{-1} E-W extension was estimated from GPS data in the region which was explained by gravity-driven deformation using

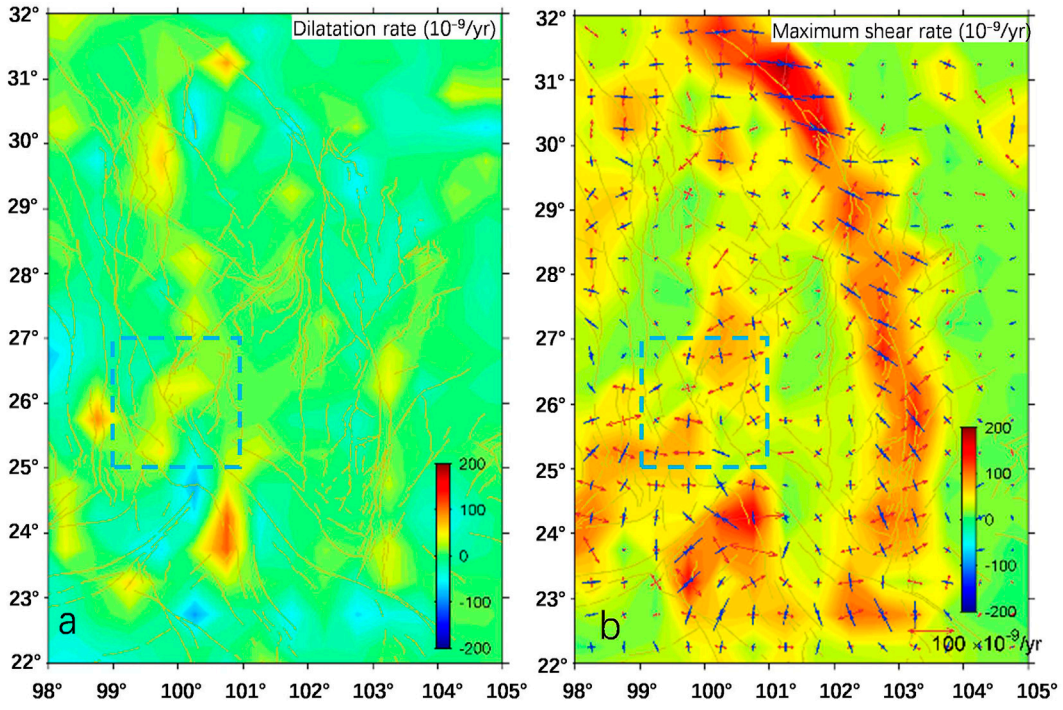

FIGURE 5
Continuum deformation field of Chuan-Dian area derived from interpolation of GPS velocities. Blue dotted square denotes the extensional area in Figure 4. **(A)** Dilatation rate, with extension positive. **(B)** Strain rates. Maximum shear strain rate is shown in background colour and principal strain rates are shown as vector pairs.

numerical simulation (Copley, 2008). To the south-west and south-east, the focal mechanisms show NE- and NW-oriented P axes, respectively. The above mechanical frame revealed that the extensional area was stretched toward both side terranes, and the eastern boundary should be delimited by the normal faults of the arc.

Analysis of GPS data

To visualize the crustal deformation field in the study area, we interpolated the GPS velocity data with respect to the Eurasian Plate during the past 25 years (Wang and Shen, 2020) using the "griddata" function of MATLAB, and utilized the expressions in spherical coordinates developed by Savage et al. (2001) to calculate strain rates. The derived GPS strain rates of Chuan-Dian area and the dilatational strain (Figure 5A) accorded with the extensional area resulted from stress inversion, where principle strain axes (Figure 5B) also revealed E-W extension.

We selected several profiles (Figure 1) perpendicular to the strike of the XSH-XJ fault to explore lateral variances of deformation in the clockwise rotating region. Velocity distributions in four profiles (Figure 6A) reveal a relatively speedy belt that covers segments with longitudes from 99.7°E to 101.5°E for A–A′, 100.2°E to 102°E for B–B′, 101.1°E to 102.7°E for C–C′, and 101.5°E to 102.8°E for D–D′, respectively. From the profiles, the belt is shown to be parallel to the Xianshuihe–Xiaojiang Fault, extending from north to south within the Sichuan–Yunnan block. Notably, the belt location is consistent with the eastern flow channel of the two in SE Tibet (Figure 1), which is approximately 200 km wide with a depth of 20–40 km, as found by Bai et al. (2010) based on their magnetotelluric survey, extending from SE Tibet into south-west China.

Based on the southward surficial movement, we use the E-W components of GPS velocities along the four profiles (Figure 6B) to describe relative movements across the clockwise rotating terrane in the SE plateau. A general feature of the E-W velocity profiles is still reflecting the same speedy belt as that of the velocity profiles. Another feature is that the E-W velocities of the profiles reveal evident segmentation, and the western and eastern areas on the two sides of the extensional zone move outward. For the profiles of B-B′, C-C′ and D-D′ in details, which cover the extensional area, three segments at different E-W rates are separated respectively by the Nujiang-Longling faults and the Binchuan fault along the western and eastern boundaries of the extensional area. The western segments of the profiles exhibit westward movement, and the eastern segments

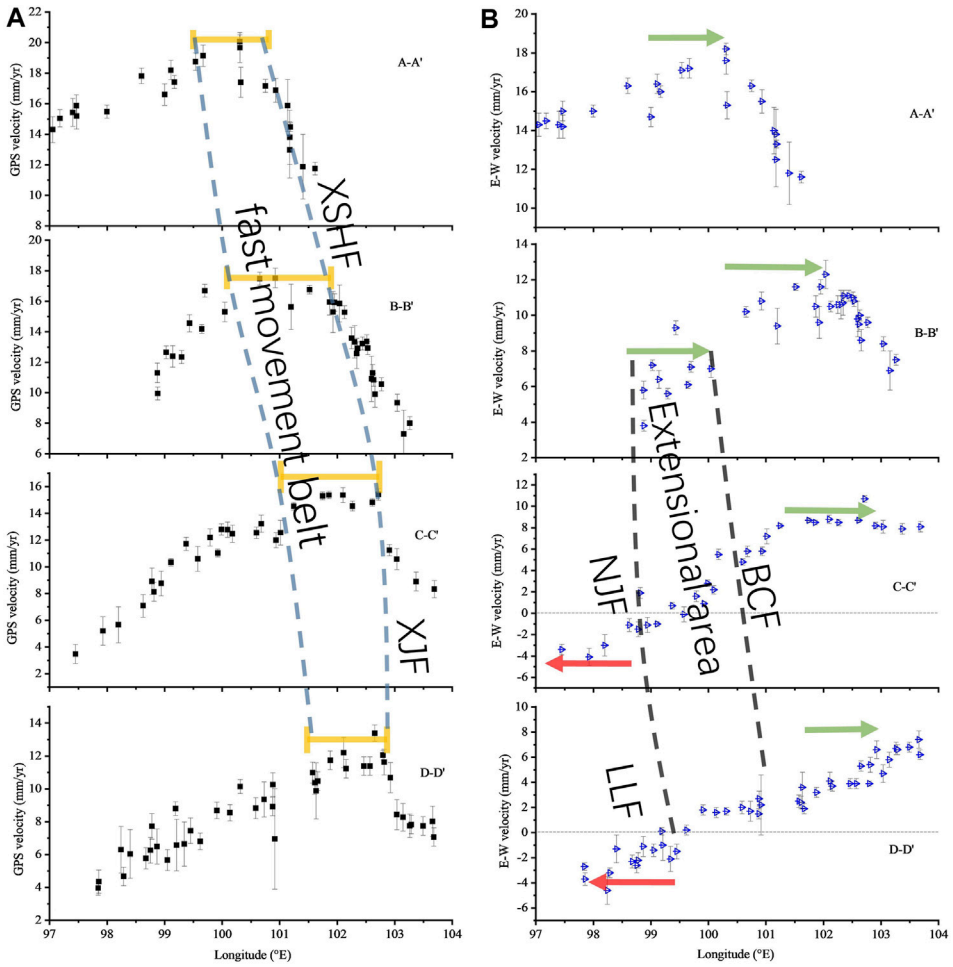

FIGURE 6
(A) GPS velocities in the four profiles shown in Figure 1. The orange line segments mark the comparatively high velocities, and two dashed lines define the fast movement belt; **(B)** GPS EW velocities in the profiles. The green arrows represent the eastward velocities, and the red ones represent the westward velocities. Two black dashed lines define the extensional area from our study. NJF = Nujiang Fault; LLF = Longling Fault; BCF = Binchuan Fault; RRF = Red-River Fault; XSHF = Xianshuihe Fault; and XJF = Xiaojiang Fault.

exhibit eastward movement; therefore, the middle terrane between them must have been stretched outward. The other flow channel with high electrical conductivity in SE Tibet (Bai et al., 2010) is located along the western segments of the profiles. Combined with the above stress field, the GPS E-W velocity profiles outline the range of the extensional zone, taking the Nujiang-Longling fault system and the Binchuan fault as western and eastern boundaries, respectively.

Discussion

"Contradictory" mode of fault slip near west boundary of the speedy belt

The analysis of the GPS profiles in this study shows that there is a special belt on the west side of the XSH fault, which should be understood from different perspectives. The premise of treating it as a speedy belt is that the Chuan-Dian block in the west of the XSH-XJ fault is mainly characterized by translational motion with small strain within several decades, and distribution of movement rates in each profile show peak segment within the belt. On the other hand, according to rotation rate distribution relative to the stable Eurasia plate (Wang and Shen, 2020), this belt is gradient located in the transforming zone from clockwise rotation of the Chuan-Dian block to counterclockwise rotation of the XSH-XJ fault. On the west of the belt, the GPS velocities show linear increase from west to east along the profile strikes, which can be regarded as "uniform motion" with constant angular velocity ($v=\omega r$) in the area, and shortage of several mm/yr within the belt is revealed from the velocity profiles. Geological ages of accumulation reflected that faults in between behaved left lateral as sketched in Figure 7, which seems to "contradict" our

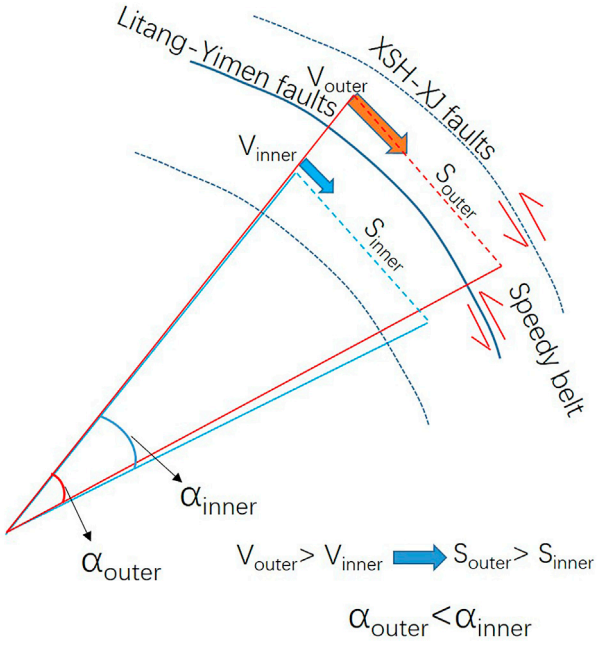

FIGURE 7
A Schematic diagram showing the speedy belt from GPS data and fault deformation near its west boundary.

understanding of fault deformation near the west boundary of the speedy belt but accords with the fact that a series of faults from north to south in the Chuan-Dian block near the west boundary of the belt (such as Litang fault, Yimen fault, etc) showed left-lateral slip (Wang et al., 1998).

Results of previous studies (Chen et al., 2014; Bao et al., 2015; Chen et al., 2016; Liu et al., 2021) on the Low-velocity zone revealed different locations of channel flows or highly disconnected and heterogeneous of the low velocity zones beneath the Chuan-Dian block, reflecting large uncertainties of geophysical results in this region. A 3D geo-electrical model from SINOPROBE MT (Dong et al., 2016), located to NW of the Chuan-Dian block area, proposed that "extensional extrusion" mechanism of the south-eastward expansion of Tibetan Plateau may result from the accumulated east-west spreading of a series of local ductile extensions zones.

The extensional area determined from our stress field inversion and GPS deformation revealed a consistent deformation pattern from surface to seismogenic depth. The coupling state between deep and shallow materials in the tensional area may be representative in the Chuan-Dian block. Based on the diversity of geophysical observations, the surficial speedy belt and the east possible crustal channel with high conductivity at the same location revealed similar coupling deformation, revealing that the region deforms by a more complex pattern. This pattern is influenced by localised low velocity zones than typical models suggested, wherein the plateau may deform through the movements of rigid crustal blocks along large strike-slip faults (Tapponnier and Molnar, 1976; Tapponnier et al., 1982), by continuous deformation (Houseman and England, 1993; Holt et al., 2000) or by crustal flow (Royden et al., 1997; Clark and Royden, 2000).

Seismic anisotropy (Sol et al., 2007) determined using shear-wave splitting analysis revealed a sharp change in the orientation of fast directions from NS in the north to EW in the south of our extensional zone, suggesting that EW strain was mechanically coupled across the crust–mantle interface and strong lower crust to transmit stress. So the coupling state of consistent deformation from shallow to depth may reach the crust-mantle boundary in this area.

Conclusions

The inverted focal mechanisms and stress field based on waveform data from our seismic network revealed that a continuously EW-oriented extensional zone existed at the edge of the SE plateau, where previous middle earthquakes lying at the east boundary of the zone exhibited normal faulting and EW-oriented extensional mechanisms. Analyses based on GPS data also revealed the EW tensional deformation. From surficial GPS velocities, we also observed a speedy belt located inside the clockwise rotating region around the eastern Himalaya syntaxis which was not previously noticed, and the belt location coincides with a crustal flow channel from the magnetotelluric study. We suggest a complex regional kinematics with a localised speedy belt and a continuously extensional zone, where material coupling and deformation compatibility were revealed within the crustal depth.

Data availability statement

The original contributions presented in the study are included in the article/Supplementary Material, further inquiries can be directed to the corresponding author.

Author contributions

KW analyzed data and wrote the manuscript. XF determined the focal mechanisms.

Acknowledgments

We thank Mingpei Jin, Honghu Ma, Wenjie Dang, and their colleagues for field work and extraction of seismic phases. We thank Peixun Liu, Shunyun Chen, Yanshuang Guo, and Yanqun

Zhuo for giving helpful suggestions. We thank National Nonprofit Fundamental Research Grant of China, Institute of Geology, China Earthquake Administration (grant number IGCEA2210) and the National Key R&D Program of China (grant number 2018YFC1503303) for providing financial supports.

Conflict of interest

The authors declare that the research was conducted in the absence of any commercial or financial relationships that could be construed as a potential conflict of interest.

The reviewer MH declared a shared affiliation with the authors to the handling editor at the time of review.

Publisher's note

Supplementary material

The Supplementary Material for this article can be found online at: https://www.frontiersin.org/articles/10.3389/feart.2022.976380/full#supplementary-material

References

Bai, D., Unsworth, M. J., Meju, M. A., Ma, X., Teng, J., Kong, X., et al. (2010). Crustal deformation of the eastern Tibetan Plateau revealed by magnetotelluric imaging. *Nat. Geosci.* 3, 358–362. doi:10.1038/ngeo830

Bao, X., Sun, X., Xu, M., Eaton, D. W., Song, X., Wang, L., et al. (2015). Two crustal low-velocity channels beneath SE Tibet revealed by joint inversion of Rayleigh wave dispersion and receiver functions. *Earth Planet. Sci. Lett.* 415, 16–24. doi:10.1016/j.epsl.2015.01.020

Burchfiel, B. C., Zhiliang, C., Yupinc, L., and Royden, L. H. (1995). Tectonics of the longmen Shan and adjacent regions, central China. *Int. Geol. Rev.* 37, 661–735. doi:10.1080/00206819509465424

Chen, H., Zhu, L., and Su, Y. (2016). Low velocity crustal flow and crust-mantle coupling mechanism in Yunnan, SE Tibet, revealed by 3D S-wave velocity and azimuthal anisotropy. *Tectonophysics* 685, 8–20. doi:10.1016/j.tecto.2016.07.007

Chen, M., Huang, H., Yao, H., van der Hilst, R., and Niu, F. (2014). Low wave speed zones in the crust beneath SE Tibet revealed by ambient noise adjoint tomography. *Geophys. Res. Lett.* 41, 334–340. doi:10.1002/2013GL058476

Chen, Z., Burchfiel, B. C., Liu, Y., King, R. W., Royden, L. H., Tang, W., et al. (2000). Global Positioning System measurements from eastern Tibet and their implications for India/Eurasia intercontinental deformation. *J. Geophys. Res.* 105, 16215227–16216227. doi:10.1029/2000JB900092

Clark, M. K., and Royden, L. H. (2000). Topographic ooze: Building the eastern margin of Tibet by lower crustal flow. *Geology* 28, 703–706. doi:10.1130/0091-7613(2000)28<703:TOBTEM>2.0.CO;2

Copley, A. (2008). Kinematics and dynamics of the southeastern margin of the Tibetan Plateau. *Geophys. J. Int.* 174 (3), 1081–1100. doi:10.1111/j.1365-246X.2008.03853.x

Dong, H., Wei, W., Jin, S., Ye, G., Zhang, L., Jing, J., et al. (2016). Extensional extrusion: Insights into south-eastward expansion of Tibetan Plateau from magnetotelluric array data. *Earth Planet. Sci. Lett.* 454, 78–85. doi:10.1016/j.epsl.2016.07.043

England, P., and Houseman, G. (1986). Finite strain calculations of continental deformation: 2. Comparison with the India-asia collision zone. *J. Geophys. Res.* 91, 3664–3676. doi:10.1029/JB091iB03p03664

Fu, Y. V., Li, A., and Chen, Y. J. (2010). Crustal and upper mantle structure of southeast Tibet from Rayleigh wave tomography. *J. Geophys. Res.* 115, B12323. doi:10.1029/2009JB007160

Gan, W., Molnar, P., Zhang, P., Xiao, G., Liang, S., Zhang, K., et al. (2021). Initiation of clockwise rotation and eastward transport of Southeastern tibet inferred from deflected fault traces and GPS observations. *The Geol. Soc. Amer.* 134 (5–6), 1129–1142. doi:10.1130/B36069.1

Hardebeck, J. L. (2002). A new method for determining first-motion focal mechanisms. *Bull. Seismol. Soc. Am.* 92, 2264–2276. doi:10.1785/0120010200

Hardebeck, J. L., and Michael, A. J. (2006). Damped regional-scale stress inversions: Methodology and examples for southern California and the Coalinga aftershock sequence. *J. Geophys. Res.* 111 (B11310). doi:10.1029/2005jb004144

Hardebeck, J. L., and Shearer, P. M. (2003). Using S/P amplitude ratios to constrain the focal mechanisms of small earthquakes. *Bull. Seismol. Soc. Am.* 93, 2434–2444. doi:10.1785/0120020236

Holt, W. E., Chamot-Rooke, N., Pichon, X. L., Haines, A. J., Shen-Tu, B., and Ren, J. (2000). Velocity field in Asia inferred from Quaternary fault slip rates and global positioning system observations. *J. Geophys. Res.* 105, 19185–19209. doi:10.1029/2000JB900045

Houseman, G., and England, P. (1993). Crustal thickening versus lateral expulsion in the Indian-Asian continental collision. *J. Geophys. Res.* 98, 12233–12249. doi:10.1029/93JB00443

Kisslinger, C. (1980). Evaluation of S to P amplitude ratios for determining focal mechanisms from regional network observations. *Bull. Seismol. Soc. Am.* 70, 999–1041. doi:10.1785/BSSA0700040999

Li, Y., Wu, Q., Zhang, R., Tian, X., and Zeng, R. (2008). The crust and upper mantle structure beneath Yunnan from joint inversion of receiver functions and Rayleigh wave dispersion data. *Phys. Earth Planet. Interiors* 170, 134–146. doi:10.1016/j.pepi.2008.08.006

Liu, Q. Y., van der Hilst, R. D., Li, Y., Yao, H. J., Chen, J. H., Guo, B., et al. (2014). Eastward expansion of the Tibetan Plateau by crustal flow and strain partitioning across faults. *Nat. Geosci.* 7, 361–365. doi:10.1038/ngeo2130

Liu, Y., Yao, H., Zhang, H., and Fang, H. (2021). The community velocity model V.1.0 of southwest China, constructed from joint body- and surface-wave travel-time tomography. *Seismol. Res. Lett.* 92, 2972–2987. doi:10.1785/0220200318

Martinez-Garzon, P., Kwiatek, G., Ickrath, M., and Bohnhoff, M. (2014). MSATSI: A MATLAB package for stress inversion combining solid classic methodology, a new simplified user-handling, and a visualization tool. *Seismol. Res. Lett.* 85, 896–904. doi:10.1785/0220130189

Rau, R. J., Wu, F. T., and Shin, T. C. (1996). Regional network focal mechanism determination using 3D velocity model and SH/P amplitude ratio. *Bull. Seismol. Soc. Am.* 86, 1270–1283.

Royden, L. H., Burchfiel, B. C., King, R. W., Wang, E., Chen, Z., Shen, F., et al. (1997). Surface deformation and lower crustal flow in Eastern Tibet. *Science* 276, 788–790. doi:10.1126/science.276.5313.788

Savage, J. C., Gan, W., and Svarc, J. (2001). Strain accumulation and rotation in the eastern California sheat zone. *J. Geophys. Res.* 106 (21), 109955–B11022.

Snoke, J. A., 2003. FOCMREC: FOCal MEChanism determinations. Available at: http://www.geol.vt.edu/outreach/vtso/focmec/. doi:10.1016/S0074-6142(03)80291-7

Sol, S., Meltzer, A., Bürgmann, R., van der Hilst, R., King, R., Chen, Z., et al. (2007). Geodynamics of the southeastern Tibetan Plateau from seismic anisotropy and geodesy. *Geol.* 35, 563–566. doi:10.1130/G23408A.1

Tapponnier, P., and Molnar, P. (1976). Slip-line field theory and large-scale continental tectonics. *Nature* 264, 319–324. doi:10.1038/264319a0

Tapponnier, P., Peltzer, G., Le Dain, A. Y., Armijo, R., and Cobbold, P. (1982). Propagating extrusion tectonics in Asia: New insights from simple experiments with plasticine. *Geol.* 10, 611–616. doi:10.1130/0091-7613(1982)10<611:petian>2.0.co;2

Wang, E., Burchfiel, B. C., Royden, L. H., Chen, L., Chen, Z., Li, W., et al. (1998). Late cenozoic xianshuihe-xiaojiang, red river, and dali fault systems of southwestern sichuan and central yunnan, China. *Geol. Soc. Am. Spec. Pap.* 327, 1–108. doi:10.1130/0-8137-2327-2.1

Wang, H., Wright, T. J., and Biggs, J. (2009). Interseismic slip rate of the northwestern Xianshuihe fault from InSAR data. *Geophys. Res. Lett.* 36, L03302. doi:10.1029/2008gl036560

Wang, M., and Shen, Z. (2020). Present-day crustal deformation of continental China derived from GPS and its tectonic implications. *J. Geophys. Res. Solid Earth* 125, e2019. doi:10.1029/2019JB018774

Xu, X., Wen, X., Zheng, R., Ma, W., Song, F., and Yu, G. (2003). Pattern of latest tectonic motion and its dynamics for active blocks in Sichuan-Yunnan region. *China. Sci. China (Earth Sci.).* 46, 210–226. doi:10.1360/03dz0017

Xu, Z. J., and Song, X. (2010). Joint inversion for crustal and pn velocities and moho depth in eastern margin of the Tibetan plateau. *Tectonophysics* 491, 185–193. doi:10.1016/j.tecto.2009.11.022

Yang, Y., Yao, H., Wu, H., Zhang, P., and Wang, M. (2020). A new crustal shear-velocity model in Southwest China from joint seismological inversion and its implications for regional crustal dynamics. *Geophy. J. Int.* 220 (2), 1379–1393. doi:10.1093/gji/ggz514

Yao, H., van der Hilst, R. D., and Montagner, J. (2010). Heterogeneity and anisotropy of the lithosphere of SE Tibet from surface wave array tomography. *J. Geophys. Res.* 115 (B12), B12307. doi:10.1029/2009JB007142

Zhang, P., Shen, Z., Wang, M., Gan, W., Burgmann, R., Molnar, P., et al. (2004). Continuous deformation of the Tibetan Plateau from global positioning system data. *Geol.* 32, 809–812. doi:10.1130/G20554.1

Zhao, L., Xie, X., He, J., Tian, X., and Yao, Z. (2013). Crustal flow pattern beneath the Tibetan Plateau constrained by regional Lg-wave Q tomography. *Earth Planet. Sci. Lett.* 383, 113–122. doi:10.1016/j.epsl.2013.09.038

frontiers | Frontiers in Earth Science

TYPE Original Research
PUBLISHED 19 September 2022
DOI 10.3389/feart.2022.993984

OPEN ACCESS

EDITED BY
Zhenjie Wang,
China University of Petroleum, China

REVIEWED BY
Mahdi Behyari,
Urmia University, Iran
Shunying Hong,
China Earthquake Administration, China
Guangcai Feng,
Central South University, China

*CORRESPONDENCE
Guohong Zhang,
zhanggh@ies.ac.cn

SPECIALTY SECTION
This article was submitted to Structural Geology and Tectonics, a section of the journal Frontiers in Earth Science

RECEIVED 14 July 2022
ACCEPTED 24 August 2022
PUBLISHED 19 September 2022

CITATION
Fan X, Zhang G, Zhao D, Xie C, Huang C and Shan X (2022), Fault geometry and kinematics of the 2021 Mw 7.3 Maduo earthquake from aftershocks and InSAR observations.
Front. Earth Sci. 10:993984.
doi: 10.3389/feart.2022.993984

Fault geometry and kinematics of the 2021 Mw 7.3 Maduo earthquake from aftershocks and InSAR observations

Xiaoran Fan[1], Guohong Zhang[1,2]*, Dezheng Zhao[1], Chaodi Xie[3], Chuanchao Huang[3] and Xinjian Shan[1]

[1]State Key Laboratory of Earthquake Dynamics, Institute of Geology, Beijing, China, [2]Institute of Disaster Prevention, Yanjiao High Tech Zone, Sanhe City, China, [3]School of Earth Sciences, Yunnan University, Kunming, China

The 2021 Mw 7.3 Maduo earthquake revealed the significant seismic hazard of faults developed within the Bayan Har Block of eastern Tibet, China (e.g., the Kunlun Pass–Jiangcuo Fault). Relocated aftershock data are in good agreement with the Interferometric Synthetic Aperture Radar (InSAR) coseismic displacement field and field investigations. In this study, we used aftershock point cloud fitting to model the relocated aftershocks of the Maduo earthquake, and obtained the detailed geometry and characteristics of the seismogenic fault. Based on InSAR coseismic deformation, the geometric model of the seismogenic fault and its slip distribution were retrieved. The results show that this event was shallow (0–10 km) and characterized by sinistral strike-slip motion. We identified four asperities along the fault strike; the maximum slip of 4.84 m occurred on the eastern segment of the fault, in an area where the strike changed. The results suggest that the central segment of the main seismogenic fault is mature and smooth, while western and eastern segments are complex and immature.

KEYWORDS

2021 Mw7.3 Maduo earthquake, aftershock point cloud fitting, InSAR coseismic deformation, fault geometry, slip distribution

1 Introduction

On 22 May 2021, a Mw 7.3 earthquake occurred in Maduo County, China; the event was located in the interior of the Bayan Har Block and close to the Kunlun Fault. According to the China Earthquake Networks Center (CENC), the epicenter was located at 98.34°E & 34.58°N with a focal depth of 10 km. The W phase focal mechanism reported by the United States Geological Survey (USGS) indicates dominant left-lateral strike-slip motion. Field investigations conducted immediately after the earthquake, Interferometric Synthetic Aperture Radar (InSAR) coseismic deformation, and regional tectonics all confirm that the seismogenic fault was the Kunlun Pass–Jiangcuo Fault (KPJF), located between the Maduo–Gande Fault (MGF) to the north and the Gande South Rim Fault (GSF) to the south (Figure 1). InSAR and field data indicate a surface rupture zone of ~160 km in length,

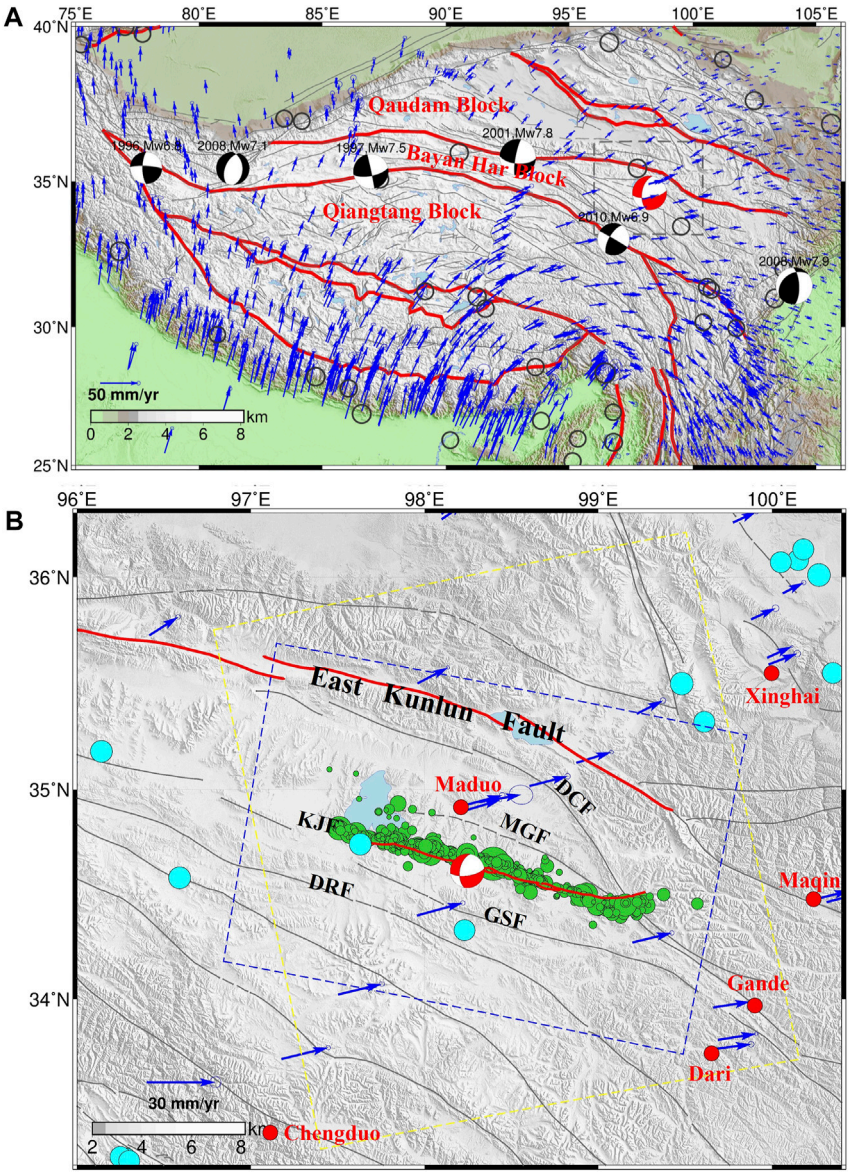

FIGURE 1
Tectonic setting and strong historical earthquakes on the Tibetan Plateau. **(A)** Tectonic setting of the Tibetan Plateau and Bayan Har Block. The red beach ball represents the United States Geological Survey (USGS; https://earthquake.usgs.gov/earthquakes) focal mechanism of the 2021 Mw 7.3 Maduo earthquake. Gray lines represent active faults, and red lines represents block boundary faults. Blue arrows show Global Positioning System (GPS) interseismic velocities with ellipses indicating uncertainties. Black circles represent historical earthquakes of Mw ≥ 7.0 (1 January 1976–20 May 2021; https://www.globalcmt.org). **(B)** Source region of the 2021 Maduo earthquake. Blue dots indicate historical Mw > 5 earthquakes. (1 January 1990–20 May 2021; https://www.globalcmt.org). Green circles are aftershocks. Red circles are nearby cities. The red line donates the surface rupture of the 2021 Maduo earthquake. The blue and purple boxes are the spatial coverage of the Synthetic Aperture Radar (SAR) images on ascending and descending orbits, respectively. Blue arrows are the same as in **(A)**.

featuring complex local surface structures such as tensile step zones, shear fractures, tensile and shear cracks, compression, and swelling (Chen et al., 2021; Zhi-min et al., 2021; Pan et al., 2022; Ren et al., 2022). The obvious segmentation of the surface rupture adds complexity to the interpretation of fault segmentation and subsurface geometry of the seismogenic fault.

Strong earthquakes tends to occur along major boundary faults that surround the Bayan Har Block (Zhang et al., 2003; Parsons et al., 2008; Tobita et al., 2011; Xu et al., 2013; Fang et al., 2018); historic examples include the 2008 Mw 7.8 Wenchuan earthquake, 2010 Mw 6.9 Yushu earthquake, 2017 Mw 7.0 Jiuzhaigou earthquake, and 2008 Mw 7.3 Yutian earthquake. Among the

block bounding faults, the Kunlun Fault on the northern margin and the Xianshuihe–Yushu–Malgaechaka Fault on the southern margin facilitate the eastward movement of crustal material (Li et al., 2004; Qi-Dong et al., 2010; Qi-Dong et al., 2014) and are considered likely candidates for future large earthquakes (Wen et al., 2011). However, secondary faults near the Kunlun Fault zone, including the MGF, KPJF, GSF and Dari Fault (DRF), are systematically overlooked and their seismic hazards significantly underestimated. This changed with the 2021 Mw 7.3 Maduo earthquake, which was unusual in that it occurred within the Bayan Har Block. This event showed that secondary faults parallel to the main boundary faults have the ability to host strong earthquakes (Mw > 7), albeit with the main boundary faults bearing most of the tectonic loading and release. Thus, the geometry and kinematics of the source fault of the Maduo earthquake is of great importance for better understanding of seismogenesis along secondary faults within the Bayan Har Block.

When complex fault geometry constrained by aftershocks is used as *a priori* information, the robustness of the fault slip model constrained by InSAR observations is potentially improved, and uncertainties in the slip model caused by simplification of fault geometry is reduced (Dietz and Ellsworth, 1990; Ziv, 2006; Chiarabba et al., 2009; Wan et al., 2016). Compared with geodetic (Global Navigation Satellite System [GNSS], InSAR, etc.) and seismic waveform data, relocated aftershock data can constrain the geometry of the deep fault with higher resolution as each aftershock can be regarded as an observation point (Hauksson, 2010; Powers and Jordan, 2010; Valoroso et al., 2014). Previous studies have shown that spatio-temporal evolution of aftershocks reflects the complex activity of the deep portion of the fault, including surrounding structures and secondary fractures (Perrin et al., 2021). Aftershocks of the Maduo earthquake confirmed the geometric complexity of the deep seismogenic fault (Wang et al., 2021).

As such, the 2021 Maduo earthquake provides a rare opportunity to obtain the fault geometric parameters from both aftershocks and InSAR measurements, and to discuss the physical and mechanical properties of the seismogenic fault. In this study, we used an integrated inversion of both point cloud-fitted relocated aftershock data and InSAR coseismic deformation measurements to evenly more robustly reveal the complexity of the seismogenic source fault and slip distribution of the Maduo earthquake.

2 Aftershock data and fault plane fitting

2.1 Aftershock data

In this study, we used 1,240 relocated aftershocks that occurred in the 9 days after the earthquake (Wang et al., 2021). The aftershock distribution shows a very obvious linear trend along a NW–SE direction (Figure 2A) between the GSF to the south and MGF & Dago-Changmahe Fault (DCF) to the north; it interests with the latter two faults at the eastern end and with the southern margin of Eling Lake at the western end. Aftershocks show obvious segmentation characteristics, with dense clusters along the western segment, relatively sparse clusters along the central segment, and a large gap along the eastern segment. In addition, aftershocks along the eastern segment bifurcated when they intersect the MGF; most aftershocks shifted to the north, while a smaller number continued to extend southeast for ~10 km. The majority of aftershocks were concentrated at 5–15 km depth (Figure 2B). According to previous research on aftershock clusters, the geometry of the fault has varied dip angles from west to east.

2.2 Fault plane fitting method

Before mathematical fitting, the outlier factor analysis algorithm was used to filter aftershocks, with outliers removed to ensure the accuracy of subsequent fault plane fitting. Outlier factors (LOF) based on the density of clusters, tokening aftershocks with a much lower density than neighboring clusters as an outlier, were used to remove outliers that deviated significantly from the fault plane (Figure 3; Breunig et al., 2000). We also filtered out those outliers with abnormal spatial distributions.

First, we calculated the distance $rd(p,o)$ between point p and point:

$$rd(p,o) = max\{kd(p), d(p,o)\} \quad (1)$$

where $kd(p)$ is the distance from point p to the nearest k-th point, and $d(p,o)$ is the actual distance between p and o. The local density of point p is defined as $lrd_k(p)$, and

$$lrd_k(p) = \frac{|N_k(p)|}{\sum_{o \in N_{k(p)}} rd_k(p,o)} \quad (2)$$

where, $N_k(p)$ is the number of all points within the kd(p) distance from point p. The LOF value of point p can be expressed as:

$$LOF_k(p) = \frac{\sum_{o \in N_{k(p)}} lrd_k(o)}{|N_k(p)| lrd_k(p)} \quad (3)$$

After obtaining the LOF values of each aftershock, we found that points with LOF >1.5 were obvious outliers; these were removed for subsequent calculations (Figure 3).

Then, we projected the three dimensional (3D) aftershocks onto a two dimensional plane to fit the geometry of the fault (Wang et al., 2019). This method has been used by Wang et al. in the 2016 Central Italy earthquake. They used aftershock data to quickly discover the geometry of four main faults and three secondary faults. We divide the aftershocks into regions according to their

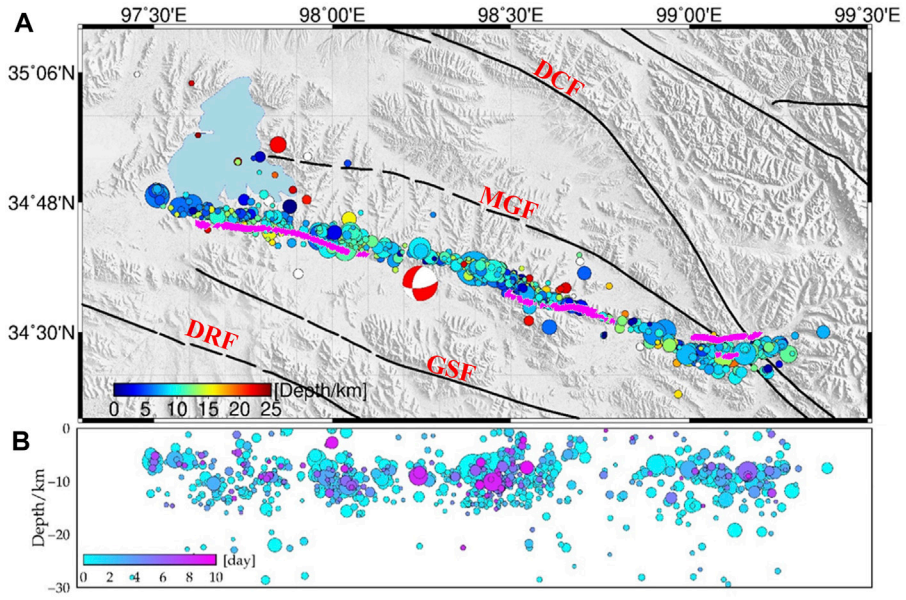

FIGURE 2
Spatiotemporal evolution of aftershocks following the 2021 Mw 7.3 Maduo earthquake. **(A)** Map of aftershock locations, where colored circles are aftershocks at different depths and the solid black line is the active fault. The pink lines are the surface ruptures. The red beach ball represents the United States Geological Survey (USGS; https://earthquake.usgs.gov/earthquakes) mainshock focal mechanism. MGF: Maduo–Gande Fault, DCF: Dagou–Changmahe Fault, GSF: Gande South Rim Fault, DRF: Dari Fault. **(B)** Depth distribution of aftershocks along the fault zone, where colors denote days after the mainshock.

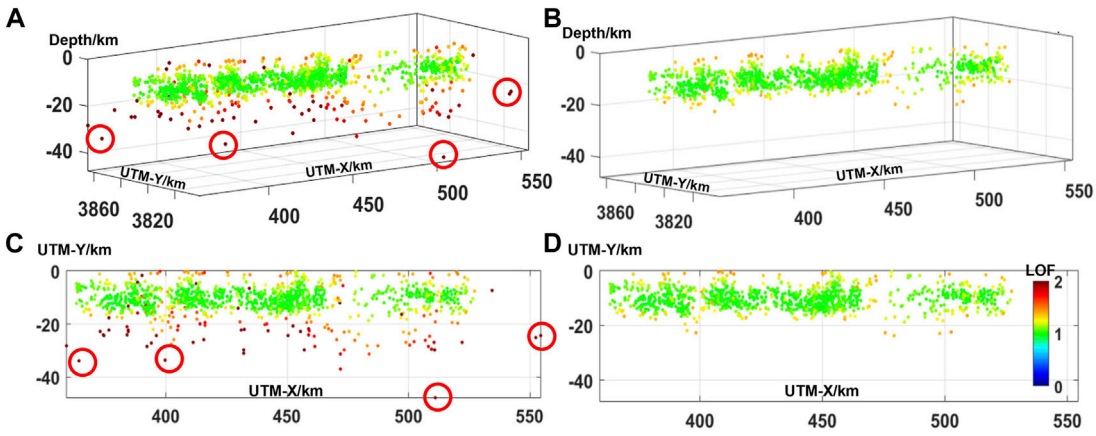

FIGURE 3
Relocated aftershock data **(A,C)** before and **(B,D)** after filtering. Aftershocks in red are those identified as outliers based on the outlier factors (LOF).

distribution trends. Based on the singular value decomposition (SVD) algorithm, 3D aftershock distributions were mathematically matched with the fault planes (Wang et al., 2019).

A more accurate fit was achieved by performing a loop procedure, as shown in Figure 4, to filter out the influence of outliers.

The location, length, and depth of the fault are *a priori* parameters that need to be manually identified. We believe that aftershocks basically occur on faults, so the area where aftershocks are obviously concentrated is the location of faults; The length of the fault is determined by the

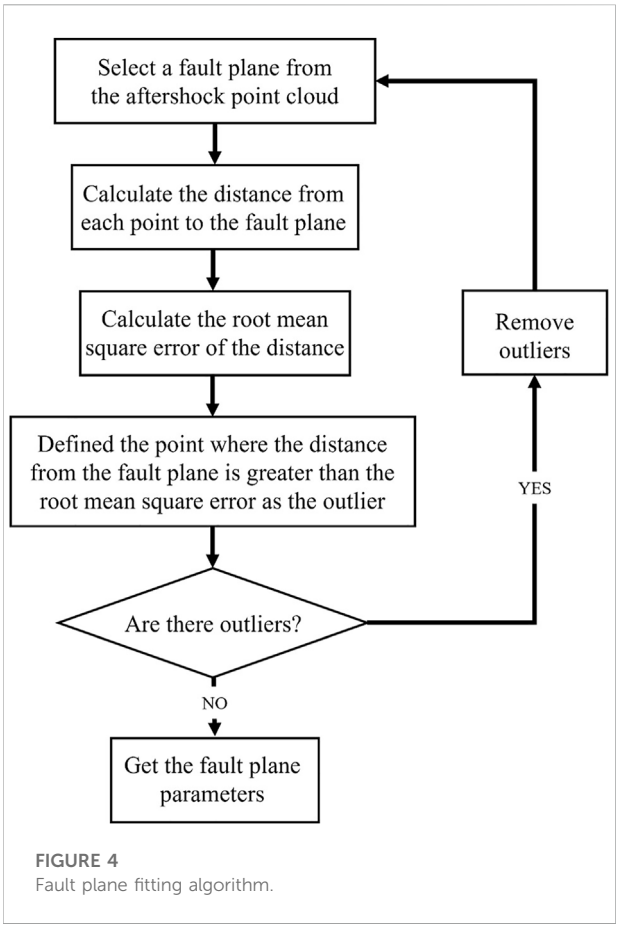

FIGURE 4
Fault plane fitting algorithm.

segmentation of the reference surface rupture and the zoning state of aftershocks. According to the nature of the strike-slip earthquake and the depth distribution of aftershocks, the fault depth is set as 0–20 km. In other words, according to the segmentation of aftershocks and faults, different rectangular ranges were selected, and aftershocks within each range were used to fit the fault parameters within that rectangular range. Then, the precise geometric parameters of the fault could be quickly calculated by plane fitting. From the obtained fault orientation (a, b, c), the strike and dip of the fault were calculated by:

$$strike = atan2\left(sign(c) \times a,\ sin(c) \times b\right) \tag{4}$$

$$dip = acos\left(\frac{c}{\sqrt{a^2 + b^2 + c^2}}\right) \tag{5}$$

where sign(n) indicates that the element in parentheses is equal to one if n is regular and -1 if n is negative.

The advantage of the proposed method is that it reduces the subjectivity and tedious work of artificial identification, and the fault parameters are obtained by mathematical method, have more reliable information about the depth of the fault.

2.3 Aftershock fitted fault plane parameters

We established a preliminary fault geometry model with five segments (F1, F2, F4–F6; Figure 5 and Table 1) based on the fault plane fitting method described above. F1 is nearly parallel to the main fault and occurs at depths of 0–20 km depth; it did not break the surface. F2, F4, and F5 represent the main seismogenic fault and F6 is the eastern branch fault. The model is in good agreement with surface ruptures observed in the field and with InSAR coseismic deformation along the western (F1 in Figure 5) and eastern (F4–F6 in Figure 5) segments. However, it deviates ~4 km north of the surface rupture along the central segment (F2 in Figure 5), for which we also identified a wide aftershock zone (Figure 5C). After filtering and mathematically fitting the aftershocks, we identified another segment (F3 in Figure 5), which is consistent with both the surface ruptures observed by field investigation and the InSAR coseismic measurements.

Within the fault geometric parameters, the location and length of the fault were determined from the manually selected aftershocks, with the selection criteria being the aftershock distribution characteristics. After repeated tests, we found that the impact of manual frame selection error on the geometric parameters was mainly associated with the length and depth, while the error in fault strike and dip angle was ~1°, which indicates the internal reliability of the parameters. The algorithm we used could only obtain simple and plane fault models (REFS). However, our aftershock fitted fault plane model (AFFP) model is consistent with the fault segmentation of field investigation, unlike the model in Jun et al. (2021) and He et al. (2021). Moreover, we used F2 to explain the mismatch between aftershocks and the surface trace, which was not considered in past studies. Our final AFFP model is stable and can reflect the actual situation of aftershock data; as such, we used this model to explore the fault slip distribution of the Maduo earthquake.

3 InSAR coseismic data and fault slip inversion

3.1 InSAR coseismic displacement

We derived coseismic displacement associated with the Maduo earthquake using Sentinel-1 IW mode SAR images. We selected tracks that completely covered the seismic region. The pre-earthquake (20 May 2021) and post-earthquake (26 May 2021) images were processed using the GAMMA software (Werner et al., 2000). The National Aeronautics and Space Administration (NASA) Shuttle Radar Topography Mission (SRTM) 3-arc-sec digital elevation model (DEM) was used to geocode the images and remove topographic phases. During processing, SAR images were multi-looked in the range (by 10)

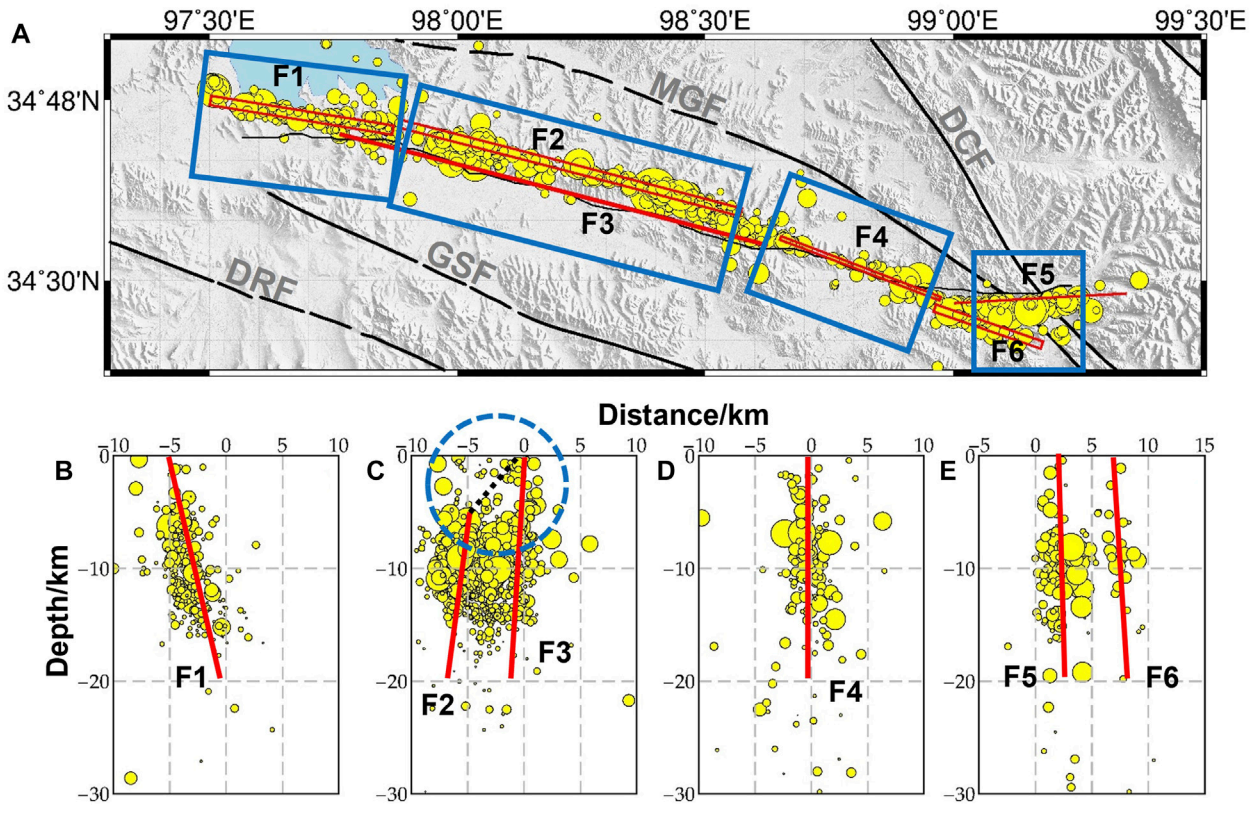

FIGURE 5
Results of fault geometry fitting and profiles. **(A)** Segmentation of the fitted fault plane. Red boxes are the surface projection of the inferred fault plane from aftershocks, blue boxes denote the swath used to project aftershock data, and the solid red line is fault trace projected up-dip. **(B–E)** Aftershock profiles within each segment of the fault.

TABLE 1 Best fault parameters of each fault segment.

Fault segment	Strike/°	Dip angle/°	Start point and end point/Longitude, latitude	Length/km	Depth of leading edge/km	Base depth of fault plane/km
F1	−260	83	97.5033°E, 34.8071°N	34	0	20
			97.8715°E, 34.7576°N			
F2	−75	84	97.8828°E, 34.7542°N	65	6	20
			98.5696°E, 34.6069°N			
F3	−75	89	97.7641°E, 34.7415°N	92	0	20
			98.6233°E, 34.5573°N			
F4	−69	88	98.6506°E, 34.5676°N	28	0	20
			98.9726°E, 34.4663°N			
F5	85	89	99.0018°E, 34.4618°N	36	0	20
			99.3504°E, 34.4780°N			
F6	−265	86	99.0018°E, 34.4618°N	22	0	20
			99.29872°E, 34.3833°N			

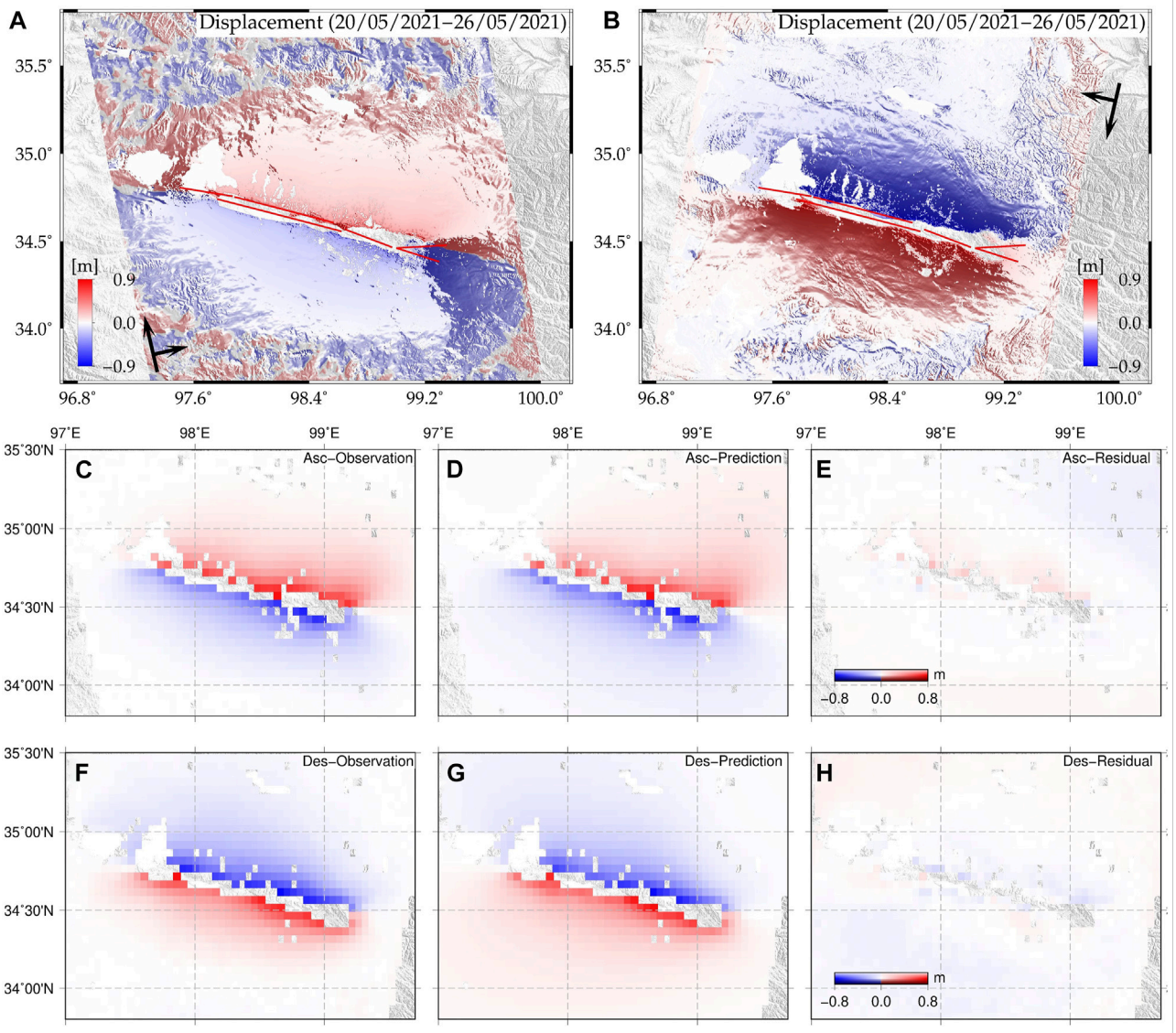

FIGURE 6
Coseismic displacement fields of the Maduo earthquake. Red lines denote the surface rupture traces from field investigations. **(A)** Ascending obits co-seismic deformation fields; **(B)** Descending obits co-seismic deformation fields. **(C–H)** Observation, predicition and residual of fault slip distribution inversion results.

and azimuth (by 2) directions. After enhanced registration with an accuracy of <0.001 pixels, the interferometric phase was filtered using an adaptive spectral filtering algorithm and then unwrapped using the minimum cost flow algorithm (Werner et al., 2002). Finally, deformation maps were projected to the geographic coordinate system to obtain the coseismic displacement fields of the Maduo earthquake (Figure 6A and Figure 6B).

The InSAR coseismic displacement fields show that the seismogenic fault of the Maduo earthquake is almost parallel to the Kunlun Fault and may be connected with the East Kunlun fault zone at its eastern end. The observed coseismic deformation had wide spatial coverage and clear discontinuities across the surface ruptures, indicating that the coseismic rupture broke the surface. Obvious geometrical distortion and bifurcation at the eastern end of the fault indicate complex fault geometry. The maximum uplift and subsidence in line-of-slight (LOS) displacement across the fault was ~0.9 m (Figure 6). The same numerical magnitudes but different symbols between ascending and descending LOS displacement fields indicate mainly sinistral strike-slip motion. The InSAR deformation is consistent with the trace of observed surface ruptures (Figure 6B and Figure 6D; Zhimin et al., 2021), with only a small amount of obvious deviation in the easternmost region.

3.2 Inversion schemes

Based on the Okada elastic half-space dislocation model (Okada, 1985), the Green's functions connecting fault parameters and the observed surface deformation were expressed as:

$$d = S(x)^{*}G + \varepsilon \tag{6}$$

where d is observed deformation, S(x) is the fault parameters, G is the Green's functions, and ε is the error associated with the observation and model. Since we established the six-segment fault model based on aftershock fitting, the parameter S(x) only contains one variable (U) to be calculated. The nonlinear function was transformed into a linear function between the coseismic slip and the observations as follows:

$$d = Gm + \varepsilon \tag{7}$$

where m is the slip on each sub-fault. We imposed a smoothness constraint to ensure that the stress drop had appropriate roughness. Then, we inverted the slip distribution to find the best solution of the objective function. The corresponding mathematical expression is:

$$F(m) = \|Gm - d\|^2 + \alpha^2\|Hm\|^2 \tag{8}$$

where α^2 is a smoothing factor, H is the Laplace operator, and $\|Hm\|^2$ is the roughness of fault slip. The steepest descent method (SDM) was used to invert the coseismic slip distribution (Wang et al., 2013; Hong-Wei et al., 2016).

Deformation field data sampled by uniform down-sampling were used for the inversion. In addition, owing to errors introduced by unwrapping, we removed InSAR deformation data in the near field of the fault (±0.02°). Finally, we obtained 6,562 and 6,339 data points for the descending and ascending tracks, respectively. We then set the maximum iteration to 10,000, which is sufficiently large for convergence. The rake angle ranged from −50° to 50°, which is consistent with the left-lateral strike-slip motion of the 2021 Maduo earthquake. The fault plane was meshed into a series of 2 × 2 km sub-faults for inversion. Notably, there are step-overs among the F3, F4, and F5 segments of the AFFP model (Figure 5).

3.3 Fault slip distribution

From the inversion results, the revolved moment magnitude of this earthquake is Mw 7.41. Four asperities were found during the inversion, along with dominant sinistral strike slip motion, which is consistent with the focal mechanism (Figure 7A and Figure 7B). In addition, we also identified some normal slip (with a rake angle of ~ -50°) at greater depths along the F3 and F5 segments. The peak slip of 4.8 m was located at the junction area of F5. Most of the coseismic slip was concentrated between 0 and 10 km depth and aftershock locations are complementary to the mainshock fault slip (Figure 8). For the residual of the inversion constrained by InSAR data, we found that predicted coseismic deformation on both ascending and descending tracks was consistent with the observations in terms of pattern and magnitude (Figures 7C–H).

Our aftershock-fitted, variable-dip, segmented fault model was able to explain the LOS displacement asymmetry on the north and south sides of the fault, and was consistent with the InSAR displacement field. Among the six segments, F2 is a secondary fault and F6 is a bifurcation fault. In the inversion results of coseismic slip distribution, the maximum slip momentum on F2 and F6 was <2 m, further confirming that F1, F3, F4, and F5 represent the main fault. The main rupture occurred in the intersection area of the F3 and F4 segments. The slip amount on the eastern fault was significantly greater than that on the western fault, confirming that the Maduo earthquake had a unilateral rupture trend. F5 had the largest slippage and formed a bifurcation structure with F6. We speculate that there may be a structure between F5 and F6 that hindered fracture extension along the same trend.

We compared our coseismic slip model with the results of four other studies. In terms of fault morphology, Jun et al. (2021) determined a single-section bending fault model with a fixed dip angle. The single-strike single-dip fault models used by Zhi-min et al. (2021) and the USGS (2021) were constrained by Global Positioning System (GPS) data and seismic wave data, respectively. He et al. (2021) used a six-segment fault model with variable strike and dip angles, reflecting the segmented characteristics of faults. Hong et al. (2022) reconstructed a model of one main fault and one secondary fault slip using Interferometric Synthetic Aperture Radar and Global Positioning System data. In terms of slip magnitude, the maximum slip of the Jun et al. (2021) and Zhi-min et al. (2021) models was ~4–5 m, located on the eastern segment; the maximum slip of the USGS (2021) model was ~3.2 m, the maximum slip of He et al. (2021) model was ~5 m, and that of the Hong et al. (2022) model was ~4.07 m. However, while the slip distributions of the different models differed, each showed multiple slip zones. The main difference between our model and theirs is that our model has more complex geometry (dip angle, segmental type and secondary fault), but the inversion results are consistent with theirs (slip magnitude and location of slip zones). The differences among the models reflect the different data sources and constraints; however, they all contribute to the study of the Maduo earthquake.

4 Discussion

4.1 Complexity of the maduo fault zone

The seismogenic structure of the 2021 Maduo mainshock was a 160 km E–W striking fault. Among the segments identified in this study, F2 and F3 run parallel to each other; F2 hosted most of the aftershocks. In past studies of the Maduo earthquake, the

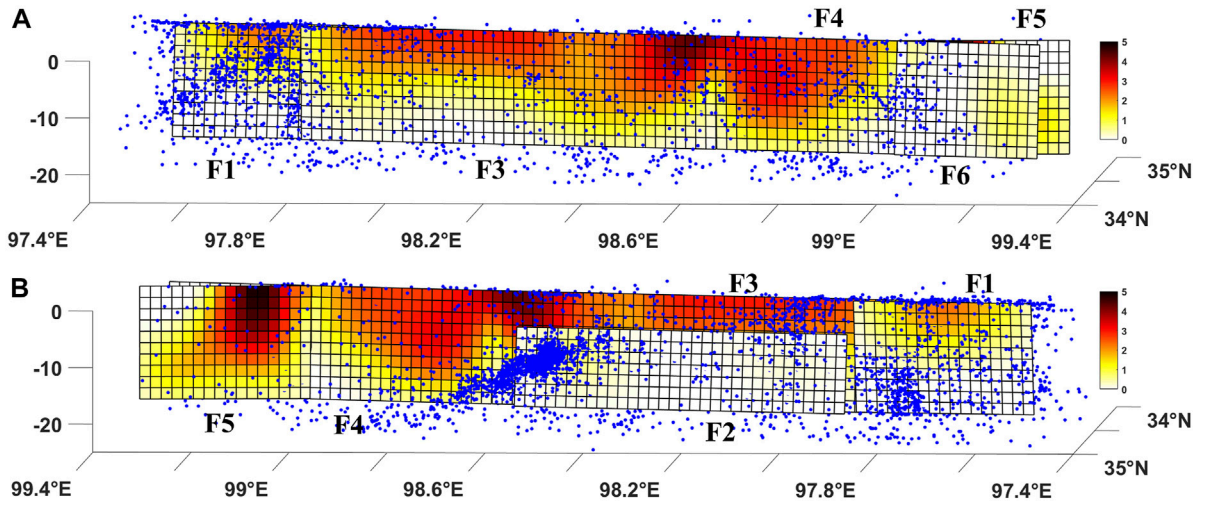

FIGURE 7
Coseismic slip distribution of the aftershock fitted fault plane (AFFP) model in a 3D viewing. **(A)** Slip distributions on the fault segments F1, F3, F4, and F6 in a 3D viewing; **(B)** Slip distribution on the secondary fault F2 and the F5 main fault in a 3D viewing. Pink circles are aftershocks within 2–15 days after the mainshock.

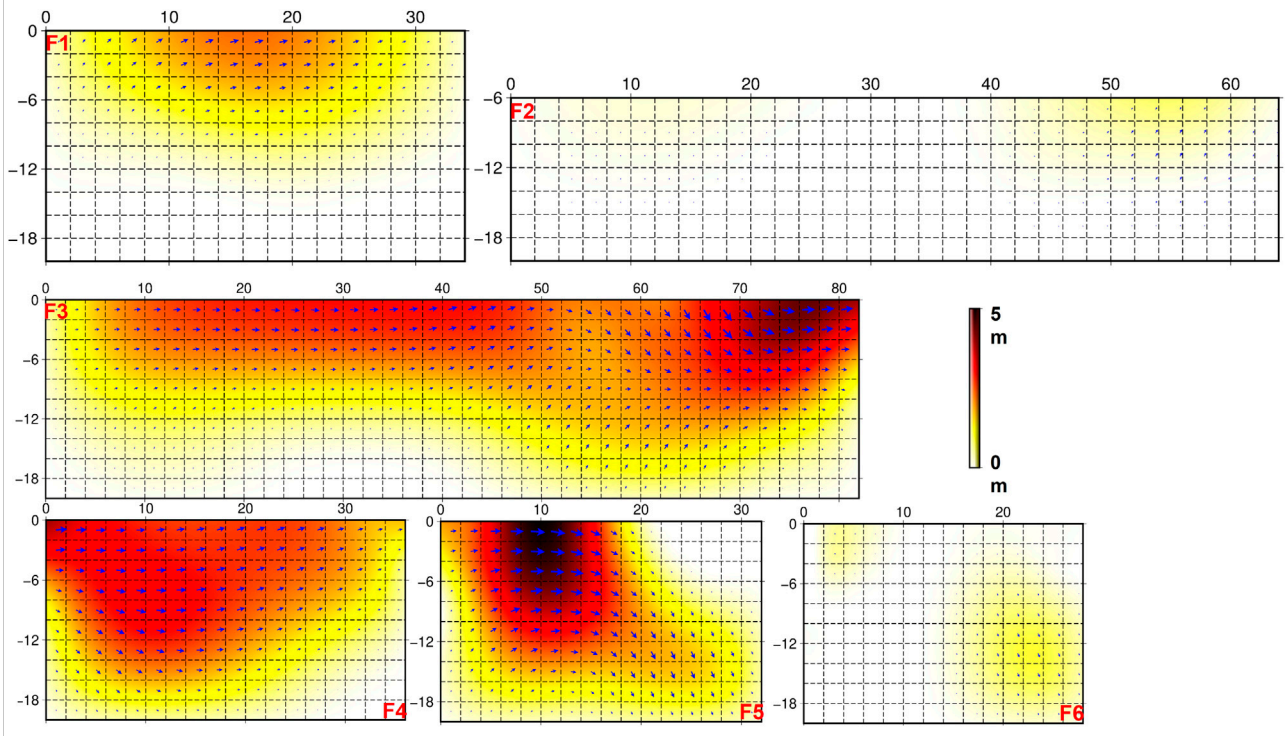

FIGURE 8
Slip distributions of the six fault segments in a 2D viewing.

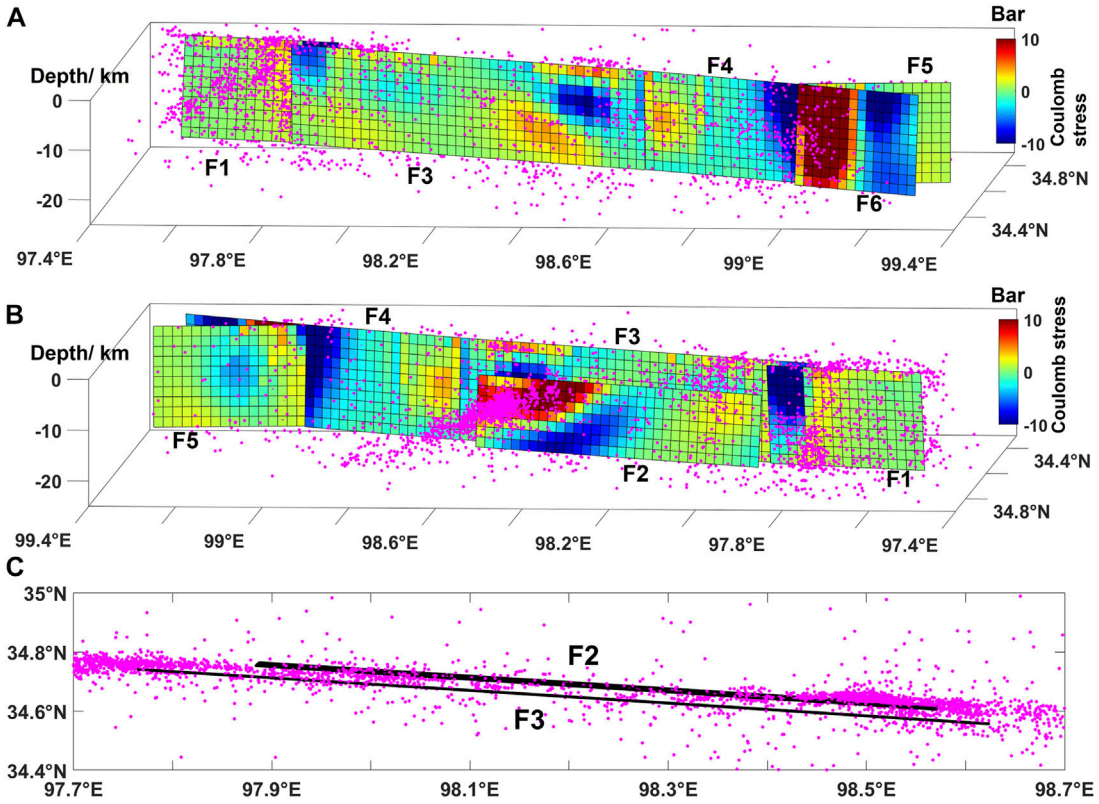

FIGURE 9
(A,B) The coulomb stress changes of the seismogenic fault plane after the Mado earthquake; **(C)** Projections of the F2, F3 faults and aftershocks on the surface. Pink circles are aftershocks within 0–15 days after the mainshock.

western part of the seismogenic fault (97.8°E~98.5°E) was assumed to have a non-vertical dip angle; for example, 65° (Zhao et al., 2021) or 72° (He et al., 2021). By comparing the aftershock data with surface trace observations, it was assumed that aftershocks located north of the surface trace indicated a north-inclined fault. However, as shown in Figure 5, this does not account for the deep aftershock characteristics. In contrast, we used the aftershock data to fit a near-vertical fault model with a good fitting degree to the surface rupture. Instead of a single inclined fault, our results suggest that aftershocks along F2 actually reveal a secondary fault parallel to the main fault (F3). Despite relatively few aftershocks, we confirmed that F3 was the main fault by removing the F3 from the model. The subsequent fitting results were inconsistent with the InSAR and offset data, confirming that F2 cannot replace F3 as the main coseismic slip surface. Our fault model only matched the observed data when slip on both F2 and F3 was assumed.

Previous studies have shown that, after a large mainshock, aftershocks can occur on secondary faults parallel to the main fault, or may be distributed along both the main fault and its secondary faults (Perrin et al., 2021). Fault zones are formed of three main features: a cataclasite core (Scholz, 1987), dilatant damage zone (Vermilye and Scholz, 1998; Faulkner et al., 2011; Savage and Brodsky, 2011), and shear deformation zone (Powers and Jordan, 2010). In a strike-slip fault, shear deformation zone contains multiple sets of secondary faults, including secondary faults parallel to the main fault. In the case of the 2021 Maduo earthquake, complex topographic and geomorphic features (e.g., near-surface water and soft sediments; Yuan et al., 2022) may have reduced the positioning accuracy of aftershocks and caused a loss of plane features. As a result, we could not judge whether the aftershock in F2 area occurred on the secondary fault parallel to the main fault or on the secondary fault conjugate to it.

Therefore, we also need to admit another case, the F2 fault obtained by the aftershock is actually a discrete rupture zone (It is composed of several secondary faults conjugated to the main fault) in the shear rupture zone of the strike-slip earthquake (Little et al., 1995). This means that most of the aftershocks in this region occur along the discrete rupture zone. Field observations of the surface fracture (Yuan et al., 2022) revealed discrete secondary cracks along the F3 segment, but no obvious continuous fracture, which also verified the existence of conjugate secondary faults. Thus, we suggest that the F2 segment of our AFFP model represents a discrete rupture zone or an immature secondary fault that was

activated by the coseismic rupture. However, in this paper, we still prefer to consider F2 as a secondary fault parallel to the main fault.

4.2 Physical and mechanical properties of the seismogenic fault

Along the seismogenic faults of continental strike-slip earthquakes, the structural maturity can vary with strike owing to the lateral propagation of the fault over time (Perrin et al., 2016). Thus, we could use our segmented fault slip parameters to describe local variation in maturity along the fault and the strain distribution characteristics of the seismogenic fault system. Previous studies have shown that, in the absence of data on net fault displacement, the geological slip rate can be also used as a proxy for net displacement in evaluating the overall maturity of the fault (Wesnousky, 1988; Stirling et al., 1996; Choy and Kirby, 2004; Manighetti et al., 2007; Hecker et al., 2010; Niemeijer et al., 2010; Dolan and Haravitch, 2014; Perrin et al., 2016); as net fault displacement increases, the fault grows and becomes more "mature"; that is, faults with large coseismic slip momentum can be considered more mature. According to Perrin et al., the total width of active shear zone around the main fault plane of mature and immature faults is 1.0–2.5km and 6–9km, respectively. In the Maduo earthquake, we believe that the aftershock distribution reveals the total width of the active shear deformation zone, which is about 5km, which proves that the seismogenic fault of the Maduo earthquake is not fully developed and mature.

According to both the slip magnitude (Figure 8) and large number of aftershocks, F2 represents an immature fault. F3 and F4, located on the central–eastern fault, have relatively smooth vertical planes; as a result, they can release a lot of stress quickly resulting in large coseismic slip and few aftershocks. Moreover, the central part of the seismogenic fault (F3 and F4) has the minimum rotation component and only slight extrusion and extensional deformation (Zhao et al., 2021), reflecting obvious linear fracture characteristics and the maturity of the segment. As such, we conclude that the main fault is relatively mature. However, the complex fault segmental structure of the Maduo earthquake shows that the seismogenic faults are generally not mature. This Maduo earthquake reveals the difficulty of assessing the seismic risk of immature strike-slip faults (Li et al., 2022).

We calculate the coseismic Coulomb stress changes (CSC) on the seismogenic fault plane using friction coefficients of 0.4 (Toda et al., 2011). The calculation results show that the maximum stress loading on the whole fault plane is ~47bar, located in the western half of fault F6, this explains the importance of F6 in tectonic development, and the maximum stress unloading is ~17bar, located in the area where the end of F4 is about to bifurcation into F5 and F6. We speculate that there may be a hard inelastic triangular structure beneath the F6 segment at the easternmost segment of the fault, and that this structure prevented the rupture from extending along the original strike. Instead, the rupture changed to a northward orientation along the F5 segment, on which there was a significant rupture and a large amount of coseismic deformation. Our results show that most aftershocks occur in the regions with positive CSC and few in the negative CSC regions (Figure 9A and Figure 9B). There are a large number of aftershocks in the stress loading area of F2 fault, which also verifies the reliability of F2 model.

5 Conclusion

A good fitting relationship between the Maduo earthquake aftershock sequence, InSAR deformation data, and field observations reveal that the seismogenic fault of the KPJF has a complex geometric structure. According to the segmented characteristics of aftershock data, we used a mathematical method to fit the AFFP with six fault segments. A secondary fault on the western end of the fault zone, segment F2, did not reach the surface. However, a continuous main fault (segments F1, F3–F5) experienced large coseismic slip that ruptured to the surface. A branch fault (segment F6) occurred at the easternmost end of the fault zone.

Using the AFFP model and InSAR deformation data to invert the fault slip distribution, we found that the earthquake was a shallow event (0–10 km) with dominant sinistral strike-slip motion. Four asperities were identified and the maximum slip of 4.84 m occurred on the eastern fault zone in an area where the strike changed. We speculate that the central segments of the main seismogenic fault are smooth and mature, with the exception of a parallel secondary fault, while the western and easternmost segments are complex and immature.

Data availability statement

The raw data supporting the conclusion of this article will be made available by the authors, without undue reservation.

Author contributions

XF: Conceptualization, Data curation, Formal analysis, Visualization, Writing—original draft. GZ: Conceptualization, Funding acquisition, Methodology, Supervision, Writing—review and editing. DZ: Methodology, Writing—review and editing. CX: Methodology. CH: Data curation. XS: Supervision, Funding acquisition.

Funding

This research was funded by the Basic Scientific Funding of Institute of Geology, China Earthquake Administration (grant number IGCEA2005), the National Natural Science Foundation of China (grant number U2139202) and the National Key

Research and Development Program of China (grant number 2019YFC1509205).

Acknowledgments

The figures in this study were generated using the public domain Generic Mapping Tools (GMT) software. Thanks to Guangcai Feng 's team for providing InSAR deformation results as a reference comparison.

Conflict of interest

The remaining authors declare that the research was conducted in the absence of any commercial or financial relationships that could be construed as a potential conflict of interest.

The reviewer SH declared a shared affiliation with the authors XF, GZ, DZ, XS to the handling editor at the time of review.

Publisher's note

All claims expressed in this article are solely those of the authors and do not necessarily represent those of their affiliated organizations, or those of the publisher, the editors and the reviewers. Any product that may be evaluated in this article, or claim that may be made by its manufacturer, is not guaranteed or endorsed by the publisher.

References

Breunig, M. M., Kriegel, H. P., Ng, R. T., and Sander, J. (2000). "LOF: identifying density-based local outliers," in Proceedings of the 2000 ACM SIGMOD international conference on Management of data, Dallas, Texas, USA, May 16-18, 2000, 93–104.

Chen, H., Qu, C., Zhao, D., Ma, C., and Shan, X. (2021). Rupture kinematics and coseismic slip model of the 2021 Mw 7.3 Maduo (China) earthquake: Implications for the seismic hazard of the Kunlun fault. *Remote Sens.* 13 (16), 3327. doi:10.3390/rs13163327

Chiarabba, C., Amato, A., Anselmi, M., Baccheschi, P., Bianchi, I., Cattaneo, M., et al. (2009). The 2009 L'Aquila (central Italy) MW6.3 earthquake: Main shock and aftershocks. *Geophys. Res. Lett.* 36, L18308. doi:10.1029/2009GL039627

Choy, G. L., and Kirby, S. H. (2004). Apparent stress, fault maturity and seismic hazard for normal-fault earthquakes at subduction zones. *Geophys. J. Int.* 159 (3), 991–1012. doi:10.1111/j.1365-246X.2004.02449.x

Dietz, L. D., and Ellsworth, W. L. (1990). The October 17, 1989, Loma Prieta, California, earthquake and its aftershocks: Geometry of the sequence from high-resolution locations. *Geophys. Res. Lett.* 17 (9), 1417–1420. doi:10.1029/GL017i009p01417

Dolan, J. F., and Haravitch, B. D. (2014). How well do surface slip measurements track slip at depth in large strike-slip earthquakes? The importance of fault structural maturity in controlling on-fault slip versus off-fault surface deformation. *Earth Planet. Sci. Lett.* 388, 38–47. doi:10.1016/j.epsl.2013.11.043

Fang, L., Wu, J., Su, J., Wang, M., Jiang, C., Fan, L., et al. (2018). Relocation of mainshock and aftershock sequence of the <italic>M</italic>_s7.0 Sichuan Jiuzhaigou earthquake. *Chin. Sci. Bull.* 63 (7), 649–662. doi:10.1360/n972017-01184

Faulkner, D. R., Mitchell, T. M., Jensen, E., and Cembrano, J. (2011). Scaling of fault damage zones with displacement and the implications for fault growth processes. *J. Geophys. Res.* 116 (B5), B05403. doi:10.1029/2010JB007788

Hauksson, E. (2010). "Spatial separation of large earthquakes, aftershocks, and background seismicity: Analysis of interseismic and coseismic seismicity patterns in southern California," in *Seismogenesis and earthquake forecasting: The frank evison volume II* (Basel: Springer), 125–143.

He, L., Feng, G., Wu, X., Lu, H., Xu, W., Wang, Y., et al. (2021). Coseismic and early postseismic slip models of the 2021 Mw 7.4 Maduo earthquake (Western China) estimated by space-based geodetic data. *Geophys. Res. Lett.* 48 (24), e2021GL095860. doi:10.1029/2021GL095860

Hecker, S., Dawson, T. E., and Schwartz, D. P. (2010). Normal-faulting slip maxima and stress-drop variability: A geological perspective. *Bull. Seismol. Soc. Am.* 100 (6), 3130–3147. doi:10.1785/0120090356

Hong, S., Liu, M., Liu, T., Dong, Y., Chen, L., Meng, G., et al. (2022). Fault source model and stress changes of the 2021 Mw 7.4 Maduo earthquake, China, constrained by InSAR and GPS measurements. *Bull. Seismol. Soc. Am.* 112 (3), 1284–1296. doi:10.1785/0120210250

Hong-Wei, T., Rong-Jiang, W., Fa-Qi, D., Yong, Z., Yong-Ge, W., and Ming-Pei, J. (2016). Slip model of the 2001 Kunlun mountain MS8.1 earthquake by SDM: Joint inversion from GPS and InSAR data. *Chin. J. Geophys.* 59 (4), 404–413. doi:10.1002/cjg2.20245

Jun, H., De-zheng, Z., Xin-jian, S., Chun-yan, Q., Ying-feng, Z., Wen-yu, G., et al. (2021). Coseismic deformation field, slip distribution and Coulomb stress disturbance of the 2021 Mw7. 3 Maduo earthquake using Sentinel-1 InSAR observations. *Seismol. Egology* 43 (3), 677. doi:10.3969/j.issn.0253-4967.2021.03.013

Li, C., Li, T., Shan, X., and Zhang, G. (2022). Extremely large off-fault deformation during the 2021 Mw 7.4 Maduo earthquake, Tibetan Plateau. *Seismol. Res. Lett.* XX, 1–13.

Li, H., Qi, X., Zhu, Y., Yang, J., Tapponnier, P., Shi, L., et al. (2004). Asymmetrical Co-seismic surface ruptures in the east Kunlun earthquake (Ms-8.1), northern Tibetan plateau, China. *Acta Geol. Sinica-Chinese Ed.* 78 (5), 633–640. doi:10.1007/BF02873097

Little, T. A. (1995). Brittle deformation adjacent to the Awatere strike-slip fault in New Zealand: Faulting patterns, scaling relationships, and displacement partitioning. *Geol. Soc. Am. Bull.* 107 (11), 1255–1271. doi:10.1130/0016-7606(1995)107<1255:BDATTA>2.3.CO;2

Manighetti, I., Campillo, M., Bouley, S., and Cotton, F. (2007). Earthquake scaling, fault segmentation, and structural maturity. *Earth Planet. Sci. Lett.* 253 (3-4), 429–438. doi:10.1016/j.epsl.2006.11.004

Niemeijer, A., Marone, C., and Elsworth, D. (2010). Fabric induced weakness of tectonic faults. *Geophys. Res. Lett.* 37 (3). doi:10.1029/2009GL041689

Okada, Y. (1985). Surface deformation due to shear and tensile faults in a half-space. *Bull. Seismol. Soc. Am.* 75 (4), 1135–1154. doi:10.1785/bssa0750041135

Pan, J., Li, H., Chevalier, M. L., Tapponnier, P., Bai, M., Li, C., et al. (2022). Co-seismic rupture of the 2021, M 7.4 Maduo earthquake (northern Tibet): Short-cutting of the Kunlun fault big bend. *Earth Planet. Sci. Lett.* 594, 117703. doi:10.1016/j.epsl.2022.117703

Parsons, T., Ji, C., and Kirby, E. (2008). Stress changes from the 2008 Wenchuan earthquake and increased hazard in the Sichuan basin. *Nature* 454 (7203), 509–510. doi:10.1038/nature07177

Perrin, C., Manighetti, I., Ampuero, J. P., Cappa, F., and Gaudemer, Y. (2016). Location of largest earthquake slip and fast rupture controlled by along-strike change in fault structural maturity due to fault growth. *J. Geophys. Res. Solid Earth* 121 (5), 3666–3685. doi:10.1002/2015JB012671

Perrin, C., Waldhauser, F., and Scholz, C. H. (2021). The shear deformation zone and the smoothing of faults with displacement. *JGR. Solid Earth* 126 (5), e2020JB020447. doi:10.1029/2020JB020447

Powers, P. M., and Jordan, T. H. (2010). Distribution of seismicity across strike-slip faults in California. *J. Geophys. Res.* 115 (B5), B05305. doi:10.1029/2008JB006234

Qi-Dong, D., Shao-Ping, C., Ji, M., and Peng, D. (2014). Seismic activities and earthquake potential in the Tibetan Plateau. *Chin. J. Geophys.* 57 (5), 678–697. doi:10.1002/cjg2.20133

Qi-Dong, D., Xiang, G., Gui-Hua, C., and Hu, Y. (2010). Recent tectonic activity of Bayankala fault block and the Kunlun Wenchuan earthquake series of the Tibetan Plateau. *Earth Sci. Front.* 17 (5), 163.

Ren, J., Xu, X., Zhang, G., Wang, Q., Zhang, Z., Gai, H., et al. (2022). Coseismic surface ruptures, slip distribution, and 3D seismogenic fault for the 2021 Mw 7.3 Maduo earthquake, central Tibetan Plateau, and its tectonic implications. *Tectonophysics* 827, 229275. doi:10.1016/j.tecto.2022.229275

Savage, H. M., and Brodsky, E. E. (2011). Collateral damage: Evolution with displacement of fracture distribution and secondary fault strands in fault damage zones. *J. Geophys. Res.* 116 (B3), B03405. doi:10.1029/2010JB007665

Scholz, C. H. (1987). Wear and gouge formation in brittle faulting. *Geol.* 15 (6), 493–495. doi:10.1130/0091-7613(1987)15<493:WAGFIB>2.0.CO;2

Stirling, M. W., Wesnousky, S. G., and Shimazaki, K. (1996). fault trace complexity, cumulative slip, and the shape of the magnitude-frequency distribution for strike-slip faults: A global survey. *Geophys. J. Int.* 124 (3), 833–868. doi:10.1111/j.1365-246X.1996.tb05641.x

Tobita, M., Nishimura, T., Kobayashi, T., Hao, K. X., and Shindo, Y. (2011). Estimation of coseismic deformation and a fault model of the 2010 Yushu earthquake using PALSAR interferometry data. *Earth Planet. Sci. Lett.* 307 (3-4), 430–438. doi:10.1016/j.epsl.2011.05.017

Toda, S., Stein, R. S., Sevilgen, V., and Lin, J. (2011). Coulomb 3.3 graphic-rich deformation and stress-change software for earthquake, tectonic, and volcano research and teaching—user guide. *U. S. Geol. Surv. open-file Rep.* 1060, 63.

Valoroso, L., Chiaraluce, L., and Collettini, C. (2014). Earthquakes and fault zone structure. *Geology* 42 (4), 343–346. doi:10.1130/G35071.1

Vermilye, J. M., and Scholz, C. H. (1998). The process zone: A microstructural view of fault growth. *J. Geophys. Res.* 103 (B6), 12223–12237. doi:10.1029/98JB00957

Wan, Y., Shen, Z. K., Bürgmann, R., Sun, J., and Wang, M. (2016). Fault geometry and slip distribution of the 2008 Mw 7.9 Wenchuan, China earthquake, inferred from GPS and InSAR measurements. *Geophys. J. Int.* 208, 748–766. doi:10.1093/gji/ggw421

Wang, C., Ke, J., Jiang, J., Lu, M., Xiu, W., Liu, P., et al. (2019). Visual analytics of aftershock point cloud data in complex fault systems. *Solid earth.* 10 (4), 1397–1407. doi:10.5194/se-10-1397-2019

Wang, R., Parolai, S., Ge, M., Jin, M., Walter, T. R., and Zschau, J. (2013). The 2011 M w 9.0 Tohoku earthquake: Comparison of GPS and strong-motion data. *Bull. Seismol. Soc. Am.* 103 (2B), 1336–1347. doi:10.1785/0120110264

Wang, W., Fang, L., Wu, J., Tu, H., Chen, L., Lai, G., et al. (2021). Aftershock sequence relocation of the 2021 Ms7. 4 Maduo earthquake, qinghai, China. *Sci. China Earth Sci.* 64 (8), 1371–1380. doi:10.1007/s11430-021-9803-3

Wen, X. Z., Du, F., Zhang, P. Z., and Long, F. (2011). Correlation of major earthquake sequences on the northern and eastern boundaries of the Bayan Har block, and its relation to the 2008 Wenchuan earthquake. *Chin. J. Geophys.* 54 (3), 706–716. doi:10.3969/j.issn.0001-5733.2011.03.010

Werner, C., Wegmüller, U., and Strozzi, T., (2002). "Processing strategies for phase unwrapping for INSAR applications," in proceedings of the European conference on synthetic aperture radar (EUSAR 2002), Bern, Switzerland, May 13, 2002, 353–356.

Werner, C., Wegmueller, U., Strozzi, T., and Wiesmann, A. (2000). "Gamma SAR and interferometric processing software," in Proceedings of the ers-envisat symposium, Gothenburg, Sweden, 16-20 Oct, 1620.

Wesnousky, S. G. (1988). Seismological and structural evolution of strike-slip faults. *Nature* 335 (6188), 340–343. doi:10.1038/335340a0

Xu, X., Tan, X., Yu, G., Wu, G., Fang, W., Chen, J., et al. (2013). Normal-and oblique-slip of the 2008 Yutian earthquake: Evidence for eastward block motion, northern Tibetan Plateau. *Tectonophysics* 584, 152–165. doi:10.1016/j.tecto.2012.08.007

Yuan, Z., Li, T., Su, P., Sun, H., Ha, G., Guo, P., et al. (2022). Large surface-rupture gaps and low surface fault slip of the 2021 Mw 7.4 Maduo earthquake along a low-activity strike-slip fault, Tibetan plateau. *Geophys. Res. Lett.* 49 (6), e2021GL096874. doi:10.1029/2021GL096874

Zhang, P., Deng, Q., Zhang, G., Ma, J., Gan, W., Min, W., et al. (2003). Active tectonic blocks and strong earthquakes in the continent of China. *Sci. China Ser. D Earth Sci.* 46 (2), 13–24. doi:10.1360/03dz0002

Zhao, D., Qu, C., Chen, H., Shan, X., Song, X., and Gong, W. (2021). Tectonic and geometric control on fault kinematics of the 2021 Mw7. 3 Maduo (China) earthquake inferred from interseismic, coseismic, and postseismic InSAR observations. *Geophys. Res. Lett.* 48 (18), e2021GL095417. doi:10.1029/2021GL095417

Zhi-min, L., Wen-qiao, L., Tao, L., Yue-ren, X., Peng, S., Peng, G., et al. (2021). seismogenic fault and coseismic surface deformation of the Maduo Ms7. 4 earthquake in qinghai, China: A quick report. *Seismol. Egology* 43 (3), 722. doi:10.3969/j.issn.0253-4967.2021.03.016

Ziv, A. (2006). On the role of multiple interactions in remote aftershock triggering: The Landers and the Hector Mine case studies. *Bull. Seismol. Soc. Am.* 96 (1), 80–89. doi:10.1785/0120050029

frontiers | Frontiers in Earth Science

TYPE Original Research
PUBLISHED 05 January 2023
DOI 10.3389/feart.2022.1000349

OPEN ACCESS

EDITED BY
Caijun Xu,
Wuhan University, China

REVIEWED BY
Guangcai Feng,
Central South University, China
Yu Zhou,
Sun Yat-sen University, China
Lingyun Ji,
The Second Monitoring and Application Center, China Earthquake Administration, China

*CORRESPONDENCE
Xiaogang Song,
sxghohai@ies.ac.cn

SPECIALTY SECTION
This article was submitted to Structural Geology and Tectonics, a section of the journal Frontiers in Earth Science

RECEIVED 22 July 2022
ACCEPTED 13 September 2022
PUBLISHED 05 January 2023

CITATION
Yang Y, Song X, Gong W and Qu C (2023), Fault slip of the 2022 Mw6.7 Menyuan, China earthquake observed by InSAR, and its tectonic implications. *Front. Earth Sci.* 10:1000349. doi: 10.3389/feart.2022.1000349

Fault slip of the 2022 Mw6.7 Menyuan, China earthquake observed by InSAR, and its tectonic implications

Yuetong Yang, Xiaogang Song*, Wenyu Gong and Chunyan Qu

State Key Laboratory of Earthquake Dynamics, Institute of Geology, China Earthquake Administration, Beijing, China

In this article the ascending and descending Sentinel-1A satellite data are used to investigate the coseismic slip model of the 2022 Mw6.7 Menyuan earthquake in Qinghai, China. The optimal slip model indicates that this event ruptured two fault segments. The main rupture concentrated on the western Lenglongling fault (LLLF) with a purely left-lateral striking-slip motion. A small part of the eastern Tuolaishan fault (TLSF) section was also ruptured, and the motion on it is mainly oblique slip at depth, with an obvious thrust component. Combined with the rupture characteristics of historical events, GPS velocity map, and slip rate studies, we suggest that the TLSF–LLLF junction is a demarcation point where the deformation partitioning pattern has changed. Along the whole LLLF segment, the oblique convergence has completely partitioned into slip on the purely strike-slipping LLLF and thrusting faults in the north. The TLSF segment accommodates a fraction of compressional shortening, which compensates for the discrepancy in the left-lateral slip rate between the LLLF and TLSF. Such transformation in the strain partitioning pattern is likely to be determined by the geometric relationship between the fault strike and the direction of regional block movement.

KEYWORDS

the Lenglongling fault, the Tuolaishan fault, the 2022 Mw6.7 Menyuan earthquake, Menyuan earthquake, InSAR, deformation partitioning pattern

Introduction

On 8 January 2022, an Mw6.7 earthquake struck ~59 km far away from Menyuan County in the Qinghai Province of northwestern China at the western section of the Qilian–Haiyuan fault (QL-HYF) zone. According to the focal-mechanism solution reported by the United States Geological Survey (USGS) and Global Centroid Moment Tensor (GCMT), the fault movement caused by the main shock was dominated by an NWW left-lateral strike-slip with a thrust component (Table 1; Figure 1).

As the leading edge of the northeastern Tibetan Plateau, the QL-HYF zone accommodates about a quarter of the convergence rate driven by the ongoing collision of the India and Eurasia plates, as shown in previous investigations (e.g.,

TABLE 1 Focal mechanisms of the 2022 Menyuan earthquake reported by different studies.

Source	Location of the epicenter		Depth (km)	Focal mechanism		Mag. (*Mw*)
	Lon. (°*E*)	Lat. (°*N*)		(Strike/dip/rake) (°)		
USGS	101.29	37.83	13.0	NP 1	13°/75°/178°	6.61
				NP 2	104°/88°/15°	
GCMT	101.31	37.80	14.8	NP 1	14°/89°/172°	6.70
				NP 2	104°/82°/1°	
This study	101.27	37.80	~3.0	NP 1	-	6.69
				NP 2	115°/88°/1°	

USGS: United States Geological Survey; GCMT: Global Centroid Moment Tensor.

Molnar & Tapponnier, 1975; England & Houseman, 1985; Tapponnier et al., 1990; Pichon et al., 1992; England & Molnar, 1997; Tapponnier et al., 2001; Flesch et al., 2001; Yuan et al., 2013; Zuza et al., 2018). The strain distribution of the NE Tibetan Plateau from the recent Global Navigation Satellite System (GNSS) and interferometric synthetic aperture radar (InSAR) observations (Wang and Shen, 2020; Huang et al., 2022; Ou et al., 2022; Figure 1B) shows dominant shearing deformation on the middle of the northeast edge of the Tibetan Plateau and extrusion deformation on the eastern and western areas. The left-lateral shearing deformation largely focuses on the QL–HYF zone. Previous studies have suggested that an ESE trending continuously transferred deformation along fault segments of the QL–HYF zone from west to east (Gaudermer et al., 1995; Lasserre et al., 2002; Yuan et al., 2004; Zheng et al., 2013; Yao et al., 2019). However, recent studies do not seem to support such a tectonic transformation model. Field geological investigations at the middle QL–HYF zone show that the strain on the middle Lenglongling fault (LLLF) tends to be transferred northeast forward to the eastern LLLF, rather than transmitted eastward to the Jinqianghe fault (JQHF) (Guo et al., 2019, 2020; Gao et al., 2021). InSAR observations from Envisat and Sentinel-1 satellites present slip partitioning and segmented movement for the 1,000-km QL–HYF system (Daout et al., 2016; Huang et al., 2022; Ou et al., 2022). As for the western section of the QL–HYF (the TLSF and further west), the fault slip rate and strain partitioning have not been properly investigated. Previous research (IGLIS, 1993; Yuan et al., 2003; Deng et al., 2007; Xu et al., 2016) concentrated on the left-lateral shear movement on the TLSF and suggested a dominant sinistral strike-slip on the TLSF. Huang et al. (2022) suggested that the Qilianshan absorbs ~4 mm/yr left-lateral shear discrepancy between the TLSF and middle segment of the QL–HYF by shortening, given a low dip-slip rate on the TLSF from the InSAR profile inversion. However, the recent cross-fault GPS and leveling profiles show an obvious shortening and vertical deformation across the TLSF (Li et al., 2022, Supplementary Figure S1). It is controversial how the strain is partitioned along the western section of the QL–HYF and other faults in the north. The present-day slip rates estimated from InSAR cross-fault profiles (Huang et al., 2022; Ou et al., 2022) show an obvious step between the Tuolaishan fault (TLSF) segment and LLLF segment, where the 2022 Menyuan event occurred. It is a good opportunity to investigate the tectonic role of the TLSF and LLLF sections in the deformation transformation model of the northeast edge of the Tibetan Plateau from this earthquake.

In this study, both the ascending and descending interferograms from the Sentinel-1A satellite, whose tropospheric delays were corrected by a method dedicated to the small-to-moderate-magnitude earthquake proposed by Gong et al. (2022), were used to investigate the coseismic displacements of the Menyuan earthquake. Combined with previous geodetic and geological observations, we try to 1) determine the slip kinematics of the 2022 Mw6.7 Menyuan earthquake and discuss its tectonic implications and 2) analyze how the tectonic deformation is transformed from the TLSF to LLLF. Our results will help to improve understanding of the deformation partitioning patterns in the western section of the northeastern edge of the Tibetan Plateau.

Tectonic setting

As a major tectonic structure in the northeastern margin of the Tibetan Plateau, the QL–HYF zone plays an important role in accommodating the northeastward expansion of the Tibetan Plateau into the continental interior (e.g., Lasserre et al., 2002; Duvall and Clark, 2010; Zheng et al., 2013; Guo et al., 2017; Huang et al., 2022). Located at the convergence boundaries between Tibet, Gobi–Alashan block and Ordos block, it presents a geometrical complexity along faults, composed of several segments (Figures 1A,B), i.e., the TLSF, LLLF, JQHF, Maomaoshan fault (MMSF), Laohushan fault (LHSF), Haiyuan fault (HYF), and Liupanshan fault (LPSF) from west to east. Fault

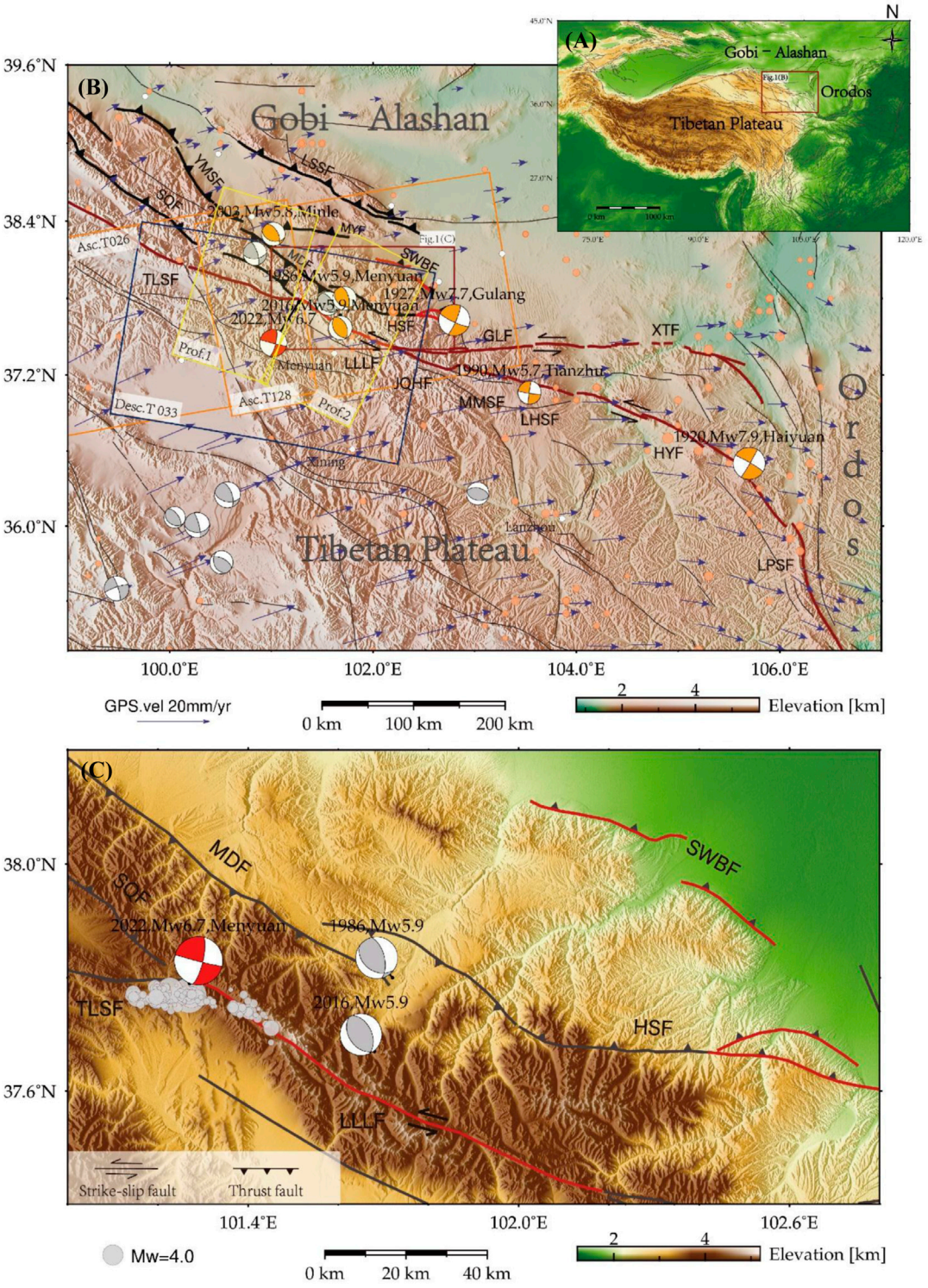

FIGURE 1
Tectonic setting of the 2022 Mw6.7 Menyuan earthquake. **(A)** Tectonic setting of the Qilian–Haiyuan fault (QL–HYF) zone. **(B)** Main faults in the NE Tibetan Plateau. Active faults are from Deng et al. (2007) (https://www.activefault-datacenter.cn/map). The Mw 5.7 + historical earthquakes that occurred along the QL–HYF zone since 1920 are marked by the GCMT focal mechanisms. Arrows indicate GPS velocities from Wang and Shen, (2020). The orange and blue rectangles outline the coverage of ascending and descending Sentinal-1 SAR data. Two yellow rectangles outline the coverage of the GPS profiles across the TLSF and LLLF, which are shown in Supplementary Figure S1. TLSF: Tuolaishan fault; LLLF: Lenglongling fault; JQHF: Jinqianghe fault; MMSF: Maomaoshan fault; LHSF: Laohushan fault; HYF: Haiyuan fault; LPSF: Liupanshan fault; GLF: Gulang fault; XTF: (*Continued*)

FIGURE 1 (Continued)
Xiangshan–Tianjingshan fault; HSF: Huangcheng–Shuangta fault; SWBF: Southern Wuwei Basin fault; SQF: Sunan–Qilian fault; YMSF: Yumushan fault; MDF: Minle–Damaying fault; MYF: Minle–Yongchang fault; LSSF: Longshoushan fault. **(C)** Tectonic map in the seismogenic area of the 2022 Mw6.7 Menyuan earthquake. The surface rupture of the 1927 Gulang earthquake in red is modified from Guo et al. (2020). The gray circles present the aftershocks within the first 10 days after the main shock was recorded by the local seismometer array (Fan et al., 2022). Two moderate-thrust earthquakes that occurred in this region in 1986 and 2016 are marked by the GCMT focal mechanisms.

TABLE 2 Focal mechanisms of the historical tectonic events (Mw> 5.7) in the QL–HYF zone.

Tectonic event	Location of the epicenter		Depth (km)	Focal mechanism	Mag. (*Mw*)	Rupture type
	Lon. (°*E*)	Lat. (°*N*)		(Strike/dip/rake) (°)		
1920, Haiyuan	105.54	36.48	6.0	110°/90°/10°	7.9	Strike-slip
1927, Gulang	102.37	38.05	10.0	110°/45°/45°	7.7	Strike-slip with slight thrust
1986, Menyuan	101.72	37.80	15.0	346°/60°/113°	5.9	Thrust
1990, Tianzhu	10.354	37.06	15.0	98°/85°/−3°	5.7	Strike-slip
2003, Minle	101.02	38.30	15.0	331°/58°/116°	5.8	Thrust with slight strike-slip
2016, Menyuan	101.68	37.67	14.3	335°/47°/96°	5.9	Thrust

The focal mechanism of the 1920 Haiyuan earthquake is sourced from Ou et al. (2020), and the focal mechanism of the 1927 Gulang earthquake is sourced from Molnar and Deng (1984). Others are sourced by Global Centroid Moment Tensor.

kinematics and seismicity on those fault segments have been extensively studied by using both geological and geodetic observations over the last decades. Although a high west-to-east decreasing strike-slip rate (19 ± 5 mm/yr and 12 ± 4 mm/yr) is suggested for the QL–HYF by early geological studies (Zhang et al., 1988; Lasserre et al., 1999; Lasserre et al., 2002), the follow-on research studies give a relatively consistent estimate with an arc-shaped distribution, from 0–2 mm/yr in the western end to 4.5–9 mm/yr in the middle section, and then decreasing to 0–2 mm/yr in the eastern end near the LPSF (e.g., He et al., 2001; Gan et al., 2007; Li et al., 2009; Duvall and Clark, 2010; Loveless and Meade, 2011; Zheng et al., 2013; Jiang et al., 2017; Liu et al., 2018; Shao et al., 2020). InSAR observations (Daout et al., 2016; Song et al., 2019; Huang et al., 2022; Ou et al., 2022) provide a detailed slip rate and slip partitioning map on the QL–HYF and some northerly located faults, such as the Gulang fault (GLF), Xiangshan–Tianjingshan fault (XTF), Huangcheng–Shuangta fault (HSF), Southern Wuwei Basin fault (SWBF), Sunan–Qilian fault (SQF), Yumushan fault (YMSF), Minle–Damaying fault (MDF), Minle–Yongchang fault (MYF), and Longshoushan fault (LSSF) (Figures 1B,C). The QL–HYF zone was seismically active in the past century. More than six Mw5.5+ earthquakes occurred along it, including the 1920 Mw7.9 Haiyuan earthquake, 1927 Mw7.7 Gulang earthquake, 1986 Mw5.9 Menyuan earthquake, 1990 Mw5.7 Tianzhu earthquake, 2003 Mw5.8 Minle earthquake, and 2016 Mw5.9 Menyuan earthquake (Table 2; Figures 1B,C).

The seismogenic fault of the 2022 Mw6.7 Menyuan earthquake is the TLSF–LLLF, the western section of the QL–HYF. Tectonically, the LLLF branches into the TLSF and northerly located SQF at its western end, and the TLSF steps left in a ~3-km left-stepped en echelon pattern (Guo et al., 2019; Pan et al., 2022). The TLSF and further west have not been properly investigated due to inaccessibility and remoteness, and it is suggested to be dominated by a sinistral strike-slip (Deng et al., 2007). The recent InSAR results (Huang et al., 2022) gave a strike-slip rate map along the TLSF, and its along-strike-slip rate gradually increases from 1.8 ± 0.3 mm/yr close to Halahu in the western end, to 2.8 mm/yr in the middle, and 3.5 mm/yr along the easternmost segment. The motion on the LLLF is predominantly left-lateral strike-slip during the late Quaternary (Guo et al., 2020), following a thrusting movement due to the northeastward compression in the early Quaternary (He et al., 2001; Li et al., 2009). Most studies of the geological slip rate of the LLLF focus on the middle section. Among those studies, the two most recent studies from Jiang et al. (2017) and Guo et al. (2017) reported a consistent estimate with a slip rate of 6.6 ± 0.3 mm/yr and 6.4 ± 0.7 mm/yr, respectively, in agreement with InSAR-inverted one (6.4 ± 0.5 mm/yr) by Huang et al. (2022). Gao et al. (2021) gave a slip rate of 6.0 ± 0.8 mm/yr for the eastern section of the LLLF,

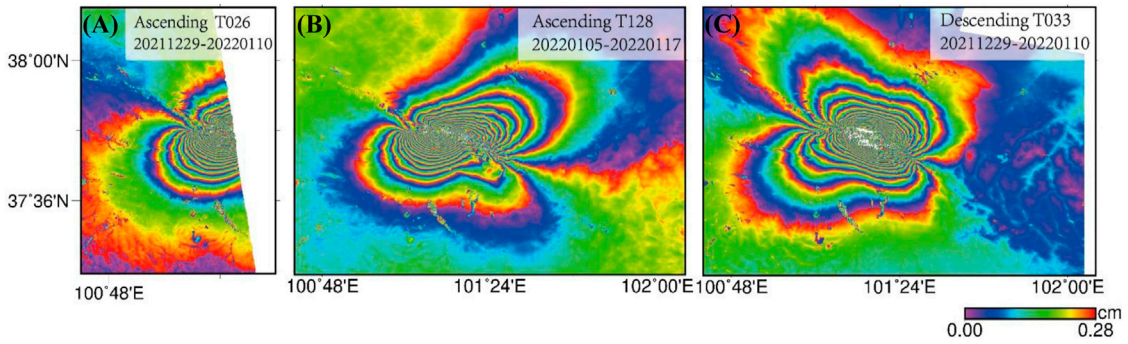

FIGURE 2
Coseismic interferograms of the 2022 Mw6.7 Menyuan earthquake observed by InSAR. **(A)** Ascending track 026, **(B)** ascending track 128, and **(C)** descending track 033 of the Sentinel-1A.

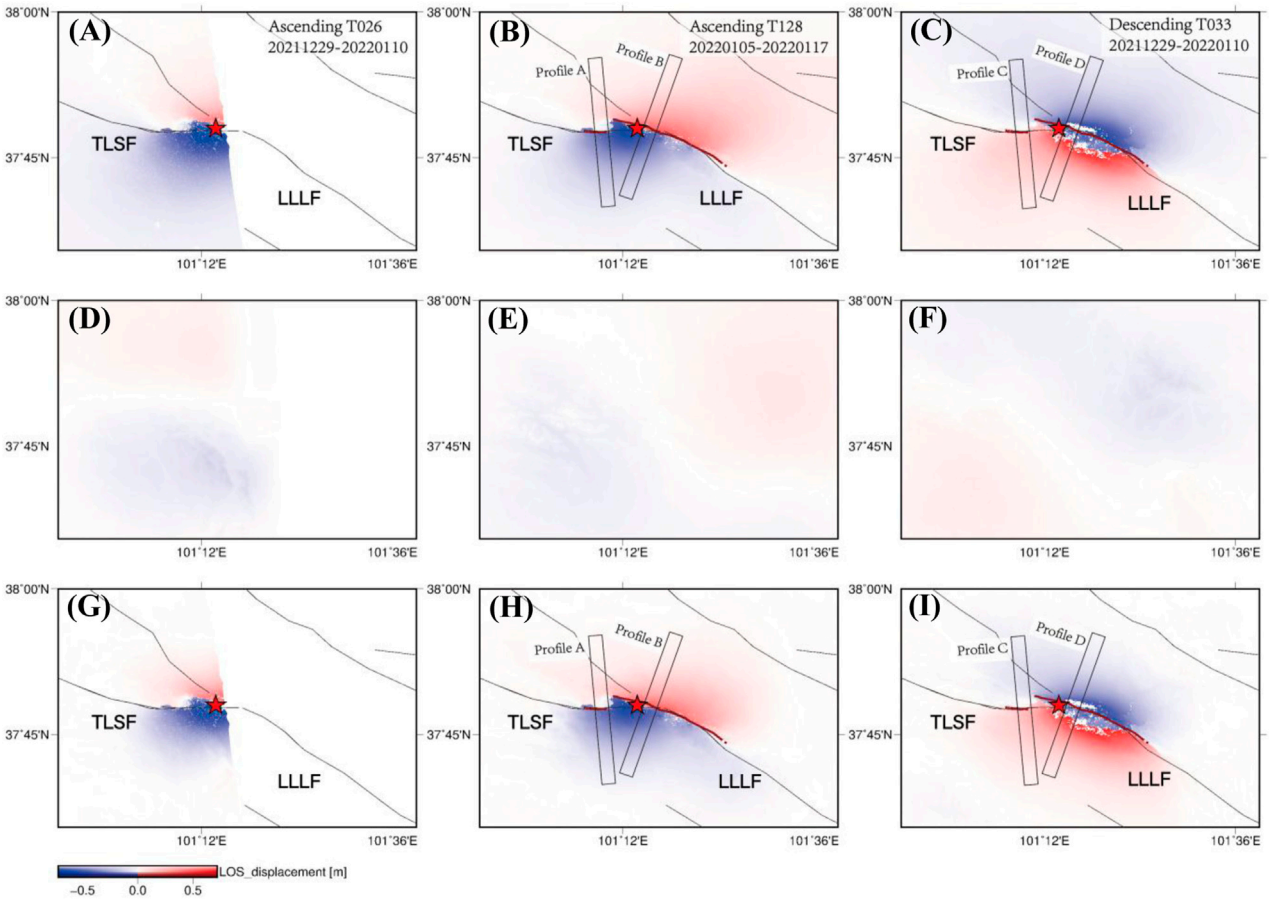

FIGURE 3
Atmospheric correction for the ascending and descending data. **(A–C)** LOS displacement maps before atmospheric correction. **(D–F)** Stratified tropospheric delay, estimated using the SSC method. **(G–I)** After atmospheric correction. The epicenter is indicated by a red star, and the dark-red line indicates the field-investigated surface rupture from Pan et al. (2022).

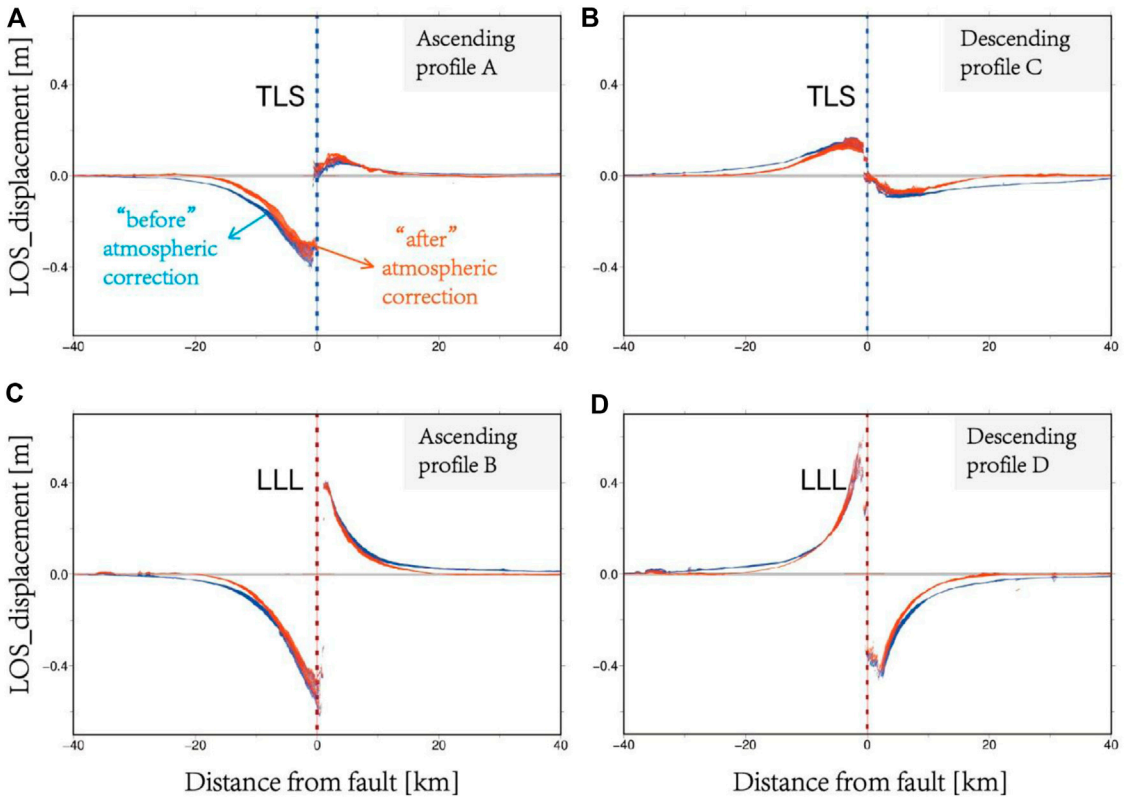

FIGURE 4
LOS displacement profiles, which are indicated in Figure 3. Profiles **(A,C)** are perpendicular to the TLSF, and profiles **(B,D)** are perpendicular to the LLLF.

similar to the estimates in the middle section. In the western section, a slip rate of 4.6 ± 0.2 mm/yr can be seen on the InSAR-inverted results (Huang et al., 2022). No Mw 5+ earthquake was recorded on the LLLF in instrumental record history. Two moderate-magnitude thrust earthquakes occurred on the MDF and northern LLLF in 1986 and 2016, respectively.

Coseismic displacement from InSAR

The C-band TOPS-mode Sentinel-1A images with different observation geometries were used to extract the coseismic displacement maps of the 2022 Menyuan earthquake in the line-of-sight (LOS) direction. The ascending (track 026 and 128) and descending (track 33) interferometric pairs were processed using GAMMA software (Wegmüller et al., 2016). Interferograms were produced with a registration accuracy higher than 0.001 pixel. A 30-m ALOS World 3D DEM was used to remove the topographic phase. The precise orbit data from the European Space Agency (ESA) were employed to reduce the orbital artifacts. After adaptive filtering (Goldstein and Werner., 1998), differential interferograms were unwrapped using the minimum cost flow (MCF) methods (Werner et al., 2002). The coseismic interferometric fringes in Figure 2 show a deforming area of ~120 × 80 km^2. Similar butterfly-shaped fringe patterns on the descending and ascending interferograms with opposite deformation directions (Figure 2) demonstrate a predominant left-lateral strike-slipping movement on the seismogenic fault of this earthquake. Two cross-fault profiles with 80 km length and 2 km width are extracted from the unwrapping results (Figure 3 and Figure 4). The results reveal that the LOS displacements on the ascending track 128 vary from -0.61 to 0.44 m; they vary from -0.68 to 0.45 m for the ascending track 026 and from -0.51–0.64 m for the descending track 033. The maximum displacement is measured to be ~0.68 m. The range offset maps are extracted from the ascending track 128 and descending track 33 Sentinel-1A data (Figure 5). A clear surface rupture can be identified based on them, which fits well with the field investigation of Pan et al. (2022) (Figure 5A).

The uncertainties in InSAR observations have a significant influence on the inversion accuracy of the fault slip models (Lohman and Simons, 2005; Dawson and Tregoning, 2007), especially for small-to-moderate-magnitude earthquakes, whose coseismic surface displacement is small, it is easy to be contaminated by noises in interferograms, such as atmospheric

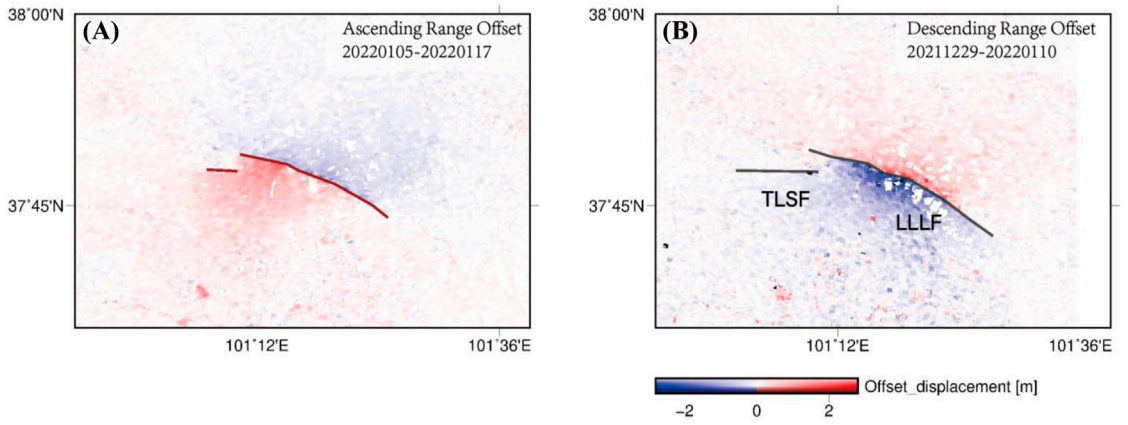

FIGURE 5
Range offsets derived from Sentinel-1A ascending track 128 **(A)** and descending track 033 **(B)** by using the offset-tracking technique. The dark-red line marked in **(A)** indicates the field-investigated surface rupture from Pan et al. (2022), and the gray line marked in **(B)** indicates the two-segment fault model used in our Slip inversion in Section 4.

noise. Simulation from Dawson and Tregoning, (2007) demonstrates coseismic deformation caused by an Mw6.2 earthquake deeper than 10 km, or an Mw 5.5 earthquake deeper than 6 km, is undetectable by the InSAR technique. Therefore, it is necessary to correct the atmospheric signals in interferograms before using them as constraints in slip inversion. Considering a relatively small deforming area generated by small-to-moderate-magnitude earthquakes, the local atmospheric effect on the interferometric phase is mainly from the stratified tropospheric delay. To mitigate the stratified tropospheric effect, a simple-stratification-correction (SSC) approach dedicated to small-to-moderate-magnitude earthquakes was implemented, whose performance has been validated using 23 real earthquakes in Gong et al. (2022). Comparing the ascending and descending results "before" and "after" correction (Figures 3, 4), we can see that the SSC performs well in reducing local stratified contribution in this event. The relative deformation between the hanging wall and footwall is reduced by ~ 2% (~2 cm) (Figure 4).

Slip inversion

To examine the coseismic slip model, the InSAR data from three tracks (26, 128, and 33) and offsets from two tracks (128 and 33) were used to invert for the slip distribution. A homogeneous elastic dislocation model was adopted to calculate the Green's function using the EDGRN program (Wang et al., 2013), and the Poisson ratio was set to 0.25. We manually cut off the near-fault InSAR data to avoid the influence of unwrapping errors due to the low coherence near the rupture. Three LOS displacement maps and two range offset data are down-sampled using the QuadTree algorithm (Jónsson et al., 2002) to reduce the data volume. Based on the surface displacement gradient on the offset results and field investigation from Pan et al. (2022), the fault surface trace is mapped, composed of a ~22.7-km-long segment on the western section of LLLF and a ~4.5-km one on the eastern section of the TLSF (Figures 3, 5A). Therefore, we assumed a south dipping two-segment fault model for the inversion (Figure 5B). We fixed the fault trace on the ground for the two segments, and then they are extended down dip and along strike. The fault planes were equally discretized into subfaults with a size of 2 km by 2 km. An efficient FORTRAN program "steepest decent method" (Wang et al., 2013) was applied to resolve the optimal slip model with the weight factors of 1.0 and 0.5 allocated to the InSAR data and offset data, respectively. A grid search method was performed to estimate the fault dips in the range of 50–90° in steps of 2°. Simultaneously, the slip distribution was determined.

To analyze the influence of atmospheric correction on coseismic slip inversion, we conducted inversions twice by using two groups of the InSAR dataset— Group A: the ascending and descending InSAR LOS displacement fields "before" atmospheric correction; Group B: ones "after" atmospheric correction. The InSAR observations, best-fitting models, residuals, and slip distribution from Group B are shown in Figures 6, 7 (see the corresponding results from Group A in Supplementary Figures S2, S3). We found that both models give a good data-model correlation (0.9617 and 0.9535), but the mean slip and moment magnitude is overestimated before atmospheric correction for this event by comparing two inversion results. The mean slips decrease by ~ 12.5% from 0.24 to 0.21 m for the eastern TLSF rupture and by ~ 18.3% from 0.82 to 0.67 m for the western LLLF rupture after correction (Table 3). Accordingly, the moment magnitude decreases from Mw6.74 to Mw6.69 after atmospheric correction, closer to the solutions from GCMT and USGS (Table 1). Both models gave a similar

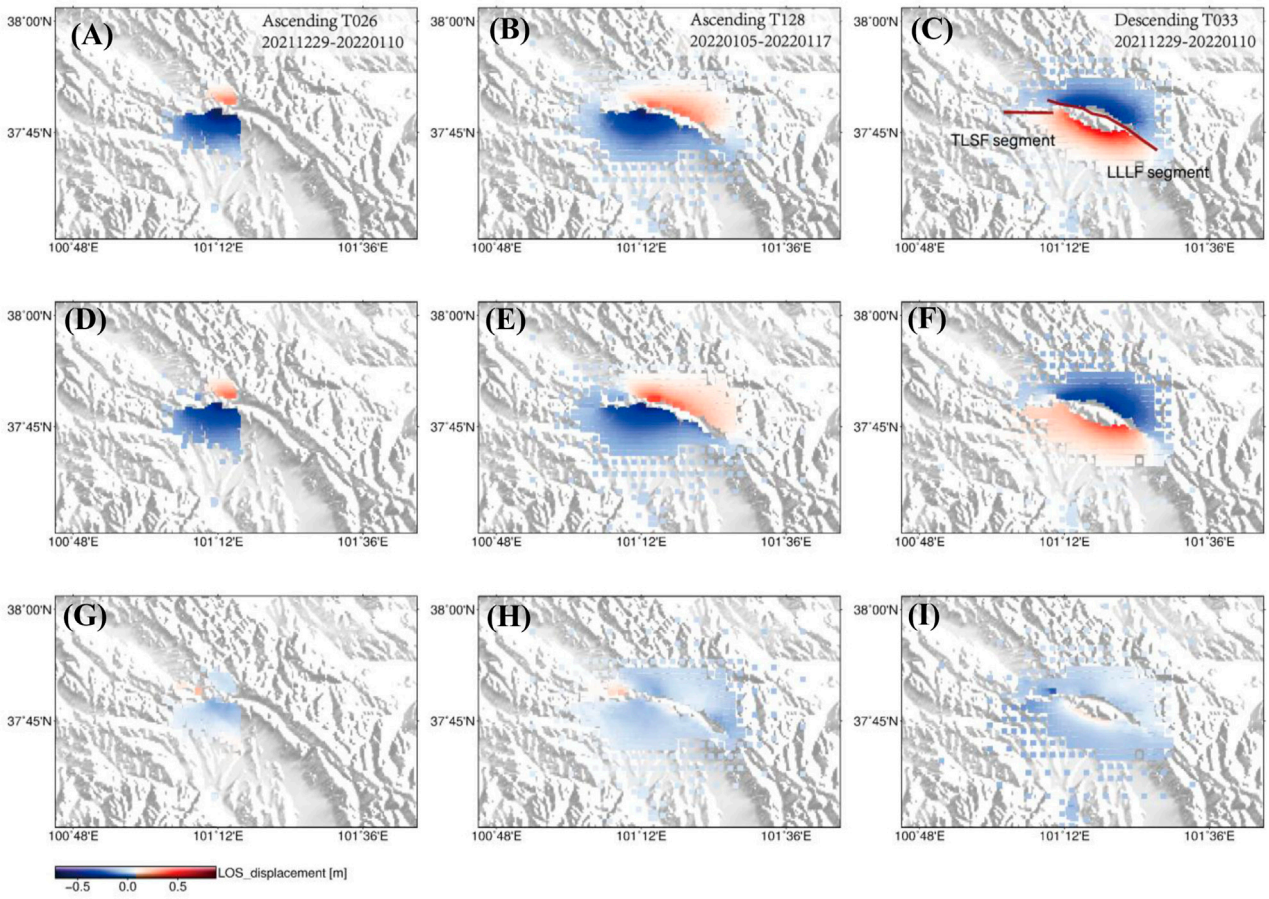

FIGURE 6
InSAR observations after atmospheric correction **(A–C)**, models **(D–F)**, and residuals **(G–I)** for the three tracks (26, 128, and 33) in inversion. The fault-traces of the TLSF and LLLF segments used for this slip inversion are indicated in red lines.

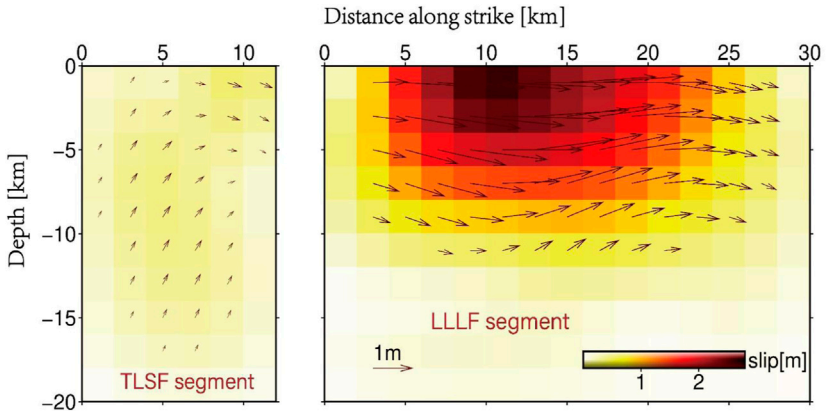

FIGURE 7
Coseismic slip distribution of the 2022 Mw6.7 Menyuan earthquake constrained by the atmospheric-corrected InSAR data.

TABLE 3 Inversion results of the 2022 Menyuan earthquake from different data set groups.

Source	Mag. (*Mw*)	Data-model correlation	Fault segment	Mean strike (°)	Mean rake (°)	Mean slip (m)
Group A	6.74	0.9617	TLSF segment	90.89	25.04	0.24
			LLLF segment	114.87	-0.78	0.82
Group B	6.69	0.9535	TLSF segment	90.89	42.16	0.21
			LLLF segment	114.87	0.41	0.67

Group A: the ascending and descending InSAR LOS displacement fields "before" atmospheric correction; Group B: ones "after" atmospheric correction.

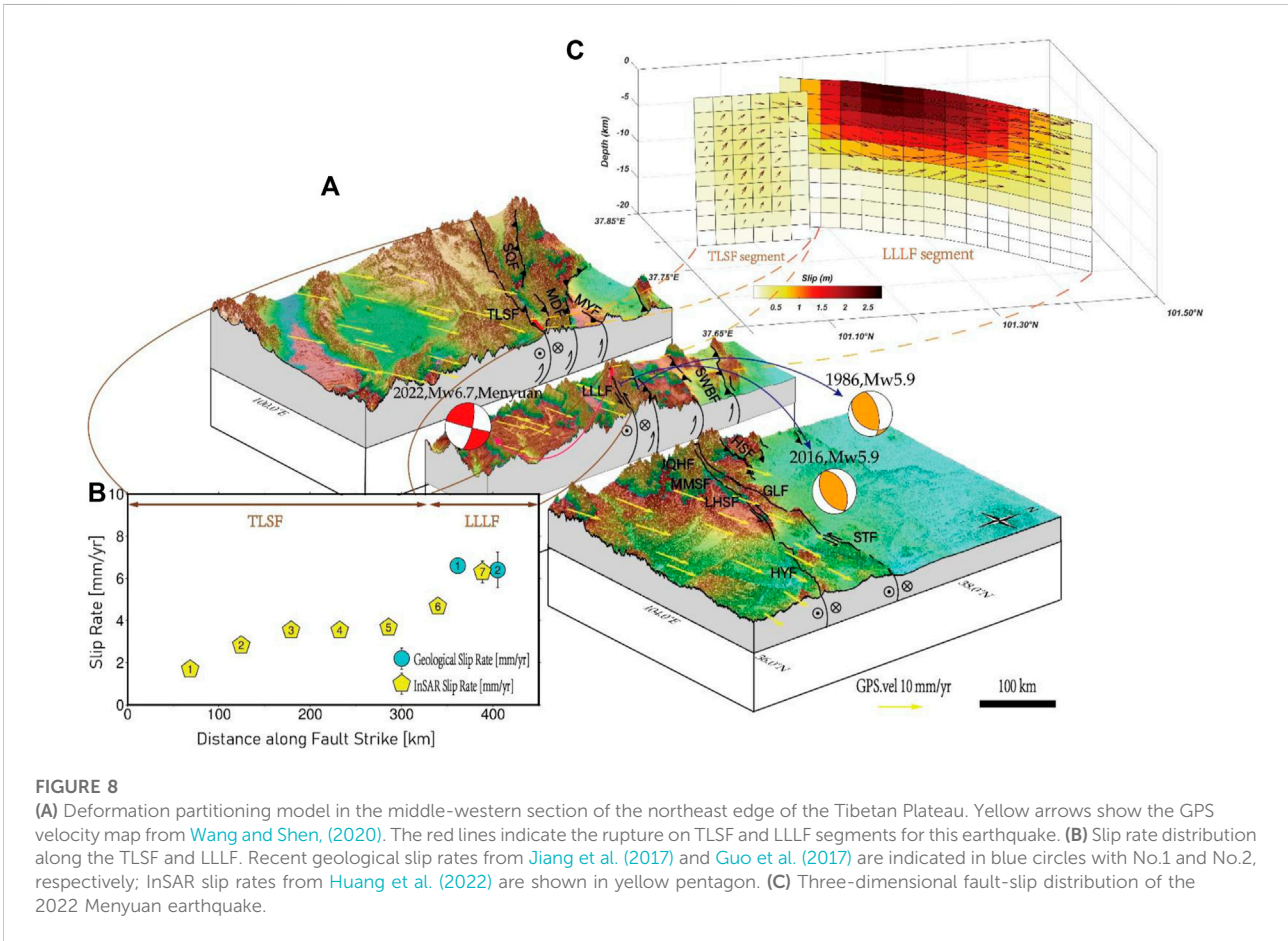

FIGURE 8
(A) Deformation partitioning model in the middle-western section of the northeast edge of the Tibetan Plateau. Yellow arrows show the GPS velocity map from Wang and Shen, (2020). The red lines indicate the rupture on TLSF and LLLF segments for this earthquake. **(B)** Slip rate distribution along the TLSF and LLLF. Recent geological slip rates from Jiang et al. (2017) and Guo et al. (2017) are indicated in blue circles with No.1 and No.2, respectively; InSAR slip rates from Huang et al. (2022) are shown in yellow pentagon. **(C)** Three-dimensional fault-slip distribution of the 2022 Menyuan earthquake.

slip distribution pattern with two asperities, located on the western LLLF rupture segment and eastern TLSF rupture segment. The main rupture concentrates on the LLLF segment with the predominant slip patches above 10 km, which takes ~80% of total releasing moment energy. The best-fitting dips for two segments are approximately vertical (88°). In agreement with the focal mechanism solutions, the slip on the LLLF rupture segment is purely left-lateral striking-slip motion with a maximum slip of 2.90 m, which is consistent with the results from Li et al. (2022) and Yu et al. (2022). On the TLSF rupture segment, another asperity with a small slip magnitude is found. In contrast to the left-lateral strike-slip movement on the LLLF segment, the motion on the TLSF segment is mainly oblique slip at depth, with an obvious thrust component.

Implications for the strain partitioning pattern in the northwestern section of the QL–HYF zone

The modeling results from Bowman et al. (2003) showed that oblique contraction or extension at depth along tectonic boundaries is expected to be accommodated on

predominantly strike-slip and dip-slip faults at the surface, which are observed in many large earthquakes on the block boundaries, such as the 2016 Mw7.0 Kumamoto earthquake in Japan: strike-slip plus normal faults (Toda et al., 2016), the 2018 Mw 7.5 Sulawesi earthquake in Indonesia: strike-slip plus normal faults (Song et al., 2019), and the 1927 M8.0 Gulang earthquake in China: strike-slip plus thrust faults (Guo et al., 2020). As block convergence boundaries in the northeast edge of the Tibetan Plateau, the QL–HYF zone is undergoing oblique compression and strain accumulation, accommodating part of the NE expansion of the Tibetan Plateau together with the GLF, XTF, HSF, and SWBF in the northwestern section of the QL–HYF (west of LLLF–JQHF–GLF triple junction), oblique convergence is partitioned into slip on the purely strike-slipping LLLF and thrusting faults in the north, which is verified by recent findings about the surface rupture of the 1927 Gulang large earthquake: a ~120-km-long strike-slip rupture along the LLLF and a ~42-km-long thrust rupture along the SWBF and eastern HSF (Guo et al., 2020). There are some questions related to such slip partitioning system that remain unknown: 1) where the oblique compression starts to be completely partitioned into left-lateral strike-slip motion and thrust faulting at the ground surface in the northwestern area of the QL–HYF zone and 2) why the same style of deformation partitioning does not maintain along the middle-east section of the QL–HYF (east of LLLF–JQHF–GLF triple junction).

The optimal slip model achieved in Section 4 shows that this earthquake has ruptured two fault segments: the western LLLF segment with pure strike-slip motion and a small part of the eastern TLSF section with an obvious oblique slip (Figure 8C). Two moderate-magnitude thrust earthquakes, the 1986 and 2016 Mw5.9 Menyuan earthquakes, also occurred in the north of LLLF. Combined with the slip-partitioning rupture in the 1927 Gulang earthquake, it is reasonable to suggest that the oblique slip at depths along the whole LLLF segment has completely partitioned into strike-slip and thrust slip at surface in the transpressional QL–HYF systems. As for the TLSF segment, the interseismic InSAR slip rate map shows an obvious step between the eastern TLSF segment (3.5 mm/yr) and LLLF segment (6.4 mm/yr) (Figure 8B). The discrepancy in the left-lateral strike-slip rate between different segments along the QL–HYF is caused by how the strain is partitioned on the QL–HYF and other faults in the north. Given that the oblique slip occurred on the fault plane on the eastern TLSF segment in this earthquake, the strike-slip rate discrepancy between the eastern TLSF segment and LLLF segment is taken up by dip-slip on the TLSF segment together with the shortening of the Qilianshan in the north. Therefore, we suggest that the TLSF–LLLF junction is a demarcation point where the strain partitioning pattern has changed (Figure 8A). Such transformation is likely to be controlled by the change of fault geometry relative to the direction of regional block movement. Geological investigation shows the TLSF steps left in a ~3-km en echelon pattern at the western end of LLLF (Guo et al., 2020; Pan et al., 2022). Likewise, in the middle-east section of the QL–HYF zone, the deformation partitioning pattern is determined by the geometric relationship between the fault strike and the region extending direction of the Tibetan Plateau. From the GPS velocity map and fault traces (Figure 1, Figure 8A), the angle between the strike of the JQHF–MMSF–LHSF segment and the direction of block movement is much smaller in comparison to the LLLF segment, especially for the GLF and western section of XTF in the north, the fault strike is almost consistent with the direction of block movement (Figure 1), so the expansion of the Tibetan Plateau is mainly absorbed on these two faults in the form of strike-slip.

Conclusion

This study carried out interferometric processing with a stratified tropospheric correction dedicated to small-to-moderate-magnitude earthquakes for the ascending and descending interferometric pairs from Sentinel-1A satellite to obtain the coseismic deformation maps for the 2022 Menyuan earthquake. The InSAR-inverted results show that the interferometric deformation maps without atmospheric correction will overestimate the mean slip and moment magnitude for this event. The optimal slip model demonstrates that two segments have been ruptured: a >20-km-long section on the western LLLF with purely left-lateral striking-slip motion and a small part of eastern TLSF with an obvious oblique slip, which implies a change in the deformation partitioning pattern at the surface. Recent slip rate studies and the rupture characteristics of historical events also support the same. The change in the strain partitioning pattern along the northeastern edge of the Tibetan Plateau is likely to be controlled by the change of fault geometry relative to the direction of regional block movement (or the regional principal compressive stress direction). Our study is important for improving understanding of the tectonic transformation style in the NE Tibetan Plateau.

Data availability statement

The original contributions presented in the study are included in the article/Supplementary Material; further inquiries can be directed to the corresponding author.

Author contributions

YYT: InSAR data processing, modeling, drawing figures, and data collection. SXG: writing, idea, and data analysis. GWY: atmospheric correction. QCY: suggestion and communication.

Funding

This study is co-supported by the National Nonprofit Fundamental Research Grant of China, Institute of Geology, China Earthquake Administration (Grant Number IGCEA2206), the National Key Research and Development Program of China (Grant Number 2019YFC1509205), and the National Science Foundation of China (Grant Number 41631073).

Conflict of interest

The authors declare that the research was conducted in the absence of any commercial or financial relationships that could be construed as a potential conflict of interest.

Publisher's note

Supplementary material

The Supplementary Material for this article can be found online at: https://www.frontiersin.org/articles/10.3389/feart.2022.1000349/full#supplementary-material

References

Bowman, D., King, G., and Tapponnier, P. (2003). Slip partitioning by elastoplastic propagation of oblique slip at depth. *Science* 300 (5622), 1121–1123. doi:10.1126/science.1082180

Daout, S., Jolivet, R., Lasserre, C., Doin, M. P., Barbot, S., Tapponnier, P., et al. (2016). Along-strike variations of the partitioning of convergence across the Haiyuan fault system detected by InSAR. *Geophys. J. Int.* 205 (1), 536–547. doi:10.1093/gji/ggw028

Dawson, J., and Tregoning, P. (2007). Uncertainty analysis of earthquake source parameters determined from InSAR: A simulation study. *J. Geophys. Res.* 112, B09406. doi:10.1029/2007jb005209

Deng, Q., Ran, Y., Yang, X., Min, W., and Chu, Q. (2007). *Active tectonic map of China (in Chinese)*. Beijing: Seismological Press.

Duvall, A. R., and Clark, M. K. (2010). Dissipation of fast strike-slip faulting within and beyond northeastern Tibet. *Geology* 38 (3), 223–226. doi:10.1130/g30711.1

England, P., and Houseman, G. (1985). Role of lithospheric strength heterogeneities in the tectonics of Tibet and neighbouring regions. *Nature* 315 (6017), 297–301. doi:10.1038/315297a0

England, P., and Molnar, P. (1997). Active deformation of Asia: From kinematics to dynamics. *Science* 278 (5338), 647–650. doi:10.1126/science.278.5338.647

Fan, L. P., Li, B. R., Liao, S. R., Jiang, C., and Fang, L. H. (2022). High-precision relocation of the aftershock sequence of the January 8, 2022, Ms6.9 Menyuan earthquake. *Earthq. Sci.* 35 (2), 138–145. doi:10.1016/j.eqs.2022.01.021

Flesch, L. M., Haines, A. J., and Holt, W. E. (2001). Dynamics of the India-Eurasia collision zone. *J. Geophys. Res.* 106 (B8), 16435–16460. Retrieved from 10.1029/2001JB000208. doi:10.1029/2001jb000208

Gan, W., Zhang, P., Shen, Z. K., Niu, Z., Wang, M., Wan, Y., et al. (2007). Present-day crustal motion within the Tibetan Plateau inferred from GPS measurements. *J. Geophys. Res.* 112 (B8), B08416. doi:10.1029/2005jb004120

Gao, F., Olaf, Zielke., Han, Z. J., Guo, P., Gai, H. L., and Dai, C. L. (2021). Faulted landforms, slip-rate, and tectonic implications of the eastern Lenglongling fault, northeastern Tibetan Plateau. *Tectonophysics* 823 (2022), 229195. doi:10.1016/j.tecto.2021.229195

Gaudemer, Y., Tapponnier, P., Meyer, B., Peltzer, G., Guo, S., Chen, Z., et al. (1995). Partitioning of crustal slip between linked, active faults in the eastern Qilian Shan, and evidence for a major seismic gap, the 'Tianzhu gap', on the Western Haiyuan fault, Gansu (China). *Geophys. J. Int.* 120 (3), 599–645. doi:10.1111/j.1365-246x.1995.tb01842.x

Goldstein, R. M., and Werner, C. L. (1998). Radar interferogram filtering for geophysical applications. *Geophys. Res. Lett.* 25, 4035–4038. doi:10.1029/1998gl900033

Gong, W. Y., Zhao, D. Z., Zhu, C. H., Zhang, Y. F., Li, C. L., Zhang, G. F., et al. (2022). A new method for InSAR stratified tropospheric delay correction facilitating refinement of coseismic displacement fields of small-to-moderate earthquakes. *Remote Sens. (Basel).* 14, 1425. doi:10.3390/rs14061425

Guo, P., Han, Z. J., Dong, S. P., Yuan, R. M., and Xie, Z. D. (2019). Surface rupture and slip distribution along the Lenglongling fault in the NE Tibetan Plateau: Implications for faulting behavior. *J. Asian Earth Sci.* 172, 190–207. doi:10.1016/j.jseaes.2018.09.008

Guo, P., Han, Z. J., Gao, F., Zhu, C. H., and Gai, H. L. (2020). A new tectonic model for the 1927 M8.0 Gulang earthquake on the NE Tibetan plateau. *Tectonics* 39. doi:10.1029/2020TC006064

Guo, P., Han, Z. J., Jiang, W. L., and Mao, Z. B. (2017). Holocene left-lateral slip-rate of the Lenglongling fault, northeastern margin of the Tibetan Plateau (in Chinese). *Seismol. Geol.* 39 (2), 323–341. doi:10.3969/j.issn.0253-4967.2017.02.005

He, W. G., Liu, B. C., Yuan, D. Y., and Yang, M. (2001). Preliminary research on the paleoearthquake along the Lenglongling active fault zone (in Chinese). *Res. Act. Fault Ser.* 8, 64–74.

Huang, Z. C., Zhou, Y., Qiao, X., Zhang, P. Z., and Cheng, X. (2022). Kinematics of the ~1000 km Haiyuan fault system in northeastern tibet from high-resolution sentinel-1 InSAR velocities: Fault architecture, slip rates, and partitioning. *Earth Planet. Sci. Lett.* 583 (2022), 117450. doi:10.1016/j.epsl.2022.117450

Institute of Geology and Lanzhou Institute of Seismology (1993). *The qilianshan–hexi corridor active fault system*. Beijing: Seismogical Press.

Jiang, W. L., Han, Z. J., Guo, P., Zhang, J. F., Jiao, Q. S., Kang, S., et al. (2017). Slip-rate and recurrence intervals of the east Lenglongling fault constrained by morphotectonics: Tectonic implications for the northeastern Tibetan Plateau. *Lithosphere* 9 (3), 417–430. doi:10.1130/l597.1

Jónsson, S., Zebker, H., Segall, P., and Amelung, F. (2002). Fault slip distribution of the 1999 Mw 7.1 hector mine, California, earthquake, estimated from satellite radar and GPS measurements. *Bull. Seismol. Soc. Am.* 92 (4), 1377–1389. doi:10.1785/0120000922

Lasserre, C., Gaudemer, Y., Tapponnier, P., Mériaux, A. S., Van Der Woerd, J., Yuan, D. Y., et al. (2002). Fast late pleistocene slip rate on the LengLong ling segment of the Haiyuan fault, Qinghai, China. *J. Geophys. Res.* 107 (B11), ETG 4-1–ETG 4-15. ETG 4-1-ETG 4-15. doi:10.1029/2000jb000060

Lasserre, C., Morel, P. H., Gaudemer, Y., Tapponnier, P., Ryerson, F., King, G., et al. (1999). Postglacial left slip rate and past occurrence of M≥8 earthquakes on the Western Haiyuan fault, Gansu, China. *J. Geophys. Res.* 104 (B8), 17633–17651. doi:10.1029/1998jb900082

Li, C. Y., Zhang, P. Z., Yin, J. H., and Min, W. (2009). Late Quaternary left-lateral slip-rate of the Haiyuan fault, northeastern margin of the Tibetan Plateau. *Tectonics* 28 (5). doi:10.1029/2008tc002302

Li, Z. H., Han, B. Q., Liu, Z. J., Zhang, M., Yu, C., Chen, B., et al. (2022a). Source parameters and slip distributions of the 2016 and 2022 menyuan, Qinghai earthquakes constrained by InSAR observations[J]. *Geomatics Inf. Sci. Wuhan Univ.* 47, 887. doi:10.13203/j.whugis20220037

Li, Z. J., Hao, M., Li, Y. H., and Song, S. W. (2022b). Three-dimensional crustal deformation and strain partitioning before the Ms 6.9 Qinghai Menyuan earthquake on January 8, 2022. *Chin. J. Geophysics-Chinese Ed.*. doi:10.6038/cjg2022Q0046

Liu, J. R., Ren, Z. K., Zhang, H. P., Li, C. Y., Zhang, Z. Q., Zheng, W. J., et al. (2018). Late Quaternary slip-rate of the Laohushan fault within the Haiyuan fault zone and its tectonic implications (in Chinese). *Chin. J. Geophys.* 61 (4), 1281–1297. doi:10.6038/cjg2018L0364

Lohman, R. B., and Simons, M. (2005). Some thoughts on the use of InSAR data to constrain models of surface deformation: Noise structure and data downsampling. *Geochem. Geophys. Geosyst.* 6, Q01007. doi:10.1029/2004GC000841

Loveless, J. P., and Meade, B. J. (2011). Partitioning of localized and diffuse deformation in the Tibetan Plateau from joint inversions of geologic and geodetic observations. *Earth Planet. Sci. Lett.* 303 (1–2), 11–24. doi:10.1016/j.epsl.2010.12.014

Molnar, P., and Denq, Q. (1984). Faulting associated with large earthquakes and the average rate of deformation in central and eastern Asia. *J. Geophys. Res.* 89, 6203–6227. doi:10.1029/JB089iB07p06203

Molnar, P., and Tapponnier, P. (1975). Cenozoic Tectonics of Asia: Effects of a Continental Collision: Features of recent continental tectonics in Asia can be interpreted as results of the India-Eurasia collision. *Science* 189 (4201), 419–426. doi:10.1126/science.189.4201.419

Ou, Q., Daout, S., Weiss, J. R., Shen, L., Lazeck´y, M., Wright, T. J., et al. (2022). Large-scale interseismic strain mapping of the NE Tibetan Plateau from sentinel-1 interferometry. *J. Geophys. Res. Solid Earth* 127, e2022JB024176. doi:10.1029/2022JB024176

Ou, Q., Kulikova, G., Yu, J., Elliott, A., Parsons, B., and Walker, R. (2020). Magnitude of the 1920 haiyuan earthquake reestimated using seismological and geomorphological methods. *JGR. Solid Earth* 125, 2019JB019244. doi:10.1029/2019JB019244

Pan, J. W., Li, H. B., Chevalier, M-L., Liu, D. L., Li, C., Liu, F. C., et al. (2022). Coseismic surface rupture and seismogenic structure of the 2022 Ms 6.9 Menyuan earthquake, Qinghai Province, China (in Chinese). *Acta Geol. Sin.* 96 (1), 215–231. doi:10.3389/feart.2022.94866

Pichon, X. L., Fournier, M., and Jolivet, L. (1992). Kinematics, topography, shortening , and extrusion in the India-Eurasia collision. *Tectonics* 11 (6), 1085–1098. doi:10.1029/92tc01566

Shao, Y., Liu-Zeng, J., Van der Woerd, J., Klinger, Y., Oskin, M. E., Zhang, J., et al. (2020). Late Pleistocene slip rate of the central Haiyuan fault constrained from optically stimulated luminescence, 14C, and cosmogenic isotope dating and high-resolution topography. *GSA Bull.* 133, 1347. doi:10.1130/b35571.1

Song, X. G., Jiang, Y., Shan, X. J., Gong, W. Y., and Qu, C. Y. (2019). A fine velocity and strain rate field of present-day crustal motion of the northeastern Tibetan plateau inverted jointly by InSAR and GPS. *Remote Sens. (Basel).* 11, 435. doi:10.3390/rs11040435

Tapponnier, P., Meyer, B., Avouac, J. P., Peltzer, G., Gaudemer, Y., Shunmin, G., et al. (1990). Active thrusting and folding in the Qilian Shan, and decoupling between upper crust and mantle in northeastern Tibet. *Earth Planet. Sci. Lett.* 97 (3-4), 382–403. doi:10.1016/0012-821x(90)90053-z

Tapponnier, P., Zhiqin, X., Roger, F., Meyer, B., Arnaud, N., Wittlinger, G., et al. (2001). Oblique stepwise rise and growth of the tibet plateau. *Science* 294 (5547), 1671–1677. doi:10.1126/science.105978

Toda, S., Kaneda, H., Okada, S., Ishimura, D., and Mildon, Z. K. (2016). Slip-partitioned surface ruptures for the Mw 7.0 16 April 2016 Kumamoto, Japan, earthquake. *Earth Planets Space* 68 (1), 188. doi:10.1186/s40623-016-0560-8

Wang, M., and Shen, Z. K. (2020). Present-day crustal deformation of continental China derived from GPS and its tectonic implications. *J. Geophys. Res. Solid Earth* 125 (2), e2019JB018774. doi:10.1029/2019jb018774

Wang, R., Diao, F., and Hoechner, A. (2013). "SDM—a geodetic inversion code incorporating with layered crust structure and curved fault geometry," in EGU General Assembly Conference, Vienna, Austria, 7–12 April 2013. paper presented at the 2013.

Wegmüller, U., Werner, C., Stroozzi, T., Wiesmann, A., Frey, O., and Santoro, M. (2016). Sentinel-1 support in the GAMMA software. *Procedia Comput. Sci.* 100, 1305–1312. doi:10.1016/j.procs.2016.09.246

Werner, C., Wegmuller, U., Strozzi, T., and Wiesmann, A. (2002). "Processing strategies for phase unwrapping for INSAR applications," in Proceedings. EUSAR, Cologne, 4-6 June, 2002.

Xu, X., Han, Z., Yang, X., Zhang, S., Yu, G., Zhou, B., et al. (2016). *Seismotectonic map in China and its adjacent regions*. Beijing: Seismogical Press.

Yao, W., Liu, Z, J., Oskin, M. E., Wang, W., Li, Z., Prush, V., et al. (2019). Re-evaluation of the Late Pleistocene slip rate of the Haiyuan fault near Songshan, Gansu province, China. *J. Geophys. Res. Solid Earth* 124, 5217–5240. doi:10.1029/2018jb016907

Yu, P. F., Chen, W., Qiao, X. J., Zhao, B., Li, G., Xiong, W., et al. (2022). Slip model of the 2022 menyuan ms 6.9 earthquake constrained by mulit-source SAR data[J]. *Geomatics Inf. Sci. Wuhan Univ.* 47 (6), 898–906. doi:10.13203/j.whugis20220093

Yuan, D., Liu, X., Zhang, P., and Liu, B. (2003). Characteristic of the modern activity of the Reshui-Riyueshan fault zone in Qinghai province. *Seismol. Geol.* 25 (1), 155–165. doi:10.3969/j.issn.0253-4967.2003.01.015

Yuan, D. Y., Ge, W. P., Chen, Z. W., Li, C. Y., Wang, Z. C., Zhang, H. P., et al. (2013). The growth of northeastern tibet and its relevance to large-scale continental geodynamics: A review of recent studies. *Tectonics* 32 (5), 1358–1370. doi:10.1002/tect.20081

Yuan, D. Y., Zhang, P. Z., Liu, B. C., Gan, W. J., Mao, F. Y., Wang, Z. C., et al. (2004). Geometrical imagery and tectonic transformation of late quaternary active tectonics in northeastern margin of qinghai-xizang plateau (in Chinese). *Acta Geol. Sin.* 78 (2), 270–278. doi:10.3321/j.issn:0001-5717.2004.02.017

Zhang, P. Z., Molnar, P., Burchfiel, B., Royden, L., Wang, Y. P., Deng, Q. D., et al. (1988). Bounds on the Holocene slip rate of the Haiyuan fault, north-central China. *Quat. Res.* 30 (2), 151–164. doi:10.1016/0033-5894(88)90020-8

Zheng, W., Zhang, P., He, W., Yuan, D., Shao, Y., Zheng, D., et al. (2013). Transformation of displacement between strike-slip and crustal shortening in the northern margin of the Tibetan Plateau: Evidence from decadal GPS measurements and late Quaternary slip rates on faults. *Tectonophysics* 584, 267–280. doi:10.1016/j.tecto.2012.01.006

Zuza, A. V., Wu, C., Reith, R. C., Yin, A., Li, J., Zhang, J., et al. (2018). Tectonic evolution of the Qilian Shan: An early Paleozoic orogen reactivated in the Cenozoic. *GSA Bull.* 130 (5-6), 881–925. doi:10.1130/B31721.1

frontiers | Frontiers in Earth Science

TYPE Original Research
PUBLISHED 12 January 2023
DOI 10.3389/feart.2022.1023106

OPEN ACCESS

EDITED BY
Xinjian Shan,
Institute of Geology, China Earthquake Administration, China

REVIEWED BY
Xiaopeng Tong,
Institute of Geophysics, China Earthquake Administration, China
Kiran Kumar Singh Thingbaijam,
GNS Science, New Zealand

*CORRESPONDENCE
Yongliang Bai,
yongliang.bai1986@gmail.com

SPECIALTY SECTION
This article was submitted to Structural Geology and Tectonics, a section of the journal Frontiers in Earth Science

RECEIVED 19 August 2022
ACCEPTED 31 October 2022
PUBLISHED 12 January 2023

CITATION
Rong Y, Bai Y, Ren M, Liang M and Wang Z (2023), Seismicity-based 3D model of ruptured seismogenic faults in the North-South Seismic Belt, China. *Front. Earth Sci.* 10:1023106. doi: 10.3389/feart.2022.1023106

Seismicity-based 3D model of ruptured seismogenic faults in the North-South Seismic Belt, China

Yilin Rong[1], Yongliang Bai[1]*, Mengjiao Ren[1], Mingjian Liang[2] and Zhenjie Wang[1]

[1]College of Oceanography and Space Informatics, China University of Petroleum, Qingdao, China, [2]Sichuan Earthquake Administration, Chengdu, China

The North–South Seismic Belt produces the most frequent strong earthquakes in the Chinese continental region, such as the MS 8.0 Wenchuan earthquake on 12 May 2008 and Ms 7.0 Lushan earthquake on 20 April 2013. This seismicity results in significant hazards. Fault geometry modeling is crucial for analyzing earthquake preparation and trigger mechanisms, simulating and predicting strong earthquakes, inverting fault slip rates, *etc.* In this study, a novel method for obtaining geometric models of ruptured seismogenic faults over a large area is designed based on datasets from surface fault traces, fault orientations, focal mechanism solutions, and earthquake relocations. This method involves three steps. 1) An initial model of the fault geometry is constructed from the focal mechanism solution data. This initial model is used to select the earthquake relocation data related to the target fault. 2) Next, a fine model of the fault geometry with a higher resolution than that of the initial model is fitted based on the selected earthquake relocation data. 3) The minimum curvature interpolation method (Briggs, 2012) is adopted to build a 3D model of the subsurface fault geometry according to the three-dimensional coordinates of nodes on all profiles of each fault/segment. Based on this method and data collected in the North–South Seismic Belt, the fine morphologies of different faults along 1,573 transverse profiles were fitted, and a 3D model of 263 ruptured seismogenic faults or fault segments in the North–South Seismic Belt was built using the minimum curvature spatial interpolation method. Since the earthquake number decreases with increasing depth, the model uncertainty increases with increasing depth. Different ruptured faults have different degrees of seismicity, so different fault models may have different uncertainties. The overall fitting error of the model is 0.98 km with respect to the interpreted results, from six geophysical exploration profiles.

KEYWORDS

North-South Seismic Belt, focal mechanism solution, earthquake relocation, ruptured seismogenic fault, 3D model

1 Introduction

As the region with the most frequent strong earthquakes in the Chinese mainland, the North–South Seismic Belt (NSSB) extends more than 800 and 2,000 km in the east-west and north-south directions, respectively (Figure 1) (Wang et al., 2015). The NSSB has generated numerous strong earthquakes that have caused significant hazards, such as the MS 8.0 Wenchuan earthquake on 12 May 2008, Ms 7.0 Lushan earthquake on 20 April 2013, MS 6.4 Yangbi earthquake on 21 May 2021, and Ms 6.8 Luding earthquake on 5 September 2022 (Dai et al., 2011; Zhou et al., 2015; Yang et al., 2022). This seismic belt extends from the western margin of the Ordos Block in the north, crosses the Qinling Orogenic Belt and Longmenshan Fault Belt, and reaches Myanmar along the Anninghe Fault (ANH. F.) (Figure 1). The relatively stable South China Block and Ordos Block in the eastern Chinese mainland are separated from the Qinghai-Tibetan Plateau in the west by the NSSB (Zhang, 2013). The NSSB is the region of interactions among the Sichuan–Yunnan Block, Bayankala Block, Qinling Orogenic Belt, East Kunlun Orogenic Belt, Qaidam-Longxi Block, Qilian Orogenic Belt, Ordos Block, and Alxa Block (Figure 1) (Zhang et al., 2015).

Seismological studies in the NSSB are of great significance, and three-dimensional models of ruptured seismogenic faults are the basis for several seismological studies. For example, fault geometric models can be used for the inversion of fault slip rates (Li et al., 2010; Wang et al., 2016; Liu et al., 2022), the analysis of seismogenic mechanisms (King, 1986; Barka and Kadinsky-Cade, 1988; Shi et al., 2019) and seismic triggering mechanisms (Lay et al., 2010; Mildon et al., 2019; Ross et al., 2019), the prediction and simulation of strong earthquakes (Silva and Vitor., 2016; Walker et al., 2019; Xin and Zhang, 2021), *etc.* At present, the geometries of ruptured seismogenic faults are imaged mainly by field geological surveys, active-source geophysical surveys, seismic tomography based on passive earthquake data, and earthquake parameter estimation.

However, subsurface fault shapes cannot be identified by surface geological surveys (Valoroso et al., 2014). Active-source geophysical surveys always have with low data coverage due to their high cost (Hubbard and Shaw, 2009; Dong et al., 2010; Li Y. et al., 2019). For seismic tomography, the resolution of data depends on the distribution of seismic rays (Dorbath et al., 1996; Dilla et al., 2018). Unevenly distributed hypocenters and limited seismic stations result in low-resolution seismic tomography (Liu et al., 2021; Zhao et al., 2021).

There are two independent methods for modeling ruptured seismogenic faults based on earthquake parameters. One method is based on hypocenters, and the other method is based on focal mechanism solutions. In the first method, the fault geometry is fitted by the distribution of hypocenters along a fault based on the relationship between the rupture area of the ruptured seismogenic fault and the magnitude of the earthquakes, as well as the attenuation of seismic wave energy (Wells and Coppersmith, 1994; Lin et al., 2007; Schaff and D., 2009). In subduction zones, the majority of earthquakes are located along the Benioff zone, so the plate boundary can be modeled based on hypocenter fitting. The slab surfaces at the main subduction zones on Earth have been obtained *via* this method (Hayes and Wald, 2009; Zhang et al., 2013). However, an initial or coarse model of fault geometry is necessary to select the earthquakes induced by the target fault when modeling the geometry of small-scale ruptured seismogenic faults because some earthquakes near the target fault may be triggered by the other faults (Schaff et al., 2002; Hayes and Wald, 2009). The 3D geometry of the Gualdo Tadino Fault in Italy was fitted based on aftershock relocations, which were selected based on the constraints of seismic reflection profiles (Ciaccio et al., 2005). A three-dimensional model of the Longmenshan Fault in China was built based on the surface ruptures and aftershock relocations due to the Wenchuan earthquake in 2008, and the hypocenters used in the fitting process were also selected under the constraints of a deep seismic-reflection profile and logging data (Li et al., 2010).

In the focal mechanism solution-based method, the fault geometry can be modeled by the dip variations estimated from focal mechanism solutions at different depths, according to the relationship between seismic wave propagation and the rupture process of ruptured seismogenic faults (Aki, 1966; Nolet, 1980; Sliver et al., 1982; Kuang et al., 2021). The variations in the dip of the rupture planes of a fault were mapped according to 24 focal mechanism solutions in the western Corinth Rift in Greece (Maxime et al., 2014). Frepoli et al. (2017) also inferred the dip angle of Apennine faults in central Italy based on focal mechanism solutions. Duan et al. (2018a) estimated the dip variations along the Dujiangyan Fault in the NSSB of China based on focal mechanism solutions. However, the number of focal mechanism solutions is always much lower than the amount of earthquake relocation data due to the limited number of seismic stations. Therefore, compared with a fault model based on earthquake relocations, a model based on focal mechanism solutions often has a lower resolution, which cannot reflect the detailed fault geometry (Ciaccio et al., 2005; Frepoli et al., 2017).

By integrating surface traces, focal mechanisms, earthquake relocations, logging data, and seismic reflection profiles, a three-dimensional fault model was developed for southern California in the United States (Plesch et al., 2007). Similarly, a three-dimensional fault model was built for the main ruptured seismogenic faults in the Sichuan–Yunnan region under the comprehensive constraints of fault traces, focal mechanism solutions, precise locations of small earthquakes, a crustal velocity model, seismic reflection profiles, and magnetotelluric data; this work was accomplished by the China Seismic Experimental Site project (http://www.cses.ac.cn/). However, this model does not cover the whole NSSB, and some major faults in this seismic belt, such as the Haiyuan Fault, Xiangshan-

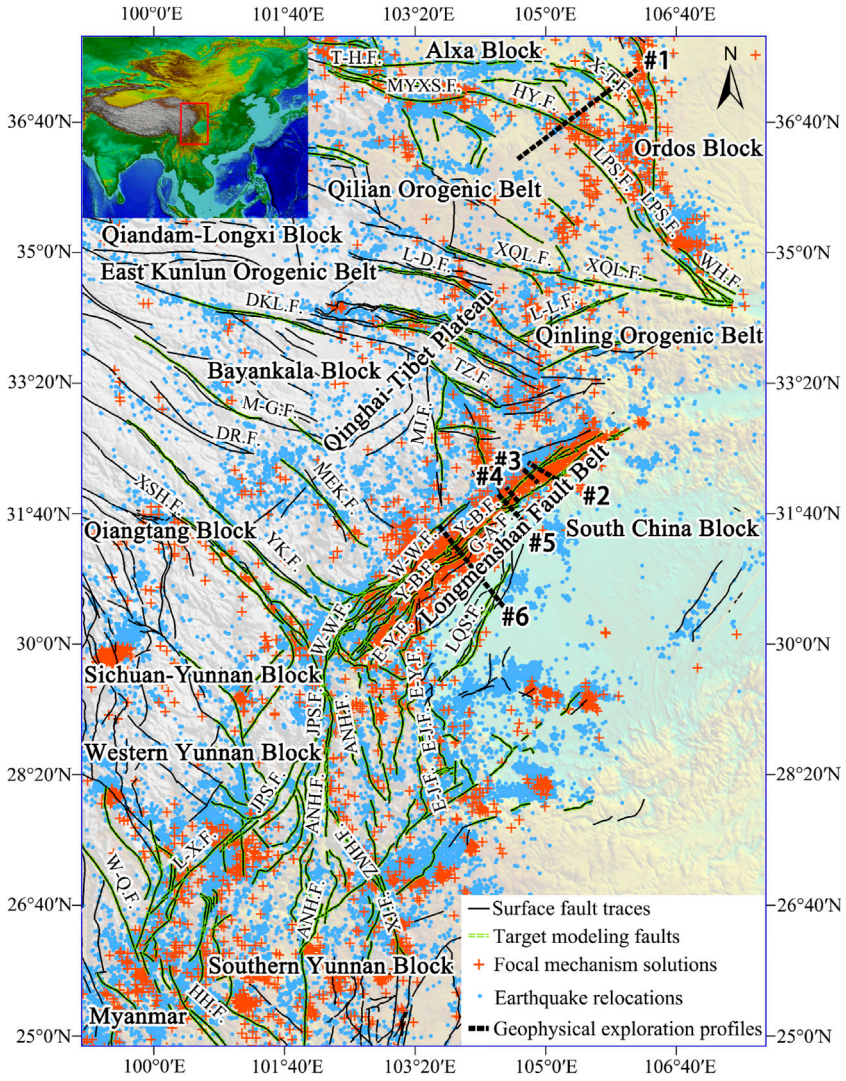

FIGURE 1
Tectonic setting and basic data distribution for fault modeling in the North–South Seismic Belt, China. ETOPO1 (Amante, 2009) is used as the topographic base map. The black solid lines represent the surface fault traces, (Xu et al., 2016), which contain 263 faults (segments): Y-B. F., Yingxiu-Beichuan Fault; G-A. F., Guanxian-Anxian Fault; W-W. F., Wenchuan-Wenmao Fault; XSH. F., Xianshuihe Fault; ZMH. F., Zemuhe Fault; ANH. F., Anninghe Fault; HH. F., Honghe Fault; DKL. F., Dongkunlun Fault; YK. F., Yuke Fault; JPS. F., Jinpingshan Fault; L-X. F., Lijiang-Xiaojinhe Fault; E-J. F., Ebian-Jinyang Fault; XJ. F., Xiaojiang Fault; DR. F., Dari Fault; HY. F., Haiyuan Fault; L-D. F., Lintan-Dangchang Fault; L-L. F., Lixian-Luojiabao Fault; LQS. F., Longquanshan Fault; MEK. F., Malkan Fault; MJ. F., Minjiang Fault; TZ. F., Tazang Fault; XQL. F., Xiqinling Fault. The green dashed lines represent the faults whose subsurface geometries are modeled in this study. The red crosses represent the positions of focal mechanism solutions (Zheng, 2019; Guo et al., 2022). The blue dots represent the relocated epicenters of earthquakes from the Sichuan Earthquake Administration. The black dotted lines represent geophysical exploration profiles: #1, an electrical structure profile across the Haiyuan Fault (Min, 2014); #2, a seismic profile across the Yingxiu-Beichuan Fault and Guanxian-Anxian Fault (Dong et al., 2010); #3, a seismic profile across the Yingxiu-Beichuan Fault (Wu et al., 2014); #4, a seismic profile across the Yingxiu-Beichuan Fault (Wu et al., 2014); #5, a seismic profile across the Yingxiu-Beichuan Fault and Guanxian-Anxian Fault (Dong et al., 2010); #6, a seismic profile across the Longquanshan Fault (Dong et al., 2010).

Tianjingshan Fault, and Weihe Fault (Lu et al., 2019), are not included. At present, a 3D fault geometric model that covers the whole NSSB is still lacking.

The coverage of active-source geophysical profiles in the NSSB, such as electrical, magnetic and seismic profiles, are very limited. Therefore, these geophysical interpretations cannot be taken as constraints for relocation data selection. In this study, the initial model of fault geometry is modeled based mainly on the focal mechanism solutions and partly on the available geological and geophysical data. The detailed shapes of the ruptured seismogenic faults are modeled by fitting the selected hypocenters according to the initial model. Finally,

TABLE 1 Information on the six collected geophysical profiles in the NSSB.

Crossing fault name	Profile type	Source	Index in Figure 1
Haiyuan Fault	Electrical Resistivity	Min (2014)	#1
Yingxiu-Beichuan Fault and Guanxian-Anxian Fault	Seismic Wave Velocity	Dong et al. (2010)	#2
Yingxiu-Beichuan Fault	Seismic Wave Velocity	Wu et al. (2014)	#3
Yingxiu-Beichuan Fault	Seismic Wave Velocity	Wu et al. (2014)	#4
Yingxiu-Beichuan Fault and Guanxian-Anxian Fault	Seismic Wave Velocity	Dong et al. (2010)	#5
Longquanshan Fault	Seismic Wave Velocity	Dong et al. (2010)	#6

we evaluate the uncertainty of the fault model based on the six geophysical exploration profiles.

2 Data and methods

2.1 Input data

The necessary input data for 3D modeling of the main ruptured seismogenic faults in the NSSB include fault traces on the Earth's surface, fault orientations, focal mechanism solutions, and relocated hypocenters. The fault orientations and focal mechanism solutions are used to construct the initial fault geometry model and choose relocated hypocenters related to the target fault. The selected relocated hypocenters are used to fit the fault geometry. In addition, geophysical interpretation profiles are also necessary to test the model uncertainty.

1) The surface trace of each fault (Figure 1) is extracted from the Seismotectonic Map of China and Adjacent Regions compiled by Xu et al. (2016), which is provided by the Data Exchange and Sharing Management Center of Active Fault Exploration in the Institute of Geology, China Earthquake Administration.
2) The fault orientations are derived from seismic, electrical and magnetic exploration. These data are compiled and provided by the Sichuan Earthquake Administration, China.
3) The focal mechanism solutions are from the National Earthquake Data Sharing Project by the China Earthquake Administration (Zheng, 2019) and the Focal Mechanism Data Set of the Chinese Mainland and Its Adjacent Areas (2009–2021), which was compiled by the Institute of Geophysics, China Earthquake Administration (Guo et al., 2022). There are 7,427 focal mechanism solutions within the NSSB in this study (Figure 1).
4) The earthquakes relocations are from the catalog of the China Seismic Experimental Site (http://www.cses.ac.cn/), including the relocated hypocenters of 127,009 earthquakes with magnitudes larger than ML 1.5 in the NSSB from January 2009 to March 2019 (Figure 1). These relocations are derived by the Sichuan Earthquake Administration using absolute and relative earthquake location methods based on the seismic phase observed by the seismic networks in the NSSB. The uncertainties of these relocated hypocenters are given as follows: the root mean square (RMS) of the travel times for 80% of the earthquakes is within 0.3 s, the horizontal error for 80% of the samples is limited to 2 km, and the vertical error for 80% of the samples is within 4 km, which are the statistics based on absolute earthquake locations.
5) Fault interpretation results along six geophysical profiles across different faults (Figure 1) are collected. The details of these profiles are listed in Table 1.

2.2 Modeling method

The geometric and kinematic parameters of ruptured seismogenic faults can be indicated well by focal mechanism solutions (Ciaccio et al., 2005; Frepoli et al., 2017), and earthquakes are mainly concentrated on ruptured seismogenic faults (Schaff et al., 2002; Hayes and Wald, 2009). Therefore, the geometry of a ruptured seismogenic fault can be modeled based on focal mechanism solutions and earthquake relocations. Our modeling method includes three main steps (Figure 2). 1) First, an initial fault model with a coarse resolution is constructed along the fault strike based on the focal mechanism solution, surface fault trace the collected fault orientation. 2) The relocated hypocenters of earthquakes due to the specific ruptured seismogenic fault are selected under the constraint of the initial fault model. The fault geometries along different cross-sections (the solid black line in Figure 3C) that are perpendicular to the fault strike are fitted based on the relocation data. 3) A three-dimensional model of the fault geometry is built by compiling all the fault shapes along different fault-crossing profiles.

2.2.1 Initial model of fault geometry along strike

To construct the fault model, the width of the fault along each fault strike-orthogonal profile needs to be delineated to extract the focal mechanism solutions and the relocated hypocenters, which are the basis for fault geometry modeling. The width of the

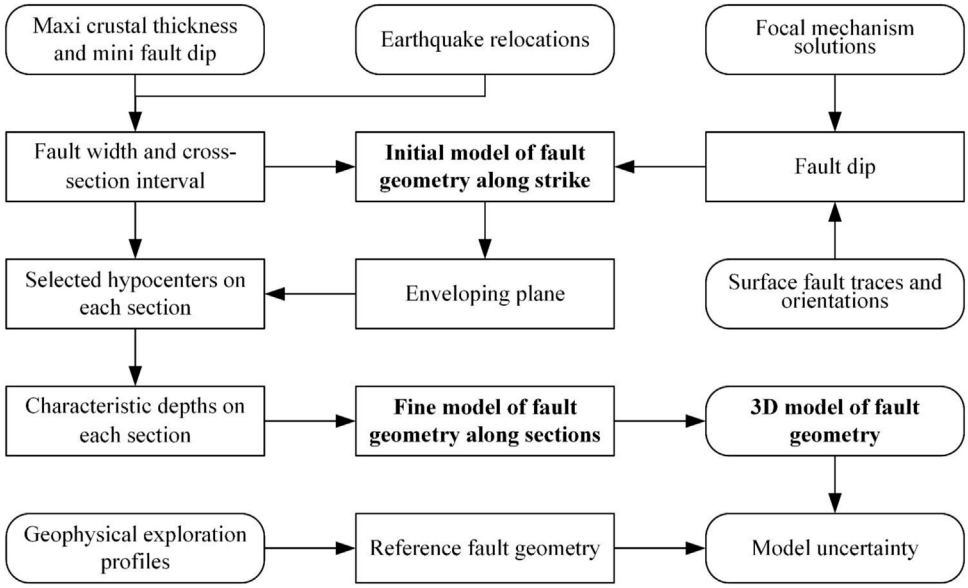

FIGURE 2
The workflow of 3D fault geometry modeling. The main stages are as follows: 1) the potential maximum fault width is derived from the maximum crustal thickness and minimum fault dip in the research region. The more precise fault width can be judged according to the distributions of the relocated hypocenters within the maximum fault width. The fault dip variations are gridded within the judged fault width based on the dips reflected by the nodal planes of focal mechanism solutions which are selected according to the surface fault traces and orientations. The low-resolution initial model of fault geometry along fault strike is constructed according to the fault dip variations. 2) The cross-section interval along each fault strike is evaluated by setting relocated hypocenter number is not less than 200 on each section within fault width. The hypocenters within the enveloping plane, which is with the highest hypocenter density, is used to calculate the characteristic depths on each section. The high-resolution fine fault geometry along each cross-section is modeled by fitting the characteristic depths. 3) The 3D fault geometry is modeled based on the fine geometries along different sections, and the uncertainty of the 3D model is estimated by taking the fault geometries from geophysical interpretation results as references.

fault is estimated through the following two steps. 1) According to the maximum crustal thickness (70 km) of the NSSB (Chen et al., 2015; Wang et al., 2017) and the minimum dip (30°) of the modeled faults, the maximum width of the fault is set to 120 km based on the trigonometric function. In this way, all the potential seismicity data related to the target fault should be within this maximum fault model width. 2) Then, a bounding region that covers the target fault can be judged according to the intensity of the relocated hypocenter distribution because the seismicity decreases with distance from the target ruptured seismogenic fault. The approximate shape of the target fault can be inferred by combining the fault orientations and the dip angle reflected by the majority of the focal mechanism solutions. The abscissa spanning between the surface outcrop point and the other intersection point between the bounding region and the fault model is regarded as the width of the target fault, which can be modeled according to seismicity data. While ensuring that the width is not underestimated, this process also eliminates the need to introduce the seismicity data of adjacent faults because of setting an overly large width.

The focal mechanism solutions are extracted within this width. Based on the fault strike according to the surface traces, the proper nodal plane can be chosen from the focal mechanism solution. The focal mechanism solutions, which clearly differ from the main trend and are probably caused by the other adjacent ruptured seismogenic faults, are removed from the dataset. The percentages of the removed focal mechanism solutions at different profiles vary, ranging between 10% and 20%. The gridded fault dip variations along the fault plane are interpolated according to the dips based on the extracted focal mechanism solutions *via* the kriging interpolation method. The grid size (c) is estimated by the following equation (Hengl, 2006):

$$c = 0.25\sqrt{\frac{A}{N}}, \tag{1}$$

where A is the area of the fault plane and N is the number of focal mechanism solutions. Finally, the initial model of the fault geometry can be derived based on the fault dip variations along the fault plane.

2.2.2 Fine model of fault geometry along cross-sections

Relative to the initial model in the former step, the fine model of the fault geometry is based on fitting the relocated hypocenters

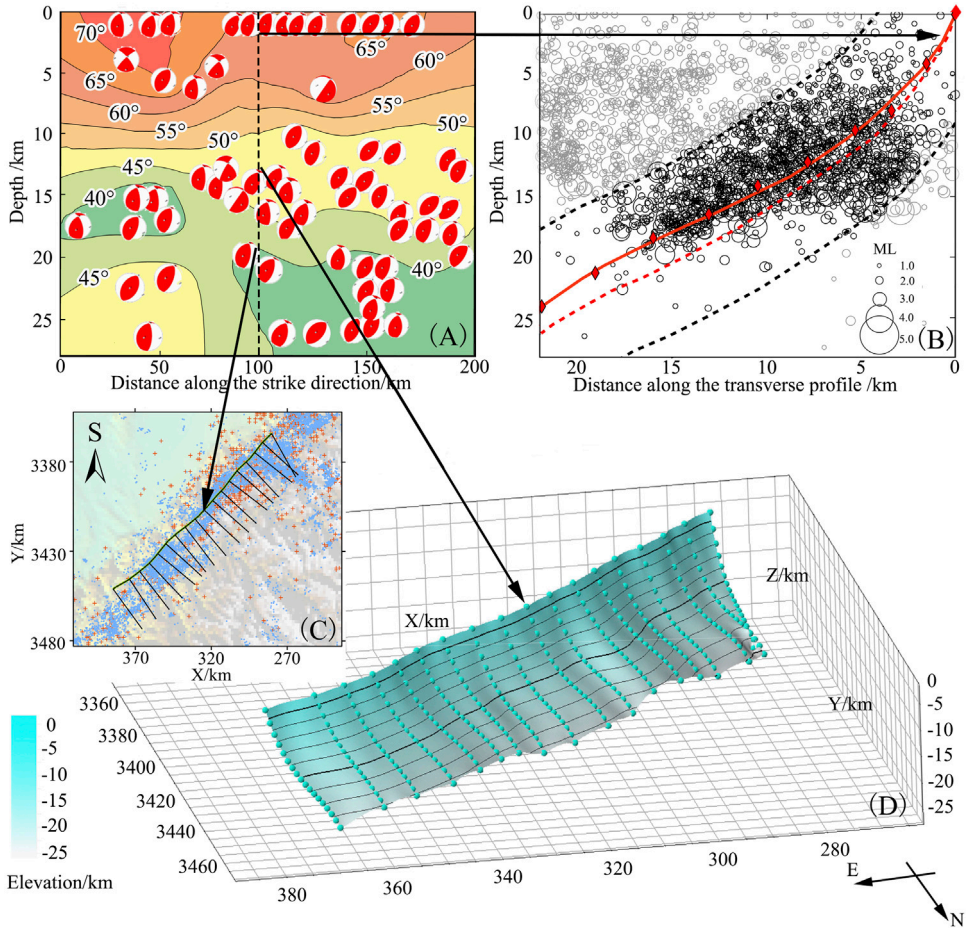

FIGURE 3
Three-dimensional modeling process for subsurface geometry taking the middle segment of the Yingxiu-Beichuan Fault as an example. **(A)** Fault dip variations according to the focal mechanism solutions; **(B–C)** Fine model of fault geometry along profile by fitting the selected and relocated hypocenters; **(D)** 3D model of the fault plane.

along different fault-strike-orthogonal profiles. These profiles have the same interval along the fault strike. A small cross-section interval means a high model resolution along strike, but it also means few earthquake relocations and a low vertical resolution for the fault geometry along each profile. Therefore, to obtain a fault model with enough details in both the horizontal and vertical directions based on the finite number of relocated hypocenters, we should balance the number of cross-sections and that of earthquake relocations on each profile. The profile length is determined by the horizontal width of the initial model of fault geometry. According to our multiple tests, one suitable choice is that the minimum number of earthquake relocations along each profile is 200. Based on this condition, the profile interval along strike and the profile number can be obtained when the minimum number of earthquake relocations along each profile is slightly larger than 200. When there are not more than 200 relocated hypocenters related to one fault, the fault geometry is fitted along only one profile at the fault center and orthogonal to the strike. Then, the three-dimensional fault model is derived by extending this along-profile geometry according to the surface trace.

To fit the detailed fault shape along one profile, the relocated earthquake hypocenters within the region surrounded by two neighboring profiles are extracted. Then, an enveloping plane (the black dashed lines in Figure 3B) is constructed by taking the initial model line as the symmetry axis (the red dashed line in Figure 3B). To obtain enough relocated hypocenters whose source earthquakes are related to the target fault and to exclude as many hypocenters not related to the target fault as possible, this envelope should have as high a hypocenter density and as large an area as possible. The density of the relocated hypocenters in the envelop region usually first increases and then decreases with increasing envelope width because

TABLE 2 Geometry modeling parameters for the main faults.

Fault name	Fitted fault length/km	Number of focal mechanism solutions	Number of earthquake relocations	Number of fitted profiles	Maximum fitted depth/km
Yingxiu-Beichuan Fault	560.4	2,500	16,606	62	27.4
Xianshuihe Fault	405.3	297	4,331	32	29.4
Anninghe Fault	362.2	173	2043	30	26.9
Wenchuan-Wenmao Fault	318.5	1744	11,664	45	22.4
Guanxian-Anxian Fault	310.2	1759	9,485	41	30.3
Honghe Fault	169.2	84	1,310	22	18.0
Zemuhe Fault	144.7	66	1,182	23	21.4
Xiaojiang Fault	101.7	108	1,123	18	23.5

TABLE 3 The RMSE between the geophysical interpretation results and the fitting results based on 2–4 order polynomial by the method of this study.

Profile index	Fault name	RMSE of the ruptured seismogenic fault models/km		
		By 2 order polynomial	By 3 order polynomial	By 4 order polynomial
#1	Haiyuan Fault	2.43	2.05	2.11
#2	Guanxian-Anxian Fault	1.52	1.07	1.02
#2	Yingxiu-Beichuan Fault	0.83	0.44	0.39
#3	Yingxiu-Beichuan Fault	1.08	0.67	0.51
#4	Yingxiu-Beichuan Fault	1.33	0.61	0.63
#5	Yingxiu-Beichuan Fault	1.77	1.15	1.33
#5	Guanxian-Anxian Fault	1.02	0.64	0.60
#6	Longquanshan Fault	1.80	1.21	1.37

the earthquakes caused by fault activity are located near the fault plane. Therefore, the envelope with the maximum relocated hypocenter density is the optimal one. In particular, when there are other active faults near the target fault, hypocenters associated with other faults should be artificially removed.

The depths of nodes with equal intervals along the initial model of fault geometry are fitted based on the selected hypocenters. The spacing of nodes is taken as 2.5 km (Zhang et al., 2013; Duan et al., 2018b). The characteristic depth of each node is estimated by the weighted average method (Zhang et al., 2013), which can be expressed as:

$$Z_{(x)} = \sum_{i=1}^{i=n} \left(\frac{\Omega_i \mu_i}{\sum_{i=1}^{i=n} \Omega_i} \right), \tag{2}$$

where $Z_{(x)}$ is the characteristic depth of the x-th node, n is the number of earthquake relocation data on the profile, μ_i is the focal depth of the i-th earthquake, and $\Omega_i(M_i, x_i)$ is the weight of the i-th earthquake. According to the relationship between earthquake magnitude and the main rupture plane area of the fault (Wells and Coppersmith, 1994) and the attenuation law of seismic waves (Winkler and Nur, 1982), the weight $\Omega_i(M_i, x_i)$ can be estimated by the following equation (Zhang et al., 2013):

$$\Omega_i = 10^{M_i} \exp\left(-\frac{(x - x_i)^2}{2D} \right), \tag{3}$$

where x is the abscissa of the target node, x_i is the abscissa of the i-th earthquake relocation on the profile, M_i is the magnitude of the earthquake, and D is the interval of the cross-sections on the fault. The estimated final positions of nodes are shown as solid diamonds in Figure 3B. The use of 2-4 order polynomial fitting is suggested, and the cubic polynomial is the most widely adopted one in similar modeling research (Hayes et al., 2009; Zhang et al., 2013; Duan et al., 2018b). Therefore, we also apply a cubic polynomial to fit all the nodes along the profile to refine the model of fault geometry (the solid red line in Figure 3B), and reliability of it is establish by comparing the effect of 2-4 order polynomial fitting in the 3.2 uncertainty and discussion.

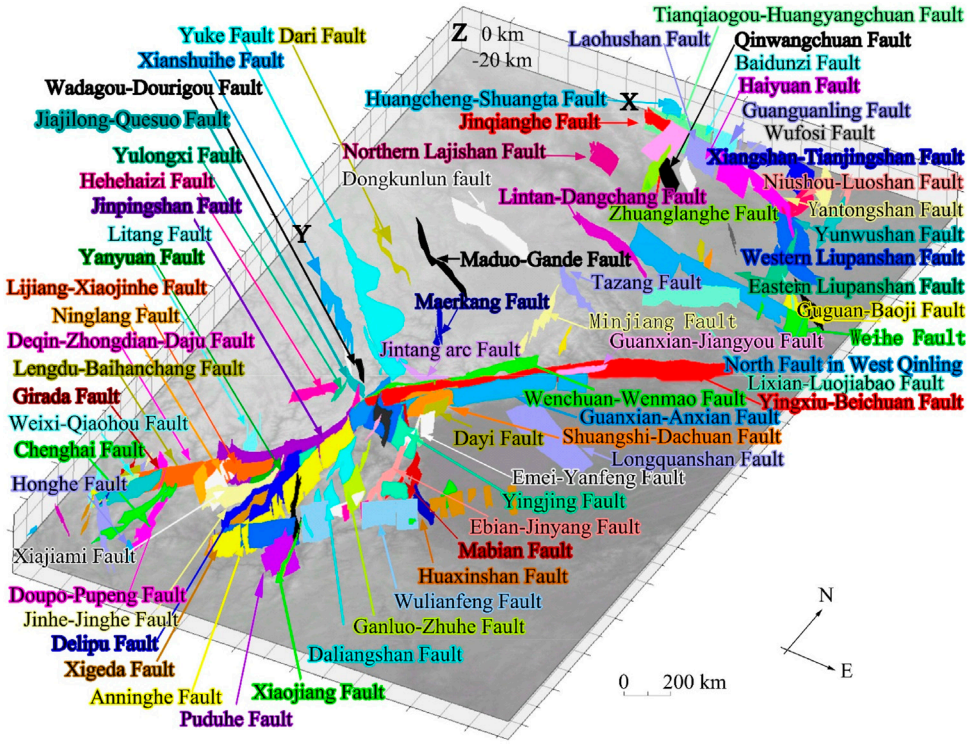

FIGURE 4
Oblique view of the 3D model of 263 ruptured seismogenic faults in the North–South Seismic Belt. ETOPO1 (Amante, 2009) is used as the base map and placed at a depth of 20 km, and the vertical exaggeration is 3X.

2.2.3 Three-dimensional model and its uncertainty of fault geometry

Some of the faults are composed of different segments according to the surface traces. In this case, the unit of the three-dimensional fault geometry modeling is the fault segment. Otherwise the unit is the whole fault. Then, the minimum curvature interpolation method (Briggs, 2012) is adopted to build the 3D model of the subsurface fault geometry according to the three-dimensional coordinates of nodes on all profiles of each fault/segment. The uncertainty of this 3D model is estimated by comparing the modeled fault geometry with the published fault geometry, where the latter is based on active-source geophysical explorations. The fault depth differences between our model and the reference result at the points along the profile with a constant horizontal interval are used to estimate the root mean square error (RMSE) of our model. The RMSE can be calculated as follows:

$$\mathrm{RMSE} = \sqrt{\frac{\sum_{i=1}^{n} (y_i - y_i')^2}{n}}, \quad (4)$$

where y_i and y_i' are the fault plane depth at the i-th point from our model and the reference result, respectively, and n is the number of comparison points. A smaller RMSE means a smaller uncertainty in our fitted fault model.

3 Results and discussion

3.1 3D model of ruptured seismogenic faults in the NSSB

The middle segment of the Yingxiu-Beichuan Fault is taken as an example to illustrate the fault modeling steps and selection of some parameters. Previous studies suggest that the fault dip angle is between 50° and 70° here, and the strike ranges from 210° to 230° (Lei and Zhao, 2009; Li et al., 2013; Nie et al., 2013; Si et al., 2014; Wang et al., 2014; Li et al., 2016; Meng et al., 2020). According to these conditions, 67 focal mechanism solutions in total are selected for this fault section, as shown in Figure 3A. Finally, the along-strike initial geometric model of the middle section of the Yingxiu-Beichuan Fault is modeled by interpolation of these focal mechanism solutions (Figure 3A).

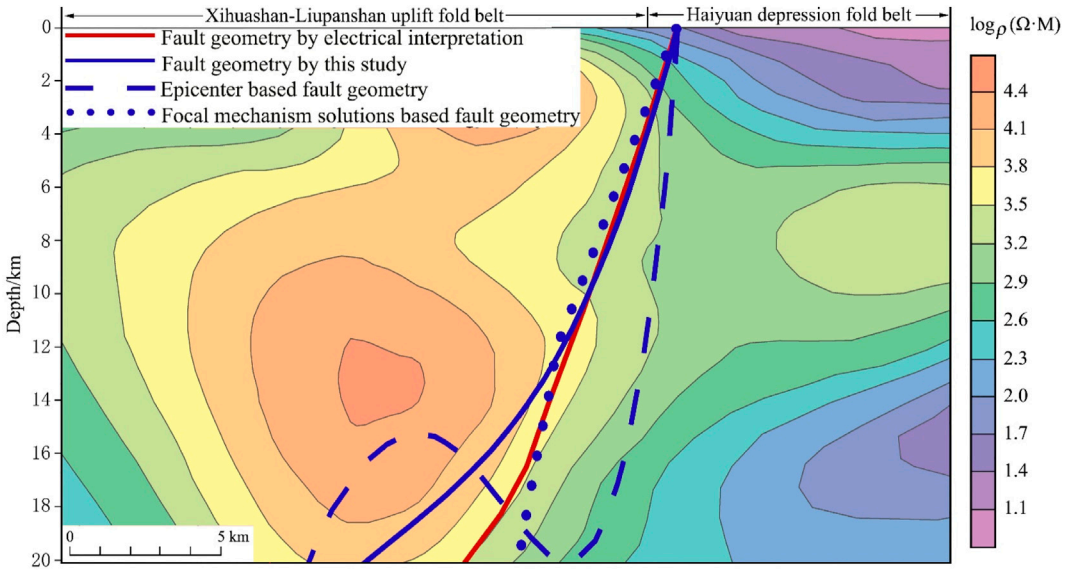

FIGURE 5
Comparison between the Haiyuan Fault geometry obtained from a geophysically interpreted profile (Min, 2014) and the three kinds of fitting results based on earthquake data. The electrical structure (Min, 2014) is taken as the base map.

In total, 18transverse profiles perpendicular to the middle segment of the Yingxiu-Beichuan Fault are constructed with a 10-km interval (Figure 3C). On average, 425 hypocenters are distributed along each profile, with a maximum of 926 and a minimum of 237. The central profile (Figure 3B) is selected to show the modeling results. The envelope region is 9 km wide; in other words, the distance between the upper and bottom black dashed lines in Figure 3B is 9 km. There are nine calculation nodes with an interval of 2.5 km whose characteristic depths (the red solid diamonds in Figure 3B) are fitted by 926 relocated hypocenters (the black hollow circle in Figure 3B), and the maximum burial depth of this fine model (red solid line in Figure 3B) is 23.8 km. Finally, the three-dimensional fault plane model (Figure 3D) of the middle segment of the Yingxiu-Beichuan Fault is obtained based on the fine models of fault geometry along the 18 transverse profiles (the solid black line in Figure 3C).

To model the 3D geometries of the 263 main ruptured seismogenic faults (fault segments) in the NSSB, the fine fault shapes along a total of 1,573 transverse profiles are fitted. The final 3D model covers all the main ruptured seismogenic faults, such as the Yingxiu-Beichuan Fault, Xianshuihe Fault, and Haiyuan Fault (Figure 4). The fitted fault length at the Earth's surface, the number of fitted cross-sections, the maximum depth of the fault model, and some other parameters of the main faults in the 3D model are listed in Table 2; the detailed statistics are reported in Supplementary Table A1.

3.2 Uncertainty and discussion

Uncertainty is mainly caused by two aspects in our ruptured seismogenic fault geometry model, on the one hand, the uncertainty is determined by the order of polynomial used to fit the characteristic depth, on the other hand, is caused by the input data. For the former, the effect of 2-4 order polynomial fitting has been tested, the overall fitting error of them are 1.47 km, 0.98 km and 1.00 km respectively comparing geophysical interpretation results (Table 3). Comparatively, the 2 order polynomial is the worst, the 3 order is the best, and the fitting effects of the 3 order and 4 order polynomials are similar.

As for the latter, there are different uncertainties such as the uncertainties in the focal mechanism solutions and the relocated hypocenters, and the number of hypocenters related to other faults used in the modeling. According to statistics, the focal mechanism solutions and relocated hypocenters used in this study decrease in number with increasing depth below a specific depth (Figure 3B). Fewer relocated hypocenters at the fault bottom means that the weight of the relocated hypocenters on the upper part becomes higher (Eq. 3), so the fitted node depth at the fault bottom will be shallower than that in reality. This process trends to yield listric fault models (Figures 5, 6). Therefore, the uncertainty at the bottom of the model tends to be larger than that of the shallow part (Figures 5, 6). The qualities of seismicity data also vary among different cross-sections or along different faults, so the model uncertainty also varies along strike or between different faults (Table 4).

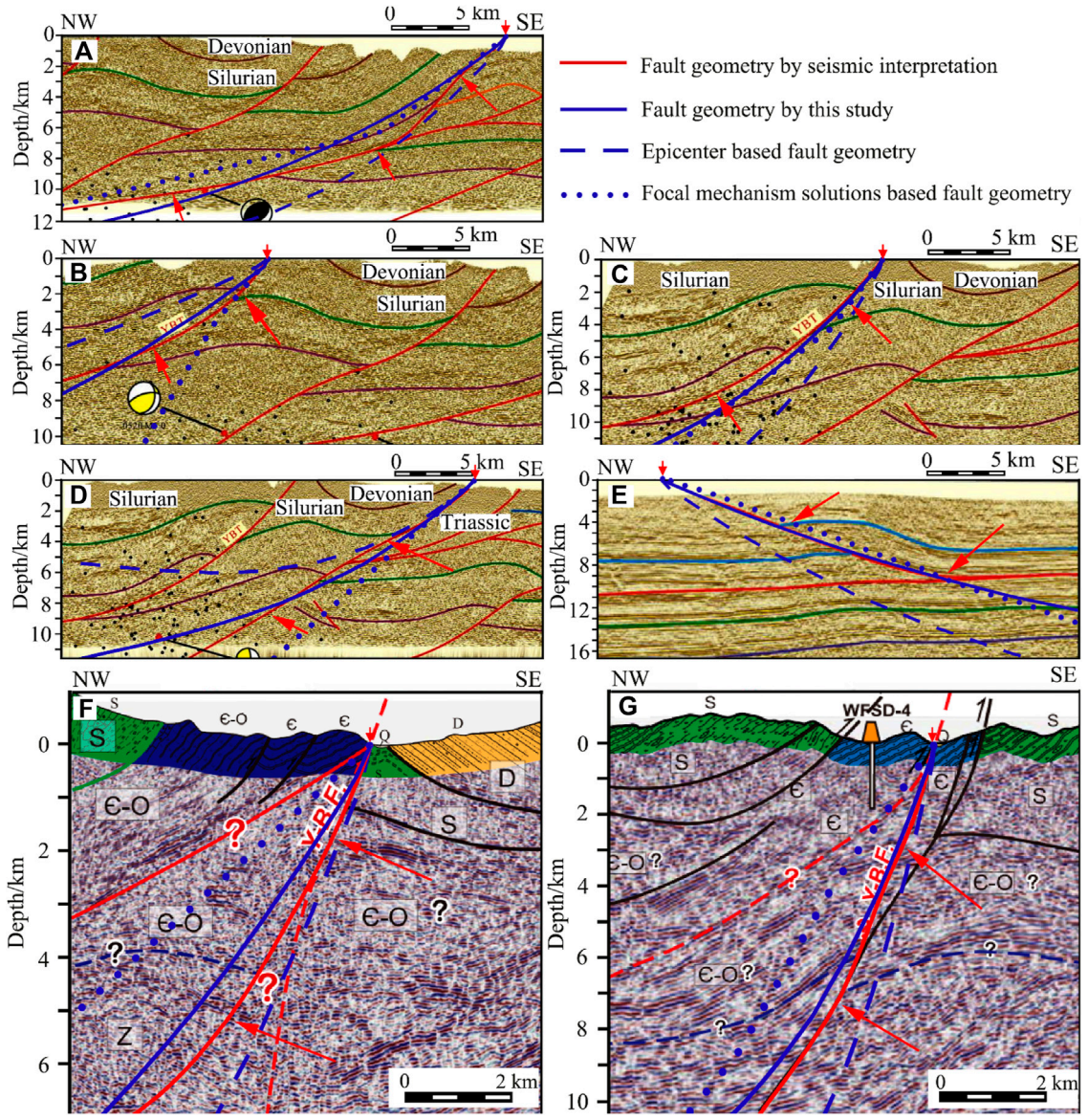

FIGURE 6
Comparison between the fault geometries obtained from seismic interpretation and the fitting results based on earthquake data. **(A,B)** are from Profile #2 (Dong et al., 2010); **(C,D)** are from Profile #5 (Dong et al., 2010); **(E)** is from Profile #6 (Dong et al., 2010); **(F)** is from Profile #4 (Wu et al., 2014); and **(G)** is from Profile #3 (Wu et al., 2014).

In addition, it is impossible to remove all the relocated hypocenters related to other faults based on the initial fault model, even though we attempt to do so. Therefore, this incomplete removal also introduces uncertainty to the fault geometry models.

The uncertainty of the three-dimensional ruptured seismogenic fault model in the NSSB is estimated by taking the fault geometries from the six collected geophysical interpretation profiles as the reference. The RMSEs of the 3D model are shown in Table 4. Since the fault model can also be constructed based only on focal mechanisms, which is the same as our initial model of fault geometry, or only by fitting hypocenters along the profile without earthquake selection, Table 4 also provides the RMSEs of the fault model when using these two simplified methods. Among the three modeling methods, the approach designed in this study derives the smallest RMSE overall, which is 0.98 km. The fault geometries based on geophysical profile interpretations and the three different fitting methods are plotted on the geophysical profiles (Figures 5, 6). The comparison results suggest that the

TABLE 4 The RMSE between the geophysical interpretation results and the fitting results based on different methods.

Profile index	Fault name	RMSE of the ruptured seismogenic fault models/km		
		By the method of this study	By the hypocenter-based method	By the focal mechanism solution-based method
#1	Haiyuan Fault	2.05	6.54	1.67
#2	Guanxian-Anxian Fault	1.07	2.04	0.91
#2	Yingxiu-Beichuan Fault	0.44	1.70	5.35
#3	Yingxiu-Beichuan Fault	0.67	2.36	3.01
#4	Yingxiu-Beichuan Fault	0.61	1.85	2.21
#5	Yingxiu-Beichuan Fault	1.15	3.74	1.82
#5	Guanxian-Anxian Fault	0.64	2.41	2.66
#6	Longquanshan Fault	1.21	4.36	1.88

method of this study can best match the geophysical interpretation results among the three kinds of fitted results in most cases.

4 Conclusion

A new method for 3D modeling of ruptured seismogenic fault geometry based on seismicity is designed in this study. The focal mechanism solutions related to the target ruptured seismogenic fault are chosen by comparing their internal consistency or the consistency of each with the collected fault orientations, and the selected solutions are used to construct the initial model of fault geometry. The initial geometric model is further adopted to determine the earthquake relocation data related to the target fault. Subsequently, these earthquake relocations are employed to refine the fault model. This method can avoid the disadvantage of constructing only a low-resolution fault model when using focal mechanism solutions alone due to the limited amount of data. Moreover, it can also reduce the modeling uncertainty by removing the ambiguity of hypocenters with respect to other nearby fault or faults under the constraint of the initial geometric models.

Combining the surface traces of ruptured seismogenic faults in the NSSB, the initial geometric models of 263 faults (segments) are modeled based on the focal mechanism solutions under the constraints of prior data on fault orientations obtained from seismic, electrical and magnetic exploration. Moreover, detailed fault geometries along a total of 1,573 strike-perpendicular profiles are fitted based on the selected hypocenters. Finally, the minimum curvature interpolation method is adopted to build a three-dimensional model for the ruptured seismogenic faults in the NSSB. When taking six geophysical interpretation profiles as a reference, the average RMSE of this model is 0.98 km which is smaller than those of the other two traditional methods. The model uncertainty at the bottom is higher than that near the top because of the limited number of earthquakes, and the uncertainties for different sections of each fault may also differ because of the unevenly distributed earthquake data.

Data availability statement

The datasets presented in this study can be found in online repositories. The names of the repository/repositories and accession number(s) can be found in the article/ Supplementary Material.

Author contributions

YR: Methodology, Validation, Modeling, Writing - Original Draft, Writing—Review Editing YB: Conceptualization, Methodology, Validation, Formal analysis, Writing—Original Draft, Writing—Review Editing MR: Modeling, Writing—Review Editing ML: Data providing, Writing—Review Editing ZW: Writing—Review Editing All authors contributed to manuscript revision, read, and approved the submitted version.

Funding

This study was supported by the National Key Research and Development Program of China (Grant No. 2019YFC1509204), the National Natural Science Foundation of China (No. 42176068), the Natural Science Foundation of Shandong, China (No. ZR2020MD065), the Open Fund of State Key Laboratory of Earthquake Dynamics (No. LED2019B01), and the National Program of Geological Survey (DD20191008).

Acknowledgments

The China Seismic Experimental Site provided earthquake relocation data, the National Earthquake Data Sharing Project of the China Earthquake Administration supplied focal mechanism solution data, and the Data Exchange and Sharing Management Center of Active Fault Exploration in the Institute of Geology from the China Earthquake Administration provided surface fault trace data. We would like to express our deepest gratitude to these agencies and projects.

Conflict of interest

The authors declare that the research was conducted in the absence of any commercial or financial relationships that could be construed as a potential conflict of interest.

Publisher's note

Supplementary material

The Supplementary Material for this article can be found online at: https://www.frontiersin.org/articles/10.3389/feart.2022.1023106/full#supplementary-material.

References

Aki, K. (1966). Generation and propagation of G waves from the Niigata earthquake of June 16, 1964. 2. Estimation of earthquake movement, released energy, and stress-strained drop from G wave spectrum. *Bull. Earthq. Res. Inst.* 44.

Amante, C. (2009). *ETOPO1 1 arc-minute global relief model : Procedures, data sources and analysis*. http://www.ngdc.noaa.gov/mgg/global/global.html.

Barka, A., and Kadinsky Cade, K. (1988). Strike slip fault geometry in Turkey and its influence on earthquake activity. *Tectonics* 7, 663–684. doi:10.1029/tc007i003p00663

Briggs, I. C. (2012). Machine contouring using minimum curvature. *Geophysics* 39, 39–48. doi:10.1190/1.1440410

Chen, S., Zheng, Q.-Y., and Xu, W.-M. (2015). Joint optimal inversion of gravity and seismic data to estimate crustal thickness of the southern section of the north-south seismic belt. *Chin. J. Geophys.* 58, 3941–3951.

Ciaccio, M. G., Barchi, M. R., Chiarabba, C., Mirabella, F., and Stucchi, E. (2005). Seismological, geological and geophysical constraints for the Gualdo Tadino Fault, umbria–marche apennines (central Italy). *Tectonophysics* 406, 233–247. doi:10.1016/j.tecto.2005.05.027

Dai, F., Xu, C., Yao, X., Xu, L., Tu, X., and Gong, Q. (2011). Spatial distribution of landslides triggered by the 2008 Ms 8.0 Wenchuan earthquake, China. *J. Asian Earth Sci.* 40, 883–895. doi:10.1016/j.jseaes.2010.04.010

Dilla, D. A., Ade, A., Mochamad, N., Birger-Gottfried, L., and Wiwit, S. (2018). Velocity structure of the earthquake zone of the M6.3 Yogyakarta earthquake 2006 from a seismic tomography study. *Geophys. J. Int.* 216, 439–452. doi:10.1093/gji/ggy430

Dong, J., Li, Y., Lin, A., Wang, M., Wei, C., Wu, X., et al. (2010). Structural model of 2008 Mw 7.9 Wenchuan earthquake in the rejuvenated Longmen Shan thrust belt, China. *Tectonophysics* 491, 174–184. doi:10.1016/j.tecto.2009.08.040

Dorbath, C., Oppenheimer, D., Amelung, F., and King, G. (1996). Seismic tomography and deformation modeling of the junction of the San Andreas and Calaveras faults. *J. Geophys. Res.* 101, 27917–27941. doi:10.1029/96jb02092

Duan, H., Chen, S., Li, R., and Yan, Q. (2018a). Fault geometrical model of Dujiangyan section in Longmenshan fault zone. *Earthq. Sci.* 31, 126–136. doi:10.29382/eqs-2018-0126-2

Duan, H., Zhou, S., and Li, R. (2018b). Estimation of dip angle of Haiyuan faults based on seismic data. *Chin. J. Geophys. (in Chinese)* 61, 3713–3721.

Frepoli, A., Cimini, G. B., Gori, P. D., Luca, G. D., Marchetti, A., Monna, S., et al. (2017). Seismic sequences and swarms in the Latium-Abruzzo-Molise Apennines (central Italy): New observations and analysis from a dense monitoring of the recent activity. *Tectonophysics* 712, 312–329. doi:10.1016/j.tecto.2017.05.026

Guo, X., Jiang, C., Han, L., Yin, H., and Zhao, Z. (2022). *Focal mechanism data set in Chinese mainland and its adjacent area(2009-2021*. [EB/OL]. 10.12080/nedc.11.ds. 2022.0004 https://data.earthquake.cn (or CSTR:12166.11.ds.2022.0004.

Hayes, G. P., and Wald, D. J. (2009). Developing framework to constrain the geometry of the seismic rupture plane on subduction interfaces a priori– a probabilistic approach. *Geophysical Journal International* 176, 951–964. doi:10.1111/j.1365-246x.2008.04035.x

Hayes, G. P., Wald, D. J., and Keranen, K. (2009). Advancing techniques to constrain the geometry of the seismic rupture plane on subduction interfaces a priori: Higher-order functional fits. *Geochem. Geophys. Geosyst.* 10. doi:10.1029/2009gc002633

Hengl, T. (2006). Finding the right pixel size. *Computers & Geosciences* 32, 1283–1298. doi:10.1016/j.cageo.2005.11.008

Hubbard, J., and Shaw, J. H. (2009). Uplift of the Longmen Shan and Tibetan plateau, and the 2008 Wenchuan (M = 7.9) earthquake, 458. *Translated World Seismology*, 194–197.

King, G. (1986). Speculations on the geometry of the initiation and termination processes of earthquake rupture and its relation to morphology and geological structure. *Pure and applied geophysics* 124, 567–585. doi:10.1007/bf00877216

Kuang, W., Yuan, C., and Zhang, J. (2021). Real-time determination of earthquake focal mechanism via deep learning. *Nat. Commun.* 12, 1432–1438. doi:10.1038/s41467-021-21670-x

Lay, T., Ammon, C. J., Kanamori, H., Rivera, L., Koper, K. D., and Hutko, A. R. (2010). The 2009 Samoa–Tonga great earthquake triggered doublet. *Nature* 466, 964–968. doi:10.1038/nature09214

Lei, J., and Zhao, D. (2009). Structural heterogeneity of the Longmenshan fault zone and the mechanism of the 2008 Wenchuan earthquake (Ms 8.0). *Geochem. Geophys. Geosyst.* 10. doi:10.1029/2009gc002590

Li, H., Wang, H., Xu, Z., Si, J., Pei, J., Li, T., et al. (2013). Characteristics of The fault-related rocks, fault zones and the principal slip zone in the wenchuan earthquake fault scientific drilling project hole-1 (WFSD-1). *Tectonophysics* 584, 23–42. doi:10.1016/j.tecto.2012.08.021

Li, H., Wang, H., Yang, G., Xu, Z., Li, T., Si, J., et al. (2016). Lithological and structural characterization of the longmen Shan Fault Belt from the 3rd hole of the wenchuan earthquake fault scientific drilling project (WFSD-3). *Int. J. Earth Sci.* 105, 2253–2272. doi:10.1007/s00531-015-1285-9

Li, X., Hergert, T., Henk, A., Wang, D., and Zeng, Z. (2019a). Subsurface structure and spatial segmentation of the Longmen Shan fault zone at the eastern margin of Tibetan Plateau: Evidence from focal mechanism solutions and stress field inversion. *Tectonophysics* 757, 10–23. doi:10.1016/j.tecto.2019.03.006

Li, Y., Dong, J., Shaw, J. H., Hubbard, J., Lin, A., Wang, M., et al. (2010). Structural interpretation of the coseismic faults of the Wenchuan earthquake: Three-dimensional modeling of the Longmen Shan fold-and-thrust belt. *J. Geophys. Res.* 115, B04317. doi:10.1029/2009jb006824

Li, Y., Lu, R., He, D., Wang, X., Liu, Y., Xu, X., et al. (2019b). Transformation of coseismic faults in the northern Longmenshan tectonic belt, eastern Tibetan Plateau: Implications for potential earthquakes and seismic risks. *Journal of Asian earth sciences* 177, 66–75. doi:10.1016/j.jseaes.2019.03.013

Lin, G., Shearer, P. M., and Hauksson, E. (2007). Applying a three-dimensional velocity model, waveform cross correlation, and cluster analysis to locate southern California seismicity from 1981 to 2005. *J. Geophys. Res.* 112, B12309. doi:10.1029/2007jb004986

Liu, Y., Wen, Y., Li, Z., Peng, Y., and Xu, C. (2022). Coseismic fault model of the 2017 MW 6.5 Jiuzhaigou earthquake and implications for the regional fault slip pattern. *Geodesy and Geodynamics* 13, 104–113. doi:10.1016/j.geog.2021.09.009

Liu, Y., Yao, H., Zhang, H., and Fang, H. (2021). The community velocity model V.1.0 of southwest China, constructed from joint body and surface wave travel time tomography. *Seismological Research Letters* 92, 2972–2987. doi:10.1785/0220200318

Lu, R., Liu, Y., Xu, X., Tan, X., He, D., and Yu, G. (2019). Three-dimensional model of the lithospheric structure under the eastern Tibetan Plateau: Implications for the active tectonics and seismic hazards. *Tectonics* 38, 1292–1307. doi:10.1029/2018TC005239

Maxime, G., Anne, D., Sophie, L., Hélène, L., Pascal, B., and Francesco, P. (2014). Focal mechanisms of earthquake multiplets in the Western part of the Corinth Rift (Greece): Influence of the velocity model and constraints on the geometry of the active faults. *Geophysical Journal International* 197, 1660–1680. doi:10.1093/gji/ggu059

Meng, F., Zhang, G., Qi, Y., Zhou, Y., Zhao, X., and Ge, K. (2020). Application of combined electrical resistivity tomography and seismic reflection method to explore hidden active faults in Pingwu, Sichuan, China. *Open Geosciences* 12, 174–189. doi:10.1515/geo-2020-0040

Mildon, Z., Roberts, G. P., Faure Walker, J., and Toda, S. (2019). Coulomb pre-stress and fault bends are ignored yet vital factors for earthquake triggering and hazard. *Nat. Commun.* 10, 2744–2749. doi:10.1038/s41467-019-10520-6

Min, G. (2014). *The electrical structure of middle & upper crust of Ningxia Arc-shaped Structural belt and its tectonic implications*. Chengdu University of Technology.Chengdu

Nie, X., Zou, C., Pan, L., Huang, Z., and Liu, D. (2013). Fracture analysis and determination of *in-situ* stress direction from resistivity and acoustic image logs and core data in the Wenchuan Earthquake Fault Scientific Drilling Borehole-2 (50–1370 m). *Tectonophysics* 593, 161–171. doi:10.1016/j.tecto.2013.03.005

Nolet, G. (1980). Quantitative seismology, theory and methods. *Earth. Sci. Rev.* 17, 296–297. doi:10.1016/0012-8252(81)90044-1

Silver, P. G., and Jordan, T. H. (1982). Optimal estimation of scalar seismic moment. *Geophys. J. Int.* 70 (3), 755–787. doi:10.1111/j.1365-246x.1982.tb05982.x

Plesch, A., Shaw, J. H., Benson, C., Bryant, W. A., Carena, S., Cooke, M., et al. (2007). Community fault model (CFM) for southern California. *Bulletin of the Seismological Society of America* 97, 1793–1802. doi:10.1785/0120050211

Ross, Z. E., Trugman, D. T., Hauksson, E., and Shearer, P. M. (2019). Searching for hidden earthquakes in Southern California. *Science* 364, 767–771. doi:10.1126/science.aaw6888

Schaff, D., P. (2009). Waveform cross-correlation-based differential travel-time measurements at the northern California seismic network. *Bulletin of the Seismological Society of America* 95, 2446–2461. doi:10.1785/0120040221

Schaff, D. P., Bokelmann, G. T. H. R., Beroza, G. C., Waldhauser, F., and Ellsworth, W. L. (2002). High-resolution image of calaveras fault seismicity. *J. Geophys. Res.* 107 (5-1), ESE 5-1–ESE 5-16. doi:10.1029/2001jb000633

Shi, X., Tapponnier, P., Wang, T., Wei, S., Wang, Y., Wang, X., et al. (2019). Triple junction kinematics accounts for the 2016 Mw 7.8 Kaikoura earthquake rupture complexity. *Proc. Natl. Acad. Sci. U. S. A.* 116, 26367–26375. doi:10.1073/pnas.1916770116

Si, J., Li, H., Kuo, L., Pei, J., Song, S., and Wang, H. (2014). Clay mineral anomalies in the Yingxiu–Beichuan fault zone from the WFSD-1 drilling core and its implication for the faulting mechanism during the 2008 Wenchuan earthquake (Mw 7.9). *Tectonophysics* 619, 171–178. doi:10.1016/j.tecto.2013.09.022

Silva, V. (2016). Critical issues in earthquake scenario loss modeling. *Journal of Earthquake Engineering* 20, 1322–1341. doi:10.1080/13632469.2016.1138172

Valoroso, L., Chiaraluce, L., and Collettini, C. (2014). Earthquakes and fault zone structure. *Geology* 42, 343–346. doi:10.1130/g35071.1

Walker, J., Visini, F., Roberts, G., Galasso, C., McCaffrey, K., and Mildon, Z. (2019). Variable fault geometry suggests detailed fault Slip Rate profiles and geometries are needed for fault-based probabilistic seismic hazard assessment (PSHA). *Bulletin of the Seismological Society of America* 109, 110–123. doi:10.1785/0120180137

Wang, C., Ding, X., Li, Q., Shan, X., and Liu, P. (2016). Using an integer least squares estimator to connect isolated InSAR fringes in earthquake slip inversion. *IEEE Trans. Geosci. Remote Sens.* 54, 2899–2910. doi:10.1109/tgrs.2015.2507601

Wang, H., Li, H., Si, J., Sun, Z., and Huang, Y. (2014). Internal structure of the Wenchuan earthquake fault zone, revealed by surface outcrop and WFSD-1 drilling core investigation. *Tectonophysics* 619, 101–114. doi:10.1016/j.tecto.2013.08.029

Wang, S., Liu, B., Zhang, J., Liu, B., Duan, Y., Song, X., et al. (2015). Study on the velocity structure of the crust in southwest yunnan of the North-South Seismic belt—results from the menghai-gengma-lushui deep seismic sounding profile. *Sci. China Earth Sci.* 58, 2175–2187. doi:10.1007/s11430-015-5189-0

Wang, X. C., Ding, Z. F., Wu, Y., and Zhu, L. P. (2017). Crustal thicknesses and Poisson's ratios beneath the northern section of the north-south seismic belt and surrounding areas in China. *Chinese Journal of Geophysics* 60, 2080–2090.

Wells, D. L., and Coppersmith, K. J. (1994). New empirical relationships among magnitude, rupture length, rupture width, rupture area, and surface displacement. *Bull.seism.soc.am* 84, 974–1002.

Winkler, K. W., and Nur, A. (1982). Seismic attenuation: Effects of pore fluids and frictional-sliding. *Geophysics* 47, 1–15. doi:10.1190/1.1441276

Wu, C., Li, H., Leloup, P. H., Yu, C., Si, J., Liu, D., et al. (2014). High-angle fault responsible for the surface ruptures along the northern segment of the Wenchuan Earthquake Fault Zone: Evidence from the latest seismic reflection profiles. *Tectonophysics* 619, 159–170. doi:10.1016/j.tecto.2013.09.015

Xin, D., and Zhang, Z. (2021). On the comparison of seismic ground motion simulated by physics-based dynamic rupture and predicted by empirical attenuation equations. *Bulletin of the Seismological Society of America* 111, 2595–2616. doi:10.1785/0120210077

Xu, X. W., Han, Z. J., and Yang, X. P. (2016). *Seismotectonic map in China and its adjacent regions*. Beijing: Seismogical Press.

Yang, T., Li, B., Fang, L., Su, Y., Zhong, Y., Yang, J., et al. (2022). Relocation of the foreshocks and aftershocks of the 2021 Ms 6.4 Yangbi earthquake sequence, Yunnan, China. *J. Earth Sci.* 33, 892–900. doi:10.1007/s12583-021-1527-7

Zhang, L., Shao, Z., Ma, H., Wang, X., and Li, Z. (2013). The plate contact geometry investigation based on earthquake source parameters at the Burma arc subduction zone. *Sci. China Earth Sci.* 56, 806–817. doi:10.1007/s11430-012-4578-x

Zhang, P. (2013). A review on active tectonics and deep crustal processes of the Western Sichuan region, eastern margin of the Tibetan Plateau. *Tectonophysics* 584, 7–22. doi:10.1016/j.tecto.2012.02.021

Zhang, S., Wu, Z., and Jiang, C. (2015). The central China North–South seismic belt: Seismicity, ergodicity, and five-year pi forecast in testing. *Pure Appl. Geophys.* 173, 245–254. doi:10.1007/s00024-015-1123-9

Zhao, P., Chen, J., Li, Y., Liu, Q., Yin, X., Guo, B., et al. (2021). Growth of the northeastern Tibetan plateau driven by crustal channel flow: Evidence From High-Resolution Ambient Noise Imaginga, e2021GL093387.48 doi:10.1029/2021gl093387

Zheng, S. Y. (2019). *China earthquake focal mechanism solution database construction*. China Earthquake Administration: Institute of seismology.

Zhou, S., Fang, L., and Liu, B. (2015). Slope unit-based distribution analysis of landslides triggered by the April 20, 2013, Ms 7.0 Lushan earthquake. *Arab. J. Geosci.* 8, 7855–7868. doi:10.1007/s12517-015-1835-2

frontiers | Frontiers in Earth Science

TYPE Methods
PUBLISHED 17 January 2023
DOI 10.3389/feart.2023.1101165

OPEN ACCESS

EDITED BY
Xinjian Shan,
China Earthquake Administration, China

REVIEWED BY
Dedalo Marchetti,
Jilin University, China
Kaiguang Zhu,
Jilin University, China
Zhong-Hu Jiao,
China Earthquake Administration, China

*CORRESPONDENCE
Qingyan Meng,
mengqy@radi.ac.cn

SPECIALTY SECTION
This article was submitted to Structural Geology and Tectonics, a section of the journal Frontiers in Earth Science

RECEIVED 17 November 2022
ACCEPTED 03 January 2023
PUBLISHED 17 January 2023

CITATION
Wu P, Meng Q, Zhang Y, Zhan C, Allam M, Zhang L and Hu X (2023), Coarse-graining research of the thermal infrared anomalies before earthquakes in the Sichuan area on Google Earth engine.
Front. Earth Sci. 11:1101165.
doi: 10.3389/feart.2023.1101165

Coarse-graining research of the thermal infrared anomalies before earthquakes in the Sichuan area on Google Earth engine

Pengcheng Wu[1,2], Qingyan Meng[2,3]*, Ying Zhang[4], Chengxiang Zhan[2,5], Mona Allam[2,6], Linlin Zhang[2,3] and Xinli Hu[2,3]

[1]College of Engineering, Tibet University, Lhasa, China, [2]Aerospace Information Research Institute, Chinese Academy of Sciences, Beijing, China, [3]Hainan Research Institute, Aerospace Information Research Institute, Chinese Academy of Sciences, Sanya, China, [4]Department of Geophysics, School Earth and Space Sciences, Peking University, Beijing, China, [5]School of Science, China University of Geosciences, Beijing, China, [6]Environment and Climate Changes Research Institute, National Water Research Center, El Qanater El Khairiya, Egypt

Seismo-induced Thermal infrared (TIR) anomalies has been proposed as a significant precursor of earthquakes. Several methods have been proposed to detect Thermal infrared anomalies that may be associated with earthquakes. However, there is no comparison of the influence for Thermal infrared extraction methods with a long time statistical analysis. To quantify the effects of various techniques used in Thermal infrared anomaly extraction, in this paper, we offer a complete workflow of their comparative impacts. This study was divided into three parts: anomaly detection, statistical analysis, and tectonic factor research. For anomaly detection, daily continuous nighttime surface temperature (ConLST) data was obtained from the Google Earth Engine (GEE) platform, and each different anomaly detection method was used to detect Thermal infrared outliers in the Sichuan region (27°-37°N, 97°-107°E). During statistical analysis, The heated core model was applied to explore Thermal infrared anomalies which is to filter anomalies unrelated to earthquakes by setting time-space-intensity conditions. The 3D error diagram offers scores to assume the best parameter set using training-test-validation steps. In the final part, we considered information on stresses, active faults, and seismic zones to determine the optimal parameters for extracting the Thermal infrared anomalies. The Kalman filter method detected the highest seismic anomaly frequency without considerating the heating core condition. The Autoencoder and Isolation Forest methods obtain the optimal alert type and parameter set to determine if the anomaly is likely earthquake-related. The RST method performs optimally in the final part of the workflow when it considers physical factors such as active faults, seismic zones, and stresses. However, The six methods we have chosen are not sufficient to contain the entire Thermal infrared anomaly extraction. The consideration of tectonic factors in the research remains poorly developed, as statistical methods were not employed to explore the role of constructive factors. Nevertheless, it is a significant factor in comparing anomaly extraction methods and precursor studies.

KEYWORDS

earthquakes, thermal infrared anomaly, anomaly detection, google earth engine, comparison of methods

1 Introduction

Earthquakes often occur with a rapid release of energy from Earth's crust, resulting in enormous casualties and damages (Jin et al., 2019). It is a very complex and broad topic, related to motions of the Earth's surface mass and interior at various scales, as well as microscopic processes, such as the generation of electric charge and chemical reactions (Jin et al., 2006; Jin et al., 2007; Jin et al., 2010; Cambiotti et al., 2011). From the time of ancient Greek civilization to the present, information on earthquake precursors, including tilt, global positioning system (GPS) data, hydrological data, the temperature variations and chemical substances in groundwater, electromagnetic fluctuations, and emissions of radon and other ionized gases, have been collected in abundance (Molchanov et al., 1992; Jin et al., 2006; Hayakawa et al., 2011; Hayakawa et al., 2013, 11; Hayakawa, 2018). Therefore, strengthening the monitoring of seismic activity using different techniques is necessary (Jiao et al., 2018). With the evolution of technology, many multidisciplinary earthquake monitoring systems have been constructed, providing fundamental infrastructure for studying and using pre-earthquake phenomena.

Remote sensing techniques that contribute to numerous aspects of earthquake risk prediction are widely deployed (Geiß and Taubenböck, 2013). Satellite remote sensing technology has unique advantages over traditional, ground-based monitoring methods. Remote sensing data offer a variety of geophysical and geochemical parameters, providing abundant data for pre-seismic anomaly detection (Bakun et al., 2005; Jiao and Shan, 2022). Moreover, remote sensing data are characterized by round-the-clock availability, long timescale, multi-resolution and convenient acquisition. This has led to widespread use in volcano monitoring, flood forecasting, landslide simulation, and precursor prediction.

Since the last decade, themal infrared (TIR) anomalies have been regarded as observable precursors before earthquakes by instruments on board satellites (Hassanien and Darwish, 2021). Many geophysical parameters, such as top-of-atmosphere (TOA) brightness temperature (BT), outgoing longwave radiation (OLR), surface temperature, and latent heat flux, that reflect thermal radiation information using satellite observations and products were employed (Ouzounov et al., 2006; Ouzounov et al., 2007). The precursors we focus on in this paper are land surface temperature (LST) anomalies, using satellite observations before earthquakes. Although many LST products have been used in earthquake prediction (e.g., Terra/Aqua moderate-resolution imaging spectroradiometer (MODIS), national oceanic and atmospheric administration-advanced very-high-resolution radiometer (NOAA-AVHRR) and Landsat), MODIS LST data are the most products used till now with spatial resolution of 1 km and temporal resolution of daily scales (Wan, 2014, 6; Bhardwaj et al., 2017). Researchers have conducted several long-term statistical studies to demonstrate the correlation between TIR anomalies and earthquakes (Zhang and Meng, 2018; Genzano et al., 2021). Once the statistical correlation between earthquake precursors and earthquakes is determined, the next step is to elucidate the mechanism of the generation of pre-earthquake signals. In addition to TIR anomalies, other researchers found other quantities that are statistically related to the earthquake such as ionospheric anomalies

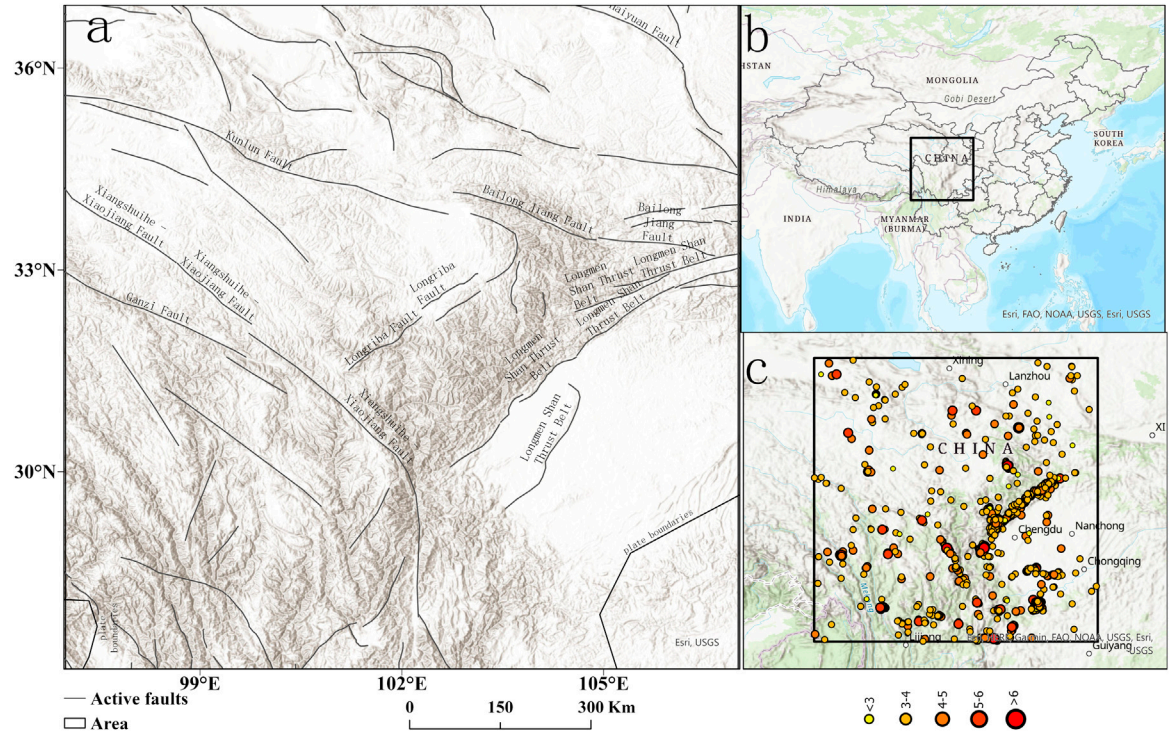

FIGURE 1
(A) is the location of the study area and the distribution of active faults, **(B)** illustrates that the study area is at the junction of Yunnan, Sichuan and Gansu in China, and **(C)** is the magnitude 3–8 earthquakes that have occurred in the study area in 2010-2020.

TABLE 1 The thresholds of the different methods.

Methods	Threshold(θ)
RST	2,2.5,3,3.5,4,4.5,5
IQR	2,2.5,3,3.5,4,4.5,5
Wavelet transform	2,2.5,3,3.5,4,4.5,5
Kalman filter	2,2.5,3,3.5,4,4.5,5
Isolation forest	0.5,0.6,0.7,0.8,0.9,0.95
Autoencoder	0.02,0.025,0.03,0.035,0.04,0.045,0.05

(Parrot and Li, 2018). As we all know, the relationships regarding TIR anomalies and earthquake mechanisms are still not completely understood. Therefore, in this paper, we attempted to demonstrate the relationship between TIR anomalies and earthquakes from a statistical approach.

To identify the TIR anomalies that may relate to earthquakes, many different methods analyzing remote sensing products (LST data) have been used. These methods are classified and discussed as follows. First, statistical or mathematical methods are, such as the mean, median, interquartile range (IQR), Kalman filter, and z-score often used to extract TIR anomalies. (Blackett et al., 2011; Qin et al., 2012; Zoran, 2012). The robust satellite techniques (RST) approach has been widely implemented for environmental problems such as seismic anomaly detection, volcano monitoring, and oil spill events (Zhang and Meng, 2018; Eleftheriou et al., 2021; Filizzola et al., 2022; Genzano et al., 2015; Tramutoli et al., 2018). The RST approach was applied to define and discriminate possible pre-seismic TIR anomalies from other signal variations commonly related to known or unknown natural/observational factors that can be responsible for the" false alarms" proliferation (Wang et al., 2015). Wavelet analysis, which has the features of multi-resolution analysis in space-time, is one of the most popular methods for detecting seismic anomalies. With the rapid development of artificial intelligence, machine learning methods such as artificial neural network (ANN), particle swarm optimization (PSO), support vector machine (SVM), and adaptive network based fuzzy inference system (ANFIS) are being increasingly used for detection of TIR anomalies that is possibly related to earthquakes. Overall, the machine learning method is a strong tool for both earthquake prediction and precursor detection. However, there is a lack of evaluation criteria for seismic thermal anomaly extraction methods based on the extensive practice of numerous extraction methods.

In this study, we constructed a set of thermal anomaly extraction evaluation systems to compare different methods to extract thermal anomalies that may be associated with earthquakes, All the developed systems can be classified as coarse-graining problems. Section 2 introduced the data and the method used in this study. Then, Section 3 presents the results. Finally, we present the discussion and conclusions from the study in Sections 4 and Sections 5, respectively.

2 Materials and methods

2.1 Study area

The demonstration area (Figure 1B) is located at the junction of the Qinghai, Gansu, Sichuan, and Yunnan provinces. The area is delimited by 27°–37°N,97°-107°E, at the southeastern margin of the Qinghai–Tibetan plateau (Figure 1A). A series of faults are located in the region, among which the most prominent is the sinistral Xianshuihe–Anninghe–Zemuhe–Xiaojiang fault system (Yuan, 2008). The majority of faults in the study area trend northwest, north-south, and northeast. A number of strong earthquakes (Figure 1C) have occurred in the past, including the 12 May 2008 Ms 8.0 Wenchuan earthquake, the 3 August 2014 Ms 6.6 Ludian earthquake, and the 1 June 2022 Ms 6.1 Lushan earthquake (Chen et al., 2016, 5; Wang and Shen, 2020). The local deformation rates in the region of the sinistral shear across the southeast section of the Xianshuihe fault were about 9–10 mm/yr. Across the Anninghe and Zemuhe sections of the fault system deformation rate was approximatively 10 mm/yr (Wang et al., 2015).

2.2 Data and preprocess

2.2.1 Earthquake catalog and decluster

The earthquakes in our study extended geographically between 27° and 37°N and 97° to 107°E, and temporally between 2010 and 2020. The initial data we used were downloaded from the China Earthquake Networks Center (http://data.earthquake.cn). Usually, seismic studies use the magnitude-frequency distribution (MFD) to estimate earthquake rates and b-values according to the Gutenberg-Richter law (Gutenberg and Richter, 1949). Therefore, we performed a fundamental analysis of the above data, which should be identified using the "declustering process" for foreshocks, aftershocks, and seismic swarms.

Reasenberg's algorithm determines mainshocks and aftershocks by constructing the time-space domain of the seismic sequence. The algorithm assumes an interaction zone centered on each earthquake, which is dynamically modeled with spatial (R_{fact}) and temporal (τ_{max}) parameters (Reasenberg, 1985, 1969–1982). Given t>0, the probability of observing n earthquakes in the time interval [t, t+C] is given by Eq. 1 (Talbi et al., 2013)

$$P(\xi[t,t+\tau]) = n = \frac{e^{-\lambda(t)\tau}[\lambda(t)\tau]^n}{n!} \quad (1)$$

$$\lambda(t) \text{ follows the Omoril law: } \lambda(t) = k(t+c)^{-p} \quad (2)$$

Where R_{fact} is proportional to the source dimension, τ_{max} is determined using a heterogeneous Poisson process for aftershocks, and ξ is the process that counts the number of aftershocks occurring in the time interval [t, t+τ]. where k, c, and p are positive constants representing the Omori law parameters.

2.2.2 Satellite data and pretreatment

We used the datasets required for investigation from the GEE, including the Moderate Resolution Imaging Spectroradiometer (MODIS), land surface temperature (LST and National Centers for Environmental Prediction (NCEP) Climate Forecast System Version 2 (CFSv2)) (Saha et al., 2011). Since there were missing values and cloud masks in the MODIS LST data, We used the CFSv2 coupled with temporal Fourier analysis (TFA) (Shiff et al., 2021). We obtained a continuous data set for our study to extract thermal infrared anomalies (TIR), which we called conLST on the GEE platform. Therefore, the daily nighttime conLST data for 2010–2020 used for our research were derived with 1 km spatial resolution.

The spatial resolution of the data determines the speed of the calculations and result is an issues that must be considered. Therefore, in our study, we downscaled the spatial resolution from the initial spatial resolution of the ConLST data 1–50 km, according to a study of the effects of data at different spatial scales in seismic thermal anomalies by (Zhan et al., 2022).

2.3 Methods

We introduced coarse-graining into the TIR anomaly study to express the research process, was initially similar to adjusting the objective working distance in observing cells with a microscope. In this paper, we proposed a group of relative concepts, including coarse thermal infrared anomaly (CTIR) and refined thermal anomaly infrared (RTIR), which aimed to distinguish between anomalies obtained by anomaly detection techniques on time-series satellite data and thermal anomalies that may be linked to earthquakes. The method section includes (CTIR) extraction, RTIR detection, and evaluative criteria, looking at the advantages and disadvantages of the different methods.

2.3.1 CTIR detection methods

Six anomaly detection methods were selected, including robust satellite techniques and interquartile range in statistical methods, wavelet transform in signal analysis, Kalman filter in filtering techniques, isolated forest in machine learning, and autoencoder in deep learning. Some of these have been widely used for seismic thermal anomaly extraction, while others are better methods for anomaly extraction techniques. In Table 1, the thresholds for various methods to determine CTIR and the choice of foundation are shown.

2.3.1.1 Robust satellite techniques (RST)

The RST method was proposed by Tramutoli et al., 2013, and is based on satellite data rather than requiring ancillary data. Therefore, they can be entirely automated for operational real-time monitoring purposes (Eleftheriou et al., 2016). This method is based on multi-temporal analysis of a historical dataset of satellite observations acquired under similar observational conditions (Panda et al., 2007).

Because the RST was applied to thermal monitoring of earthquake-prone areas, TIR fluctuations were identified using the robust estimator of TIR anomalies (RETIRA). With different data sources and application environments, the index was eventually used as an absolutely local index of change in the environment (ALICE), which was computed as follows:

$$\otimes_{\Delta T}(x,y,t) = \frac{\Delta T(x,y,t) - \mu_{\triangle T}(x,y)}{\sigma_{\triangle T}(x,y)} \tag{3}$$

Where x,y represent the coordinates of the center of the ground resolution unit; and t is the time of the image, $t \in \tau$, where t defines the homogeneous domain of multi-annual satellite images acquired at the same time of day and the same period of the year (month). $\Delta T(x,y,t) = T(x,y,t) - T(t)$ is the difference between the on-time value of the TIR brightness temperature T (x,y,t) measured at locations x, y, at acquisition time t, and its spatially calculated average value T(t) over the study area. $\mu_{\triangle T}(x,y)$ is the time average ($t \in \tau$) of ΔT (x,y,t) calculated on the cloud-free records of the selected dataset for locations x, y. $\sigma_{\triangle T}(x,y)$ is the standard deviation value of ΔT (x,y,t) for image positions x, y ($t \in \tau$).

2.3.1.2 Interquartile range (IQR)

Interquartile range (IQR) is a well-known method for anomaly detection, In descriptive statistics that represents a set of data arranged in order. Regarding seismic anomaly extraction, some researchers used the upper quartile and lower quartile to distinguish seismic anomalies from data (Liu et al., 2004; Akhoondzadeh, 2013). This method can be calculated using the following equations:

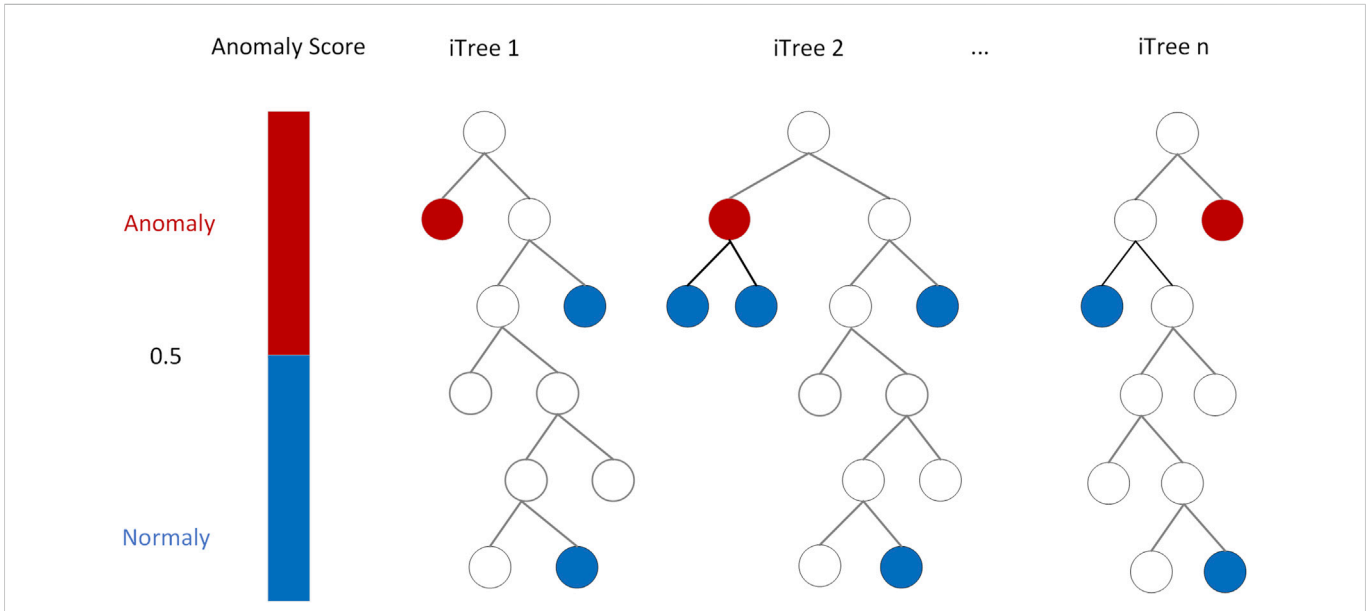

FIGURE 2
Graph example illustrating n trees of an isolate forest. It consists of two steps: step 1. isolation operations of data points using randomly constructed binary search tree; step 2. binary tree with the isolated point. The average path in red is the shortest, the earliest to be distinguished and is probably the outlier point.

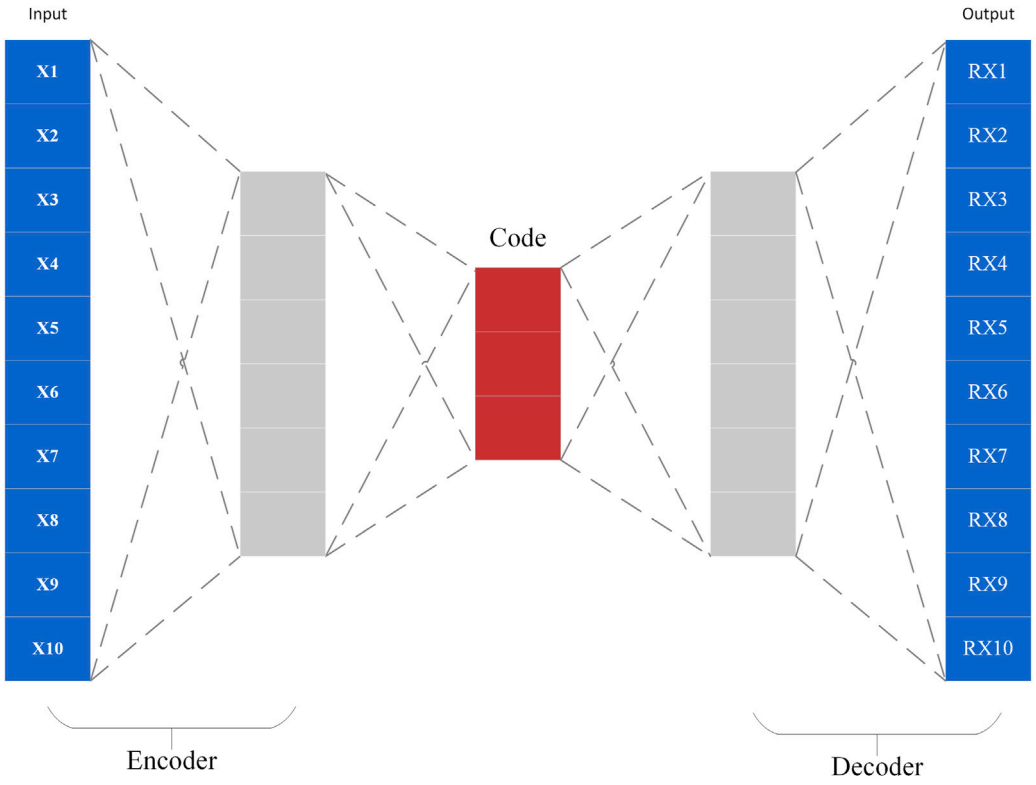

FIGURE 3
Graph example illustrating the encoder–decoder architecture of auto-encoder. First the input passes through the encoder, which is a fully-connected ANN, to produce the code. The decoder, which has the similar ANN structure, then produces the output only using the code. Final calculation of the original and reconstructed image as anomalies.

$$x_{upper} = M + \theta \times IQR \tag{4}$$

$$x_{lower} = M - \theta \times IQR \tag{5}$$

$$x_{lower} < x < x_{upper} \tag{6}$$

x, x_{upper}, x_{lower}, M, IQR and θ are parameters, higher bound, lower bound, median value, interquartile range and threshold for exceptions, respectively. The data parameters for the θ values are in Table 1.

2.3.1.3 Wavelet transformation (WT)

The wavelet transform is a representation of the function time domain (spatial domain) and frequency (Gao et al., 2020). This was used as a data-mining tool to detect seismic anomalies with satellite data. Xiong et al. (2009) assessed several wavelet methods and selected two real continuous Daubechies Wavelets and Gaussian Derivative Wavelets (Xiong et al., 2009). In this study, we used the following to calculate conLST times series of earthquakes anomalies with respect to the temporal background field. Due to the variability of our data, the Daubechies 8D wavelet was applied to identify anomalies in the data. The low-frequency seasonal components and high-frequency noise were eliminated using the wavelet transform components.

$$WT(a,b) = f(t)\varphi(t) = \frac{1}{\sqrt{a}} \int_{-\infty}^{+\infty} f(t)\varphi\left(\frac{t-b}{a}\right)dt \tag{7}$$

Where, the a is the scaling factor, b is the location parameter, f is the complex conjugate of continuous wavelet function and f (t) is the time series under analysis.

2.3.1.4 Kalman filter (KF)

The Kalman filter is a recursive solution to optimize the described systems in the state space. This is a collection of mathematics equations to optimize prediction equations using an estimation of state variables and minimization of error covariance (Saradjian and Akhoondzadeh, 2011). Multiple iterations of this calculation may obtain the best estimate. Assuming the state equation of the dispersive Kalman filter is as follows

$$x_{k+1} = \phi_{k+1} x_k + F_k \mu_k \tag{8}$$

$$Y_k = H_k X_k + v_k \tag{9}$$

Where X_{k+1} is the state vector, Φ_{k+1} is the transfer matrix, F_K is the system driver matrix, Y_k is the observation vector, H_k is the observed coefficient vector, v_k is the noise of observation, and μ_k is the noise-of-state sequence, the mean value of which is 0

2.3.1.5 Isolation forest (IF)

Isolation Forest proposed different types of model-based method that explicitly isolates anomalies rather than profiling normal instances. It has been widely used for anomaly extraction by (Liu et al., 2008). The method builds an ensemble of iTrees for a given dataset; anomalies are the instances with short average path lengths on the iTrees. Figure 2 provides a graph illustrating an example of the structure of n trees in the Isolation Forest.

In the article, isolation forests were used to extract CTIR, although they were seldom applied in earthquake precursor studies. The first

TABLE 2 The rules include rules for heating core model and rules for determining whether it is related to earthquakes.

Types	Conditions	Equation	Notes
Heat core rules	Temporal persistence rule	$\exists\beta \in R,\ CTIR_{i,\alpha} \cap CTIR_{i+1,\beta} \neq \varnothing$	TIR anomalies should last for at least 2 days in the same area
	Spatial coverage	$area_{min} \le AREA(CTIR_{i,\alpha}) \le area_{max}$	AREA (CTR_i) is the area of $DTR_{i,\alpha}$
	Spatial persistence	$AREA(CTIR_{i,\alpha} \cap CTIR_{i+1,\beta}) \ge \mu^{*} Min\{AREA(CTIR_{i,\beta}), AREA(CTIR_{i+1,\beta})$	Min{A, B} is the minimum of the value A and B. μ a is the threshold factor (0, 1)
	Intensity persistence rule	$\begin{cases} CTIR_{i,\alpha} \cap CTIR_{i+1,\beta} = \triangle_{i+1,\beta}^{i,\alpha} \neq \varnothing \\ AREA(CTIR_{i,\alpha}) > AREA(CTIR_{i+1,\beta}) \\ \sum_{(x,y)\in\triangle} i+1, \beta^{i,\alpha}\{conLST(x,y,i) - \theta\} \le \\ \sum_{(x,y)\in\triangle} i+1, \beta^{i,\alpha}\{conLST(x,y,i+1) - \theta\} \end{cases}$ OR $\begin{cases} CTIR_{i,\alpha} \cap CTIR_{i+1,\beta} = \triangle_{i+1,\beta}^{i,\alpha} \neq \varnothing \\ AREA(CTIR_{i,\alpha}) \le AREA(CTIR_{i+1,\beta}) \\ \sum_{(x,y)\in\triangle} i+1, \beta^{i,\alpha}\{conLST(x,y,i) - \theta\} \le \\ \sum_{(x,y)\in\triangle} i+1, \beta^{i,\alpha}\{conLST(x,y,i+1) - \theta\} \end{cases}$	As the stress increases or decreases, the thermal anomaly strength of the heated core and the range of thermal anomaly effects should also increase or decrease In this section, we introduce the iou factor to calculations $\frac{Area(CTIR_{i,\alpha} \cap CTIR_{i+1,\beta})}{Area(CTIR_{i,\alpha} \cup CTIR_{i+1,\beta})} > iou$
The correspondence rules	Temporal rule	$t - T\_last(RTIR_n) \le T$	
	Distance rule	$D_{Euclidean}(P,Q) = max(\lvert P_i - Q_i \rvert)$	We used Euclidean distance in this part
	Magnitude rule	m ≥ M	M is a magnitude threshold

(training) stage builds isolation trees using subsamples of the training set. The second (testing) stage passes the test instances through isolation trees to obtain an anomaly score for each instance.

Given a sample set of m instances, isolation forests gives the average path length of unsuccessful searches in Binary Search Tree as (Liu et al., 2012):

$$c(m) = 2H(m-1) - \frac{2(m-1)}{m} \tag{10}$$

where n is the testing data size,m is the size of the sample set and H is the harmonic number, which can be estimated by H(i) =ln(i)+gamma, where gamma =.5772156649 is the Euler-Mascheroni constant.

Then, the anomaly scores s∈[0,1] of a test pixel x are defined as follows:

$$s(x,m) = 2^{-\frac{E(h(x))}{c(m)}} \tag{11}$$

Where E (h(x)) is the average value of h(x) from a collection of iTrees. It is interesting to note that for any given instance x:if s is close to 1 then x is very likely to be an anomaly.if s is smaller than .5 then x is likely to be a normal value.if for a given sample all instances are assigned an anomaly score of around .5, then it is safe to assume that the sample does not have any anomaly.

2.3.1.6 Autoencoder (AE)

Autoencoder is an unsupervised neural network that uses a neural network to generate a low-dimensional representation of a high-dimensional input. Autoencoder contains two main parts, encoder, and decoder (as shown in Figure 3). The encoder is used to discover a compressed representation of the given data, and the decoder is used to reconstruct the original input. During training, the decoder forces the autoencoder to select the most informative features, which are eventually saved in the compressed representation. The final compressed representation is in the middle coder layer. The difference between the original input vector x and the reconstructed vector z is called the reconstruction error $\|x - z\|$ (Hinton and Salakhutdinov, 2006). The autoencoder updates the weight of the network by minimizing the reconstruction error L (Bao et al., 2021):

$$h = \sigma(W_{xh}x + b_{xh}) \tag{12}$$

$$z = \sigma(W_{hx}h + b_{hx}) \tag{13}$$

$$\|x - z\| \tag{14}$$

The encoder in Eq. 12 maps the input vector x to the hidden representation h using a non-linear affine mapping. The decoder in Eq. 13 maps the hidden representation h back to the original input space as a reconstruction by the same transformation as the encoder. The difference between the original input vector x and the reconstructed z is known as the reconstruction error, as in Eq. 14.

2.3.2 RTIR detection methods

We obtained CTIR (i,α) from different methods, as shown in Section 2.3.1, to further obtain RTIR (i,α), the thermal anomaly possibly associated with the earthquake. In this section, we used the heating core proposed by (Zhang et al., 2021). To obtain RTIR (i,α). The model can remove noise that is unrelated to the seismic activity. We set the following limits: a series of time-space intensity (TSI) qualifications (Table 3), including the temporal persistence rule, spatial coverage rule, spatial persistence rule, and intensity persistence rule. All the CTIRs will be filtered with the above four rules, and the thermal infrared anomalies patches (CTIRs) are the remaining filtered results of CTIR (i,α), CTIR (i,α+1), and CTIR (i+1, β). CTIRs will be merged into TIR anomalies after the above rules are satisfied. The above extraction process depends on the parameters (θ, $Area_{min}$, $Area_{max}$, iou, T, D, M).

TABLE 3 Parameters to extract DTIRs and determine the correspondence between DTIRs and earthquakes.

Parameter	Value	Description
θ	The θ for the different methods is shown in Table 1	The upper threshold for identifying the anomalies
$area_{min}$	3,6,9 (50 km × 50 km)	The minimum area of TIR anomalies
$area_{max}$	20,30,40 (50 km × 50 km)	The minimum area of TIR anomalies
iou	0.1,0.2,0.3,0.4,0.5	Iou is a stricter factor iou (intersection over union) todetermine the threshold of spatial persistence rule
μ	0.6	A factor to help us determine the area of "heating core"
T	10,20,30,40,50,60 (day)	Duration of the anomaly
D	2,4,6,8,10 (50 km)	The Euclidean distance between the earthquake and the anomaly
M	3,3.5,4,4.5,5,5.5	M is the minimum threshold for a new seismic catalogue

Next, we set a series of rules to determine the correspondence between earthquakes and RTIR anomalies in Table 2, including the temporal, distance, and magnitude rules. In the distance rule, we used the Euclidean distance as the shortest distance between the EQ (x, y, t, m), which is an event occurring at (x, y) on day t with magnitude m. RTIRn is less than or equal to D. To set parameters that consider different geological, meteorological, and environmental backgrounds. A training-test-validate approach was used to determine the best parameters for extracting TIR anomalies associated with earthquakes. We can obtain the optimal set of parameters and perform outlier extraction using the above parameters.

2.3.3 3D error diagram

In this part, we used P1, P2, and loss parameters to evaluate the effectiveness of different methods in CTIR anomalies in training–test–validation sets. P1 is the *p*-value for the false negative rate (FNR)-based alarms and P2 is the *p*-value for the positive predictive value (PPV)-based alarms. The significance level is a range of estimates for an unknown parameter, the 95% confidence level is the most commonly used to set. Therefore, the confidence interval for both P1 and P2 was set to .05 in this study, and loss (Eq. 15) is the evaluation score given by the 3D error diagram (Zhang et al., 2023; Zhang et al., 2021).

$$Loss = \sqrt{w_1 * STCW^2 + w_2 * FNR^2 + w_3 * (1 - PPV)^2} \quad (15)$$

The w2 and w3 are weights measuring the relative costs of the *y* and *z*-axis. In this study, we set w1=*w*2 = *w*3 = 1. STCW is a space-time correlation window corrected by the Molchan diagram, weighted by the relative intensity (RI) index (Zechar and Jordan, 2008).

$$FNR = FN/(TP2 + FN) \quad (16)$$

TP2 is the total number of earthquakes that correspond to RTIRs, FN is the total number of earthquakes that do not correspond to RTIRs.

$$PPV = TP1/(TP1 + FP) \quad (17)$$

$$FDR = 1 - PPV \quad (18)$$

TP1 is the total number of RTIRs that correspond to earthquakes, FP is the total number of RTIRs that do not correspond to earthquakes.

We used the training–testing–validating step to evaluate the best parameters from the 56,700 different vectors (Table 3). This can avoid mistaking normal seasonal warming for TIR anomalies to some extent. In the test step, the RTIRs data and earthquake catalog data from 2010.01.01 to 2012.12.13 will be used as the training dataset. At the same time, we performed the model on the validation set, which contains RTIRs data and earthquake catalog data from 2013.01.01 to 2016.12.31 in the test step and the data from 2017.01.01 to 2020.12.31 as the test dataset, called the validation step. The values of P1,P2, Loss are given in the above steps.

We obtained the values of P1 and P2 for each group of parameters. We determined a threshold of .05 for P1 and P2 based on the method of confidence levels in statistics. The values of P1 and P2 have divided the given alerts into four classes based on the results in the training-test-validation step: Type I: P1≤.05 and P2≤.05, Type II: P1>.05 and P2≤.05, Type III: P1≤.05 and P2>.05, and Type IV: P1 > .05 and P2>.05. Type I, II, and III alarms effectively predict earthquakes, although type II and III are not optimal. Type IV alarms are not effective at predicting earthquakes.

3 Results

3.1 Declustering result

The results of the original earthquake catalog and declustering data, analysis using R, are shown in Figure 4A, original; b, declustering). According to the earthquake catalog description, there were 1,140 seismic events in the region, and 899 events remained in the catalog after declustering, including seven with Ms>6. This produced a plot consisting of six subplots: Figures 4A, B show the spatial distribution of events, while Figures 4D–F, J–L plots show how the latitude (Figures 4D, J), longitude (Figures 4E, K) and magnitude of events change over time (Figures 4F, L), with two plots visually inspecting the completeness and time stationarity of the catalog. Figures 4C, I allows for cumulative magnitude to denote the number of events in the catalog with a magnitude greater than or equal to m (we selected m=3 in the article). The plot (Figures 4B, H) of log10(Nm) *versus* m shows the linear relation expected from the Gutenberg-Richter law. The plot of Nt *versus* t is linear during the considered study period. Despite this, a non-linear trend is evident over the time span 2010–01-01–2021-01-01 (4,018 days), probably due to the Mw=6.7 20 April 2013 Lushan earthquake occurrance. The Gutenberg–Richter law states that log10(Nm) = a—bm for some a and b, which is equivalent to assuming that m follows an exponential distribution (Roeloffs, 1988; Pulinets 2006).

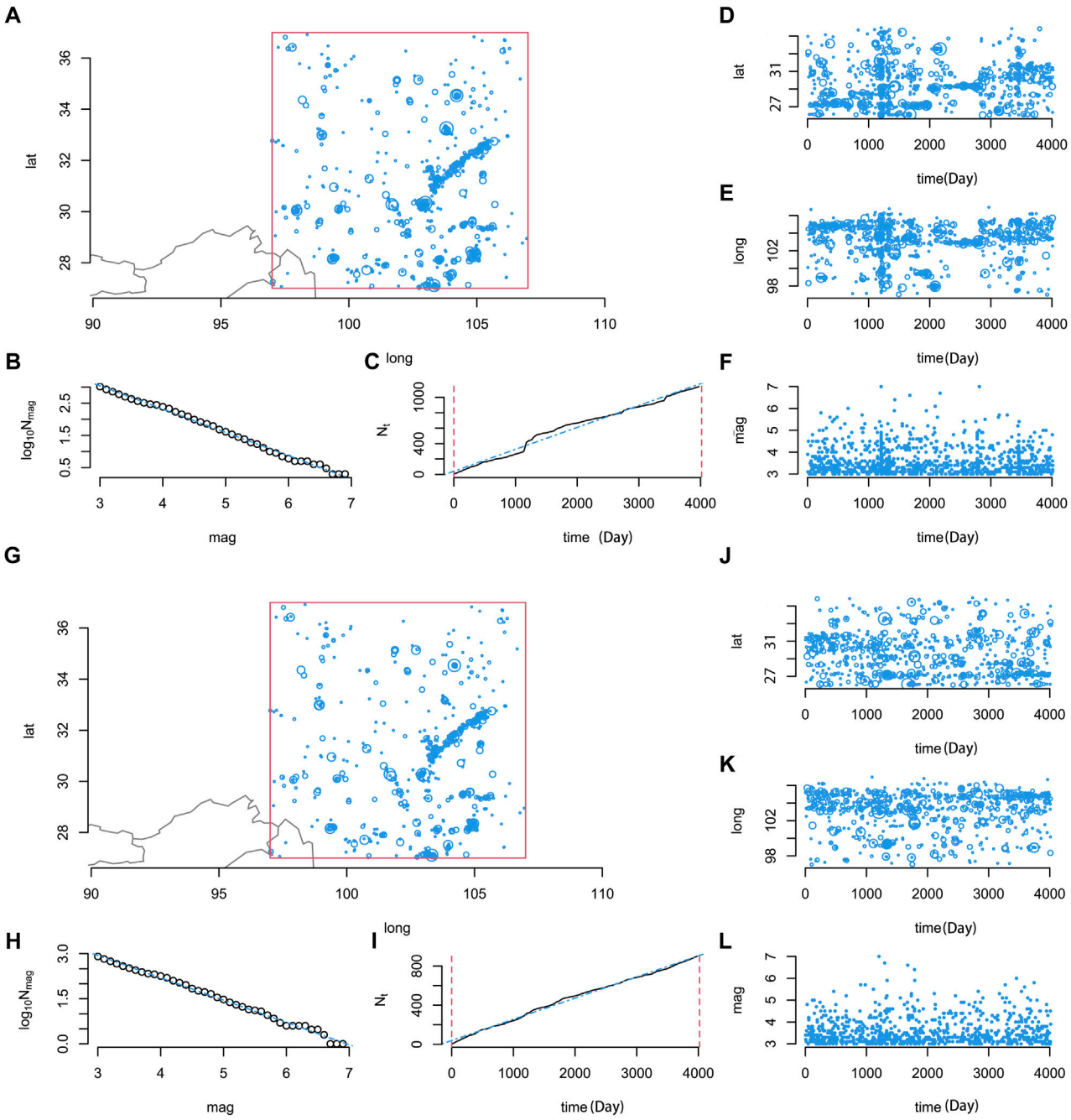

FIGURE 4
(A) is the original seismic catalog, **(B)** is the de-clustering seismic catalog. Location of epicenters **(A, G)**, logarithm of frequency by magnitude **(B, H)**, cumulative frequency over time **(C, I)** and latitude, longitude and magnitude against time **(D–F)**, **(J–L)** of 1140 earthquakes with magnitude greater than or equal to 3 occurred between 2010-01-01 and 2021-01-01 in Sichuan and its vicinity (27°–37°N and 97°–107°E), extracted from the China Earthquake Networks Center (http://data.earthquake.cn). The plots are created by R.

3.2 Result for the type of alarms

We used six different methods to extract CTIRs in Section 2.3.1 without filtering by the rules (Table 2) that effectively predict earthquakes. First, we used alarm types to evaluate the advantages and disadvantages of the different methods, which was carried out by calculating the alarm types generated by 56,700 sets of parameters during the training–test–validation process.

In the training steps, we focused on the number of type alarms generated in the 56,700 parameters set. The number of alerts of each type was calculated as a ratio of the total alert data volume. The results indicate that (Figure 5A) the autoencoder and isolation forest methods produced more type-I alarms than the other methods, and the Kalman filter method was the worst performer. Among the type I alarms, the significant percentages were AE and IF, accounting for 58.49% and 16.37% of the total. Although type II and type III alarms are unlike type I alarms, which are effective for predicting

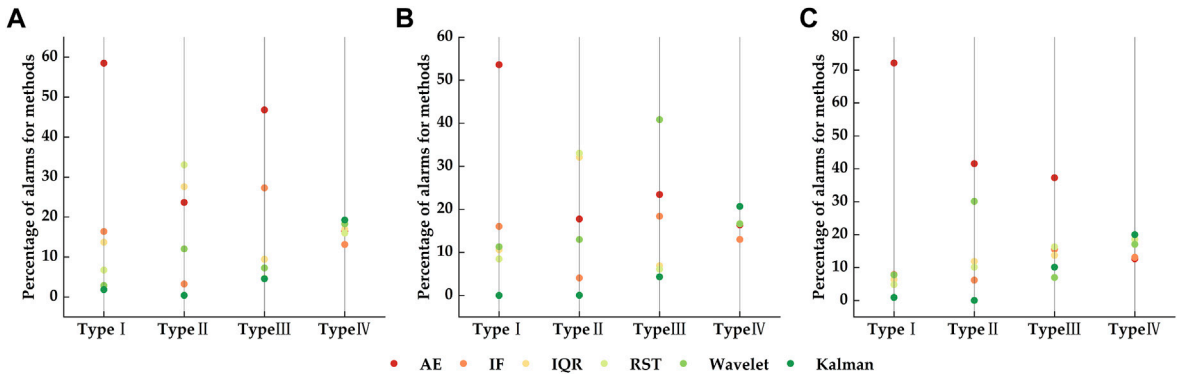

FIGURE 5
The result of type alarms. **(A–C)** represent the ratio of each type of alert generated by different methods to the overall training **(A)**, test **(B)** and validation **(C)** steps. **(A–C)** display relatively consistent features; warm and cold color scatter represent the proportion of alerts of that type generated by the method, with warm colors representing the proportion and cold colors the opposite.

earthquakes from the FNR and PPV perspective, they are still counted and analyzed. Therefore, other alert types were given in proportion to the ones generated by the above methods (Figure 5A). Below we showed the number of alerts with type Ⅰ: AE>IF> IQR>RST>KF>WT.

To test the effect of the 56,700 sets of parameters obtained in the training step, we filtered the above parameters in CTIRs and earthquake catalogs from 2013 to 2016 with the heat core. The plots (Figure 5B) were also presented below regarding the type of alert. In test step results, the AE and IF methods, which generated the most alerts, remained optimal. Among the type Ⅰ alarms, the significant percentages were AE and IF, accounting for 53.6% and 16.02% of the total. Below, we give the number of alerts for the type Ⅰ method from major to minor: AE>IF>WT>IQR>RST>KF.

We obtained the alert types corresponding to 56,700 sets of parameters through a training–test steps, which led us to explore the strength of each method. However, in the paper, we should add validation step to explore the impact of the method. In terms of the type Ⅰ alarm, the proportion of the number of alarms for AE are 72.14%. Below, we provide the number of alerts for the type Ⅰ method from greater to lesser: AE>IF> WT> IQR>RST>KF (Figure 5C). Overall, the AE and IF methods generated more data for type Ⅰ alerts in the training–test–validation steps. In the following, we will further determine the parameters of each method corresponding to type Ⅰ alarms and obtain the optimal parameters for each method.

3.3 Result of optimal parameters

Each parameter produces P1 and P2 values at each step, so three P1 and P2 values should be available for each parameter. In Section 3.2, we obtained the parameters of type Ⅰ alarms (P1≤.05,P2≤.05) in each method's training–test–validation steps. To further evaluate the various methods for refining the extraction of infrared thermal (RTIR) anomalies, the optimal parameters of each method were searched. ($train_{p1} \cap train_{p2}$) are parameters of type Ⅰ alarms in the training step; ($test_{p1} \cap test_{p2}$) are parameters of type Ⅰ alarms in the test step; ($validation_{p1} \cap validation_{p2}$) are parameters of type Ⅰ alarms in the validation step. We classified type Ⅰ alerts (P1≤.05,P2≤.05) parameter sets into three categories according to the values of P1, P2, and loss in the training–test–validation stages D1 (D1 = ($train_{p1} \cap train_{p2}$) ∩ ($test_{p1} \cap test_{p2}$) ∩ ($validation_{p1} \cap validation_{p2}$) ≠∅) represents parameters that passed the significance tests of FNR and FDR in the training–test–validation steps D2 (D2 = ($train_{p1} \cap train_{p2}$) ∩ ($test_{p1} \cap test_{p2}$) ≠∅) and D3 (D3 = ($train_{p1} \cap train_{p2}$) ∩ ($test_{p1} \cap test_{p2}$) = ∅) represent the parameter set intersection in the training-test, respectively, while no parameters produced intersection in the three steps.

In order to distinguish between the three types and visualisation, we labeled the corresponding D1,D2, D3 with the red, yellow and blue signs presented in Figure 6. Loss is the weighted sum of FDR, FNR and STCW, the lower the Loss is the better the alarms are. Only Loss values that pass the P1 and P2 tests are significant, D1 corresponds to three steps of Loss values ($Loss_{train}$, $Loss_{test}$, $Loss_{validation}$), D2 has two Loss values ($Loss_{train}$, $Loss_{test}$) and D3 has one Loss value ($Loss_{train}$). Obviously, the corresponding Loss values are generated in the training-test-valiadtion phase. The $Loss_m$ is the mean value of the above three session loss value. Finding the optimal set (θ, $Area_{min}$, $Area_{max}$, iou, T, D, M) of parameters is determined by the alert types and Loss values we have described above. Only the parameters of AE and IF methods resulted in D1, where it passed significance in the training–test–validation steps for both P1, P2. In terms of the autoencoder (Figure 6A), the symbol marked in red is the result with the lowest $Loss_m$=.754. The best parameter set of D1 (θ=.015, $Area_{max}$=30, $Area_{min}$=9, iou=.2, T=10, D=10, M=3) was tested in test and validation steps. The result of the next steps (in test step: PPV = 72.4%, FNR = 44.4%, STCW =45.1%, P1= $9*10^{-9}$ and P2 = $2*10^{-9}$, in validation step: PPV = 67.6%, FNR = 50.9%, STCW =45.1%, P1= .00602, and P2 = .00115) indicates that these alarms are type I alarms. The lowest $Loss_m$ (.703) is presented in Figure 6B, with a red point showing the isolation forest. The optimal parameters for D1 consist of (θ=.6, $Area_{max}$=20, $Area_{min}$=9, iou=.2, T=10, D=40, M=4.5). The result can be described by these parameters (in test step: PPV = 47.8%, FNR = 42.1%, STCW = 31.1%, P1= .0119 and P2 = .0114, in validation step: PPV = 42.5%, FNR = 44.1%, STCW = 37.8%, P1= .000898, and P2 = .016).

The yellow sign in Figures 6C–E means that they are the best parameters of type D2 for the IQR, WT and RST methods. They indicate that P1 and P2 passed the significance test in the training–test steps (P1≤.05,P2≤.05), which are the relative optimal parameters in the method. For IQR methods, the best parameter is θg = (θ=2,

10.3389/feart.2023.1101165

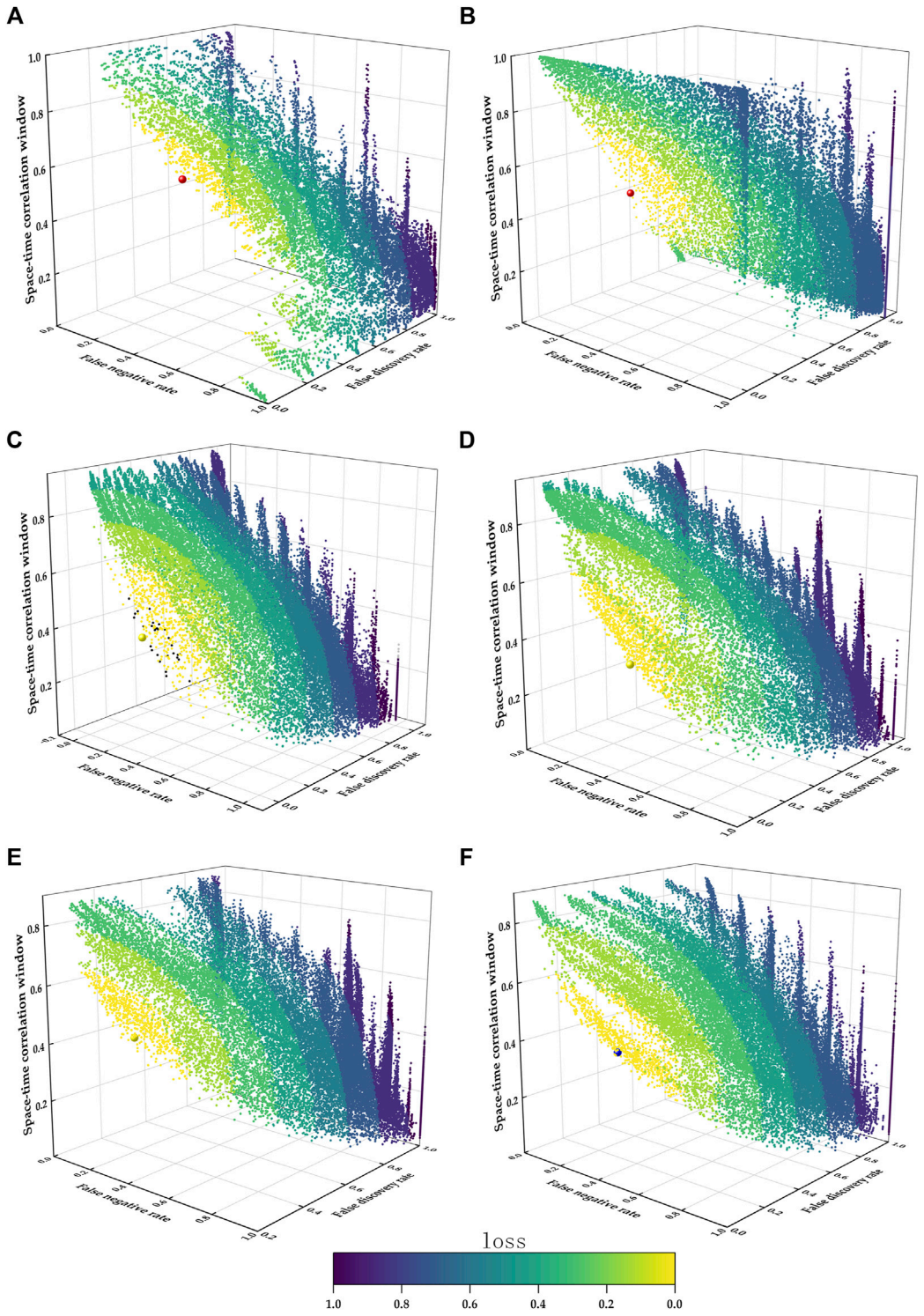

FIGURE 6
The result of the best parameters for methods. **(A–F)** represent the optimal parameters of each method to the overall training step [**(A)**: AE, **(B)** IF, **(C)** IQR, **(D)** WT, **(E)** RST, **(F)** Kalman]. The *x*-axis and *y*-axis of the diagram are the fraction of space-time occupied by alarms and the FNR, respectively, and the *z*-axis is the FDR (FDR= 1-PPV). The symbol marked by red, yellow, and blue are the parameter sets with the lowest $Loss_m$.

$Area_{max}$=40, $Area_{min}$=3, iou=.3, T=10, D=10, M=3) with the lowest $Loss_m$= .842 ((in test step: PPV = 64.6%, FNR = 7.59%, STCW = 76.7%, P1= .0282 and P2 = .000173). The optimal parameters of the two remaining methods can be described as follows: WT = (θ=4.5, $Area_{max}$=30, $Area_{min}$=6, iou=.3, T=10, D=10, M=3) with the lowest $Loss_m$= .677 (in test step: PPV = 61.3%, FNR = 45.4%, STCW =73.8%, P1=.001671 and P2 =.003098); RST= (θ=2, $Area_{max}$=20, $Area_{min}$=3, iou=.4, T=10, D=10, M=3) the lowest $Loss_m$= .809 (in test step: PPV = 67.3%, FNR = 15.9%, STCW = 70.4%, P1= .0181 and P2 = .00000622). In the validation step, the alert types for the different methods are type

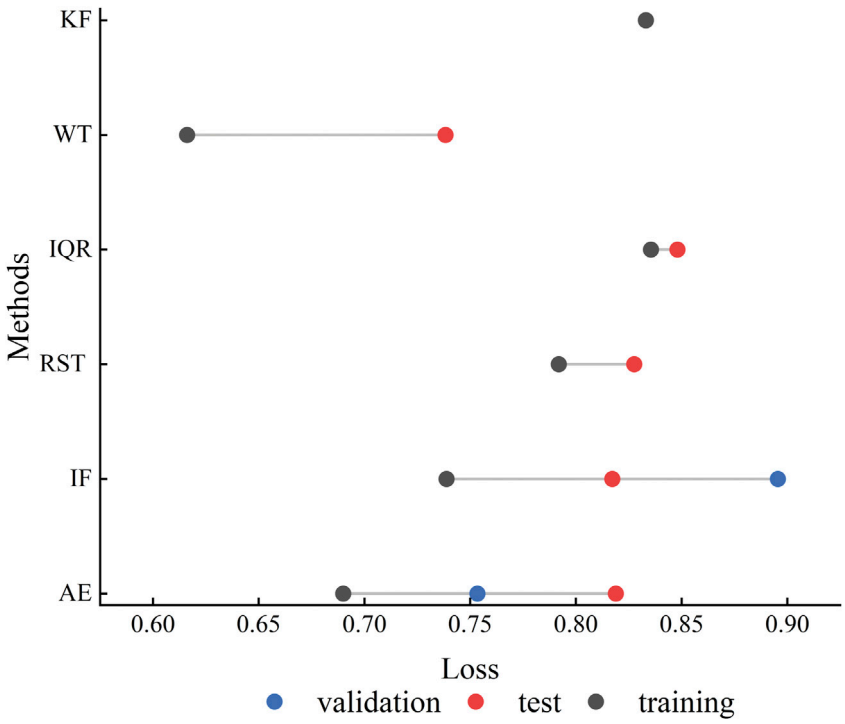

FIGURE 7
The result of the Loss values for six methods. (AE,IF,RST,IQR,WT,KF). The *x*-axis is the Loss value and the *y*-axis represents the different methods. Three colors correspond to the training-test-validation steps (red is the training phase, blue is the test phase and black is the validation phase).

TABLE 4 The optimal parameters for each method.

Methods	θ	$area_{max}$	$area_{min}$	Iou	D	T	M
AE	.015	30	9	0.2	10	10	3
IF	0.6	20	9	0.2	10	40	4.5
IQR	2	40	3	0.3	10	10	3
WT	4.5	30	6	0.3	10	10	3
RST	2	20	3	0.4	10	10	3
Kalme	2	20	3	0.4	10	20	5

II(IQR: P1=.999, P2=.000258,WT: P1=.012, P2=.00014, RST: P1=.99, P1=.0000429), which are effective for predicting earthquakes from the view of FNR. People can effectively avoid as many false alarms as possible if they reducing risk according to these alarms.

The optimal parameter of type D3 is indicated by the blue symbol (Figure 6F) for the Kalman filter method with the lowest $Loss_m$= .833. The best method is θg = (θ=2, $Area_{max}$=20, $Area_{min}$=3, iou=.4, T=10, D=20, M=5, in the training step: PPV = 29.5%, FNR = 42.9%, STCW = 83.3%, P1= .01048 and P2 = .00254). The alert types in the test step are type IV(P1=.842, P2=.879). In the validation step, The alert types are type III(P1=.00365, P2=.0998).

The alarm type is our main concern for the above results and indicates the best parameter for each step. Therefore, we have plotted Figure 7 to indicate the loss values at each stage for the different methods. As shown in Figure 7, the optimal parameters fall into the D1 of AE and IF methods which means that the optimal parameters pass both the P1 and P2 significance tests in the training-test-validation step. The other three methods are optimal parameters for the D2 class including RST, IQR and WT. These approaches best parameters produce intersection sets in the training-testing phase. Only the optimal parameters of the KF is in the training phase. We obtained the optimal set of parameters for the minimum $Loss_m$. They can be found in Table 4 for each method. It can be observed that the M and D parameters of the optimal parameters are relatively uniform across the six methods. RTIR anomalies are generated from the above parameters as the basic parameters for subsequent analysis results. Results of TIR anomalies.

3.4 Results of TIR anomalies

In Section 3.3, we obtained the optimal parameters for each method to extract TIR anomalies correlated with a statistically significance to the seismic activity. We extracted RTIR anomalies using the above parameters based on the heating core rule in our other work. To better compare the results generated by the different steps of the workflow, we have named the TIR exceptions corresponding to the steps CTIR anomlies, RTIR anomlies. The 'heating core' rules are effective in eliminating these TIR-anomalous signals, which are unlikely to be associated with earthquakes. We compared the number of anomalies for each method between unfiltered suspected TIR anomalous signals and filtered suspected TIR anomalous signals. Coarse-graining will be further discussed in this section.

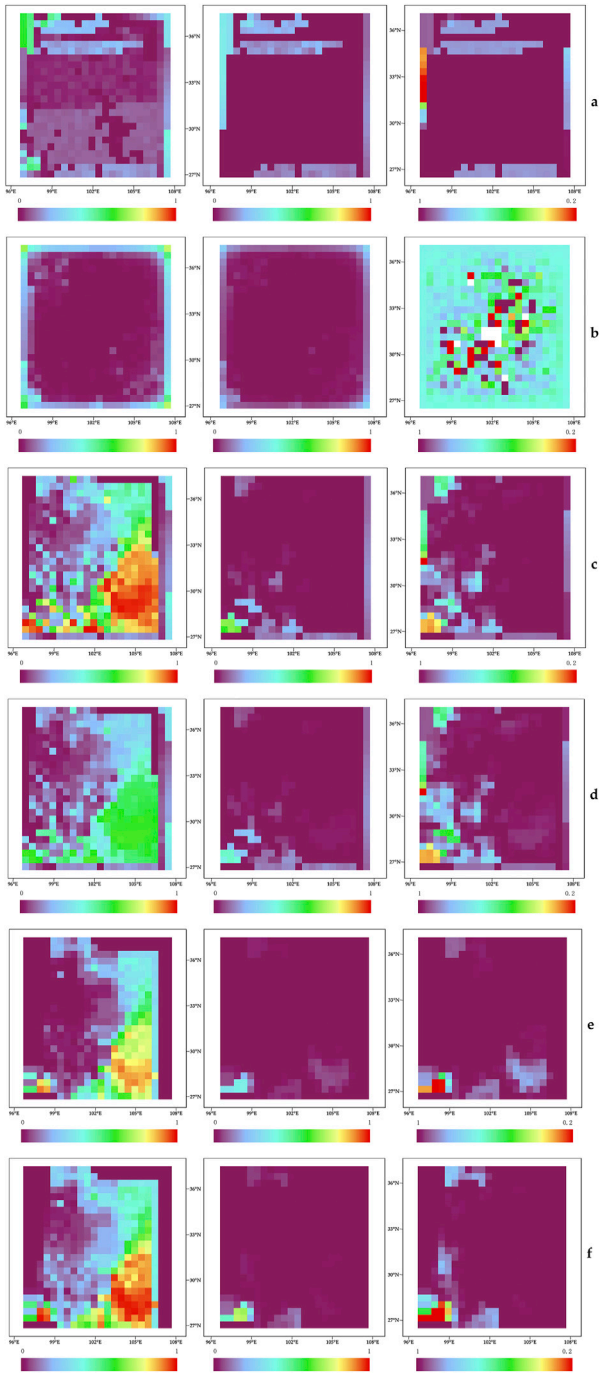

FIGURE 8
The result of frequency of the RIT and CTIR anomalies generated by each method in 2010–2020 [**(A)**: AE, **(B)** IF, **(C)** IQR, **(D)** RST:, **(E)** WT, **(F)** Kalman], The *x*-axis represents the longitude; the *y*-axis represents the latitude. Subplot-left is the frequency of RIR Signal of the whole area, while Subplot-center is the frequency of CTIR Signal. Subplot-right is the ratio of the frequency of removed TIR anomalous signals from RTIR to the frequency of CTIR results (ratio = $(TIR_{RTIR}\text{-}TIR_{CTIR})/TIR_{RTIR}$).

To study the filtering effect of the non-seismic anomalies of the heated kernel model on different methods, we showed the number of day with thermal anomalies for RTIR and CTIR, representing anomalies with filtering before and after. The average CTIR anomalous signal number of the day, derived using the AE method, is 2731, while the average RTIR abnormal signatures number of the day, derived using the AE method, is 1021. The abnormal days of CTIR anomalous signatures for the IF method are 1125, compared to 2961 for the RTIR anomalous signals. The RST and IQR methods indicate that the number of abnormal days in the RTIR session is 3677 and 2524, while in CTIR, the results are strongly filtered, and the number is 1523 and 1040. The 3002 days generated RTIR anomalies that consisted of many non-seismic anomalous factors, extracted under the WT method; meanwhile, 1,168 days of anomalies were identified as CTIR unusual signatures. Only 225 days presented the RTIR anomaly, which is apparently less relative to the 11-year time interval derived by the Kalman filter method based on the CTIR being 3967. As a result, we can see the heating core rules that we set for different ways, which can effectively filter non-seismic anomalous signals. The identification rules significantly reduce the number of TIR anomalies in the coarse-graining process (from RTIR to CTIR anomalies).

In the above, we discussed the number of anomalous days to describe the filtering effect of heating cores on different methods. We designed the process to study the coarse-grained seismic thermal anomaly, which sets a series of time, spatial, and intensity conditions based on the heating core model to obtain the CTIR anomalies from RTIR signals. In Figure 8, we show the spatial distribution of the proportion of RTIR and CTIR anomaly frequencies and the associated proportions generated by each method in 2010–2020. Figures 8A–E corresponds to each method, while each left, middle, and right subplot represents RTIR anomalous and CTIR signals, respectively, showing the ratio of the frequency of removed TIR anomalous signals to the frequency of RTIR anomalies. As shown in Figure 8 a-left, for the unfiltered results of AE method results, the frequency of the RTIR signal in the middle is much lower than that in the west, east, north, and south. In the CTIR step, Figure 8 a-middle shows that the signal frequency of the results were significantly lower throughout the study area, and the frequency was highest in the northwest corner, followed by the north and south, and lowest in the center. As shown in Figure 8A-left, 90% of RTIR signals were removed in the middle, while in the north and south, about 80% RTIR signals were removed. Similar descriptions are used to express the spatial distribution of TIR anomalies for different methods, including RTIR, CTIR, and proportion. The left and middle panels of Figure 8B show a similar spatial distribution, with high-frequency anomalies in the four corners and many banded anomalous frequencies in the middle using the IF method. The overall anomaly removal rate is 90%. The TIR anomalies extracted by RST and IQR show the same spatial distribution characteristics in Figures 8C, D. As the left panels show, the study area was covered by RTIR anomalies, where the highest frequency of anomalies occurred in the southeast corner. From the RTIR to CTIR steps, the TIR anomalies in the southwest corner were more reserved and showed banding under the RST method. This process still removes 70%–80% of the RTIR signal, even though 20%–30% of the anomalies are retained in the southwest. The RTIR anomalies extracted by the WT method are mainly distributed in the southeast, as shown in Figure 8. e-left. High-frequency anomalies appear in the southwest after filtering the anomalies in Figure 8E-middle. The filtration percentage is still between 10% and 20%, which means that most of the RTIR is removed with Figure 8E-left. The Kalman filter method contributes the highest anomaly frequency values, with high values distributed in the south-east in Figure 8F-left. The filtered result is similar to the previous method in Figure 8F-middle.

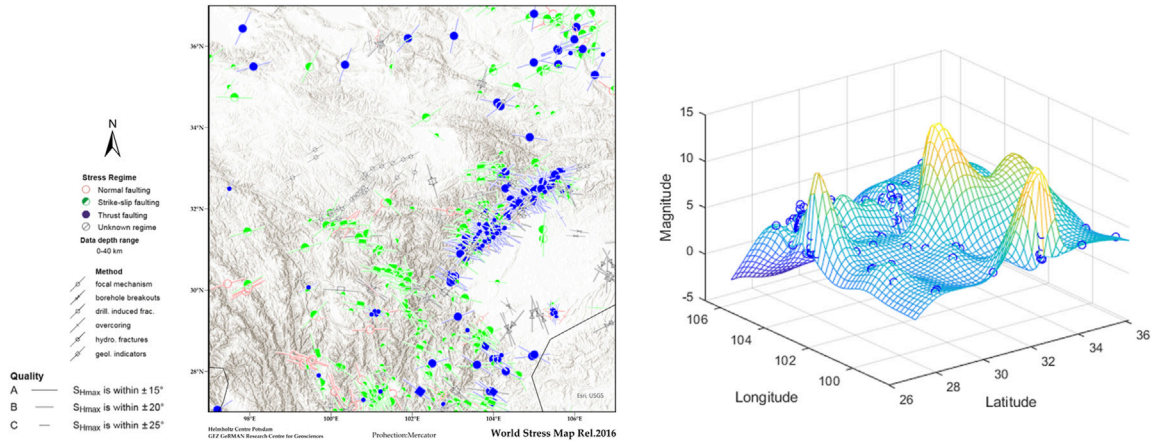

FIGURE 9
Left subplot is stress map of the study area (the data are provided by http://www.world-stress-map.org/); right subplot is 3D seismic belts–earthquake distribution map; there are three seismic belts, including the Western Yunnan belt, Western Yunnan belt, and Anning river belt.

3.5 Results of comparison among different methods

In Section 3.4, we analyzed the spatial anomaly frequency distribution of TIR anomalies using each method. There are anomalies in the southwest region, extracted by the different techniques in Figure 8. Meanwhile, the southwest region is the junction zone of plate tectonics between the India Plate and Gansu–Qinghai–Tibetan Plate, as shown in Figure 1. In the precursor study, Ishibashi et al. divided the LST anomalies into tectonic precursor types, which are a link in a chain of particular local tectonism in each individual area preceding the earthquake (Molchan, 1990). Therefore, we further determined the advantages of the above methods using the relationship between the above RTIR anomaly and active fracture zones, stress distribution and seismic belts. Several active fracture zones exist, such as the Xianshui River–Anning River faultline and the Longmenshan faultline. As shown in Figure 9-left, the stress distribution is similar to the fault belt.

The CTIR thermal anomalies extracted show no tectonic features using the AE method since the frequency anomalies distribution of the extracted multi-year did not correspond to stresses, seismic belts and fracture zones. Surprisingly, the CTIR anomaly frequency spatially corresponded to the Xianshui River–Anning River rift zone extracted by the IF method, but its frequency is lower in value between 300 and 400 days. For the first time, isolated forests were used for seismic thermal anomaly extraction, and the results suggest that this is a promising method. The spatial distribution of the RTIR anomaly frequencies extracted by RST and IQR is similar to those mentioned previously. When we consider the tectonic factors, we found that the RTIR anomaly frequency extracted by RST is consistent with the stress distribution characteristics near the fracture zone. RTIR anomalies are not correlated with stress, the active fault distribution extracted by the IQR method, even though the CTIR results are similar to those extracted by the RST method. The RTIR anomaly frequency distribution has a block shape, which is not relative to the constructive factors extracted using the WT method. The Kalman filter method produced lower quality results because no TIR anomaly was corresponding to the physical/geographical factors.

Finally, we attempted to present a comparative summary of each method based on the previous results. In the RTIR result, the Kalman filter method produced a higher frequency of TIR anomalies compared to other methods. This result is consistent with the study that showed that the Kalman filter method performed best, with the most extreme and erratic variations in the LST (Molchan, 1991). In the CTIR step, AE and IF showed the optimal parameters and the type of alert, while the poorly performing method was the Kalman filter. The IQR and RST methods are robust, as shown in both RTIR and CTIR results, including the RTIR results showing a high frequency of anomalies, and the optimal parameters in CTIR are the category II optimal parameters. Type III optimal parameters indicate a weak statistical correlation between anomalies and earthquakes under the heated core filtering rule. We introduced tectonic information to view the CTIR anomaly and determined the correlation between the anomalies and earthquakes. By integrating the relationship between the RTIR anomalous signal and the constructive factors, we found that RST maintains a relatively favorable anomaly frequency and spatial distribution. It is worth further examining the IF method because it produces RTIR anomalies that fit the space characteristics of the construct distribution. Therefore, we ranked the advantages of the following methods in different steps, according to the results:

CTIR: KF > RST > IQR > WT > AE > IF;
RTIR: AE > IF > RST > IQR > WT > KF;
Rank: RST > IF > IQR > WT > KF > AE.

4 Discussion

4.1 Choice of data input

The current LST products are limited, due to missing data due to pixels that are overcast by clouds. To solve this problem, we implemented NCEP and LST data to fill in the missing data based on the GEE platform. Therefore, we used conLST data derived from a Google Earth Engine with Temporal Fourier Analysis (TFA) as the

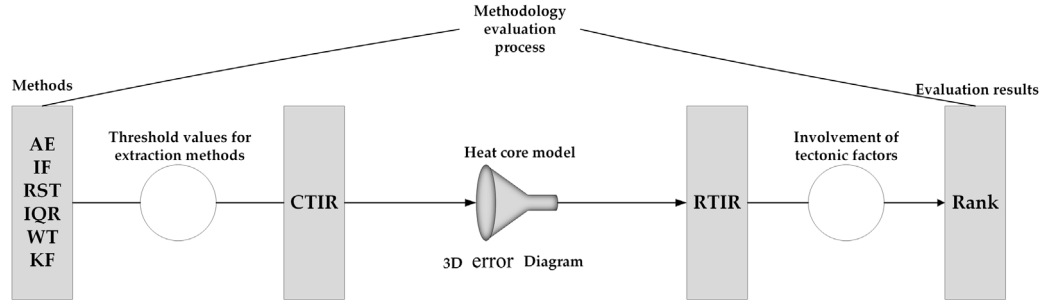

FIGURE 10
TIR anomaly method evaluation flow chart.

experimental data for anomaly extraction, which can generate daily, daytime and nighttime data. Regarding the temporal resolution, the daily nighttime data are used to exclude the conLST data covered by the cloud. To reduce the efforts of computational and anomaly continuity, we resampled the conLST data with 50 km spatial resolution. We declustered the seismic catalog using the Reasenberg method to separate earthquakes in the seismicity catalog into independent and dependent earthquakes.

4.2 Methods of TIR detection

There are several methods for extracting TIR precursors of earthquakes more than these six methods mentioned in our article. We summarize the current types of TIR precursor extraction methods using the meta-analysis literature methods, including mathematical/statistical methods, wavelet transforms, filtering methods, machine learning and deep learning. However, many classical methods and intelligent approaches are not used, for example autoregressive integrated moving average (ARIMA), artificial neural network (ANN), support vector machine (SVM) (Akhoondzadeh, 2013), Eddy field method and Z-score method. On the other hand, many methodological improvements were not considered and implemented, such as the wavelet transform, which can be improved in several ways. At the same time, there is no more in-depth study of machine learning and deep learning methods like CNN, LSTM and random forest.

The threshold effect continues throughout our research. We used a survey of the literature or the principles of anomaly extraction methods to determine the thresholds for each session. Thus, there are problems: the parameters may be absent or inherently incorrect, as obtained from the publications. The threshold θ is slightly different for each method in table 2-1. For example, AE and IF have no thresholds for reference as there is no literature on their application to seismic anomaly extraction. Therefore we can only define the threshold based on the characteristics of the method (e.g. .5 for IF as an important exception threshold). Only the RST threshold has a lot of thresholds in long-term studies for the other four methods.

Many works have been conducted to statistically analyze the relationship between TIR anomalies and earthquakes. However, there are still doubts regarding the correlation between earthquakes and TIR precursors. Recently, Zhang et al., 2021 provided strong statistical evidence of TIR anomalies and earthquakes by constructing the heating core model (Zhang et al., 2021). To filter thermal anomalies in CTIR that are unrelated to earthquakes, we used training–testing–validation steps to set many parameters to extract RTIR anomalies and determine the correspondence between TIR precursors and earthquakes in the next step (train–testing steps in the original study). We obtained the optimal parameters for each method by the above steps. In our research, the optimal global parameters are discussed more, ignoring the most local parameters that can be extracted under the characteristics of the study area. The spatial variable parameters will be studied in the future to better understand the mechanism of TIR anomalies and earthquakes.

Although we used statistical methods to evaluate the influence of TIR anomaly extraction, tectonic background factors were not quantified and statistically analysed in this study. For example, Yang et al., 2022 studied the relationship between quantified bright temperature anomalies and stress. (Qi et al., 2021). showed the evolution process of positive microwave brightness temperature (MBT) anomalies basically reflected the joint effect of crustal stress and seismogenic environment and regional coversphere on surface microwave radiation. Therefore, Extending the heating core model may be an important tool to improve mechanistic understanding with additional physical/geological contexts.

4.3 Declustering

Seismicity declustering is widely used to separate an earthquake catalog into foreshocks, mainshocks, and aftershocks in seismology (Talbi et al., 2013). Many declustering methods have been proposed over the years such as Reasenberg, Window Methods, Stochastic Declustering et, al. There is the doubt whether declustering the seismic catalog when we perform a correlation study between TIR anomalies and the earthquake. In fact, declustering implies the extraction of mainshocks of higher magnitude than foreshocks and aftershocks. Therefore, associating the anomaly with the largest magnitude earthquake may imply relating it to the mainshock. (Marchetti et al., 2022). found is beneficial to extract possible seismo-anomalies after comparing the effect of the presence or absence of declustering. Of course it needs further research to discuss the necessity of declustering.

4.4 Limitations

This study still has a lot of limitations. There are many parameter settings in multiple study sessions, but the selection of parameters did not take more factors into account. Although we have demonstrated the relationship between anomalies and earthquakes using statistical analysis, the mechanism of TIR seismic anomalies is yet unclear. In order to set the

parameter for each step, we use information from the literature. However, we admit that the existing literature is descriptive rather than exploratory. We use a training-test-validation approach to obtain the optimal parameters, but the original set of parameters still affects our results. It is well known that the mechanism of TIR precursors has never been determined, However, There are theories such as p-hole activation theory, remote sensing rock mechanics, and seismo-ionosphere coupling theory (Saraf et al., 2009; Freund, 2011). Therefore, from a statistical perspective, we can only determine whether the anomaly is related to the earthquake. The improvements from MD were applied in research, but the 3D error diagram is still is under review (Zhang et al., 2023). Threshold questions about each method of quantifying the impact of parameters remains unresolved. Perhaps it can be resolved in future study.

5 Conclusion

In this paper, we proposed an evaluation process used to compare the effectiveness of TIR anomaly extraction methods. As shown in Figure 10, the process was divided into three parts: CTIR anomaly extraction, RTIR anomaly extraction and constructive factor filtering. Eleven years (2010–2020) of daily conLST data, acquired from GEE, were used to identify LST fluctuations relationship with M≥3 that earthquakes occurred in the study area over the same period. Multiple parameters or sets of parameters were used in various parts of the research to avoid the mistakes caused by one parameter. Therefore, we employed the training–test–validation steps to obtain the optimal parameters and determined the merits of this method, determine from the optimal parameter type. To verify and improve the evaluation process that we have proposed, we selected some previously studied methods (RST, IQR, WT, KF), and methods that have not been used for seismic thermal anomaly extraction (IF, AE).

The results of our experiments are as follows:

- The heating core model can effectively improve the detection of TIR anomalies caused by earthquakes, and remove to some degree the TIR anomalies not caused by earthquakes. At the same time, the heated core model plays a filtering role for different anomaly extraction methods This can establish a strong statistical relationship between TIR anomalies and earthquakes.
- The ranking is given below for each step regarding the merits of the method through our proposed evaluation process: In the RTIR step: Kalme filter>RST>IQR>WT>AE>IF; in the CTIR step: CTIR: AE>IF>RST>IQR>WT>Kalme filter; the results after considering the constructive factors: RST>IF>IQR>WT>Kalme filter>AE. We introduced tectonic factors to avoid the non-causal correlation problem, although a high statistical correlation was generated between the TIR anomalies and the earthquake in the previous two steps.
- No method that can completely extract the thermal anomalies associated with earthquakes. The process provides a multifaceted evaluation of the extraction method, including the number of anomalies, statistical relationships, and physical/geographical factors.

Data availability statement

The original contributions presented in the study are included in the article/Supplementary Material, further inquiries can be directed to the corresponding author.

Author contributions

For Conceptualization, PW; Software, PW; Supervision, QM; Validation, LZ; Visualization, MA; XH Writing—original draft, PW; Writing—review and editing, QM and CZ. All authors have read and agreed to the published version of the manuscript.

Funding

This research was supported by: the National Natural Science Foundation of China Major Program, grant number 42192580,42192580; the National Key Research and Development Program of China: 2019YFC1509202; the National Natural Science Foundation of China, grant number 42201384; the National Key Research and Development Program of China: 2020YFC0833100.

Conflict of interest

The authors declare that the research was conducted in the absence of any commercial or financial relationships that could be construed as a potential conflict of interest.

Publisher's note

References

Akhoondzadeh, M. (2013). A comparison of classical and intelligent methods to detect potential thermal anomalies before the 11 August 2012 Varzeghan, Iran, earthquake (Mw = 6.4). *Nat. Hazards Earth Syst. Sci* 13, 1077–1083. doi:10.5194/nhess-13-1077-2013

Bakun, W. H., Aagaard, B., Dost, B., Ellsworth, W. L., Hardebeck, J. L., Harris, R. A., et al. (2005). Implications for prediction and hazard assessment from the 2004 Parkfield earthquake. *Nature* 437, 969–974. doi:10.1038/nature04067

Bao, Z., Yong, S., Wang, X., Yang, C., Xie, J., and He, C. (2021). Seismic reflection analysis of AETA electromagnetic signals. *Appl. Sci.* 11, 5869. doi:10.3390/app11135869

Bhardwaj, A., Singh, S., Sam, L., Joshi, P. K., Bhardwaj, A., Martín-Torres, F. J., et al. (2017). A review on remotely sensed land surface temperature anomaly as an earthquake precursor. *Int. J. Appl. Earth Observation Geoinformation* 63, 158–166. doi:10.1016/j.jag.2017.08.002

Blackett, M., Wooster, M. J., and Malamud, B. D. (2011). Exploring land surface temperature earthquake precursors: A focus on the Gujarat (India) earthquake of 2001: Earthquake land temperature study. *Geophys. Res. Lett.* 38. doi:10.1029/2011GL048282

Cambiotti, G., Bordoni, A., Sabadini, R., and Colli, L. (2011). GRACE gravity data help constraining seismic models of the 2004 Sumatran earthquake. *J. Geophys. Res.* 116, B10403. doi:10.1029/2010JB007848

Chen, H., Xie, Q., Dai, B., Zhang, H., and Chen, H. (2016). Seismic damage to structures in the M s6.5 Ludian earthquake. *Earthq. Eng. Eng. Vib.* 15, 173–186. doi:10.1007/s11803-016-0314-4

Eleftheriou, A., Filizzola, C., Genzano, N., Lacava, T., Lisi, M., Paciello, R., et al. (2016). Long-term RST analysis of anomalous TIR sequences in relation with earthquakes occurred in Greece in the period 2004–2013. *Pure Appl. Geophys.* 173, 285–303. doi:10.1007/s00024-015-1116-8

Eleftheriou, A., Filizzola, C., Genzano, N., Lacava, T., Lisi, M., Paciello, R., et al. (2021). Correction to: Long-term RST analysis of anomalous TIR sequences in relation with earthquakes occurred in Greece in the period 2004-2013. *Pure Appl. Geophys.* 178, 1529. doi:10.1007/S00024-021-02692-4

Filizzola, C., Corrado, A., Genzano, N., Lisi, M., Pergola, N., Colonna, R., et al. (2022). RST analysis of anomalous TIR sequences in relation with earthquakes occurred in Turkey in the period 2004–2015. *Remote Sens.* 14, 381. doi:10.3390/rs14020381

Freund, F. (2011). Pre-earthquake signals: Underlying physical processes. *J. Asian Earth Sci.* 41, 383–400. doi:10.1016/j.jseaes.2010.03.009

Gao, J., Wang, B., Wang, Z., Wang, Y., and Kong, F. (2020). A wavelet transform-based image segmentation method. *Optik* 208, 164123. doi:10.1016/j.ijleo.2019.164123

Geiß, C., and Taubenböck, H. (2013). Remote sensing contributing to assess earthquake risk: From a literature review towards a roadmap. *Nat. Hazards* 68, 7–48. doi:10.1007/s11069-012-0322-2

Genzano, N., Filizzola, C., Paciello, R., Pergola, N., and Tramutoli, V. (2015). Robust Satellite Techniques (RST) for monitoring earthquake prone areas by satellite TIR observations: The case of 1999 Chi-Chi earthquake (Taiwan). *Journal of Asian Earth Sciences* 114, 289–298. doi:10.1016/j.jseaes.2015.02.010

Genzano, N., Filizzola, C., Hattori, K., Pergola, N., and Tramutoli, V. (2021). Statistical correlation analysis between thermal infrared anomalies observed from MTSATs and large earthquakes occurred in Japan (2005–2015). *J. Geophys Res. Solid Earth* 126, 108. doi:10.1029/2020JB020108

Gutenberg, B., and Richter, C. (1949). *Seismicity of the Earth and associated phenomena*. Princeton University Press. Available at: https://books.google.com.hk/books?id=BEVaXVPHstQC.

Hassanien A. E. and Darwish A. (Editors) (2021). *Machine learning and big data analytics paradigms: Analysis, applications and challenges* (Cham: Springer International Publishing). doi:10.1007/978-3-030-59338-4

Hayakawa, M. (2018). "Earthquake precursor studies in Japan," in *Geophysical monograph series*. Editors D. Ouzounov, S. Pulinets, K. Hattori, and P. Taylor (Hoboken, NJ, USA: John Wiley & Sons), 7–18. doi:10.1002/9781119156949.ch2

Hayakawa, M., Hobara, Y., Ohta, K., Izutsu, J., Nickolaenko, A. P., and Sorokin, V. (2011). Seismogenic effects in the ELF schumann resonance band. *Trans. Inst. Electr. Eng. Japan.A* 131, 684–690. doi:10.1541/ieejfms.131.684

Hayakawa, M., Hobara, Y., Rozhnoi, A., Solovieva, M., Ohta, K., Izutsu, J., et al. (2013). The ionospheric precursor to the 2011 march 11 earthquake based upon observations obtained from the Japan-pacific subionospheric VLF/LF network. *Terr. Atmos. Ocean. Sci.* 24, 393. doi:10.3319/tao.2012.12.14.01(aa)

Hinton, G. E., and Salakhutdinov, R. R. (2006). Reducing the dimensionality of data with neural networks. *Science* 313, 504–507. doi:10.1126/science.1127647

Jiao, Z.-H., Zhao, J., and Shan, X. (2018). Pre-seismic anomalies from optical satellite observations: A review. *Nat. Hazards Earth Syst. Sci.* 18, 1013–1036. doi:10.5194/nhess-18-1013-2018

Jiao, Z., and Shan, X. (2022). Pre-seismic temporal integrated anomalies from multiparametric remote sensing data. *Remote Sens.* 14, 2343. doi:10.3390/rs14102343

Jin, S., Li, Z. C., and Park, P.-H. (2006). Seismicity and GPS constraints on crustal deformation in the southern part of the Korean Peninsula. *Geosci. J.* 10, 491–497. doi:10.1007/BF02910442

Jin, S., Park, P., and Zhu, W. (2007). Micro-plate tectonics and kinematics in Northeast Asia inferred from a dense set of GPS observations. *Earth Planet. Sci. Lett.* 257, 486–496. doi:10.1016/j.epsl.2007.03.011

Jin, S., Zhu, W., and Afraimovich, E. (2010). Co-seismic ionospheric and deformation signals on the 2008 magnitude 8.0 Wenchuan Earthquake from GPS observations. *Int. J. Remote Sens.* 31, 3535–3543. doi:10.1080/01431161003727739

Jin, S., Jin, R., and Liu, X. (2019). *GNSS atmospheric seismology: Theory, observations and modeling*. Singapore: Springer Singapore. doi:10.1007/978-981-10-3178-6

Liu, J. Y., Chuo, Y. J., Shan, S. J., Tsai, Y. B., Chen, Y. I., Pulinets, S. A., et al. (2004). Pre-earthquake ionospheric anomalies registered by continuous GPS TEC measurements. *Ann. Geophys.* 22, 1585–1593. doi:10.5194/angeo-22-1585-2004

Liu, F. T., Ting, K. M., and Zhou, Z.-H. (2008). "Isolation forest," in Proceeding of the 2008 Eighth IEEE International Conference on Data Mining (Pisa, Italy: IEEE), 413–422. doi:10.1109/ICDM.2008.17

Liu, F. T., Ting, K. M., and Zhou, Z.-H. (2012). Isolation-based anomaly detection. *ACM Trans. Knowl. Discov. Data* 6, 1–39. doi:10.1145/2133360.2133363

Marchetti, D., De Santis, A., Campuzano, S. A., Zhu, K., Soldani, M., D'Arcangelo, S., et al. (2022). Worldwide statistical correlation of eight years of swarm satellite data with M5.5+ earthquakes: New hints about the preseismic phenomena from space. *Remote Sens.* 14, 2649. doi:10.3390/rs14112649

Molchan, G. M. (1990). Strategies in strong earthquake prediction. *Phys. Earth Planet. Interiors* 61, 84–98. doi:10.1016/0031-9201(90)90097-H

Molchan, G. M. (1991). Structure of optimal strategies in earthquake prediction. *Tectonophysics* 193, 267–276. doi:10.1016/0040-1951(91)90336-Q

Molchanov, O. A., Kopytenko, Yu. A., Voronov, P. M., Kopytenko, E. A., Matiashvili, T. G., Fraser-Smith, A. C., et al. (1992). Results of ULF magnetic field measurements near the epicenters of the Spitak (M_s = 6.9) and Loma Prieta (M_s = 7.1) earthquakes: Comparative analysis. *Geophys. Res. Lett.* 19, 1495–1498. doi:10.1029/92GL01152

Ouzounov, D., Bryant, N., Logan, T., Pulinets, S., and Taylor, P. (2006). Satellite thermal IR phenomena associated with some of the major earthquakes in 1999–2003. *Phys. Chem. Earth Parts A/B/C* 31, 154–163. doi:10.1016/j.pce.2006.02.036

Ouzounov, D., Liu, D., Chunli, K., Cervone, G., Kafatos, M., and Taylor, P. (2007). Outgoing long wave radiation variability from IR satellite data prior to major earthquakes. *Tectonophysics* 431, 211–220. doi:10.1016/j.tecto.2006.05.042

Panda, S. K., Choudhury, S., Saraf, A. K., and Das, J. D. (2007). MODIS land surface temperature data detects thermal anomaly preceding 8 October 2005 Kashmir earthquake. *Int. J. Remote Sens.* 28, 4587–4596. doi:10.1080/01431160701244906

Parrot, M., and Li, M. (2018). "Statistical analysis of the ionospheric density recorded by the DEMETER satellite during seismic activity," in *Geophysical monograph series*. Editors D. Ouzounov, S. Pulinets, K. Hattori, and P. Taylor (Hoboken, NJ, USA: John Wiley & Sons), 319–328. doi:10.1002/9781119156949.ch18

Pulinets, S. (2006). Space technologies for short-term earthquake warning. *Advances in Space Research* 37, 643–652. doi:10.1016/j.asr.2004.12.074

Qi, Y., Wu, L., Ding, Y., Liu, Y., Chen, S., Wang, X., et al. (2021). Extraction and discrimination of MBT anomalies possibly associated with the Mw 7.3 maduo (Qinghai, China) earthquake on 21 may 2021. *Remote Sens.* 13, 4726. doi:10.3390/rs13224726

Qin, K., Wu, L. X., De Santis, A., and Cianchini, G. (2012). Preliminary analysis of surface temperature anomalies that preceded the two major Emilia 2012 earthquakes (Italy). *Ann. Geophys.* 55, 40. doi:10.4401/ag-6123

Reasenberg, P. (1985). Second-order moment of central California seismicity, 1969-1982. *J. Geophys. Res.* 90, 5479–5495. doi:10.1029/JB090iB07p05479

Roeloffs, E. A. (1988). Hydrologic precursors to earthquakes: A review. *Pageoph* 126, 177–209. doi:10.1007/BF00878996

Saha, S., Moorthi, S., Wu, X., Wang, J., Nadiga, S., Tripp, P., et al. (2011). *NCEP climate Forecast system version 2 (CFSv2) 6-hourly products*. doi:10.5065/D61C1TXF

Saradjian, M. R., and Akhoondzadeh, M. (2011). Thermal anomalies detection before strong earthquakes ($M > 6.0$) using interquartile, wavelet and Kalman filter methods. *Nat. Hazards Earth Syst. Sci.* 11, 1099–1108. doi:10.5194/nhess-11-1099-2011

Saraf, A. K., Rawat, V., Choudhury, S., Dasgupta, S., and Das, J. (2009). Advances in understanding of the mechanism for generation of earthquake thermal precursors detected by satellites. *International Journal of Applied Earth Observation and Geoinformation* 11, 373–379. doi:10.1016/j.jag.2009.07.003

Shiff, S., Helman, D., and Lensky, I. M. (2021). Worldwide continuous gap-filled MODIS land surface temperature dataset. *Sci. Data* 8, 74. doi:10.1038/s41597-021-00861-7

Talbi, A., Nanjo, K., Satake, K., Zhuang, J., and Hamdache, M. (2013). Comparison of seismicity declustering methods using a probabilistic measure of clustering. *J. Seismol.* 17, 1041–1061. doi:10.1007/s10950-013-9371-6

Tramutoli, V., Aliano, C., Corrado, R., Filizzola, C., Genzano, N., Lisi, M., et al. (2013). On the possible origin of thermal infrared radiation (TIR) anomalies in earthquake-prone areas observed using robust satellite techniques (RST). *Chemical Geology* 339, 157–168. doi:10.1016/j.chemgeo.2012.10.042

Tramutoli, V., Genzano, N., Lisi, M., and Pergola, N. (2018). "Significant Cases of Preseismic Thermal Infrared Anomalies," in *Geophysical Monograph Series*. Editor D. Ouzounov, S. Pulinets, K. Hattori, and P. Taylor (Hoboken, NJ: John Wiley and Sons, Inc.), 329–338. doi:10.1002/9781119156949.ch19

Wan, Z. (2014). New refinements and validation of the collection-6 MODIS land-surface temperature/emissivity product. *Remote Sens. Environ.* 140, 36–45. doi:10.1016/j.rse.2013.08.027

Wang, F., Wang, M., Wang, Y., and Shen, Z.-K. (2015). Earthquake potential of the Sichuan-Yunnan region, Western China. *J. Asian Earth Sci.* 107, 232–243. doi:10.1016/j.jseaes.2015.04.041

Wang, M., and Shen, Z. (2020). Present-day crustal deformation of continental China derived from GPS and its tectonic implications. *J. Geophys. Res. Solid Earth* 125. doi:10.1029/2019JB018774

Xiong, P., Bi, Y., and Shen, X. (2009). "A wavelet-based method for detecting seismic anomalies in remote sensing satellite data," in Machine Learning and data Mining in pattern recognition *lecture notes in computer science*. Editor P. Perner (Berlin, Heidelberg: Springer Berlin Heidelberg), 569–581. doi:10.1007/978-3-642-03070-3_43

Yang, X., Zhang, T., Lu, Q., Long, F., Liang, M., Wu, W., et al. (2022). Variation of Thermal Infrared Brightness Temperature Anomalies in the Madoi Earthquake and Associated Earthquakes in the Qinghai-Tibetan Plateau (China). *Front. Earth Sci.* 10, 823540. doi:10.3389/feart.2022.823540

Yuan, Y. (2008). Impact of intensity and loss assessment following the great Wenchuan Earthquake. *Earthq. Eng. Eng. Vib.* 7, 247–254. doi:10.1007/s11803-008-0893-9

Zechar, J. D., and Jordan, T. H. (2008). Testing alarm-based earthquake predictions. *Geophys. J. Int.* 172, 715–724. doi:10.1111/j.1365-246X.2007.03676.x

Zhan, C., Meng, Q., Zhang, Y., Allam, M., Wu, P., Zhang, L., et al. (2022). Application of 3D error diagram in thermal infrared earthquake prediction: Qinghai–tibet plateau. *Remote Sens.* 14, 5925. doi:10.3390/rs14235925

Zhang, Y., Guy, O., Shyam, N., Didier, S., and Meng, Q. (2023) A new 3-D error diagram: An effective and better tool for finding TIR anomalies related to earthquakes. *IEEE Trans. Geoscience Remote Sens.* [under review].

Zhang, Y., and Meng, Q. (2018). A statistical analysis of TIR anomalies extracted by RST in relation with earthquake in sichuan area with use of MODIS LST data. *Earthq. Hazards*. doi:10.5194/nhess-2018-214

Zhang, Y., Meng, Q., Ouillon, G., Sornette, D., Ma, W., Zhang, L., et al. (2021). Spatially variable model for extracting TIR anomalies before earthquakes: Application to Chinese Mainland. *Remote Sens. Environ.* 267, 112720. doi:10.1016/j.rse.2021.112720

Zoran, M. (2012). MODIS and NOAA-AVHRR l and surface temperature data detect a thermal anomaly preceding the 11 March 2011 Tohoku earthquake. *Int. J. Remote Sens.* 33, 6805–6817. doi:10.1080/01431161.2012.692833

frontiers | Frontiers in Earth Science

TYPE Original Research
PUBLISHED 17 January 2023
DOI 10.3389/feart.2022.1012773

OPEN ACCESS

EDITED BY
Zhenjie Wang,
China University of Petroleum (Huadong), China

REVIEWED BY
Wanpeng Feng,
School of Earth Sciences and Engineering, Sun Yat-sen University, China
Shengji Wei,
Nanyang Technological University, Singapore

*CORRESPONDENCE
Xiaoli Liu,
liuxl.j@163.com
Jing Liu-Zeng,
liu_zeng@tju.edu.cn

SPECIALTY SECTION
This article was submitted to Structural Geology and Tectonics, a section of the journal Frontiers in Earth Science

RECEIVED 05 August 2022
ACCEPTED 07 November 2022
PUBLISHED 17 January 2023

CITATION
Liu X, Xia T, Liu-Zeng J, Deng D, Jia Z, Wang P, Yu P and Wang W (2023), Coseismic and early postseismic deformation of the 2020 Nima Mw 6.4 earthquake, central Tibet, from InSAR and GNSS observations. *Front. Earth Sci.* 10:1012773. doi: 10.3389/feart.2022.1012773

Coseismic and early postseismic deformation of the 2020 Nima Mw 6.4 earthquake, central Tibet, from InSAR and GNSS observations

Xiaoli Liu[1]*, Tao Xia[1], Jing Liu-Zeng[2]*, Debeier Deng[1], Zhige Jia[1], Peng Wang[3], Pengfei Yu[1] and Wenqing Wang[4]

[1]Institute of Seismology, China Earthquake Administration, Wuhan, China, [2]School of Earth System Science, Tianjin University, Tianjin, China, [3]Institute of Geology, China Earthquake Administration, Beijing, China, [4]Monitoring and Application Center of China Earthquake Administration, Xian, China

The 2020 Mw6.4 Nima earthquake is one of the largest normal-faulting earthquakes recently occurring north of the Banggong suture zone in remote central Tibet, where geologic investigation of active faults is extremely limited. We analyze jointly InSAR and GNSS observations over 9 months after the Nima earthquake and calculate the coseismic and postseismic displacement. The optimal coseismic slip model suggests this event is the result of moderate-angle down-dip slip on a complex reversed "S-shape" three-segmented structure at fault junctions of the West Yibu-Chaka fault, the Heishi fault, and an unmapped blind fault, with a small component of left-lateral slip. The superposition of seismic waves from faults with different strikes and dips accounted for a large non-double-couple component in the long-period point-source solutions. The geodetic moment released by the mainshock is 6.4 × 10^{18} N·m, equivalent to Mw 6.42. Coseismic rupture concentrated at a depth of 4–15 km, with a peak slip of 1.36 m at 8.5 km depth. The cumulative afterslip moment within 9 months after the mainshock is 1 × 10^{18} N m, about 15.6% of that released by the mainshock coseismic slip. The afterslips contributed largely to the release of additional strain energy. In addition, shallow creep on the northern part of the blind fault, and deep uplift on the east normal fault system are promoted by stress perturbations. A significant proportion of down-dip coseismic slip spreading to more than 20 km beneath the surface, and deep up-slip afterslip have implications for the rheology of down-dip extension of the dipping faults in northern Tibet. Two obvious stress loading zones of more than 1 bar highlight seismic hazards in the region, especially in the junction between normal faults and ends of the large-size sinistral Riganpei-Co and Jiangai-Zangbu faults. It is necessary to forecast accurately by longer-term afterslip observation over timescales of years for the faults. Compared with previous studies, our results suggest a more complex subsurface fault geometry linking the normal and strike-slip faults and dynamic stress adjustment in this poorly-known region of Tibet.

KEYWORDS

normal faulting earthquake, 2020 Nima earthquake, InSAR, GNSS, coseismic deformation, postseismic deformation, Tibetan plateau

1 Introduction

The Tibetan plateau comprises complex systems of connected and interacting faults. Several NS-trending rift systems developed in the central and southern part of the Tibet Plateau are aligned regularly and nearly perpendicular to the Himalayan collision arc due to the long-term effects of collision and compression of the India-Eurasia plates (Armijo et al., 1989; Tapponnier et al., 2001; Taylor et al., 2003; Kapp et al., 2008; Elliott et al., 2010; Yin and Taylor, 2011) (Figure 1). These rift systems are large in scale and accompanied by multiple groups of NS-trending normal fault systems. They are often associated with large EW-trending strike-slip faults, and together accommodate some of the spatially-varying strains in response to the India-Eurasia plate collision (Wang et al., 2014), and are bounded by the Bangong-Nujiang suture zone (BNS). There are significant differences in E-W extension rate and deformation styles on the northern and southern sides of the BNS. South of the BNS, the majority of E-W directed extension deformation is accommodated by several N-S normal-faulting systems (Molnar and Tapponnier, 1978; Armijo et al., 1989; Ha et al., 2019; Chevalier et al., 2020), with slip rates in the range of 1–3 mm/a (Harrison et al., 1995; Wu et al., 2015; Ha et al., 2019; Chevalier et al., 2020; Wang et al., 2020). However, the extension is not obvious in the central plateau north of the BNS, and the active tectonics is primarily marked by a series of discrete conjugate strike-slip faults. At the tail end of these faults, N-S normal-faulting plays a subsidiary role in the E-W extension of the plateau (Yin et al., 1999; Taylor et al., 2003; Taylor and An, 2009; Han et al., 2018). The late Quaternary slip rate of corresponding normal faults is mostly limited to 0.3–0.7 mm/a (Blisniuk and Sharp, 2003; Wu et al., 2015; Li et al., 2019).

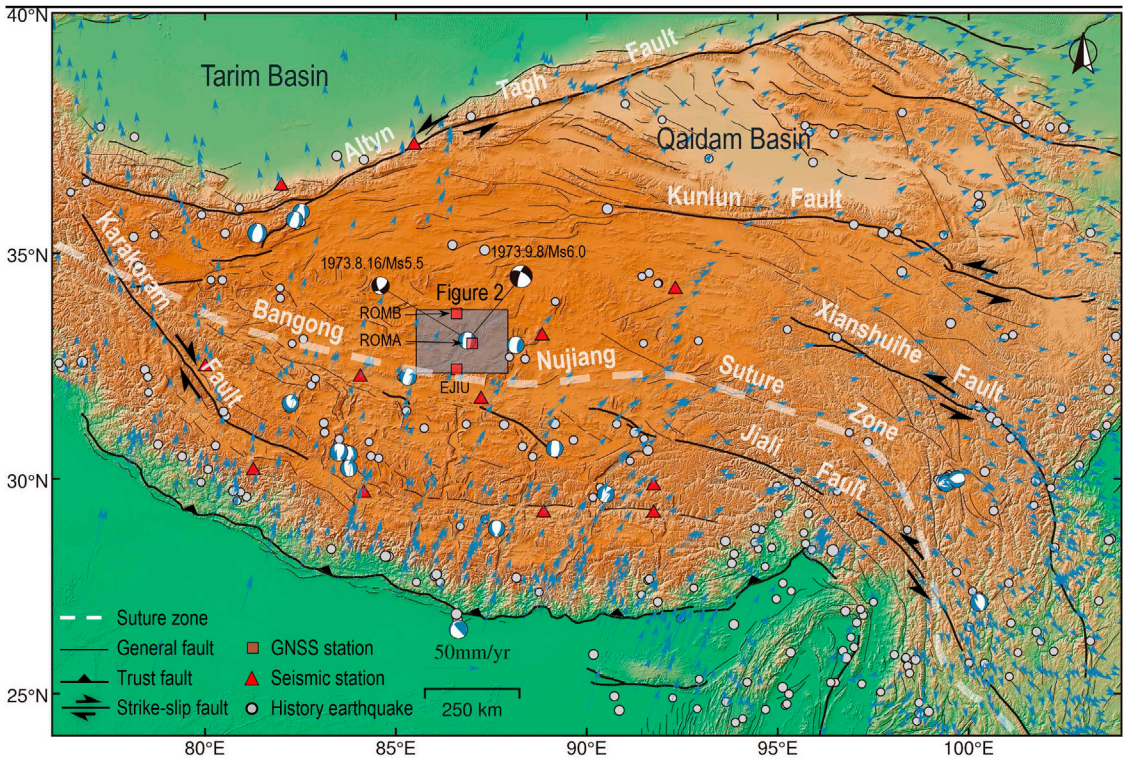

FIGURE 1
Topographic and tectonic setting map of the Tibetan plateau overlain. Light-blue circles, white and blue beach balls denote earthquakes with magnitude larger than Mw 4.5 and focal mechanisms of Mw ≥ 6 normal faulting earthquakes from 1 January 1966 to 1 April 2021 from the GCMT catalog, respectively. Black and white beach balls denote focal mechanisms of Ms ≥ 5.5 earthquake in 1973 (Molnar and Tapponnier, 1978). Red triangles denote the seismic stations used in this study. Black rectangles depict footprints of this study area. Black lines indicate regional active faults from Tapponnier (Tapponnier et al., 2001). Blue arrows indicates GPS velocities from Wang (Wang and Shen, 2020). Thrust faults have barbs on the upper plate, arrows indicate the direction of horizontal motion for strike-slip faults. The dashed white line is the Bangong Nujiang suture zone.

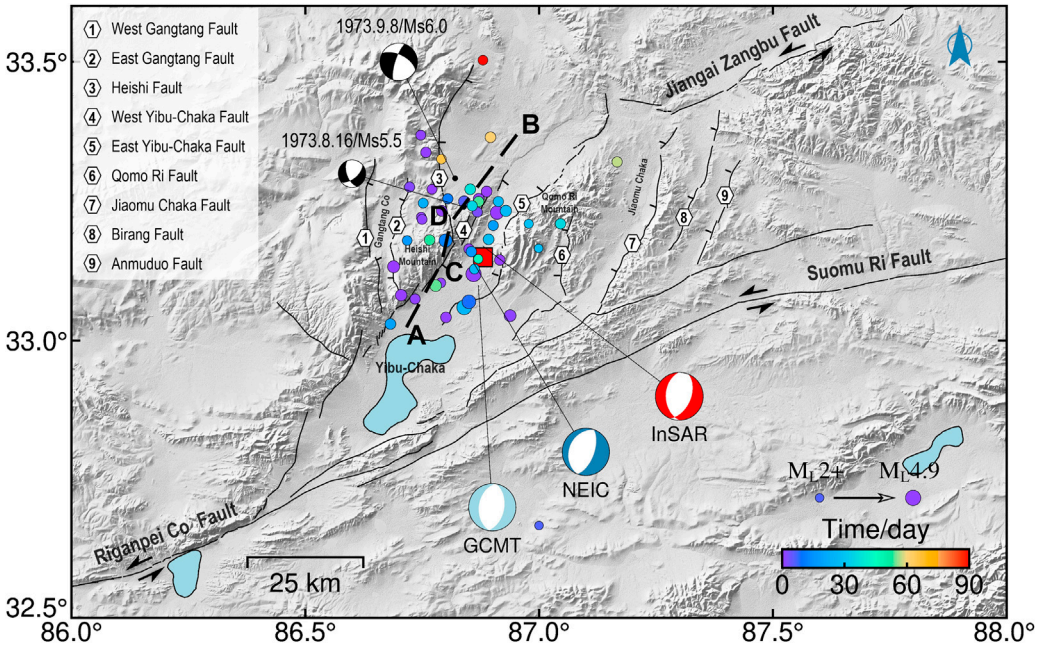

FIGURE 2
Topographic and tectonic setting map of the Yibu-Chaka graben. Black lines indicate regional active faults modified after Taylor and Yin (Taylor and An, 2009) and interpreted from satellite images. Focal mechanism solutions of the 2020 Nima event from different organizations in Table 1 and three color beach balls denote focal mechanisms of the mainshock from the GCMT and USGS catalogs, and this paper, respectively. The solid color circles are aftershocks within 9 months after the mainshock reported in the CENC ($M_L \geq 2.7$) catalogs, and the circle sizes indicate the magnitude of aftershocks. The black dash line is the derived fault trace *via* the geodetic dataset. Captions are as for Figure 1.

In central Tibet, NS-trending normal faults are kinematically linked with and subsidiary to the strike-slip faults. Moderate to large earthquakes are infrequent in central Tibet compared with the high seismicity in plateau margins. However, the Riganpei-Co, Yibu-Chaka, and Jiangai-Zangbu fault (RYJF) system (Figure 2) is important to note which held several moderate magnitude events since 1973. The ~340 km long Riganpei Co fault is a NE-strike sinistral fault zone, conjugated with the EES-striking Gaize Dong-Co fault, lying on the southern side of the BNS (Taylor et al., 2003). It starts in Dongcuo Basin in the south, extends NEE~NNE to the pull-apart Yibu Chaka basin, and then connects with the sinistral Jiangai-Zangbu fault on the north side of the basin (Taylor et al., 2003). The Yibu-Chaka basin is dissected by a series of NS~NNE-striking normal faults into a symmetric horst-graben system, characterized by a negative flower structure (Gao et al., 2022). The largest graben is the Yibu-Chaka graben in the central of the basin, which connects two opposite dipping sets of domino normal fault blocks and is bounded by two primary normal faults (the west and east Yibu-Chaka faults, abbreviated as the WYF and EYF) (Li et al., 2021). A variety of late Quaternary features, including pressure ridges, sag ponds, and offset alluvial fans are identified along with the extensional fault system (Taylor et al., 2003). Well-defined offsets of 30–100 m of these units along the southwestern strike-slip portion of this fault were well-characterized and documented to estimate its Late Quaternary slip rate (Taylor et al., 2003).

Recent moderate magnitude earthquakes of normal type are more frequent in this region. The Nima-Gaize earthquake sequence of Ms = 6.4, 5.9, and 5.4 in 2008 occurred in the junction of the southern end of the Riganpei-Co fault and the Gaize Dong-Co fault in southern-central Tibet (Ryder et al., 2010). A three Ms > 5.3 moderate earthquake sequence in 1973 occurred in the north of the Yibu-Chaka graben (Molnar and Tapponnier, 1978). The Nima Mw 6.4 earthquake in the center of the Yibu-Chaka graben on 22 July 2020 was the newest and strongest event in the RYJF system. The reported epicenter of the 2020 Nima earthquake was located in the Heishi range on the west of the Yibu-Chaka basin by the China Earthquake Networks Center (CENC) and the center of the Yibu-Chaka basin by the US Geological Survey (USGS), and the GCMT(https://www.globalcmt.org/CMTsearch.html) (Figure 2), respectively. Seismological long-period point-source moment tensor solution shows a relatively large non-double-couple (non-DC) component of >21% (Table 1). The significant non-DC component hints the mainshock is not properly represented with a single planar fault. This event may not be a simple shearing tectonic earthquake and is associated with geometrically complex shear faulting (Frohlich, 1994; Julian et al., 1998).

TABLE 1 Fault plane parameters for the mainshock from InSAR studies, and as listed in the CENC, USGS, and GCMT Catalogs.

Model	Latitude (°)	Longitude (°)	Centroid (km)	Strike (°)	Dip (°)	Rake (°)	Slip (m)	Moment (10^{18}N.m)	Non-DC (%)	Magnitude
CENC	33.19	86.81	10	10	50	−81				Ms6.6
USGS	33.144	86.864	10	20	61	−91		3.2	21	Mww6.3
GCMT	33.10	86.87	16.8	10	48	−88		5.01	43	Mw6.4
*Ji et al. (2021)	33.16	86.8	9.5	28	48	−92.3	1.1	4.9		Mw6.39
*Yang et al. (2021a)			6.3	30	48.3	−80	1.2			Mw6.3
*Li et al. (2021)	33.18	86.89	7.5	28	48	−87	1.5	4.7		Mw6.4
*Gao et al. (2022) (Constant strike)	33.18	86.88	6.9	28.8	49.4	−78.6	1.2	4.02		Mw6.28
*Gao et al. (2022) (Variable strike)	33.18	86.88	7.5		45.5°–55.5°		1.39	3.84		Mw6.36
*Model_1	33.17	86.88	—	40	50	−180	—	—		—
*Model_2	33.17	86.88	7.7	36	50	−74	0.87	5.45		Mw6.38
*Model_3	33.17	86.88	8.5	AC: 30	45	−78	1.36	6.4	3.65	Mw6.42
				CD: 13	50					
				DB: 37	45					

The location indicates the centroid location or hypocenters, except for the InSAR models (*), which show the up-dip projection of the fault center to the surface.

Inversion of coseismic and postseismic deformations helps understanding the mechanics of fault interaction, the process of postseismic stress transfer, and viscous rheology properties of the lithosphere (Bürgmann and Dresen, 2008). InSAR is an ideal tool to study the 2020 Nima earthquake processing in this extremely remote part of Tibet. Several studies from InSAR data have suggested that the Nima earthquake occurred on the WYF with a constant-strike angle (Yang et al., 2021a; Ji et al., 2021; Li et al., 2021) or a previously unmapped branch with a variable-strike angle (Gao et al., 2022), instead of the EYF (Liu et al., 2021). Based on Sentinel-1 C-band Synthetic Aperture Radar (SAR) datasets after the mainshock, Yang et al. suggested that the postseismic deformation was dominated by aseismic slip with nearly pure normal faulting (Yang et al., 2021a). Gao et al. thought the postseismic deformation was caused by slow slip on a parallel branch to the west of the seismogenic fault. (Gao et al., 2022). Therefore, we inverted jointly continuous GNSS observations and Sentinel-1 datasets to determine the seismogenic fault, the coseismic and postseismic slip distributions associated with the 2020 Nima event. Furthermore, we calculated the Coulomb failure stress (CFS) change due to the coseismic and postseismic slip. Finally, we attempted to investigate fault interaction triggered by the event, the relationship between afterslip and aftershocks, as well as the mechanics of postseismic deformation.

2 Materials and methods

The study area is located in central Tibet with an average altitude of greater than 4,300 m, where only a few GNSS stations are available. The known coseismic or postseismic slip models of the Nima earthquake are inverted using only the Sentinel-1 C-band SAR interferometry images (Yang et al., 2021a; Ji et al., 2021; Li et al., 2021; Gao et al., 2022). Three continuous GNSS stations near the deformation center (Figure 1) is deployed in 2018, under a collaboration between Tianjin University (led by Jing Liu-Zeng) and Institute of Geology, China Earthquake Administration. One of the GNSS stations, named station ROMA (86.88°E, 33.15°N; Point 1 in Figure 2) is just near the epicenter and recorded continuously sub-centimeter 3-D displacements. Therefore, to illuminate finely the geometry complexity of the seismogenic fault and the cause of postseismic deformation associated with this event, we combine the three GNSS observations and 101 Sentinel-1 image pairs from 14 July 2020 to 28 April 2021 (detailed information listed in Supplementary Table S2) to constrain jointly the fault geometry and slip distribution as the processing workflow in Figure 3.

2.1 Data preprocessing

2.1.1 GNSS data preprocessing

The raw RINEX files of three continuous GNSS stations are preprocessed using the GAMIT/GLOBK software (Herring et al., 2018) to separate irrelevant signals and obtain GNSS displacement time series. In Step 1 (Figure 3), we remove pole-shift, troposphere phase delay, Earth tide errors seasonal noise, and step signals caused by antenna replacement. The secular linear velocity in the ITRF2008 frame is estimated with an integrated pre-earthquake velocity field compiled with

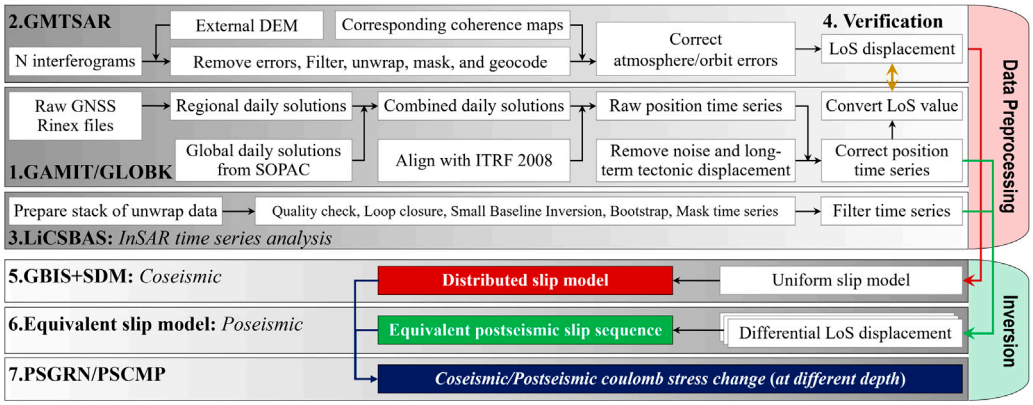

FIGURE 3
Inversion processing flowchart of coseismic and postseismic slip models with GNSS and InSAR datasets.

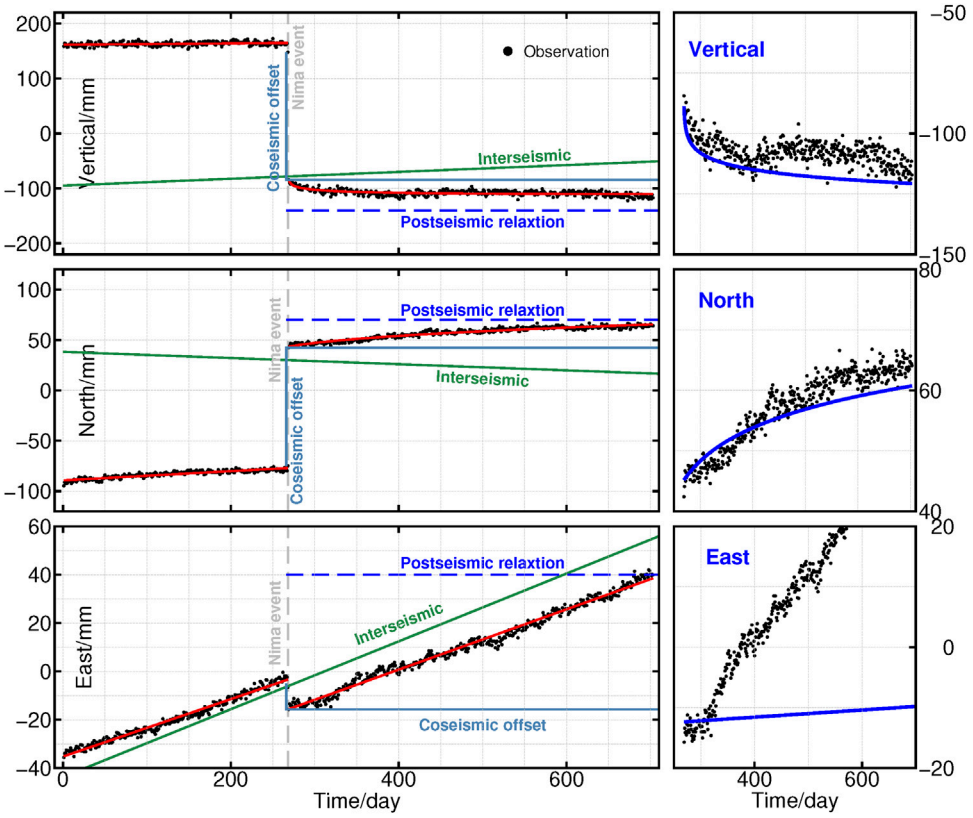

FIGURE 4
Position time series of postseismic transient motion in the second year at the near-field GNSS station ROMA (black dots) and the modeled curve (blue lines) for various combinations of Tibetan mantle transient and steady-state viscosities. The left panel shows the complete time series at this station, with the grey vertical lines, dark blue lines, and blue dashed lines representing the time of the mainshock, the coseismic offset, and the postseismic relaxation. The red and green lines in the left panel and blue lines in the right panel indicate the total signal, 1-dimensional linear fitting of the long-period interseismic tectonic estimate, and the modeled curve, respectively.

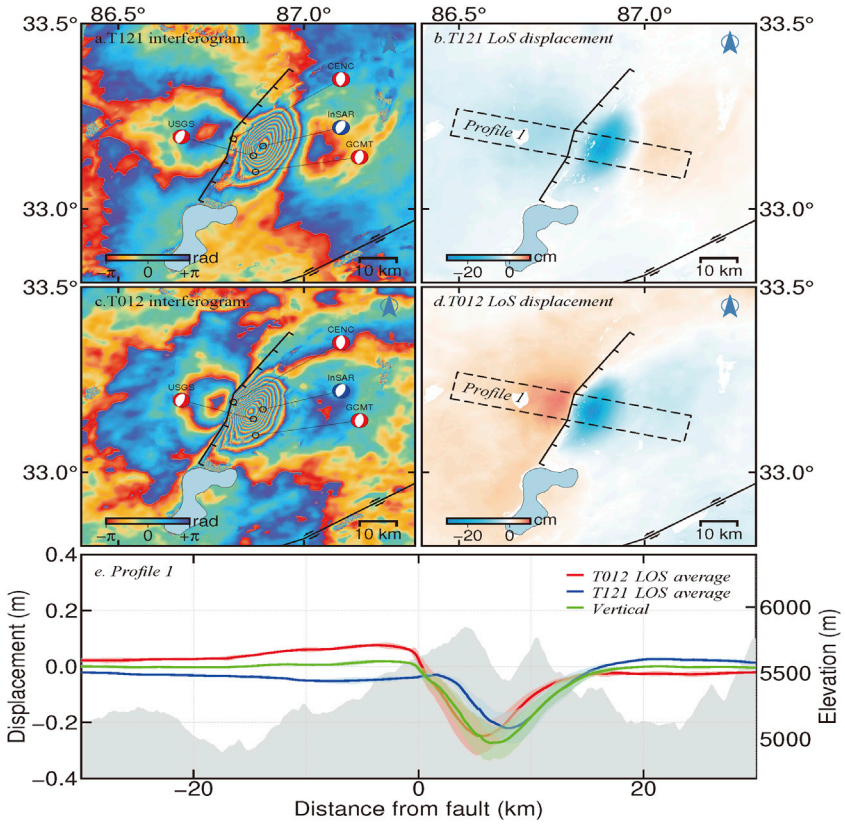

FIGURE 5
Coseismic LoS deformation of T012A and T121D for the 2020 Nima earthquake. The red, blue, and green solid lines and shadows in Panel e indicate coseismic LoS displacements of T012A and T121D and coseismic vertical displacements for the 2020 Nima earthquake of Profile 1 in Panel b.

recently published velocities (McKenzie et al., 2000; England et al., 2013). We use the least square method to fit the original coordinate time series according to Eq. 1 to extract the post-seismic deformation from the total signal, without the long-term tectonic interseismic tectonic signal, seasonal noise, step signals, and derive a corrected time series is shown in Figure 4.

$$X(t) = A\,ln\left(1 + \frac{t - t_0}{\tau}\right) + B(t) + C_1\,sin(2\pi t) + C_2\,cos(2\pi t) + C_3\,sin(4\pi t) + C_4\,cos(4\pi t) + \sum_{i=1}^{N} D_i H(t) \quad (1)$$

where $Aln(1 + (t - t_0)/t_0)$ represents post-seismic deformation; B is the linear rate of long-term tectonic movement; C_i $(i = 1, 2, 3, 4)$ describes noise associated with seasonal changes; $H(t)$, and D_i respectively are instrument step functions and the signal generated by permanent seismic displacement.

2.1.2 InSAR data preprocessing

The coseismic SAR data are preprocessed with the open-source GMTSAR software (https://topex.ucsd.edu/gmtsar/). In Step 2 (Figure 3), Set a multi-look factor of 20:4 in the range and azimuth direction to improve the deformation field SNR and remove system noise. The orbit error and topographic phase are removed using precision orbit files and the 1 arc-second (~30 m) resolution DEM from the Shuttle Rader Topography Mission (SRTM) (Farr and Kobrick, 2000). Interferograms were filtered and unwrapped respectively *via* the Goldstein filtering method (Goldstein and Werner, 1998) and the least-cost flow unwrapping method (Chen and Zebker, 2001). Tropospheric delay is removed *via* the GACOS model (Yu et al., 2018). Residual errors were removed by a linear fitting according to a one-dimensional covariance relation. Besides, some decorrelation regions in the interferograms associated with the Yibu Chaka lake and Jiangai Zangbu river water cover are masked (Figure 5).

In Step 3 (Figure 3), we downloaded 41 postseismic interferograms of T012A and 56 postseismic interferograms of T121D from 26 July 2020 to 28 April 2021 from the LiCSAR web portal (https://comet.nerc.ac.uk/COMET-LiCS-portal). We construct two groups of Spatial-temporal interference networks using the LiCSBAS method (Lazecký et al., 2020) to

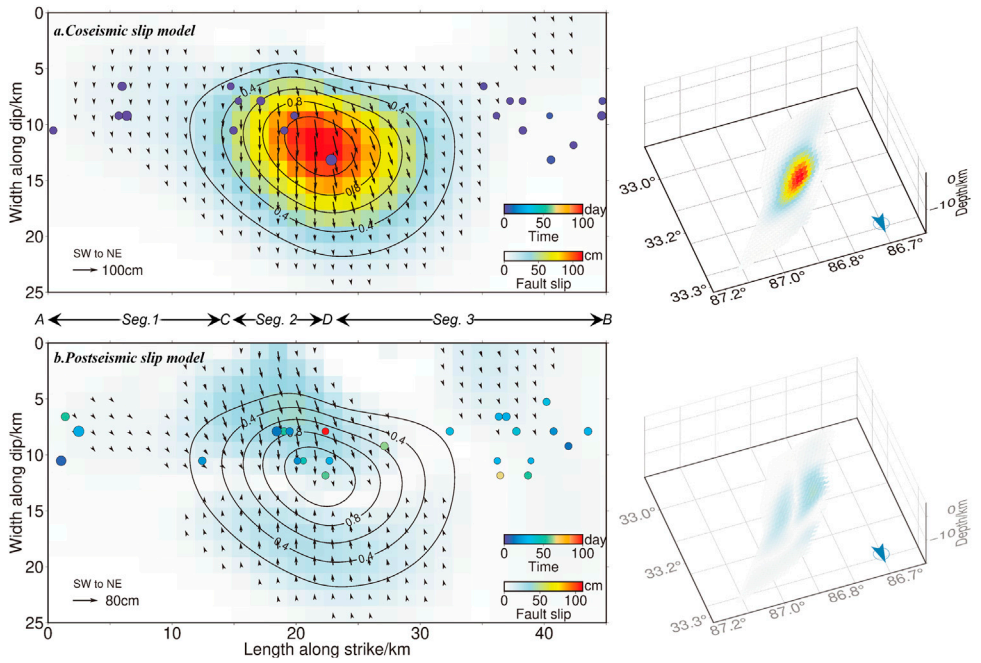

FIGURE 6
Two and three-dismension coseismic and postseismic slip models of the 2020 Nima earthquake. Color circle points indicate the initial 8-day and latter aftershocks, respectively. Characters **(A,B)** inidicate the faulting trace in Figures 2, 9, 10.

derive postseismic displacement time series (Figure 6, and Supplementary Figures S1–S7).

2.1.3 Cross verification of GNSS and InSAR displacements

We used the GNSS displacement sequence of station ROMA near the epicenter as the reference position to verify the postseismic motions derived from InSAR data. We converted the east, north, and up-component motions of each GNSS station into the line of sight (LoS) direction by the affine transformation, respectively. And then a logarithmic empirical Eq. (2) is used to fit the GNSS and InSAR displacement sequences, respectively.

$$X(t) = Aln\left(1 + \frac{t - t_0}{\tau}\right) \quad (2)$$

where A represents afterslip amplitude; t is the time series after the mainshock (t_0); τ describes the attenuation time of afterslip signs. Postseismic displacement sequences at Point 1, 2, and 3 in Figure 7 shows a high consistency between the GNSS and InSAR postseismic displacement sequences within 9 months after the mainshock (Supplementary Figure S8), which validates the filtered displacement sequences are reliable. As the LoS of the descending orbit is roughly parallel to the fault, the weak nonlinear displacement signs for descending orbit datasets are dropped even further during the spatio-temporal filtering processing.

2.2 Coseismic slip modeling

In Step 5 (Figure 3), we carry out a nonlinear inversion algorithm with the GBIS software package (Bagnardi and Hooper, 2018) based on the Okada model (Okada, 1985), to search for an optimal uniform slip model (Figure 5) and a subsample data of coseismic LoS displacement. The downsampled ascend and descend LoS displacement sequence, and the corrected GNSS east, north, and up-direction displacement sequence are inputted as three single data sets, and the distributed coseismic slip is modeled with the SDM software package (www.gfz-potsdam.de) (Wang et al., 2011) based on the layered earth structure in Figure. S13, with Poisson's ratio of 0.25. With the same layered model, each fault plane was subdivided into an array of rectangular patches 1 km ×1 km, Green's functions on each patch are computed by the PSGRN code (Wang et al., 2006). The weight ratio of GNSS and InSAR is set to 2, the smooth factor is 0.2. The initial fault parameters refer to the searched uniform slip model parameters (strike, dip, width, and length). For a fitting model with a high correlation coefficient and low residual error, it is necessary to adjust adequately the fault strike and dip (Table 1). Detailed inversion procedures are described in (Xia et al., 2022).

There is no obvious surface rupture observed, which makes it difficult to directly ascertain the seismogenic fault. Previous

InSAR research suggested different results on the seismogenic fault for the 2020 Nima earthquake, such as the east-dip WYF with a constant strike (Yang et al., 2021a; Ji et al., 2021; Li et al., 2021) or an unmapped east-dip branch fault with variable strikes and dips (Gao et al., 2022), instead of the west-dip EYF determined by geology (Liu et al., 2021). To determine the geometry parameters of the seismogenic fault, we check multiple alternative slip models (Table 1). For Model 1, referring to the previously mapped EYF (Line 5 in Figure 2), we set the bounds of [−90°, 0°] for the dip angle [0°, 50°], for the strike angle in 5° intervals, but the derived rake is -180° with a very small fitting degree of 30.3%. This result shows that the focus mechanism is pure strike-slip and incompatible with the regional tectonic background and the seismological focus mechanism solutions (Table 1). For Model 2, referring to the mapped WYF, we set a constant strike angle of 36°, a variable dip of [0°, 90°]. The root-mean-square (RMS) misfit residuals between the model and observations decreases with increasing dip, but the improvement is imperceptible for dips of >50°, and a corresponding rake of ~74° with a not too high correlation coefficient of 88%.

We found the RMS misfit is sensitive to changing the strike of the fault planes, which hints the seismogenic fault is not a straight single fault rather than a curve with variable strike and dip. We suppose the seismological trace along the trace ACDB in Figure 2 (Model 3 in Table 1), and set the bounds of [0°, 60°] for the dip angle, [0°, 50°] for the strike angle in 5° intervals, the misfit decays steeply, the correlation coefficient is greater than 99%. The RMS misfit residuals between the observations and simulated coseismic displacements are 0.6 cm and 0.7 cm in the LOS direction of T012A, T121D; and 1.7 cm and 1.4 cm in the East-West and North-South direction of GNSS observation, respectively (Supplementary Figure S9). As shown in Figure 6, the coseismic slip model is generally consistent with that suggested by (Gao et al., 2022), and shows more details than that derived by (Yang et al., 2021a; Ji et al., 2021; Li et al., 2021). Therefore, the model (segment 1: strike/dip/rake =28°/45°/−78°, segment 2: strike/dip/rake =13°/50°/−78°, segment 3: strike/dip/rake =36°/45°/−78°) is selected as our optimal coseismic slip model for the following analysis. The final model is a three-segmented fault with variable dips and strikes, and an average slip of −78°. Based on equations (8.83–8.91) in Thorne and Wallace (Lay and Wallace, 1995), the percentage of CLVD component is calculated and is 3.65. The peak slip of 1.36 m occurred at a depth of 8.5 km. Assuming a shear modulus of 30 GPa, the seismic moment tensor is $6.4 \times 10^{18}\, N \cdot m$, equivalent to Mw 6.42 (Table 1).

2.3 Postseismic slip modeling

It is difficult to separate the mainshock and the initial 8-day aftershocks in InSAR observations. We can only derive the coseismic deformation with the first 8-day postseismic deformation and the latter postseismic deformation. In Step 6 of Figure 3, as the same time windows and periods for InSAR and GPS observations, we firstly carry out the equivalent postseismic slip model (Li and Bürgmann, 2021) to derive differential LoS displacement sequence (Supplementary Figures S10, S11), and then combine the corrected GNSS displacement sequence to fit the postseismic slip models (Supplementary Figure S12) as the same procedure in Section 2.3. Error evaluation of the derived postseismic displacement and more data processing detailed can be found in another paper (Morishita et al., 2020). The pattern of observations and simulated postseismic displacements by the model is consistent with that of the coseismic, a significant displacement region occurred in the subsidence zone of the coseismic rupture and extend farther to the east of the coseismic rupture fault (Figure 7), the RMS misfit residuals are 1.3 cm and 1.4 cm in the LOS direction of T012A, T121D; and 1.1 and 1.3 cm in the East-West and North-South direction of GNSS observation, respectively. As shown in Figures 7E,F, the residuals mainly occurred near regions with large afterslip and the bottom right corner. So that, we think our postseismic slip model (Figure 6) is reliable.

The equivalent postsesimic slip shows afterslip occurred mainly near Segment 2 and the junction of Segment 2 and 3 (Figure 6). The cumulative afterslip moment within 9 months after the mainshock is $1 \times 10^{18}\, N \cdot m$, about 15.6% of that released by the mainshock coseismic slip. It is consistent with the estimated results based on typical crustal earthquake sequences (Kagan and Houston, 2005). Figure 8 shows the growth rate of cumulative displacement decays rapidly with time, it implies an obvious nonlinear trend. Most postseismic displacement concentrates in the first month after the mainshock, and from the sixth month, there was almost no apparent deformation.

2.4 Coulomb failure stress change

To characterize the process of postseismic stress transfer and the relationship between afterslip and aftershocks, based on a biviscous Burgers body (Supplementary Figure S13) with the friction coefficient of 0.4, Young's modulus of 30 GPa, Poisson's ratio of 0.25, we calculated the CFS change with depth (2–20 km) by the coseismic and postseismic faulting model (Figures 9, 10), as well as the profile of the coseismic CFS on the faulting surface with depth (Figure 11).

3 Discussion

3.1 Geometry complexity of the seismogenic fault

As shown in Figure 12, our finial coseismic slip model suggests a complex reversed "S-shape" fault structure

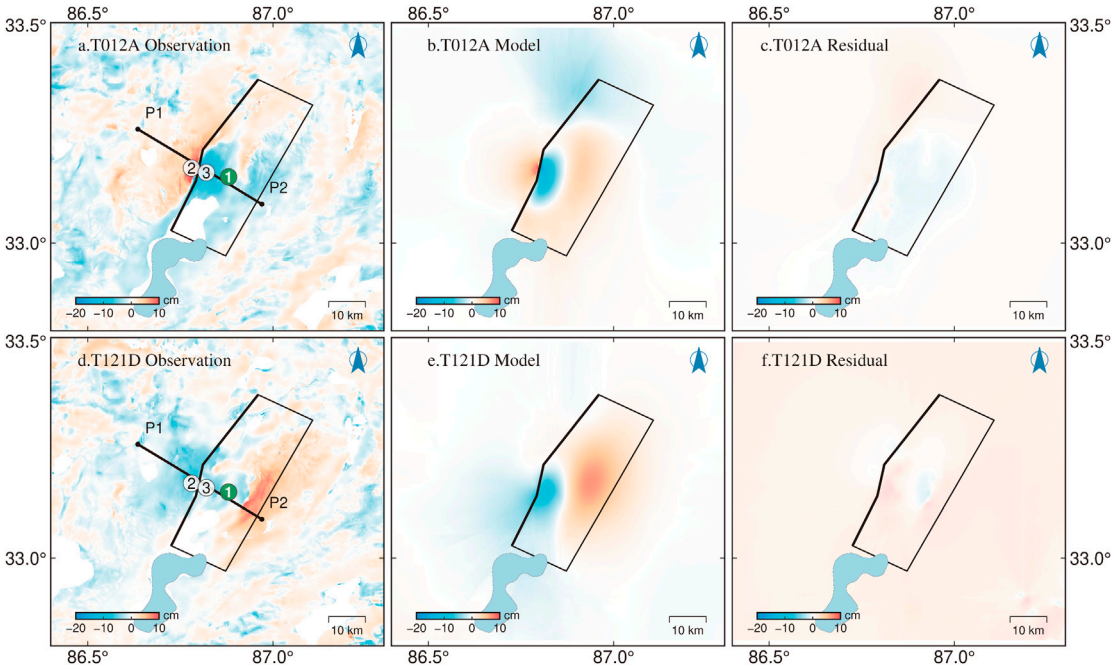

FIGURE 7
Postseismic deformation of the 2020 Nima earthquake inverted by the SDM method with residuals between the observations and simulated postseismc deformation by the model. Black box shows the surface projection of the rupture fault plane, which is derived from the optimal distributed slip model and thick black west side denotes the inferred seismogenic fault trace. The thick black line between P1 to P2 indicates the profile be addressed in Figure 8. The circles marked with 1, 2 and 3 indicate sample points in Supplementary Figure S8.

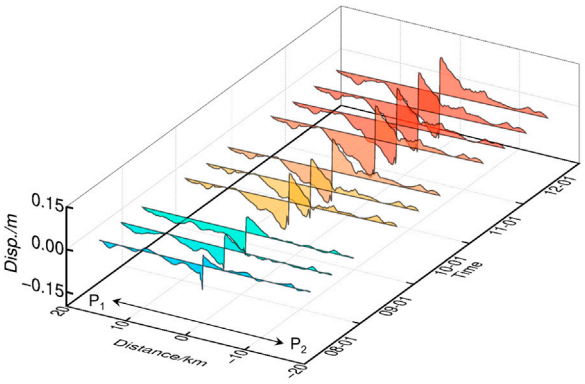

FIGURE 8
Cumulative postseismic displacement sequence of T012A along the profile P_1-P_2 in Figure 7. The color gradient from blue to red indicates amplitude of the displacement increment over time.

consisting of three segments within different dips of 45°–50°. The dip value is close to the other results (Table 1), and also consistent with the field observed fault dip of 45°–50°(Liu et al., 2021). No low-angle fault plane is found for this earthquake.

The overall trend of the seismogenic fault is about 28° and is well consistent with the orientation of regional existing geologic structures and the region shearing stress direction (Taylor et al., 2003). Large angle rotation of the rupture direction is unusual during earthquake propagation (Preuss et al., 2019). The seismogenic fault trace of the 2020 Nima earthquake shows two distinct rotations along the strike. As shown in Figure 12, Segment AC (strike/dip = 28°/45°) stretches about 15 km almost along the preexisting N36°E-striking WYF associated with sharp fault morphology (Molnar and Tapponnier, 1978). The significant slip concentrates on Segment CD (strike/dip = 13°/50°) at depths of 4–15 km. The rupture did not go on along the WYF, but rotated by about 15° to the north and along the bend of ~8 km near the intersection of the WYF and the HF. From the epicenter (located near point D) to the north, along Segment DB (strike/dip = 37°/45°), the rupture caused again a rotation of ~24°, and keep the N37°E direction and is parallel to the northern segment of the WYF.

The first rotation of the rupture strike was near the intersection of the WYF and the HF, with a lower fracture coefficient of the rock at the multi-faulting junction and thus stress localization, stress at the fault tip more easily exceeds a critical value and then promotes rupture propagation. The InSAR-derived source occurred near the north end (point D)

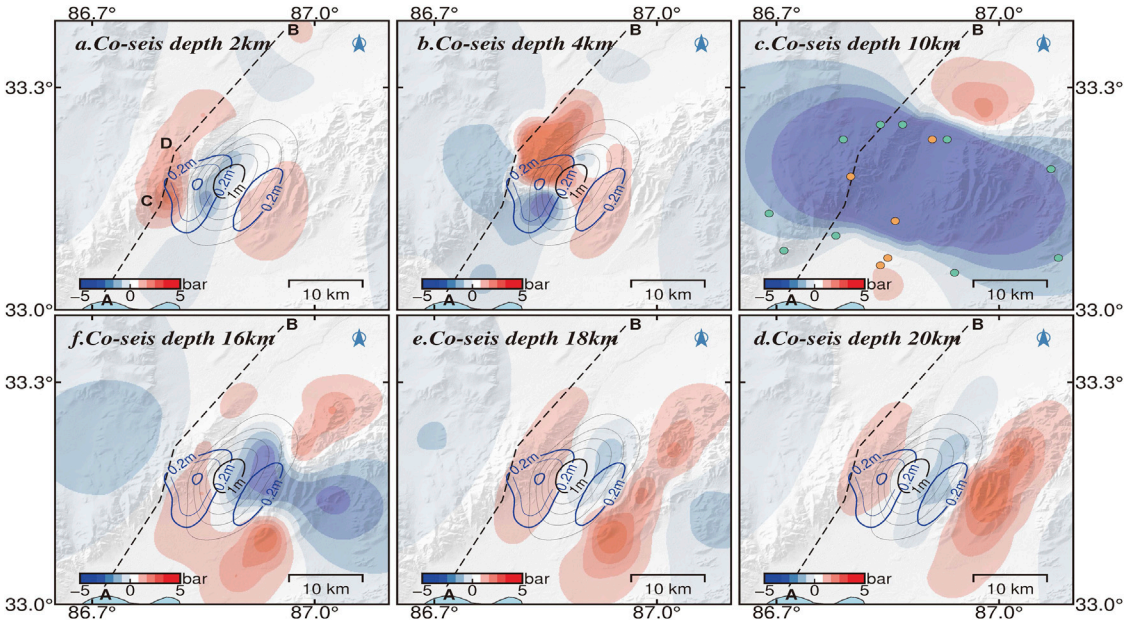

FIGURE 9
Coseismic Coulomb stress changes at different depths for the 2020 Nima earthquake. The dotted line AB indicates the seismogenic fault. The black (0.2 m interval) and blue (0.1 m interval) lines indicate the coseismic and postseismic slip isoline projected on the surface, respectively. The green and yellow circles represent the latter aftershocks of 4 ≥ M ≥ 3 and ≥4, respectively.

of the bend, which may be in response to stress localization in such a relatively weak material condition (Dayem et al., 2009). The second rotation occurred on Segment DB, which is located in the hanging wall of the WYF and away from the central graben. This segment is not a previously mapped fault and is buried under the unconsolidated Holocene alluvium of the Nanliu and Jiangai-Zangbu rivers. The stress field around mature fault zones is often misaligned with existing faults (Preuss et al., 2019), and then promotes the reactivation of inactive and potentially blind or unknown branches, on account of long-term reorientation of stresses because of strain accumulation, construction complexity, and so on. Therefore, we suggest that it is likely to be a younger blind fault parallel to the remote stress field, which is reactivated during this event. In addition, the aftershock distribution pattern is not a familiar band along the seismogenic fault, rather than a fan with the center axis of the seismogenic fault (Figure 2). Such a fan pattern is consistent with the lateral extension of the negative flower structure of the Yibu-Chaka graben. Taken together, the relaxation process of the 2020 Nima earthquake may be dominated by the multi-segmented fault rupture, consisting of the inherited activity of the preexisting WYF and the dynamic-triggering activity of the blind fault.

More generally, the multi-segmented rupture of moderate earthquakes had been observed in other regions by geodetic data. The 2008 Nima-Geizhe double earthquakes (Mw 6.4 and Mw 5.9) occurred in the southern end of the Yibug-Caka-Rigen fault, and rupture two parallel NNE-trending normal faults (He and Gilles, 2010). The 2018 Mw 6.4 earthquake simultaneously ruptured the north segment of the east-dip sinistral Milun Fault and an unknown west-dipping fault, but the postseismic slip occurred only in the south segment of the Milun fault (Yang et al., 2018). The 2017 Sulphur Peak M5.3 earthquake simultaneously triggered shear and extensional fractures on a group of intersecting faults (Pollitz et al., 2019). The synthetic inversion result of remote seismic waves, InSAR, and aftershock precise location datasets uncover the 2020 Stanley Mw 6.5 earthquake was mainly strike-slip, with both normal dip-slip and thrust components with a non-DC component ratio of 35%, which reflect the simultaneous rupture of a group of opposite-dipping sinistral faults and normal faults (Yang et al., 2021b).

The non-DC component reflects the complexity of the focal mechanism (Zhu and Ben-Zion, 2013). Like the Stanley earthquake, the 2020 Nima earthquake ruptured a multi-segmented fault with variable strike and dip and produced also a non-DC component of 3.65%, which may be associated with the existence of splay subfaults (Kuge and Lay, 1994), although the value is less than the results from the long-period point-source solutions (Table 1), possibly because of different source data and estimation procedures. When shearing ruptures of intersected faulting planes are not parallel to each other with different geometry, observed

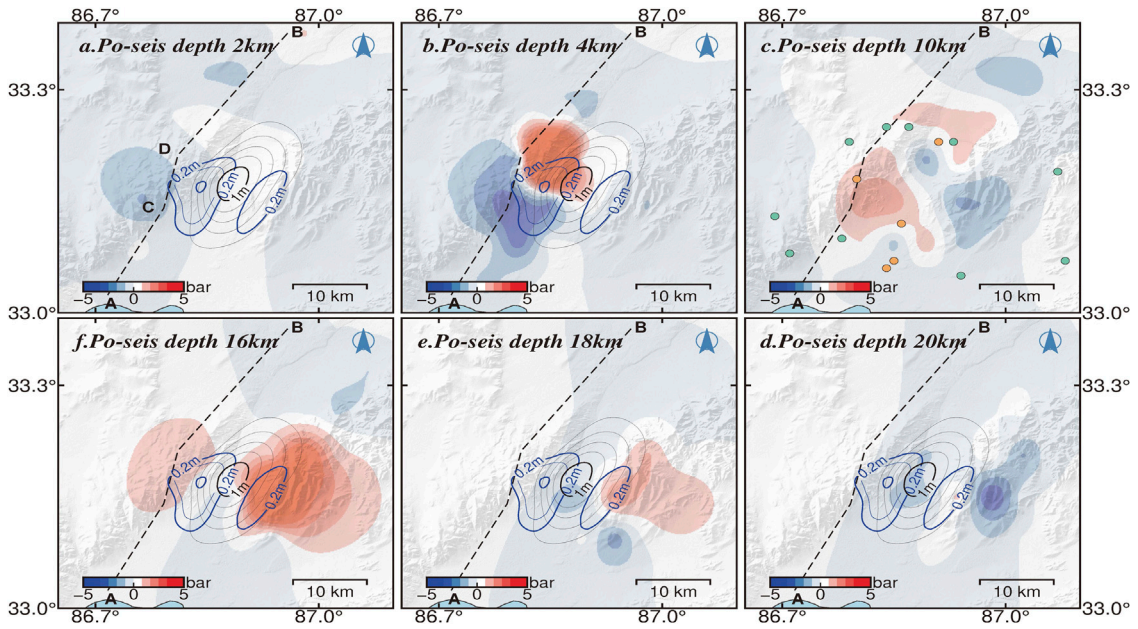

FIGURE 10
Postseismic Coulomb stress changes at different depths for the 2020 Nima earthquake. Captions are as for Figure 9.

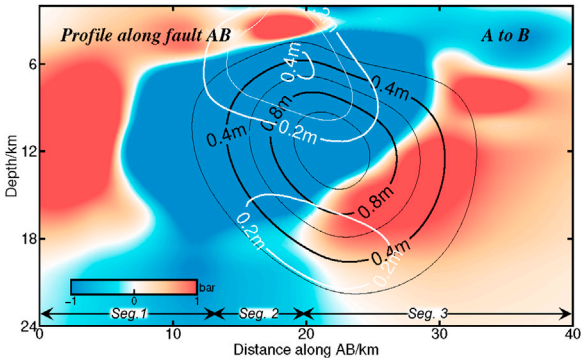

FIGURE 11
Coseismic Coulomb stress change at different depths along the faulting trace. The black and white lines indicate the coseismic and postseismic slip isoline projected on the surface, respectively. Caption is as for Figures 2, 6.

seismic waves from these faults with different strikes are added together and indistinguishable, and then resolved as a single event. In this way, the sum of the moment tensors of the different faults will give a seeming composite mechanism with an obvious non-DC component (Julian et al., 1998), which hints at the predictable geometry complexity of the seismogenic fault. The 2020 Nima earthquake indicates that moderate earthquakes may also occur on the complex fault structure, particularly in geologically complex regions, although do not contribute to building topographic relief (Wang et al., 2014).

3.2 Mechanics of postseismic deformation

The spatiotemporal distribution of postseismic deformation provides important clues to the mechanism of afterslip. Yang et al. suggested that the postseismic deformation was dominated by aseismic slip (Yang et al., 2021a), which is inconsistent with the result of slow slip on a parallel branch to the west of the seismogenic fault suggested by Gao et al. (Gao et al., 2022). As shown in Figure 7, the postseismic slip zone was complementary to the coseismic slip zone in space (Wallace et al., 2018), and the significant postseismic slip concentrated on Segment 2. The latter $M \geq 3$ aftershocks mostly occurred in the negative coseismic CFS zone (Figure 9). Although the stress along Segment AC had fully released, that along Segment CD is still loading weakly beneath the focus depth. The cumulative seismic moment was not fully released by the mainshock and aftershocks. The cumulative postseismic moment over 9 months is ~15.6% of the seismic moment and is larger than 8% over 6 months estimated by Yang et al. (Yang et al., 2021a), but the moment contributed by aftershocks is only a few percent of the total postseismic moment. Therefore, afterslip may mostly contribute to the release of additional seismic energy.

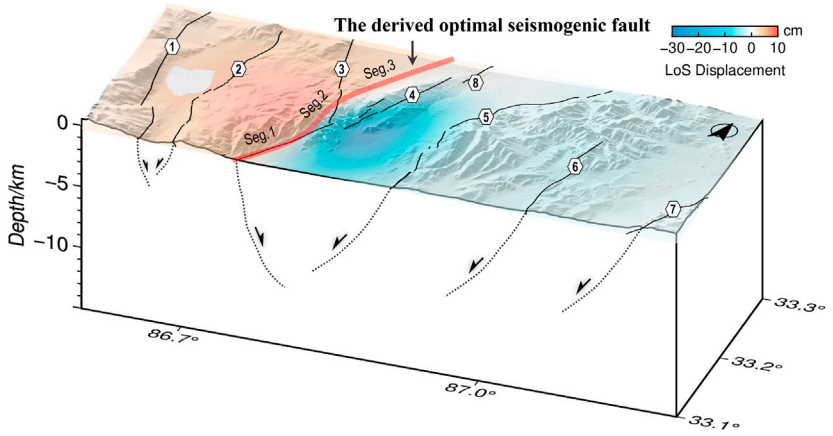

FIGURE 12
3D structure of the active normal faults in the Yibu-Chaka graben and the derived optimal seismogenic fault of the 2020 Nima earthquake. Black lines in the section indicate normal faulting. Caption is as for Figures 2, 6.

In addition, two relatively obvious stress loading zones occurred on Segment DB at the 4 km depth and on the EYF at the 16 km depth, respectively (Figure 10), the corresponding CFS change exceed 1 bar (Figure 11). Meanwhile, the rake angle of the upper and lower portion of the postseismic slip are opposite and with a 42 cm down-dip peak slip at the depth of ~4 km and a 31 cm peak up-slip at the depth of ~18 km, respectively (Figure 7). All focal mechanism solutions of aftershocks of M > 4.5 reported by the GCMT (Supplementary Table S3) showed primarily normal faulting with a minor left-lateral strike-slip component, and all of the aftershocks occurred in the depth of 6–9 km (Figure 7). Moreover, around the north of the seismogenic fault, Li et al. found some tectonic extension cracks and surface breaks related to surface shaking (Li et al., 2021). Therefore, we prefer to suggest that creeping into the shallow zone could be facilitated by stress perturbations. Migration of the latter aftershocks (except the first 8 days), spreading generally out on the northwest and northeast sides of the seismogenic fault (Figure 2), shows the dynamic stress-releasing process after the mainshock. Taking together, such a slight deep up-slip afterslip, the lack of aftershocks in the afterslip zone, as well as the stress loading along the EYF, indicated a triggered activity on the west-dipping EYF or more normal faults on the east side of the graben. In this way, as a result of the shear stress changes and redistribution of upper crustal material from the hanging wall of the east normal faults, the weak uplift occurs as material flows in toward rupture tips along fault slip direction (Ryder et al., 2010).

In the case of Nima, the mainshock and all aftershocks occurred in the upper crust of <10 km (Figure 7), but the coseismic rupture and afterslip extended more than 20 km beneath the surface, rather than was limited to the shallow upper crust. It is obvious substantial down-dip slip occurred on the fault plane from the surface down to the depth, larger than the effective viscoelastic layer thickness of ~10 km in central Tibet (England et al., 2013; Liu-Zeng et al., 2020) and the long-term equivalent elastic thickness of 10–12 km in the Tibetan plateau (Molnar and Chen, 1983; Molnar and Lyon-Caent, 1989; Chu et al., 2009). Meanwhile, the slight deep upslip afterslip occurred in the transition zone of brittle-ductile shear deformation. These deep stress loading/releasing regimes reveal where extension of the negative flower structure at depth, which is not shallow. The extensional structure may extend deeper at depth and broader at lateral direction and reflects the complex faulting at this region. It is implications for the rheology of down-dip extension of the dipping faults or shear zones in northern Tibet (England et al., 2013; Liu-Zeng et al., 2020) and provides clues to the rheological properties of the lower crust of the Tibetan plateau (Shi et al., 2012; England et al., 2013).

3.3 Future earthquake risk

The epicenter of the 2020 Nima earthquake occurred at the center of the Yibu-Chaka graben, but the northern segment of the seismogenic structure didn't spread along the high-relief western edge of the graben. Such an apparent spatial mismatch between moderate magnitude earthquakes and long-term geomorphic expression of major active faults is surprisingly common in southern Tibet. For instance, in the 2008 Mw 6.3 Damxung earthquake, the 2005 Mw 6.2 Zhongba earthquake, and the 1992 Mw 6.1 Nyemo earthquake (Elliott et al., 2010), the Mw 5.5+ Xaitongmoin earthquake sequence in the 1990s (Wang et al., 2014), don't always occur on previously mapped faults associated with clear surface geomorphology.

The 2020 Nima earthquake implies that the potentially seismic disasters in widespread extensional zones in Tibet can occur away from the previous mapped active faults in the graben (Taylor et al., 2003), and may be more broadly distributed than implied by the clear surface topography (Wang et al., 2014). The interaction of two opposite-dipping faults is promoted by stress transfer, which can enhance seismic hazards within years after an earthquake (Jia et al., 2021). Two obvious stress loading zones of more than 1 bar, around the EYF and the east-dip blind fault, have increased the future earthquake risk. Especially, the junction between normal faults and ends of the large-scale sinistral Riganpei-Co and Jiangai-Zangbu faults has the potential for an M > 7 seismic rupture (Li et al., 2021).

4 Conclusion

We invert the coseismic and postseismic displacement of the 2020 Nima earthquake using jointly InSAR and GNSS datasets over the first 9 months. Our results suggest the Nima earthquake ruptured a complex reversed "S-shape" structure with variable strike and dip at multi-fault junctions. Multiple faults were ruptured during the event, including at least the east-dip West Yibu-Chaka fault, the northeast-dip Heishi fault, and a previously unmapped younger east-dip blind fault, and then promoted to reactivation of the west-dip normal fault system on the east side of the Yibu-Chaka graben. The geometry complexity of the seismogenic fault may lead to the large non-DC component in the long-period point-source solutions. The Coulomb failure stress change calculated by the coseismic and postseismic slip model shows that significant stress at the shallow depth of <10 km was released mainly by the mainshock and aftershocks. The shallow creep at the depth of ~4 km around the junction between the northern segment of the West Yibu-Chaka fault and the blind fault could be facilitated by stress perturbations. The deep uplift of >16 km depth extended within the brittle-ductile transition zone down-dip of the coseismic rupture zone. It indicates the rheology of the down-dip extension of the dipping faults in northern Tibet. The Coulomb failure stress change of >1 bar around the East Yibu-Chaka fault and the blind fault highlights seismic hazards in the region, especially in the junction between normal faults and ends of the large-scale sinistral Riganpei-Co and Jiangai-Zangbu faults. It is necessary to forecast accurately by longer-term afterslip observation over timescales of years for the faults.

Data availability statement

The original contributions presented in the study are included in the article/Supplementary Material, further inquiries can be directed to the corresponding author.

Author contributions

XL and JL-Z conceived and designed the experiments; XL, TX, and DD performed the ex-periments; TX and PY analyzed the InSAR data; ZJ, PW, and WW analyzed the GNSS data; XL wrote the paper, and all co-authors contributed to the writing. All authors have read and agreed to the published version of the manuscript.

Funding

This work is supported by Science for Earthquake Resilience, China Earthquake Administration (XH22003C), the National Natural Science Foundation of China (U1839203 and 42011540385).

Acknowledgments

Our thanks go to Teng Wang, Minhan Sheng, Guixi Yi, Changsheng Jiang, Li Li, Shengle Li, Hongwei Tu, Guichun Wei, and Wei Wang for their help and discussions. All Sentinel-1A SAR data are copyrighted by the European Space Agency. Atmospheric corrected data were downloaded from the Generic Atmospheric Correction Online Service for InSAR. Most figures were made using the public domain Generic Mapping Tools (Wessel and Smith, 1998).

Conflict of interest

The authors declare that the research was conducted in the absence of any commercial or financial relationships that could be construed as a potential conflict of interest.

Publisher's note

Supplementary material

The Supplementary Material for this article can be found online at: https://www.frontiersin.org/articles/10.3389/feart.2022.1012773/full#supplementary-material.

References

Armijo, R., Tapponnier, P., and Han, T. (1989). Late Cenozoic right-lateral strike-slip faulting in southern Tibet. *J. Geophys. Res.* 94 (B3), 2787–2838. doi:10.1029/JB094iB03p02787

Bagnardi, M., and Hooper, A. (2018). Inversion of surface deformation data for rapid estimates of source parameters and uncertainties: A bayesian approach. *Geochem. Geophys. Geosyst.* 19 (7), 2194–2211. doi:10.1029/2018gc007585

Blisniuk, P. M., and Sharp, W. D. (2003). Rates of late Quaternary normal faulting in central Tibet from U-series dating of pedogenic carbonate in displaced fluvial gravel deposits. *Earth Planet. Sci. Lett.* 215 (1-2), 169–186. doi:10.1016/s0012-821x(03)00374-1

Bürgmann, R., and Dresen, G. (2008). Rheology of the lower crust and upper mantle: Evidence from rock mechanics, geodesy, and field observations. *Annu. Rev. Earth Planet. Sci.* 36 (1), 531–567. doi:10.1146/annurev.earth.36.031207.124326

Chen, C. W., and Zebker, H. A. (2001). Two-dimensional phase unwrapping with use of statistical models for cost functions in nonlinear optimization. *J. Opt. Soc. Am. A* 18 (2), 338–351. doi:10.1364/josaa.18.000338

Chevalier, M.-L., Tapponnier, P., van der Woerd, J., Leloup, P. H., Wang, S., Pan, J., et al. (2020). Late quaternary extension rates across the northern half of the yadong-gulu rift: Implication for East-West extension in southern Tibet. *J. Geophys. Res. Solid Earth* 125 (7), e2019JB019106. doi:10.1029/2019JB019106

Chu, R., Zhu, L., and Helmberger, D. V. (2009). Determination of earthquake focal depths and source time functions in central Asia using teleseismic P waveforms. *Geophys. Res. Lett.* 36 (17), L17317. doi:10.1029/2009GL039494

Dayem, K. E., Houseman, G. A., and Molnar, P. (2009). Localization of shear along a lithospheric strength discontinuity: Application of a continuous deformation model to the boundary between Tibet and the Tarim Basin. *Tectonics* 28 (3), 2264. doi:10.1029/2008TC002264

Elliott, J. R., Walters, R. J., England, P. C., Jackson, J. A., Li, Z., and Parsons, B. (2010). Extension on the Tibetan plateau: Recent normal faulting measured by InSAR and body wave seismology. *Geophys. J. Int.* 183 (2), 503–535. doi:10.1111/j.1365-246X.2010.04754.x

England, P. C., Walker, R. T., Fu, B., and Floyd, M. A. (2013). A bound on the viscosity of the Tibetan crust from the horizontality of palaeolake shorelines. *Earth Planet. Sci. Lett.* 375, 44–56. doi:10.1016/j.epsl.2013.05.001

Farr, T. G., and Kobrick, M. (2000). Shuttle radar topography mission produces a wealth of data. *Eos Trans. AGU.* 81 (48), 583–585. doi:10.1029/EO081i048p00583

Frohlich, C. (1994). Earthquakes with non-double-couple mechanisms. *Science* 264 (5160), 804–809. doi:10.1126/science.264.5160.804

Gao, H., Liao, M., Liang, X., Feng, G., and Wang, G. (2022). Coseismic and postseismic fault kinematics of the july 22, 2020, Nima (Tibet) Ms6.6 earthquake: Implications of the forming mechanism of the active N-S-trending grabens in qiangtang, Tibet. *Tectonics* 41 (3), e2021TC006949. doi:10.1029/2021TC006949

Goldstein, R. M., and Werner, C. L. (1998). Radar interferogram filtering for geophysical applications. *Geophys. Res. Lett.* 25 (21), 4035–4038. doi:10.1029/1998gl900033

Ha, G., Wu, Z., and Liu, F. (2019). Late quaternary vertical slip rates along the southern yadong–gulu rift, southern Tibetan plateau. *Tectonophysics* 755, 75–90. doi:10.1016/j.tecto.2019.02.014

Han, S., Li, H., Pan, J., Lu, H., Zheng, Y., Liu, D., et al. (2018). Co-Seismic surface ruptures in qiangtang terrane: Insight into late cenozoic deformation of central Tibet. *Tectonophysics* 750, 359–378. doi:10.1016/j.tecto.2018.11.001

Harrison, T. M., Copeland, P., Kidd, W. S. F., and Lovera, O. M. (1995). Activation of the nyainqentanghla shear zone: Implications for uplift of the southern Tibetan plateau. *Tectonics* 14, 658–676. doi:10.1029/95tc00608

He, J., and Gilles, P. (2010). Poroelastic triggering in the 9-22 january 2008 nima-gaize (Tibet) earthquake sequence. *Geology* 38 (10), p907–p910. doi:10.1130/g31104.1

Herring, T., King, R. W., Floyd, M., and McClusky, S. (2018). *Introduction to GAMIT/GLOBK release 10.7*. Cambridge: Massachusetts Institute of Technology.

Ji, Z., Zhang, Y., and Wang, S. (2021). Coseismic deformation field and fault slip distribution inversion of the Ms 6.6 Nima, Xizang earthquake by Sentinel-1A InSAR data. *Prog. Geophys.* 1, 1–10. doi:10.6038/pg2021EE0489

Jia, K., Zhou, S., Zhuang, J., and Jiang, C. (2021). Stress transfer along the western boundary of the bayan har block on the Tibet Plateau from the 2008 to 2020 yutian earthquake sequence in China. *Geophys. Res. Lett.* 48, e94125. doi:10.1029/2021gl094125

Julian, B. R., Miller, A. D., and Foulger, G. R. (1998). Non-double-couple earthquakes 1. Theory. *Rev. Geophys.* 36 (4), 525–549. doi:10.1029/98RG00716

Kagan, Y. Y., and Houston, H. (2005). Relation between mainshock rupture process and Omori's law for aftershock moment release rate. *Geophys. J. Int.* 163 (3), 1039–1048. doi:10.1111/j.1365-246X.2005.02772.x

Kapp, P., Taylor, M., Stockli, D., and Ding, L. (2008). Development of active low-angle normal fault systems during orogenic collapse: Insight from Tibet. *Geol.* 36 (1), 7–10. doi:10.1130/g24054a.1

Kuge, K., and Lay, T. (1994). Systematic non-double-couple components of earthquake mechanisms: The role of fault zone irregularity. *J. Geophys. Res.* 99, 15457–15467. doi:10.1029/94jb00140

Lay, T., and Wallace, T. C. (1995). *Modern global seismology*. San Diego: Academic Press.

Lazecký, M., Spaans, K., González, P. J., Maghsoudi, Y., Morishita, Y., Albino, F., et al. (2020). LiCSAR: An automatic InSAR tool for measuring and monitoring tectonic and volcanic activity. *Remote Sens.* 12 (15), 2430. doi:10.3390/rs12152430

Li, K., Kirby, E., Xu, X., Chen, G., Ren, J., and Wang, D. (2019). Rates of Holocene normal faulting along the Dong Co fault in central Tibet, based on 14C dating of displaced fluvial terraces. *J. Asian Earth Sci.* 183, 103962. doi:10.1016/j.jseaes.2019.103962

Li, K., Li, Y., Tapponnier, P., Xu, X., Li, D., and He, Z. (2021). Joint InSAR and field constraints on faulting during the Mw 6.4, july 23, 2020, nima/rongma earthquake in central Tibet. *JGR. Solid Earth* 126 (9), e2021JB022212. doi:10.1029/2021JB022212

Li, Y., and Bürgmann, R. (2021). Partial coupling and earthquake potential along the xianshuihe fault, China. *JGR. Solid Earth* 126 (7), e2020JB021406. doi:10.1029/2020JB021406

Liu, F.-c., Pan, J.-w., Li, H.-b., Sun, Z.-m., Liu, D.-l., Lu, H.-j., et al. (2021). Characteristics of quaternary activities along the Riganpei Co fault and seismogenic structure of the july 23, 2020 Mw6.4 Nima earthquake, central Tibet. *Acta Geosci. Sin.* 42 (1), 139–154. doi:10.3975/cagsb.2021.010402

Liu-Zeng, J., Zhang, Z., Rollins, C., Gualandi, A., Avouac, J.-P., Shi, H., et al. (2020). Postseismic deformation following the 2015 Mw7.8 gorkha (Nepal) earthquake: New GPS data, kinematic and dynamic models, and the roles of afterslip and viscoelastic relaxation. *J. Geophys. Res. Solid Earth* 125 (9), e2020JB019852. doi:10.1029/2020JB019852

McKenzie, D., Nimmo, F., Jackson, J. A., Gans, P. B., and Miller, E. L. (2000). Characteristics and consequences of flow in the lower crust. *J. Geophys. Res.* 105 (B5), 11029–11046. doi:10.1029/1999JB900446

Molnar, P., and Chen, W.-P. (1983). Focal depths and fault plane solutions of earthquakes under the Tibetan Plateau. *J. Geophys. Res.* 88 (B2), 1180–1196. doi:10.1029/JB088iB02p01180

Molnar, P., and Lyon-Caent, H. (1989). Fault plane solutions of earthquakes and active tectonics of the Tibetan Plateau and its margins. *Geophys. J. Int.* 99 (1), 123–154. doi:10.1111/j.1365-246X.1989.tb02020.x

Molnar, P., and Tapponnier, P. (1978). Active tectonics of Tibet. *J. Geophys. Res.* 83 (B11), 5361–5375. doi:10.1029/JB083iB11p05361

Morishita, Y., Lazecky, M., Wright, T. J., Weiss, J. R., Elliott, J. R., and Hooper, A. (2020). LiCSBAS: An open-source InSAR time series analysis package integrated with the LiCSAR automated sentinel-1 InSAR processor. *Remote Sens.* 12 (3), 424. doi:10.3390/rs12030424

Okada, Y. (1985). Surface deformation due to shear and tensile faults in a half-space. *Bull. Seismol. Soc. Am.* 75, 1135–1154. doi:10.1785/bssa0750041135

Pollitz, F. F., Wicks, C., Yeck, W. L., and Evans, J. (2019). fault slip associated with the 2 september 2017 M 5.3 Sulphur peak, Idaho, earthquake and aftershock sequence. *Bull. Seismol. Soc. Am.* 109 (3), 875–887. doi:10.1785/0120180206

Preuss, S., Herrendörfer, R., Gerya, T., Ampuero, J.-P., and van Dinther, Y. (2019). Seismic and aseismic fault growth lead to different fault orientations. *J. Geophys. Res. Solid Earth* 124 (8), 8867–8889. doi:10.1029/2019JB017324

Ryder, I., Bürgmann, R., and Sun, J. (2010). Tandem afterslip on connected fault planes following the 2008 Nima-Gaize (Tibet) earthquake. *J. Geophys. Res.* 115 (B3), B03404. doi:10.1029/2009JB006423

Shi, X., Kirby, E., Furlong, K. P., Wang, E., Meng, K., Phillips, F. M., et al. (2012). Preliminary constraints on rheology of the deep crust beneath central Tibet from late pleistocene—early Holocene shorelines. *Geophys. Res. Abstr.* EGU2012-10796 (14), 1.

Tapponnier, P., Zhiqin, X., Roger, F., Meyer, B., Arnaud, N., Wittlinger, G., et al. (2001). Oblique stepwise rise and growth of the Tibet Plateau. *Science* 294 (5547), 1671–1677. doi:10.1126/science.105978

Taylor, M., and An, Y. (2009). Active structures of the Himalayan-Tibetan orogen and their relationships to earthquake distribution, contemporary strain field, and Cenozoic volcanism. *Geosphere* 5 (3), 199–214. doi:10.1130/ges00217.s1

Taylor, M., Yin, A., Ryerson, F. J., Kapp, P., and Ding, L. (2003). Conjugate strike-slip faulting along the Bangong-Nujiang suture zone accommodates coeval east-west extension and north-south shortening in the interior of the Tibetan Plateau. *Tectonics* 22 (4), 1361. doi:10.1029/2002TC001361

Wallace, L. M., Hreinsdóttir, S., Ellis, S., Hamling, I., D'Anastasio, E., and Denys, P. (2018). Triggered slow slip and afterslip on the southern hikurangi subduction zone following the kaikōura earthquake. *Geophys. Res. Lett.* 45 (10), 4710–4718. doi:10.1002/2018gl077385

Wang, H., Elliott, J. R., Craig, T. J., Wright, T. J., Liu-Zeng, J., and Hooper, A. (2014). Normal faulting sequence in the Pumqu-Xainza Rift constrained by InSAR and teleseismic body-wave seismology. *Geochem. Geophys. Geosyst.* 15 (7), 2947–2963. doi:10.1002/2014GC005369

Wang, M., and Shen, Z.-K. (2020). Present-day crustal deformation of continental China derived from GPS and its tectonic implications. *J. Geophys. Res. Solid Earth* 125 (2), e2019JB018774. doi:10.1029/2019JB018774

Wang, R., Lorenzo-Martín, F., and Roth, F. (2006). PSGRN/PSCMP—A new code for calculating co- and post-seismic deformation, geoid and gravity changes based on the viscoelastic-gravitational dislocation theory. *Comput. Geosciences* 32 (4), 527–541. doi:10.1016/j.cageo.2005.08.006

Wang, R., Schurr, B., Milkereit, C., Shao, Z., and Jin, M. (2011). An improved automatic scheme for empirical baseline correction of digital strong-motion records. *Bull. Seismol. Soc. Am.* 101 (5), 2029–2044. doi:10.1785/0120110039

Wang, S., Chevalier, M.-L., Pan, J., Bai, M., Li, K., Li, H., et al. (2020). Quantification of the late Quaternary throw rates along the Yadong rift, southern Tibet. *Tectonophysics* 790, 228545. doi:10.1016/j.tecto.2020.228545

Wessel, P., and Smith, W. (1998). New, improved version of generic mapping tools released. *Eos Trans. AGU.* 79 (47), 579. doi:10.1029/98eo00426

Wu, Z., Long, C., Fan, T., Zhou, C., Feng, H., Yang, Z., et al. (2015). The arc rotational-shear active tectonic system on the southeastern margin of Tibetan Plateau and its dynamic characteristics and mechanism. *Geol. Bull. China* 34 (01), 1–31.

Xia, T., Liu, X., Yu, P., Deng, D., Yue, Z., and Gao, T. (2022). Coseismic rupture model of the 2021 shuanghu M5.7 earthquake based on sentinel-1A. *J. Geodesy Geodyn.* 42 (5), 533–540. doi:10.14075/j.jgg.2022.05.017

Yang, J., Xu, C., Wen, Y., and Xu, G. (2021a). The july 2020 Mw 6.3 Nima earthquake, central Tibet: A shallow normal-faulting event rupturing in a stepover zone. *Seismol. Res. Lett.* 93 (1), 45–55. doi:10.1785/0220210057

Yang, J., Zhu, H., Lay, T., Niu, Y., Ye, L., Lu, Z., et al. (2021b). Multi-fault opposing-dip strike-slip and normal-fault rupture during the 2020 Mw 6.5 Stanley, Idaho earthquake. *Geophys. Res. Lett.* 48 (10), e2021GL092510. doi:10.1029/2021GL092510

Yang, Y.-H., Hu, J.-C., Tung, H., Tsai, M.-C., Chen, Q., Xu, Q., et al. (2018). Co-seismic and postseismic fault models of the 2018 Mw 6.4 hualien earthquake occurred in the junction of collision and subduction boundaries offshore eastern taiwan. *Remote Sens.* 10 (9), 1372. doi:10.3390/rs10091372

Yin, A., Kap, P. A., and Paul, A. (1999). Significant late Neogene east-west extension in northern Tibet. *Geology* 27, 787–790. doi:10.1130/0091-7613(1999)027<0787:SLNEWE>2.3.CO;2

Yin, A., and Taylor, M. H. (2011). Mechanics of V-shaped conjugate strike-slip faults and the corresponding continuum mode of continental deformation. *Geol. Soc. Am. Bull.* 123 (9-10), 1798–1821. doi:10.1130/b30159.1

Yu, C., Li, Z., Penna, N. T., and Crippa, P. (2018). Generic atmospheric correction model for interferometric synthetic aperture radar observations. *J. Geophys. Res. Solid Earth* 123 (10), 9202–9222. doi:10.1029/2017jb015305

Zhu, L., and Ben-Zion, Y. (2013). Parametrization of general seismic potency and moment tensors for source inversion of seismic waveform data. *Geophys. J. Int.* 194 (2), 839–843. doi:10.1093/gji/ggt137

frontiers | Frontiers in Earth Science

TYPE Original Research
PUBLISHED 20 January 2023
DOI 10.3389/feart.2022.1058243

OPEN ACCESS

EDITED BY
Xinjian Shan,
Institute of Geology, China Earthquake Administration, China

REVIEWED BY
Zhongtai He,
Ministry of Emergency Management, China
Dongliang Liu,
Chinese Academy of Geological Sciences (CAGS), China

*CORRESPONDENCE
Lingyun Ji,
jilingyun@smac.ac.cn

SPECIALTY SECTION
This article was submitted to Structural Geology and Tectonics, a section of the journal Frontiers in Earth Science

RECEIVED 30 September 2022
ACCEPTED 29 November 2022
PUBLISHED 20 January 2023

CITATION
Yang C, Ji L, Yang Y, Su L, Wang Y and Shi H (2023), Present-day activity and seismic potential of the north Qinling fault, southern ordos block, central China, as revealed from GPS data and seismicity.
Front. Earth Sci. 10:1058243.
doi: 10.3389/feart.2022.1058243

Present-day activity and seismic potential of the north Qinling fault, southern ordos block, central China, as revealed from GPS data and seismicity

Chenyi Yang[1], Lingyun Ji[2]*, Yihai Yang[1], Lina Su[1], Ying Wang[1] and Huiren Shi[1]

[1]Shaanxi Earthquake Agency, Xi'an, China, [2]The Second Monitoring and Application Center, China Earthquake Administration, Xi'an, China

The North Qinling Fault, located at the boundary of the North China Block and the South China Block, represents an important tectonic structure between the Weihe Basin and the Qinling Mountains, and controls the subsidence and expansion of the Weihe Basin. This fault has been highly active and has caused strong earthquakes since the Holocene and in a pre-seismic stage currently, as indicated by the many paleoearthquake traces found along it. To determine the present-day activity and seismic potential of the North Qinling Fault, by inverting GPS data, we produced fault locking depth, slip rate, and regional strain fields maps; moreover, based on seismicity, we produced a seismic b-value map. Combining this information with modern seismicity, we were able to comprehensively analyze the seismic potential of different fault segments. Our inversion of GPS data showed that the slip rate of the western segment of the fault (Qingjiangkou–Xitangyu) and the correspondent locking depth are 1.33 mm/a and 13.54 km, respectively, while the slip rate of the middle segment (Xitangyu–Fengyukou) and the correspondent locking depth are 0.45 mm/a and 8.58 km, respectively; finally, the slip rate of the eastern segment (Xitangyu–Daiyu) and the correspondent locking depth are 0.36 mm/a and 21.46 km, respectively. The locking depths of the western and middle segments of the fault are shallower than 90% of the seismic cutoff depth, while the locking depth of the eastern segment of the fault is similar to 90% of the seismic cutoff depth, indicating that "deep creep" occurs in the western and middle segments, while the eastern segment is locked. Modern small earthquakes have involved the western and middle segments of the fault, while the eastern segment has acted as a seismic gap with weak seismicity, characterized by a higher shear strain value and a lower b-value. These characteristics reflect the relationship between the locking depth and seismicity distribution. The results of our comprehensive analysis, combined with field geological surveys, show that the eastern segment of the North Qinling Fault has a strong seismic potential and is presently locked.

KEYWORDS

North Qinling Fault, GPS velocity field, locking depth, slip rate, seismicity distribution, seismic potential

1 Introduction

Strong earthquakes (M_S > 7) often occur at the boundary of active blocks in the mainland (Deng et al., 2003; Xu, 2006; Zhang et al., 2013). The North Qinling Fault, an active fault located at the boundary between the North China Block and the South China Block (i.e., first order blocks in Chinese mainland), can produce strong earthquakes (Figure 1). Specifically, the North Qinling Fault lies at the southern boundary of the Weihe Basin, which has been, historically, a strong seismically active area. Three M > 7 earthquakes have been recorded here, the most representative being the 1556 M 8¼ Huaxian earthquake, which caused > 840,000 deaths (https://data.earthquake.cn). Active faults are developed in the basin, among them, the North Qinling Fault is the largest, deepest and the most active fault (Zhang et al., 1990, 1991; Shaanxi Earthquake Agency, 1996; Bai, 2018).

Although there are few records of historical earthquakes along the North Qinling Fault, there are still many traces of ancient earthquakes, landslides, and barrier lakes, implying a number of strong earthquakes should have been caused by this fault since the beginning of the Holocene, demonstrating its earthquake generating ability. Paleoearthquake trenching dating has revealed that strong earthquakes occur about every 3,000 years along the North Qinling Fault, and that we might now be close to the end of the recurrence period: in a pre-seismic stage (Shaanxi Earthquake Agency, 1996; Bai, 2018). Considering these major earthquake hazard conditions, it is ungently needed to study the present-day activity and seismic potential of the North Qinling Fault.

Since the 1980s, detailed studies based on geological exploration have been carried on the North Qinling Fault to understand its geometry, kinematics, dynamics, structural evolution, and seismic ability (Zhang et al., 1990, 1991; Shentu et al., 1991; Bai, 2018; Huang et al., 2020; Yang, 2022). However, previous research has mainly focused on paleoearthquake events and normal faulting along the fault, while, quantitative analyses of the present-day seismic potential associated to current motion (particularly the strike-slip movement of the fault) have not been conducted.

Modern geodetic monitoring (especially GPS monitoring) is an effective and widely method used to recognize ongoing crustal movements. It can be applied to obtain the fault slip rate, locking depth, and strain field, which provide information on the earthquake cycle stage of the fault (Segall and Davis, 1997; Meade and Hager, 2005; Vigny et al., 2005; Papanikolaou et al., 2005; Huang et al., 2019; Chen et al., 2020; Li et al., 2021; Song et al., 2022). Numerous high-resolution analyses of geodetic observations along the active fault have been conducted to identify any

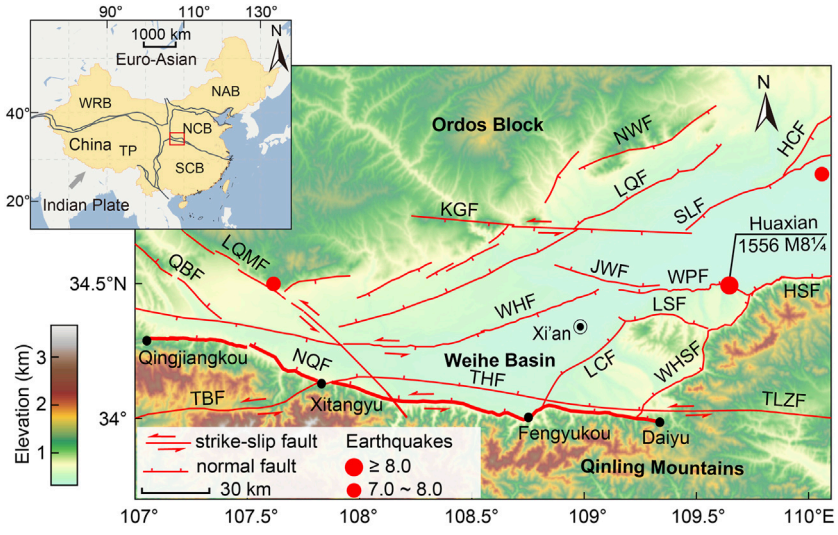

FIGURE 1
Tectonic setting of the North Qinling Fault and of the Weihe Basin. The fault data mainly refer to Deng et al. (2002) and Xu et al. (2016), while the seismic data were obtained from the National Earthquake Data Center (https://data.earthquake.cn). NCB, North China Block; SCB, South China Block; TP, Tibetan Plateau; WRB, Western Region Block; NAB, Northeast Asia Block; NQF, North Qinling Fault; THF, Taochuan–Huxian Fault; TBF, Taibai Fault; TLZF, Tieluzi Fault; LQMF, Longxian–Qishan-Mazhao Fault; QBF, Qianyang–Biaojiao Fault; WHF, Weihe Fault; LCF, Lintong –Chang'an Fault; LSF, Lishan Fault; WHSF, West Huashan Fault; WPF, Weinan Plateau Fault; HSF, Huashan Fault; JWF, Jingyang–Weinan Fault; HCF, Hancheng Fault; SLF, Shuangquan–Linyi Fault; LQF, Liquan Fault; NWF, North Weihe Fault; KGF, Kouzhen–Guanshan Fault.

connections with seismicity distribution and, hence, the current seismotectonic behavior (Sykes, 1971; Perez and Jacob, 1980; Zhang et al., 2003; Becker et al., 2005; Fialko, 2006; Parsons, 2006; Wen et al., 2007, 2008, 2013; Du et al., 2009, 2010, 2018; Wang et al., 2015; Liu et al., 2016; Li et al., 2020; Yin et al., 2020; Zhou et al., 2022).

In this study, we aimed to determine the present-day seismic potential associated with fault strike-slip movement and seismic activity along the North Qinling Fault, based on GPS data and seismicity. Firstly, we divided the North Qinling Fault into three segments from W to E (as in Zhang et al., 1991, Shaanxi Earthquake Agency, 1996 and Bai, 2018), and selected a total of three GPS profiles along the vertical direction of the fault strike (one for each segment). Based on GPS data, we inverted the slip rates, the locking depths, and the strain fields of the segments. Then, we determined any variations in the statistical properties of microseismicity (i.e., b-values and focal depth-frequency), identifying a seismic gap. The earthquake generating capacity of the fault was estimated by calculating the moment magnitude. Finally, we discussed the present-day activity and the seismic potential of the North Qinling Fault segments. The outcome of this study is vital to assess the seismic hazards and earthquake prediction in the densely populated Weihe Basin.

2 Geological setting

The North Qinling Fault is located in the northeastern part of the Tibetan Plateau, at the southern Ordos Block, central China (Figure 1). This fault formed due to multi-stage tectonic movements, which controlled the subsidence and evolution of the Weihe Basin to the N and the uplift of the Qinling Mountains to the S, since the Cenozoic. The fault dips northward (60–80°) and strikes W–E, extending from Qingjiangkou to Xitangyu, Fengyukou, and finally terminates at Daiyu, for a total length of 220 km. The N and S walls of the fault correspond to the loess plateau of the Weihe Basin and to the Qinling Mountains, respectively. Satellite images show clear linear feature for the fault; additionally, Bouguer gravity anomaly and aeromagnetic clearly indicate the occurrence of a density gradient zone along the fault (Peng et al., 1992, 2017). The North Qinling Fault can be divided into three segments according to its geometric characteristics and tectonic landforms. The western segment extends from Qingjiangkou to Xitangyu, is about 73 km long, and its approximate strike direction is SE; the middle segment extends from Xitangyu to Fengyukou, is about 90 km long, and its approximate strike direction is E–W; finally, the eastern segment extends from Fengyukou to Daiyu, is about 47 km long, and its approximate strike direction is E–W; (Zhang et al., 1991, Shaanxi Earthquake; Agency, 1996; Bai, 2018).

Previous research mainly focused on the vertical component of the North Qinling Fault. Under a of normal

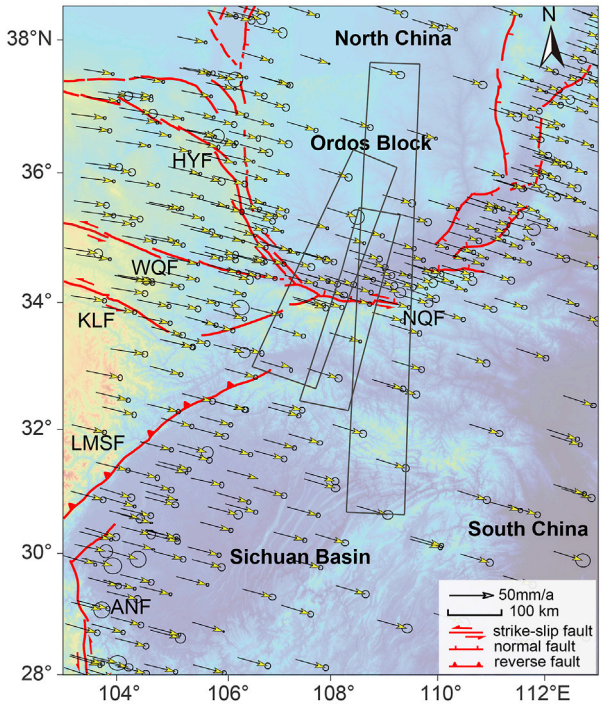

FIGURE 2
Distribution of the GPS velocity profiles across the North Qinling Fault. The black boxes indicate the profiles used for the computation of fault slip rate and locking depth. HYF, Haiyuan Fault; WQF, West Qinling Fault; KLF, Kunlun Fault; LMSF, Longmenshan Fault; ANF, Anninghe Fault; NQF, North Qinling Fault. The fault data were sourced from Zhang et al. (2013).

fault movement, the N wall has been descending, while the S wall has been ascending since the beginning of the Tertiary. Fault scarps of different scales and vertical offsets> 10 km were observed along the fault (Han et al., 2001; Liu et al., 2013; Huang et al., 2020). Regarding present-day fault activity, both the slip rate and the locking depth of the eastern segment are larger than those of the western-middle segments (Cui et al., 2019). Notably, the North Qinling Fault also shows obvious traces of sinistral strike-slip movements, which have horizontally offset rivers and terraces located in front of the Qinling Mountains (Shentu et al., 1991; Peng et al., 1992; Liu et al., 2013.; Ma, 2020).

3 Data and methods

3.1 GPS data

The GPS data used in this study come from Wang and Shen (2020). Our study mainly considered data from campaign and continuous GPS sites included in the Crustal Movement Observation Network of China (CMONOC) I and

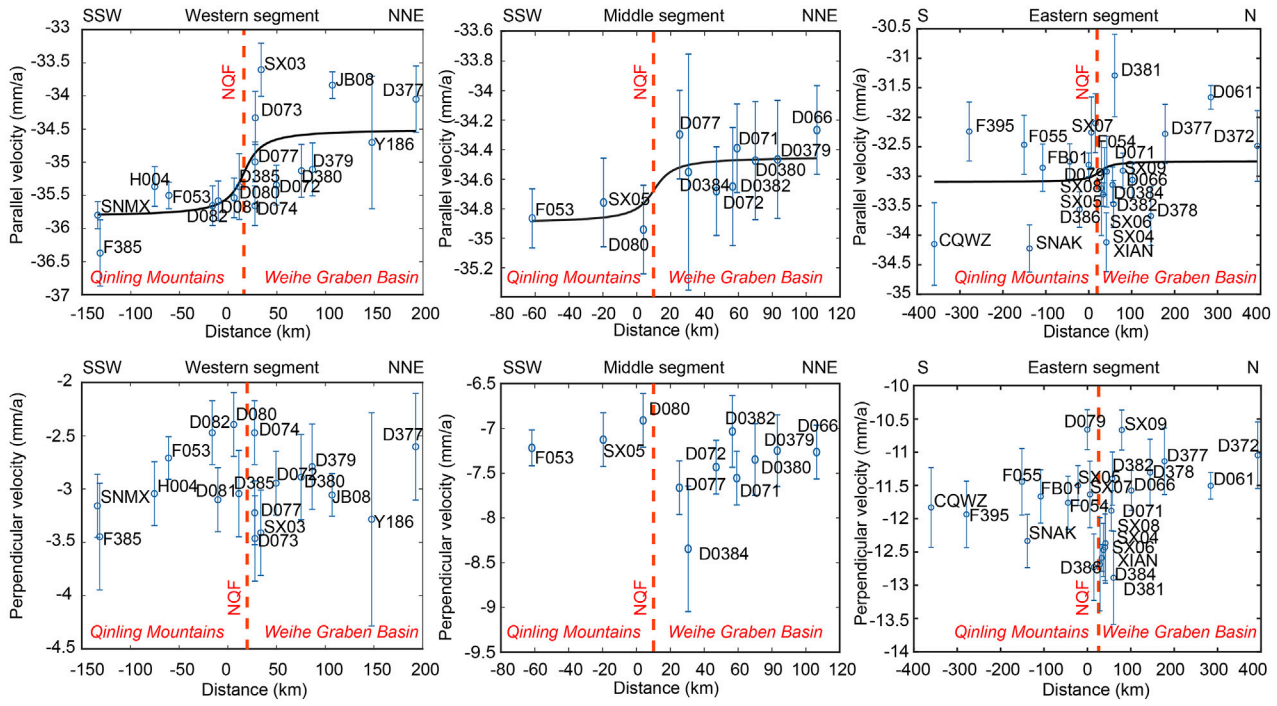

FIGURE 3
GPS velocity profiles. The top graphs refer to the direction parallel to the fault strike, while the bottom graphs refer to the direction perpendicular to the fault strike.

II project. Data from the continuous GPS sites, the campaign GPS sites of CMONOC I, and the continuous GPS sites, the campaign GPS sites of CMONOC II covered the following time spans: 1999–2016 and 1999–2015, 2009–2016 and 2009–2015, respectively. As detailed in Wang and Shen (2020), the raw GPS data obtained from 100 globally distributed IGS sites were processed all together using the GAMIT (Herring et al., 2010) software to ensure solutions of high quality and homogeneity. Particularly, the post-seismic and co-seismic deformation caused by large earthquakes have been modeled using the QOCA software (https://gipsy.jpl.nasa.gov/~qoca). In this study, the co-seismic offsets and effects of the 2005 Sumatra, 2008 Wenchuan, and 2011 Tohoku–Oki earthquakes were considered and corrected. Meanwhile, the stations with low quality (observated by the GeoTracer receiver/antenna during 1999 and 2000) and disturbed by anthropogenic activities (such as ground water and oil pumping, coal mining, etc.,) are discarded.

3.2 Viscoelastic coupling model

GPS velocity field refers to the velocities occurring parallelly and perpendicularly to a fault: they represent the strike-slip rate and the compression rate, respectively, and quantify crust activity. According to the characteristics of the GPS station and our fault segmentation, we selected three velocity profiles along the North Qinling Fault that were orthogonal to the fault strike (Figure 2). The GPS rates were decomposed into fault-parallel and fault-perpendicularly components to obtain the correspondent projection values (Figure 3). Then, the velocity component parallel to the fault strike (i.e., the strike-slip rate of the fault) was inverted. According to the viscoelastic coupling model, considering the locking depth as a dividing line, no slip movement should occur between the surface and the locking depth, but rather below the locking depth. The basic relationship among the locking depth, the long-term slip rate, and the surface movement during the horizontal slipping of the fault was obtained based on the traditional dislocation model (Savage and Burford, 1973; Savage et al., 1999):

$$V_z(x) = b_o - \frac{b_i}{\pi}\arctan\left[\frac{(x - x_i)}{h_i}\right]$$

where $V_z(x)$ is the pre-seismic slip rate of the surface, b_0 the adaptability constant, b_i is the long-term slip rate, x is the fault depth, and h_i is the locking depth at x_i. The thickness of the elastic plastic transition zone in the upper lower crust is determined to be 0 km. The determined slip rates and locking depths are shown in Table 1.

TABLE 1 Comparison between different segments of the North Qinling Fault.

Segment	Length (km)	Strike	Inversion results		90% seismic cutoff focal depth (km)	M_w	Seismic moment (10^{19} N m)	Geological slip rate (mm/a)	References
			Slip rate (mm/a)	Locking depth (km)					
Western	73.57	120°	1.33	13.54	18.4	7.23	8.81	0.29	Zhang et al., (1990) and Bai, (2018)
Middle	90.02	120°	0.45	8.58	16.97	7.35	12.02	0.61	
Eastern	47.01	90°	0.36	21.46	24	7.03	4.42	0.477	

The table shows the fault geometry, slip rate and locking depth (inverted from GPS, data), the 90% seismic cutoff focal depth, M_w, seismic moment, and geologic slip rate at the western, middle, and eastern segments of the North Qinling Fault.

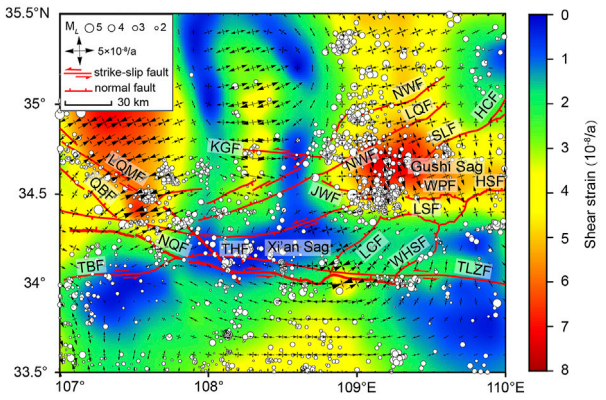

FIGURE 4
Shear strain, principal strain, active fault and modern earthquake distribution in the Weihe Basin (relocated earthquakes from January 1970 to May 2022).

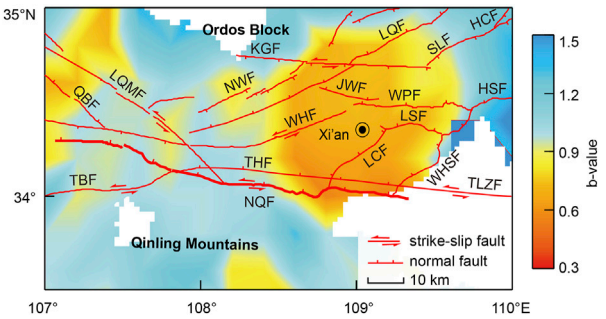

FIGURE 5
Seismic b-values and active fault distribution in the Weihe Basin.

3.3 Strain field calculation

We collected GPS velocity field data published recently (Wang and Shen, 2020) and selected those with errors< 1.5 mm/a. The improved least-square collocation method, which has a good resolution and reliability, was employed here to calculate the regional strain fields (Zhang et al., 1998; Wu et al., 2009; Shen et al., 2015). In the calculation process, it was fundamental to identify the best smoothing factor D, as well as to select a suitable interval distance range (0–500 km) and step length (1 km), in order to meet the following conditions:

$$W = \sum_{n=1}^{\#_{sta}*2} Z(i)*L(i) \gg W_t$$

where L is the weight of the distance correlation and Z is the weight of the spatial site distribution. In the calculation process, the data points over the threshold L_{max} = 10 × D km (from the calculation point) are excluded, and the optimal smoothing factor D is obtained under the condition of satisfying W_t, as well as the velocity and strain tensors [U_x, U_y, τ_x, τ_{xy}, τ_y, ω] T of all the GPS stations. In case of a sparse station distribution, the selection function $L(i) = 1/(1+\Delta Ri2/D2)$ is used instead, where ΔR is the distance between the station and the interpolation point. Station distribution and distance weighting were both considered to ensure the reliability and accuracy of the strain fields (see Figure 4).

3.4 Seismic b-value calculation

Data on modern earthquakes (that occurred between January 1970 and May 2022) were obtained from the China Earthquake Networks Center. The time series change of the minimum magnitude of completeness (Mc) in the Weihe Basin was qualitatively analyzed according to the magnitude-order method (Ogata et al., 1991) and the entire magnitude range (EMR) method (Woessner and Wiemer, 2005). The earthquake catalog of the Weihe Basin was analyzed starting from 1970, and Mc was determined considering it equal to M_L2.0. Earthquakes ≥ Mc were selected and the least square method was used to

calculate the b-values. Gridding was performed considering an interval of 0.2°, and earthquakes in the circular statistical unit with a radius of 30 km were selected. The number of events in each grid node had to be ≥ 20 in order to be considered for the calculations. For statistical grid nodes that could not meet the criteria, the statistical radius was increased to 50 km. If, after this, the number of samples was still < 20, the b-values were not calculated. The b-values are shown in Figure 5.

4 Results

4.1 Locking depths and slip rates

The distribution of GPS velocity field shows that the movement direction of the Weihe Basin is roughly SE–E. Additionally, the GPS velocity component profile fitting curve parallel to the fault is characterized by sinistral shear strain accumulation, while there is no obvious transverse compression deformation (Figure 3). The accumulation of horizontal shear strain varies along different segments, and the accumulated shear strain decreases from W to E. Detailed features were identified for each segment. 1) The GPS velocities obtained for the western segment of the fault (Qingjiangkou–Xitangyu), parallel to the fault strike, suggest an obvious sinistral strike-slip movement. The inversion results indicate a sinistral strike-slip velocity of 1.33 mm/a and a locking depth of 13.54 km. 2) The GPS velocities obtained for the middle segment of the fault (Xitangyu–Fengyukou), parallel to the fault strike, indicate an obvious sinistral strike-slip movement. The correspondent inversion results indicate a sinistral strike-slip velocity of 0.45 mm/a and a locking depth of 8.58 km. 3) The GPS velocities obtained for the eastern segment of the fault (Fengyukou–Daiyu), parallel to the fault strike, indicate an inapparent sinistral strike-slip movement. The correspondent inversion results indicate a sinistral strike-slip velocity of 0.36 mm/a and a locking depth of 21.46 km. 4) The GPS data obtained for the direction vertical to the fault strike indicate the absence of obvious tensions along the three segments.

4.2 Strain fields

Our GPS inversions showed that, in the Weihe Basin, strains have been controlled by the fault distribution, and been induced by the main fault activity; moreover, they are related to modern seismicity distribution (Figure 4).

4.2.1 Shear and principal strains in the Weihe Basin

The shear strain rate is overall higher in the eastern region and lower in the western region. A low-value area ($< 1 \times 10^{-8}$/a) was identified in the Xi'an Sag, in the southern-central part of the Weihe Basin: it is bounded by the North Qinling Fault to the S, the Lintong–Chang'an Fault to the E, and the Weihe Fault to the N. A median-value area ($\pm 2 \times 10^{-8}$/a) was instead identified in correspondence of the Lishan uplift: it is bounded by the North Qinling Fault to the S, the Lintong–Chang'an Fault to the W, and the Lishan Piedmont Fault to the N. Finally, a high-value area ($> 4 \times 10^{-8}$/a) was found in the Gushi Sag, in the northeastern part of the basin, where many modern small earthquakes have occurred. This corresponds to the intersection area of the Weihe Fault with the Kouzhen–Guanshan Fault, the North Weihe Fault, and the Weinan Plateau Fault. Changes in the principal strain rate and in the direction are regulated by active faults in the Weihe Basin. The western margin of the basin is mainly controlled by the Longxian–Qishan–Mazhao Fault; here, the approximate direction of the principal compressive strain is NE–E. The southern margin of the basin is instead mainly controlled by the North Qinling Fault, which induces a principal compressive strain in the W–E direction. Meanwhile, the western–middle segment of the North Qinling Fault is subjected to the W–E principal compressive strain (consistent with the fault strike direction). The eastern segment of the fault is instead affected by a fault zone characterized with a N–NE strike (which includes the Lintong–Chang'an Fault and the West Huashan Fault), and the direction of the principal compressive strain is also N–NE. In the northeastern part of the North Weihe Fault, the main compressive strain occur in the NE–E direction. Meanwhile, in the Gushi Sag, it occurs in the N–NW direction, and its high principal strain rate corresponds to the region characterized by a high concentration of modern earthquakes.

4.2.2 Shear and principal strains along the North Qinling Fault

The shear strain rate shows an obvious gradient at the intersection of the Weihe Basin with the Qinling Mountains, controlled by the North Qinling Fault. Along this fault, the shear strain rate in the N wall is lower than that in the S wall; moreover, the shear strain rate changes considerably along the fault strike. The shear strain rate values in the western-middle segments are lower than that in the eastern segment and quite constant. A high value was noted at the intersection of the eastern segment of North Qinling Fault with the Lintong-Chang'an Fault: here, the maximum observed shear strain rate is 4×10^{-8}/a. The principal strain direction in the southern part of the basin is controlled by the North Qinling Fault and by the N–NE fault zone located to the E of it. The principal strain rate gradually increases from W to E along the North Qinling Fault, reaching its maximum value at the intersection of the North Qinling Fault with the Lintong–Chang'an Fault, where modern small earthquakes have not are rather weak.

4.3 Seismic b-values

The b-value distribution in the Weihe Basin is clearly shown in Figure 5. Higher and lower b-values occur in the

eastern and western parts of the Weihe Basin, respectively. Along the North Qinling Fault, the b-values also differ significantly from W to E, and the eastern part has the lowest b-values in the Weihe Basin. The average b-values for the eastern segment of the North Qinling Fault and Weihe Basin (0.6 ± 0.1 and 0.8 ± 0.1, respectively) are both lower than the average b-values for the western–middle segment of the North Qinling Fault (1.0 ± 0.1) over the same period.

5 Discussion

5.1 Stability analysis

5.1.1 Locking depths

Cui et al. (2019) proposed locking depths of 7.7 ± 3.58 km and 10 ± 4.47 km for the study region, which are different from those determined in this study (13.54 km, 8.58 km, and 21.46 km). Most of the difference might be explained as follows. First, it is important to note that different data sources were used in Cui et al. (2019) and in this study: those authors utilized multi-stage precise leveling data across the North Qinling Fault, while we calculated the locking depths based on GPS horizontal velocities. The influence of large earthquakes on fault movement by the leveling data was not deducted. Meanwhile, during the processing of GPS data, the co-seismic deformation caused by large earthquakes was considered, and troublesome epochs derived from the horizontal velocities were corrected. In this case, the GPS velocity could in fact reflect the crustal deformation by fault movements. Second, the locking depths inversed by considering different fault movements in Cui et al. (2019) and in this study: the leveling data and the GPS data were influenced by the normal faulting and strike-slip movement, respectively. In Shi et al. (2020), inversion of GPS data was applied to investigate a back-arc fault in the Central Andes. In that instance it was demonstrated that, even when data and processing methods are consistent, the calculated locking depths of horizontal and vertical movements can be different. In addition, the ranges and source locations of data used in Cui et al. (2019) and in our study were different. Cui et al. (2019) used two leveling lines that crossed the fault at the intersection of its western and middle segments, as well as the intersection of its middle and eastern segments. While, we selected GPS sites distributed along the whole fault, selecting three profiles according to fault segmentation. In summary, though a variety of factors may influence the correlation between the locking depths from these two methods, the locking depths inverted from the horizontal (i.e., GPS data) and vertical (i.e., leveling data) movements are generally consistent: a greater locking depth is determined for the eastern section of the fault.

5.1.2 GPS and geological slip rates

GPS and geological slip rates provide information on the fault vertical and horizontal movements, respectively (Table 1). Therefore, it is difficult to directly compare the slip rates of different motion types by GPS inversion and geological methods. Besides, geological and GPS slip rates are constrained by different influential factors. GPS measurement involves transient (i.e., generally elastic and some viscous) and permanent (i.e., plastic) components in the present day, whereas geological records only include permanent strain (Meade and Hager, 2005) and depend on the reliability of offset measurements and geochronological data (Cowgill, 2007). Thus, the GPS slip rates tends to differ from geological slip rates along the North Qinling Fault. Below, we discuss fault GPS and geological slip rates separately.

The inversion of GPS data indicates that the slip rate is equal to the velocity below the locking depth currently, and that the slip rate decrease eastwards (Table 1). Notably, the slip rate of the West Qinling Fault is 2.5 ± 0.3 mm/a (Li et al., 2021): larger than that of the North Qinling Fault. This is consistent with the current dynamic background, in which the uplift of the Tibetan Plateau is causing a large-scale sinistral strike-slip movement. The North Qinling Fault, characterized by lower slip rates, is located at the end of the eastward spreading zone. The higher slip rate of the western segment might indicate that this segment is still in a post-seismic stage and is not locked at present. Overall, the GPS and geological slip rates are in the same order of magnitude, supporting and confirming the reliability of methods applied in this study. For the geological evidence, instead, provides information on the strength of single tectonic events in relation to fault activity, and suggests that the slip rate in the western segment is lower than in the middle-eastern segments (Table 1): fault activity and earthquake seismicity should be weaker in the western segment.

5.1.3 Prominence of the North Qinling Fault

The North Qinling Fault is a major structure in a boundary zone characterized by active tectonic blocks (i.e., the North China Block and the South China Block) in mainland China (Figure 2, Zhang et al., 2013), and separates the Weihe Basin from the Qinling Mountains. We collected evidence that the North Qinling Fault is the most active and largest structure in the Weihe Basin, and it subjects the area to a high earthquake hazard. The crust structure determined based on the receiving function and deep seismic reflection, clearly indicates that the North Qinling Fault cuts off the Moho, reaching a depth of about 40 km, while the other faults occurring in the basin cut off only the upper crust (Xu et al., 2014; Guo and Chen, 2016; Si et al., 2016; Li et al., 2017; Shen et al., 2022; Zhang et al., 2022). Besides, the results of a geological survey suggest these other faults, characterized by lower geological slip rates and activities, are capable of generating only moderate earthquakes, differently from the North Qinling Fault (Shaanxi Earthquake Agency,

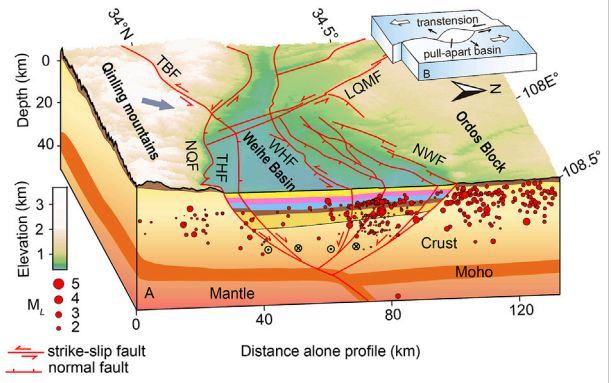

FIGURE 6
A Structural model of the Weihe Basin. B Model of the pull-apart basin.

1996). According to the above information, we can infer that the North Qinling Fault has a much higher activity and seismic potential than nearby (shallower cutting) faults. Therefore, our inversion results should mainly reflect the slip rates and locking depths of the North Qinling Fault.

5.2 Strike-slip movement of the North Qinling Fault

Some scholars argued that, since the Late Miocene–Quaternary, normal faulting has been predominant in the North Qinling Fault, which bounds the southern part of the Weihe Basin and controls its subsidence and sedimentation (Wang, 1965; Liu et al., 1981; Wang, 1986; Xie et al., 1991; Zhang et al., 1991; Li, 1992; Peng et al., 1992; Shaanxi Earthquake Agency, 1996; Han et al., 2001; Xie, 2011; Ren et al., 2012, 2013; Rao et al., 2014; Meng, 2017). Still, other studies suggest that the North Qinling Fault is currently characterized by a large-scale sinistral strike-slip movement, due to a NW–SE tensile stress affecting the Weihe Basin and caused by the eastward spreading of the Tibetan Plateau (Molnar and Tapponnier, 1975; Peltzer et al., 1985; Tapponnier et al., 1986; Zhang et al., 1995; Zhang et al., 1998; Zhang et al., 1999; Zhang et al., 2005; Zhang et al., 2019; Sun, 2005; Zhang et al., 2006; Sun and Xu, 2007; Liu et al., 2013).

In this study, the inversion of principal strain obtained from GPS data (Figure 4) indicate that strike-slip has been the primary movement mode of the North Qinling Fault for decades. Below, we discuss information suggesting that the North Qingling Fault is a sinistral strike-slip fault, whose shearing and tension control the formation of a pull-apart basin (i.e., the Weihe Basin) (Figure 6).

1) Geological survey has provided evidence of recent horizontal offset along most active faults in the Weihe Basin, and especially along the North Qinling Fault (Shentu et al., 1991; Peng et al., 1992; Liu et al., 2013.; Bai, 2018; Ma, 2020; Ma, 2020). 2) Prospecting and artificial seismic exploration have demonstrated that the crust in correspondence of the Weihe Basin is characterized by a large-scale "negative flower structure" (Zhang et al., 2021), resulting from shearing and tension. 3) Cenozoic sediments have a large thickness (> 7500 m) in the Weihe Basin, and the Quaternary sedimentary rate is high (465 m/Ma) (Sun and Xu, 2007). These are characteristics correspond to those typical of pull-apart basins. 4) The GPS velocity field suggests NW-SE movements in the Weihe Basin (England and Houseman, 1989; Clark and Royden, 2000; Qu et al., 2016), moreover, the stress field constrained by seismic activity and focal mechanism solutions indicates that the maximum horizontal principal stress direction is nearly EW along the North Qinling Fault (Yu et al., 2022), which is consistent with our studies.

5.3 Seismicity along the North Qinling Fault

5.3.1 Modern seismicity

To analyze modern seismicity along the North Qinling Fault, we selected relocated earthquakes from the period January 1970–May 2022 with the epicenter within 20 km from the reference profile following the direction of the fault strike, and drew the seismic depth transect along the North Qinling Fault (Figure 7). Although earthquakes involved in the transect refer to other faults, such as the Taochuan–Huxian Fault, the Lintong–Chang'an Fault and other secondary faults. Among them, the Taochuan–Huxian Fault can be regarded as a branch of the North Qinling Fault. Moreover, there is no explicit evidence that the Lintong–Chang'an Fault is a Holocene active fault. Hence, our seismic profile basically reflects the current seismicity along the North Qinling Fault.

The focal depth of the North Qinling Fault is generally within 30 km, but it is unevenly distributed along the fault. Notably, modern earthquakes have occurred mainly along the western and middle segments of the fault. In particular, a relatively high concentration of earthquakes was identified in the shallow layer (0–3 km) of the western and middle segments, while a clear seismic gap was revealed in the eastern segment. These facts highlight a sharp contrast in the seismicity of the western-middle and eastern segments.

5.3.2 Paleoearthquake

Although historical and modern earthquakes and rather weak along the North Qinling Fault, there is sufficient evidence of paleoearthquakes, prehistoric landslides, and barrier lakes caused by strong earthquakes along the fault (Bai, 2018; Huang et al., 2020; Yang, 2022). Paleoearthquake information can make up for deficiencies in historical and

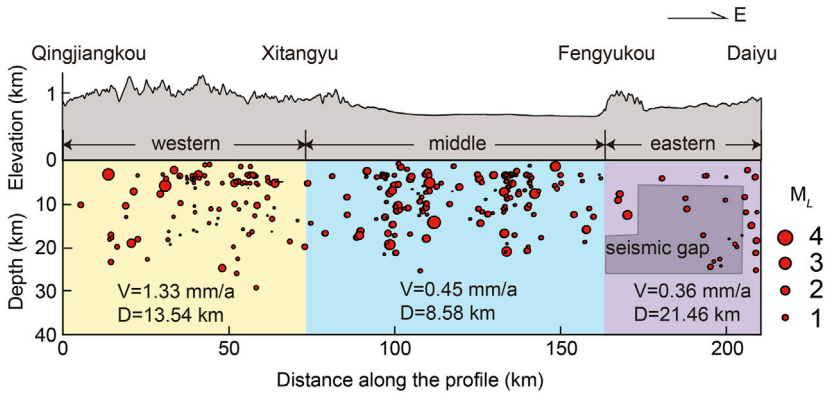

FIGURE 7
Elevation and seismic depth along the North Qinling Fault. A seismic gap can be identified in the area with sparse earthquakes.

modern seismicity information and can be used to explore the occurrence regularity of strong earthquakes along active faults over long time scales (McCalpin, 1996; Caputo and Helly, 2008). Previous studies have shown that, along the North Qinling Fault, the average recurrence interval of prehistorical earthquakes is about 3,000 years (Zhang et al., 1990; Shaanxi Earthquake Agency, 1996; Bai, 2018). By combining this information with the occurrence time of the last major earthquake, we can infer that the fault is now in a pre-seismic stage: it is approaching the recurrence period of large earthquakes.

5.4 Seismic potential of the North Qinling Fault

5.4.1 Segmentation characteristics

In this study, we adopted a segmentation that reflects the geometry of the fault, as determined from the geological survey (Zhang et al., 1991; Shaanxi Earthquake Agency, 1996; Bai, 2018). Inversions of GPS data and b-values were used to define the diversity between segments. The eastern segment, having the deepest locking depth, the highest shear and principal strain rates, the lowest b-values, and presenting a seismic gap, is the most unique. These differences suggest that, even under a homogeneous tectonic background, different segments would experience discrepant geological and present-day activities. This justifies our choice of the segmentation method, which is able to provide detailed spatial information on fault activity. On this basis, we conducted a comprehensive analysis of the fault seismic potential and timing.

5.4.2 b-values and strain fields

The b-value is typically inversely related with effective stress and closely related to the fault asperity. Large earthquakes usually occur in areas characterized by low b-values, and where a higher amount of stress is accumulated (Wiemer and Wyss, 1997; Wyss et al., 2004; Yi et al., 2006; Zhu and Huang., 2022). Thus, we employed the seismic b-value as an indicator of accumulated stress to further discuss the seismic potential of the fault. The lower average b-values of the eastern segment (Figure 5), compared to those of the other segments, indicates that a higher amount of stress is accumulated here and hence, that this area has a higher seismic potential.

The shear and principal strains typically reflect the current stress state of the crust. We noted that the shear strain and principal strain rates are both higher in the eastern segment than in the western-middle segments of the North Qinling Fault: the highest strain rates are registered at the intersection of the North Qinling Fault with the Lintong–Chang'an Fault. However, unlike the Gushi Sag (in the northeastern part of the basin), the eastern segment of the North Qinling Fault is not a seismically active area (Figure 4). Overall, the high strain rates (Figure 4) and low average b-values (Figure 5) of the eastern segment, as well as the occurrence of a seismic gap (Figure 7), indicate that a large amount energy should have accumulated in this area.

5.4.3 Moment magnitude and focal depth-frequency

Extensive research has been conducted on the relationship between earthquake moment magnitude and surface rupture length (Tocher, 1958; Slemmos, 1977; Long et al., 2006; Ran et al., 2011). In this paper, according to the empirical relationship between moment magnitude (M_W) and rupture length (L) in global strike-slip faults ($M_W = 5.16 + 1.12$ L gL, where L is in km) (Wells and Coppersmith, 1994), as well as the empirical relationship $M_W = 2/3$ (lgMo−16.1) (Chen and Liu, 2018), we calculated the moment magnitude and the seismic moment of the western, middle, and eastern segments of the North Qinling Fault. Our statistical results (Table 1) indicate that this fault has the capability of generating earthquakes with $M_W > 7$.

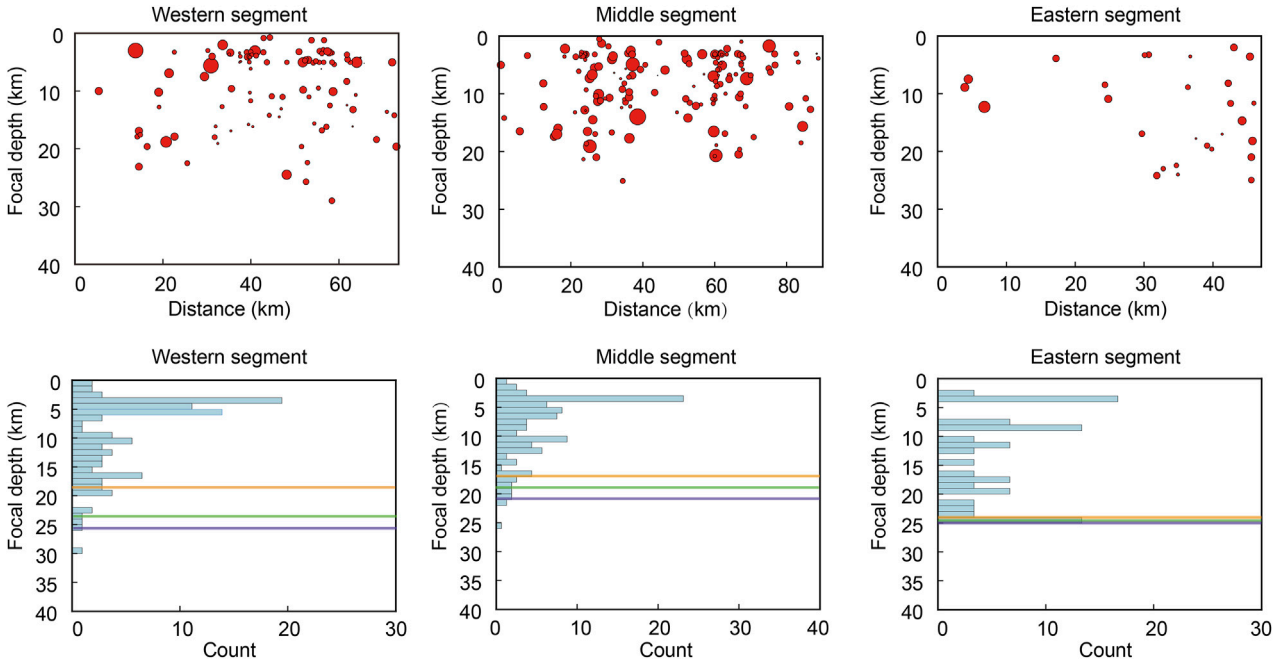

FIGURE 8
Focal depth distribution along the North Qinling Fault. The orange, green, and purple lines represent the 90%, 95%, and 99% seismic cutoff depths, respectively.

Our calculation demonstrates a strong earthquake capacity for the North Qinling Fault. The western-middle segments have shallower locking depths (i.e., 13.54 km and 8.58 km, respectively) than the eastern segment (i.e., 21.46 km) and present earthquake clustering, implying energy release. This information, combined with other results obtained in this study, implies that the eastern segment may be locked. Below, this issue is discussed quantitatively by considering the focal depth.

Previous research has demonstrated a good correspondence between the 90% seismic cutoff focal depth and the locking depth (Miller and Furlong, 1988; Williams, 1996; Richards and Shearer, 2000; Bonner et al., 2003). A comparative analysis of these depths can thus help clarifying the seismic potential of a fault. When the locking depth is shallower than the 90% seismic cutoff focal depth, "deep creep" occurs between the locking depth and the focal depth layers; in this case, stress mainly accumulates above the locking depth and major earthquakes are unlikely. When the locking depth is close to the 90% seismic cutoff depth, however, the fault is locked (Wdowinski, 2009; Schmittbuhl et al., 2015). Here, we discuss the seismic potential of the Qinling Fault by comparing the 90% seismic cutoff focal depth (within a width of 20 km and for different segments) with the locking depth (Figure 8; Table 1). The result indicates that the locking depth of the western segment should be 13.54 km [shallower than the 90% seismic cutoff depth (18.4 km)], suggesting the occurrence of "deep creep" in the layer between 13.45 and 18.4 km. The locking depth of the middle segment should be 8.58 km [only half of the 90% seismic cutoff depth (16.97 km)], suggesting the occurrence of "deep creep" in the layer between 8.58 and 16.97 km. Finally, the locking depth of this eastern segment should be 21.46 km [similar to the 90% seismic cutoff depth (24 km)], indicating that this segment is locked.

Overall, the results of our analyses suggest that the North Qinling Fault is presently in a pre-seismic stage and exhibits significant segmentation characteristics: the eastern segment, characterized by higher strain rates and accumulated stress, is obviously locked and capable of generating strong earthquakes in the near future.

6 Conclusion

Based on GPS data and seismic activity, we inverted slip rate, locking depth, shear and principal strain fields to determine the present-day activity and seismic potential of the North Qinling Fault. Our main findings are summarized below.

The North Qinling Fault, characterized by a sinistral strike-slip movement, is currently in a pre-seismic stage and makes the Weihe Basin an area of high earthquake hazard. This fault can in fact potentially generate $M_W > 7$ earthquakes. Its eastern segment, where the locking depth is close to the 90% seismic

cutoff focal depth, has relatively higher shear and principal strain rates, low b-values, and presents a seismic gap. These traits collectively suggest that the eastern segment is currently locked, and that it has a strong seismic potential that might be expressed in the near future. Therefore, a continuous, careful monitoring of this area is required.

Data availability statement

The original contributions presented in the study are included in the article/Supplementary Material, further inquiries can be directed to the corresponding author.

Author contributions

CY: Conceptualization, formal analysis, funding acquisition, methodology, software, visualization, writing—original draft. LJ: Formal analysis, methodology, writing—review and editing. YY: Conceptualization, writing—review and editing, funding acquisition. LS: Conceptualization, software. YW: Software. HS: Conceptualization.

Funding

This work was jointly supported by the Natural Science Basic Research Program of Shaanxi Province (Grant No. 2022JQ-298), the National Natural Science Foundation of China (Grant No. 42004048), and the Seismological Research Tracking Project of China Earthquake Administration (Grant No. 2022010212). Most figures were generated by using the Generic Mapping Tools software (Wessel and Smith, 1995). The relocated earthquake catalogue was provided by Liu C. and Zhang E. H.

Acknowledgments

The authors are grateful to Shi F. Q. for helpful discussion, and to Zhang W. T. and Chen X. X. for software assistance.

Conflict of interest

The authors declare that the research was conducted in the absence of any commercial or financial relationships that could be construed as a potential conflict of interest.

Publisher's note

References

Bai, X. D. (2018). *Influence study from the activity of the northern margin fault zone of Qinling Mountains on geological hazard*. Beijing, China: Institute of Engineering Mechanics, China Earthquake Administration.

Becker, T. W., Hardebeck, J. L., and Anderson, G. (2005). Constraints on fault slip rates of the southern California plate boundary from GPS velocity and stress inversions. *Geophys. J. Int.* 160 (2), 634–650. doi:10.1111/j.1365-246X.2004.02528.x

Bonner, J. L., Blackwell, D. D., and Herrin, E. T. (2003). Thermal constraints on earthquake depths in California. *Bull. Seismol. Soc. Am.* 93 (6), 2333–2354. doi:10.1785/0120030041

Caputo, R., and Helly, B. (2008). The use of distinct disciplines to investigate past earthquakes. *Tectonophysics* 453 (1-4), 7–19. doi:10.1016/j.tecto.2007.05.007

Chen, Y. G., Ding, K. H., Wang, Q., He, P., Li, S. P., and Qiao, X. J. (2020). A refined slip distribution of the 2013 M w 6.7 Lushan, China earthquake constrained by GPS and levelling data. *Geophys. J. Int.* 222 (1), 572–581. doi:10.1093/gji/ggaa202

Chen, Y. T., and Liu, R. F. (2018). Moment magnitude and its calculation. *Earthq. Res. China* 39 (2), 1–9. doi:10.3969/j.issn.1003-3246.2018.02.001

Clark, M. K., and Royden, L. H. (2000). Topographic ooze: Building the eastern margin of Tibet by lower crustal flow. *Geology* 28 (8), 703–706. doi:10.1130/0091-7613(2000)028<0703:tobtem>2.3.co;2

Cowgill, E. (2007). Impact of riser reconstructions on estimation of secular variation in rates of strike–slip faulting: Revisiting the Cherchen River site along the Altyn Tagh Fault, NW China. *Earth Planet. Sci. Lett.* 254 (3-4), 239–255. doi:10.1016/j.epsl.2006.09.015

Cui, D. X., Hao, M., Qin, S. L., and Wang, W. P. (2019). Inversion of fault dip-slip rate and locking depth in Central-Southern Shaanxi of China. *Chin. J. Geophys.* 62 (12), 4648–4657. doi:10.6038/cjg2019M0358

Deng, Q. D., Zhang, P. Z., Ran, Y. K., Yang, X. P., Min, W., and Chu, Q. Z. (2002). Basic characteristics of active tectonics in China. *Sci. China (D)* 32 (12), 1020–1030. doi:10.3321/j.issn:1006-9267.2002.12.007

Deng, Q. D., Zhang, P. Z., Ran, Y. K., Yang, X. P., Min, W., and Chen, L. C. (2003). Active tectonics and earthquake activities in China. *Earth Sci. Front.* 10 (8), 66–73. doi:10.3321/j.issn:1005-2321.2003.z1.012

Du, F., Wen, X. Z., Feng, J. G., Liang, M. J., Long, F., and Wu, J. (2018). Seismotectonics and seismic potential of the Liupanshan fault zone (LPSFZ), China. *Chin. J. Geophys.* 61 (2), 545–559. doi:10.6038/cjg2018L0181

Du, F., Wen, X. Z., and Zhang, P. Z. (2010). Post-seismic slip and deformation on the Luhuo segment of the Xianshuihe fault zone. *Chin. J. Geophys.* 53 (10), 2355–2366. doi:10.3969/j.issn.0001-5733.2010.10.009

Du, F., Wen, X. Z., Zhang, P. Z., and Wang, Q. L. (2009). Interseismic deformation across the Longmenshan fault zone before the 2008 M8.0 Wenchuan earthquake. *Chin. J. Geophys.* 52 (11), 2729–2738. doi:10.3969/j.issn.0001-5733.2009.11.007

England, P. C., and Houseman, G. A. (1989). Extension during continental convergence, with application to the Tibetan Plateau. *J. Geophys. Res.* 94 (17), 17561–17597. doi:10.1029/JB094iB12p17561

Fialko, Y. (2006). Interseismic strain accumulation and the earthquake potential on the southern San Andreas fault system. *Nature* 441 (7096), 968–971. doi:10.1038/nature04797

Guo, Z., and Chen, Y. J. (2016). Crustal structure of the eastern Qinling orogenic belt and implication for reactivation since the Cretaceous. *Tectonophysics* 683, 1–11. doi:10.1016/j.tecto.2016.06.007

Han, H. Y., Mi, F. S., and Liu, H. Y. (2001). Geomorphological structure in the Weihe Basin and neotectonic movement. *J. Seismol. Res.* 24 (3), 251–257. doi:10.3969/j.issn.1000-0666.2001.03.011

Herring, T. A., King, R. W., and McClusky, S. C. (2010). *GAMIT reference manual, GPS Analysis at MIT, Release 10.4*. Cambridge, MA: Massachusetts Institute of Technology.

Huang, W. L., Yang, Q. H., Yan, L., Su, S. R., and Zhou, Z. H. (2020). Relationship between distribution characteristics of prehistoric landslides and seismic activity along qinling piedmont fault. *J. Eng. Geol.* 28 (6), 1259–1271. doi:10.13544/j.cnki.jeg.2019-383

Huang, Y., Qiao, X. J., Freymueller, J. T., Wang, Q., Yang, S. M., Tan, K., et al. (2019). Fault geometry and slip distribution of the 2013 Mw 6.6 Lushan earthquake in China constrained by GPS, InSAR, leveling, and strong motion data. *J. Geophys. Res. Solid Earth* 124 (7), 7341–7353. doi:10.1029/2019JB017451

Li, H. Q., Gao, R., Xiong, X. S., Wang, H. Y., and Li, W. H. (2017). Moho fabrics of North Qinling belt, Weihe graben and Ordos block in China constrained from large dynamite shots. *Geophys. J. Int.* 209 (2), 643–653. doi:10.1093/gji/ggx052

Li, J. Y., Zhou, B. G., Li, T. M., Yang, Y. L., Li, Z. F., and Long, F. (2020). Seismogenic depths of the Anninghe-Zemuhe and Daliangshan fault zones and their seismic hazards. *Chin. J. Geophys.* 63 (10), 3669–3682. doi:10.6038/cjg2020N0201

Li, X., Pierce, I. K. D., Bormann, J. M., Hammond, W. C., Zhang, Z., Li, C., et al. (2021). Tectonic deformation of the northeastern Tibetan Plateau and its surroundings revealed with GPS block modeling. *JGR. Solid Earth* 126 (5), e2020JB020733. doi:10.1029/2020JB020733

Li, Y. S. (1992). *Research on ground fissure in Xi'an region and active faults in Weihe basin*. Beijing, China: Seismological Press.

Liu, J. H., Zhang, P. Z., Lease, R. O., Zheng, D. W., Wan, J. L., Wang, W. T., et al. (2013). Eocene onset and late Miocene acceleration of Cenozoic intracontinental extension in the North Qinling range–Weihe graben: Insights from apatite fission track thermochronology. *Tectonophysics* 584, 281–296. doi:10.1016/j.tecto.2012.01.025

Liu, Q., Wen, X. Z., and Shao, Z. G. (2016). Joint inversion for coseismic slip of the 2013 Ms7. 0 Lushan earthquake from GPS, leveling and strong motion observations. *Chin. J. Geophys.* 59 (6), 2113–2125. doi:10.6038/cjg20160617

Liu, S. W., and Gan, J. S. (1981). The Fenwei rift valley system. *Crustal Deform. Earthq.* 3, 110–123.

Long, F., Wen, X. Z., and Xu, X. W. (2006). Empirical relationships between magnitude and rupture length, and rupture area, for seismogenic active faults in north China. *Seismol. Geol.* 28 (4), 511–535. doi:10.3969/j.issn.0253-4967.2006.04.001

Ma, J. (2020).*1556 Hua County M8 Surface rupture and seismogenic structure of magnitude earthquake*. Doctoral dissertation. Beijing, China: Institute of Geology, China Earthquake Administration.

McCalpin, J. (1996). *Paleoseismology*. San Diego: Academic Press.

Meade, B. J., and Hager, B. H. (2005). Block models of crustal motion in southern California constrained by GPS measurements. *J. Geophys. Res.* 110 (B3), B03403–B03419. doi:10.1029/2004JB003209

Meng, Q. R. (2017). Origin of the qinling Mountains. *Sci. Sin. Terrae* 47 (4), 412–420. doi:10.1360/N072016-00422

Miller, C. K., and Furlong, K. P. (1988). Thermal-mechanical controls on seismicity depth distributions in the San Andreas Fault Zone. *Geophys. Res. Lett.* 15 (12), 1429–1432. doi:10.1029/GL015i012p01429

Molnar, P., and Tapponnier, P. (1975). Cenozoic Tectonics of Asia: Effects of a Continental Collision: Features of recent continental tectonics in Asia can be interpreted as results of the India-Eurasia collision. *Science* 189 (4201), 419–426. doi:10.1126/science.189.4201.419

Ogata, Y., Imoto, M., and Katsura, K. (1991). 3-D spatial variation of b-values of magnitude-frequency distribution beneath the Kanto District, Japan. *Geophys. J. Int.* 104 (1), 135–146. doi:10.1111/j.1365-246X.1991.tb02499.x

Papanikolaou, I. D., Roberts, G. P., and Michetti, A. M. (2005). Fault scarps and deformation rates in Lazio–Abruzzo, Central Italy: Comparison between geological fault slip-rate and GPS data. *Tectonophysics* 408 (1-4), 147–176. doi:10.1016/j.tecto.2005.05.043

Parsons, T. (2006). Tectonic stressing in California modeled from GPS observations. *J. Geophys. Res.* 111 (B3), B03407. doi:10.1029/2005JB003946

Peltzer, G., Tapponnier, P., Zhang, Z. T., and Qin, X. Z. (1985). Neogene and quaternary faulting in and along the qinling Shan. *Nature* 317 (6037), 500–505. doi:10.1038/317500a0

Peng, J. B., Lu, Q. Z., and Huang, Q. B. (2017). *Earth fissures of fenwei basin*. Beijing, China: Science Press.

Peng, J. B., Zhang, J., and Su, S. R. (1992). *Active faults and geological hazards in Weihe basin*. Xi'an, China.

Perez, O. J., and Jacob, K. H. (1980). Tectonic model and seismic potential of the eastern Gulf of Alaska and Yakataga seismic gap. *J. Geophys. Res.* 85 (B12), 7132–7150. doi:10.1029/JB085iB12p07132

Qu, W., Wang, Y. S., Zhang, Q., Wang, Q. L., and Xue, K. (2016). Current crustal deformation variation characteristics of the Fenwei basin and its surrounding areas revealed by GPS data. *Chin. J. Geophys.* 59 (3), 828–839. doi:10.6038/cjg20160306

Ran, H. L. (2011). Empirical relations between magnitude and parameters of strike-slip seismogenic active faults associated with historical earthquakes in Western China. *Seismol. Geol.* 33 (3), 577–585. doi:10.3969/j.issn.0253-4967.2011.03.008

Rao, G., Lin, A. M., Yan, B., Jia, D., and Wu, X. J. (2014). Tectonic activity and structural features of active intracontinental normal faults in the Weihe Graben, central China. *Tectonophysics* 636, 270–285. doi:10.1016/j.tecto.2014.08.019

Ren, J., Feng, X., Wang, F., Peng, J., Liu, C., Dai, W., et al. (2013). Fine crust structures of Xi'an sag in the Weihe basin revealed by a deep seismic reflection profile. *Chin. J. Geophys.* 56 (2), 513–521. doi:10.6038/cjg20130215

Ren, J. (2012). *Probe on the deep crustal structure in Weihe Basin and tectonics research of basin*. Xi'an, China: Chang'an University.

Richards-Dinger, K. B., and Shearer, P. M. (2000). Earthquake locations in southern California obtained using source-specific station terms. *J. Geophys. Res.* 105 (B5), 10939–10960. doi:10.1029/2000JB900014

Savage, J. C., and Burford, R. O. (1973). Geodetic determination of relative plate motion in central California. *J. Geophys. Res.* 78 (5), 832–845. doi:10.1029/JB078i005p00832

Savage, J. C., Svarc, J. L., and Prescott, W. H. (1999). Geodetic estimates of fault slip rates in the San Francisco Bay area. *J. Geophys. Res.* 104 (B3), 4995–5002. doi:10.1029/1998JB900108

Schmittbuhl, J., Karabulut, H., Lengliné, O., and Bouchon, M. (2015). Seismicity distribution and locking depth along the main marmara fault, Turkey. *Geochem. Geophys. Geosyst.* 17 (3), 954–965. doi:10.1002/2015gc006120

Segall, P., and Davis, J. L. (1997). GPS applications for geodynamics and earthquake studies. *Annu. Rev. Earth Planet. Sci.* 25 (1), 301–336. doi:10.1146/annurev.earth.25.1.301

Shaanxi Earthquake Agency (1996). *Active Fault zone on the northern margin of qining mountains*. Beijing, China: Seismological Press.

Shen, X. Z., Zhou, Q. M., Cheng, S. Y., Zheng, W. J., Zhang, P. Z., Zhang, D. L., et al. (2022). Contrasting crustal structures crossing the boundary region of the southwest Ordos block and its tectonic implications revealed by dense seismic arrays. *Tectonophysics* 831, 229342. doi:10.1016/j.tecto.2022.229342

Shen, Z. K., Wang, M., Zeng, Y. H., and Wang, F. (2015). Optimal interpolation of spatially discretized geodetic data. *Bull. Seismol. Soc. Am.* 105 (4), 2117–2127. doi:10.1785/0120140247

Shentu, B. M., Song, F. M., Cao, Z. Q., and Wang, Y. P. (1991). Preliminary study on late quaternary fault scarps on the northern piedmont of qiling mountain. *Seismol. Geol.* 13 (1), 15–25.

Shi, F., Li, S., and Moreno, M. (2020). Megathrust locking and viscous mantle flow induce continental shortening in Central Andes. *Pure Appl. Geophys.* 177 (6), 2841–2852. doi:10.1007/s00024-019-02403-0

Si, X., Teng, J. W., Liu, Y. S., Ma, X. Y., Qiao, Y. H., Dong, X. P., et al. (2016). Crust structure of the Qinling orogenic and the region on its north and south margins from teleseismic receiver function. *Chin. J. Geophys.* 59 (4), 1321–1334. doi:10.6038/cjg20160414

Slemmons, D. B. (1977). Faults and earthquake magnitude". (State-of-the-art for assessing earthquake hazards in the United States). Report 24. WES. Available from: https://apps.dtic.mil/sti/citations/ADA182901.

Song, S. W., Li, Y. H., and Hao, M. (2022). Active crustal deformation model of the Fen–Wei rift zone, North China: Integration of geologic, geodetic, and stress direction datasets. *Front. Earth Sci.* 10, 964800. doi:10.3389/feart.2022.964800

Sun, J. M. (2005). Long-term fluvial archives in the Fen Wei Graben, central China, and their bearing on the tectonic history of the India–Asia collision system during the Quaternary. *Quat. Sci. Rev.* 24 (10-11), 1279–1286. doi:10.1016/j.quascirev.2004.08.018

Sun, J. M., and Xu, L. L. (2007). River terraces in the Fen Wei Graben, Central China, and the relation with the tectonic history of the India-Asia collision system during the Quaternary. *Quat. Sci.* 27 (1), 20–26. doi:10.3321/j.issn:1001-7410.2007.01.003

Sykes, L. R. (1971). Aftershock zones of great earthquakes, seismicity gaps, and earthquake prediction for Alaska and the Aleutians. *J. Geophys. Res.* 76 (32), 8021–8041. doi:10.1029/JB076i032p08021

Tapponnier, P., Peltzer, G., and Armijo, R. (1986). *On the mechanics of the collision between India and Asia*. London: Geological Society.

Tocher, D. (1958). Earthquake energy and ground breakage. *Bull. Seismol. Soc. Am.* 48 (2), 147–153. doi:10.1785/BSSA0480020147

Vigny, C., Simons, W. J. F., Abu, S., Bamphenyu, R., Satirapod, C., Choosakul, N., et al. (2005). Insight into the 2004 sumatra–andaman earthquake from GPS measurements in southeast Asia. *Nature* 436 (7048), 201–206. doi:10.1038/nature03937

Wang, C. C. (1965). On the Weihe graben. *Acta Geol. Sin.* 45, 153–164.

Wang, F., Wang, M., Wang, Y. Z., and Shen, Z. K. (2015). Earthquake potential of the Sichuan-Yunnan region, Western China. *J. Asian Earth Sci.* 107, 232–243. doi:10.1016/j.jseaes.2015.04.041

Wang, J. M. (1986). On the Fenwei rift. *J. Xi'an Colle. Geol.* 8, 36–49.

Wang, M., and Shen, Z. K. (2020). Present-day crustal deformation of continental China derived from GPS and its tectonic implications. *J. Geophys. Res. Solid Earth* 125 (2), e2019JB018774. doi:10.1029/2019JB018774

Wdowinski, S. (2009). Deep creep as a cause for the excess seismicity along the San Jacinto fault. *Nat. Geosci.* 2 (12), 882–885. doi:10.1038/ngeo684

Wells, D. L., and Coppersmith, K. J. (1994). New empirical relationships among magnitude, rupture length, rupture width, rupture area, and surface displacement. *Bull. Seismol. Soc. Am.* 84 (4), 974–1002. doi:10.1785/BSSA0840040974

Wen, X. Z., Du, F., Yi, G. X., Long, F., Fan, J., Yang, P. X., et al. (2013). Earthquake potential of the Zhaotong and Lianfeng fault zones of the eastern Sichuan-Yunnan border region. *Chin. J. Geophys.* 56 (10), 3361–3372. doi:10.6038/cjg20131012

Wen, X. Z., Fan, J., Yi, G. X., Deng, Y. W., and Long, F. (2008). A seismic gap on the Anninghe fault in Western Sichuan, China. *Sci. China Ser. D-Earth. Sci.* 51 (10), 1375–1387. doi:10.1007/s11430-008-0114-4

Wen, X. Z., Yi, G. X., and Xu, X. W. (2007). Background and precursory seismicities along and surrounding the Kunlun fault before the Ms8. 1, 2001, Kokoxili earthquake, China. *J. Asian Earth Sci.* 30 (1), 63–72. doi:10.1016/j.jseaes.2006.07.008

Wiemer, S., and Wyss, M. (1997). Mapping the frequency-magnitude distribution in asperities: An improved technique to calculate recurrence times? *J. Geophys. Res.* 102 (B7), 15115–15128. doi:10.1029/97JB00726

Williams, C. F. (1996). Temperature and the seismic/aseismic transition: Observations from the 1992 Landers earthquake. *Geophys. Res. Lett.* 23 (16), 2029–2032. doi:10.1029/96GL02066

Woessner, J., and Wiemer, S. (2005). Assessing the quality of earthquake catalogues: Estimating the magnitude of completeness and its uncertainty. *Bull. Seismol. Soc. Am.* 95 (2), 684–698. doi:10.1785/0120040007

Wu, Y. Q., Jiang, Z. S., Yang, G. H., Fang, Y., and Wang, W. X. (2009). The application and method of GPS strain calculation in whole mode using least square collocation in sphere surface. *Chin. J. Geophys.* 52 (7), 1707–1714. doi:10.3969/j.issn.0001-5733.2009.07.005

Wyss, M., Sammis, C. G., Nadeau, R. M., and Wiemer, S. (2004). Fractal dimension and b-value on creeping and locked patches of the San Andreas fault near Parkfield, California. *Bull. Seismol. Soc. Am.* 94 (2), 410–421. doi:10.1785/0120030054

Xie, Z. Q., Fang, J. A., Tian, X. T., Zhang, B. W., and Wang, X. P. (1991). The evolution of the structural stress field and analysis of the formation mechanism in the Weihe Basin. *J. Xi'an Colle. Geol.* 13 (2), 46–52.

Xie, Z. Q. (2011). Structural model of earthquake preparation in Weihe extensional basin. *J. Catastrophol.* 26 (3), 18–21. doi:10.3969/j.issn.1000-811X.2011.03.004

Xu, S., Mi, N., Xu, M., Wang, L., Li, H., and Yu, D. (2014). Crustal structures of the Weihe graben and its surroundings from receiver functions. *Sci. China Earth Sci.* 57 (2), 372–378. doi:10.1007/s11430-013-4719-x

Xu, X., Han, Z., and Yang, X. (2016). *Seismotectonic Map of China and its adjacent regions*. Beijing: Seismological Press.

Xu, X. W. (2006). Active faults, associated earthquake disaster distribution and policy for disaster reduction. *Technol. Earthq. Disaster Prev.* 1 (1), 7–14. doi:10.3969/j.issn.1673-5722.2006.01.002

Yang, Q. H. (2022). *Research on the seismic activity history of faults in the northern margin of Qinling Mountains based on structural geomorphological features*. Xi'an, China: Chang'an University.

Yi, G. X., Wen, X. Z., Wang, S. W., Long, F., and Fan, J. (2006). Study on fault sliding behaviors and strong-earthquake risk of the Longmenshan-Minshan fault zones from current seismicity parameters. *Earthq. Res. China* 22 (2), 117–125. doi:10.3969/j.issn.1001-4683.2006.02.001

Yin, H. Q., Guo, X. Y., Chang, M., Zhan, W., Li, L. Y., and Xu, D. Z. (2020). Inversion of seismic hazard of the Xianshuihe fault by cross-fault and GPS crustal deformation data. *Acta Geol. Sin.* 94 (8), 2487–2499. doi:10.19762/j.cnki.dizhixuebao.2020055

Yu, Z., Shen, X., Liang, H., Zheng, W., and Liu, X. (2022). The characteristics of major faults and stress field in Weihe -- Yuncheng basin constrained by seismic activity and focal mechanism solutions. *Seismol. Geol.* (2), 395–413. doi:10.3969/j.issn.0253-4967.2022.02.008

Zhang, A. L., Chong, J., and Mi, F. S. (1990). A paleoseismological profile across piedmont fault zone at Taipingkou on northern segment of Qinling Mountains. *Seismol. Geol.* 12 (4), 333–334.

Zhang, A. L., Chong, J., and Mi, F. S. (1991). *Late quaternary activity characteristics of the fault zone in the northern margin of qinling mountains and its paleoearthquakes*. Beijing, China: Seismological Press.

Zhang, E. H., Shi, Y. Q., Zhang, Y., Li, M., Li, G. Y., Pei, H. D., et al. (2021). Extension and structural feature of the buried segment of Taochuan–Huxian Fault in the Weihe Basin. *Seismol. Geol.* 43 (6), 1485–1506. doi:10.3969/j.issn.0253-4967.2021.06.008

Zhang, P. Z., Deng, Q. D., Zhang, Z. Q., and Li, H. B. (2013). Active faults, earthquake hazards and associated geodynamic processes in continental China. *Sci. Sin. Terrae* 43 (10), 1607–1620. CNKI:SUN:JDXK.0.2013-10-005. doi:10.1360/zd-2013-43-10-1607

Zhang, P. Z., Wang, M., and Gan, W. J. (2003). Slip rates along major active faults from GPS measurements and constraints on contemporary continental tectonics. *Earth Sci. Front.* 10 (U08), 81–92. doi:10.3321/j.issn:1005-2321.2003.z1.014

Zhang, P. Z., Zheng, D. W., Yin, G. M., Yuan, D. Y., Zhang, G. L., Li, C. Y., et al. (2006). Discussion on late Cenozoic growth and rise of northeastern margin of the Tibetan Plateau. *Quat. Sci.* 26 (1), 5–13. doi:10.3321/j.issn:1001-7410.2006.01.002

Zhang, X., Jiang, Z. S., and Zhang, S. X. (1998). Whole calculation of the crustal visual strain field with the least square collocation. *Crustal Deform. Earthq.* 18 (2), 57–62.

Zhang, Y. Q., Dong, S. W., Wang, H. Y., Feng, M., Thybo, H., Li, J. H., et al. (2022). Coupled lithospheric deformation in the qinling orogen, central China: Insights from seismic reflection and surface-wave tomography. *Geophys. Res. Lett.* 49 (14). doi:10.1029/2022GL097760

Zhang, Y. Q., Vergély, P., and Mercier, J. L. (1999). Pliocene-Quaternary faulting pattern and left-slip propagation tectonics in North China. *J. Geomechan.* 5 (3), 40–46. doi:10.3969/j.issn.1006-6616.1999.03.007

Zhang, Y. Q., Ma, Y. S., Yang, N., Zhang, H. P., and Shi, W. (2005). Late Cenozoic left-slip faulting process of the east Kunlun-Qinling fault system in West Qinling region and its eastward propagation. *Acta Geosci. Sin.* 26 (1), 1–8. doi:10.3321/j.issn:1006-3021.2005.01.001

Zhang, Y. Q., Mercier, J. L., and Vergély, P. (1998). Extension in the graben systems around the Ordos (China), and its contribution to the extrusion tectonics of south China with respect to Gobi-Mongolia. *Tectonophysics* 285 (1-2), 41–75. doi:10.1016/S0040-1951(97)00170-4

Zhang, Y. Q., Shi, W., and Dong, S. W. (2019). Neotectonics of North China: Interplay between far-field effect of India-eurasia collision and pacific subduction related deep-seated mantle upwelling. *Acta Geol. Sin.* 93 (5), 971–1001. CNKI:SUN:DZXE.10.2019-05-001. doi:10.3969/j.issn.0001-5717.2019.05.001

Zhang, Y. Q., Vergély, P., and Mercier, J. L. (1995). Active faulting in and along the Qinling Range (China) inferred from SPOT imagery analysis and extrusion tectonics of south China. *Tectonophysics* 243 (1-2), 69–95. doi:10.1016/0040-1951(94)00192-C

Zhou, Y. J., Yue, H., Zhou, S. Y., Fang, L. H., Zhou, Y., Xu, L. S., et al. (2022). Microseismicity along xiaojiang fault zone (southeastern Tibetan plateau) and the characterization of interseismic fault behavior. *Tectonophysics* 833 (20), 229364. doi:10.1016/j.tecto.2022.229364

Zhu, H., and Huang, J. (2022). Spatiotemporal aftershock evolution of the 2014 M 6.4 and 5.9 kangding double shocks in sichuan, southwestern China. *Seismol. Soc. Am.* 93 (5), 2625–2639. doi:10.1785/0220220039

frontiers | Frontiers in Earth Science

TYPE Original Research
PUBLISHED 24 January 2023
DOI 10.3389/feart.2023.1059300

OPEN ACCESS

EDITED BY
Xinjian Shan,
Institute of Geology, China Earthquake Administration, China

REVIEWED BY
Ping Wang,
Lanzhou Earthquake Research Institute, China Earthquake Administration, China
R. Jayangonda Perumal,
Wadia Institute of Himalayan Geology, India

*CORRESPONDENCE
Zhenyu Zou,
407124082@qq.com

SPECIALTY SECTION
This article was submitted to Structural Geology and Tectonics, a section of the journal Frontiers in Earth Science

RECEIVED 01 October 2022
ACCEPTED 06 January 2023
PUBLISHED 24 January 2023

CITATION
Zou Z, Jiang Z, Wu Y, Cui Y and Tang H (2023), Coupling fraction model to interpret the motion of non-fully coupled strike-slip faults.
Front. Earth Sci. 11:1059300.
doi: 10.3389/feart.2023.1059300

Coupling fraction model to interpret the motion of non-fully coupled strike-slip faults

Zhenyu Zou[1]*, Zaisen Jiang[1], Yanqiang Wu[2], Yueju Cui[1] and He Tang[3]

[1]Key Laboratory of Earthquake Prediction, Institute of Earthquake Forecasting, CEA, Beijing, China, [2]First Crust Monitoring and Application Center, China Earthquake Administration, Tianjin, China, [3]Key Laboratory of Computational Geodynamics, University of Chinese Academy of Sciences, Beijing, China

Despite coupling fractions being extensively used in the interseismic period, the coexistence of locking and creeping mechanisms and the correlation between the coupling fraction and locking depth remain poorly understood because of the lack of a physical model. To overcome these limitations, in this study, we propose a coupling fraction model for interpreting the motion of non-fully coupled strike-slip faults based on the classic two-dimensional strike-slip fault model and the superposition principle. The model was constructed using numerous tiny, alternating creeping and locking segments. The deformation produced by the model is the same as that of the classic two-dimensional strike-slip fault, except for the scale factor. The model and definition of the coupling fraction can be perfectly integrated. Based on the model, we put forward a varying decoupled fraction with depth model, which considers the depth-dependent coupling fraction. The two models provide deep insights into the deformation characteristics of quasi-arctangent curves produced by non-fully coupled strike-slip faults and the local and macroscopic characteristics of fault locking in the interseismic period.

KEYWORDS

coupling fraction, deformation, strike-slip fault, locking depth, fault locking

1 Introduction

Dislocation theory, which interprets fault-motion-based deformation on the surface, has become an important physical model since the elastic rebound theory was put forward (Reid 1910; Chinnery, 1963; Okada 1985, 1992; Matsu'ura et al., 1986; Sun and Okubo, 1993, 1998; Wang et al., 2003; Steketee, 1958; Pan, 2019; Dong et al., 2021). The simplest representation of dislocation along an infinitely deep and long strike-slip fault is shown in Figure 1A. Savage and Burford (1973) reported the equation for the velocity of the model (SB73 model)—represented by a straight and vertical fault in an elastic half-space, in which uniform slip equal to the free slip rate occurs on the fault below the depth, above which the fault is fully coupled—as follows:

$$v = \frac{s}{\pi} tan^{-1}\left(\frac{x}{d}\right), \tag{1}$$

where x is the distance from the fault and d is the locking depth, which means that the fault above d is fully coupled/locked, whereas the fault below d is fully creeping. The parameter s is the free slip rate below d (Figures 1A, B). The curve produced by the SB73 model is an arctangent function (Figure 1B). Furthermore, the coupling fraction (or fault locking), which quantifies the slip deficit on the patch of a seismogenic zone relevant to the free creep below the patches, was introduced to describe the locking degrees from the shallow to the deep parts of the fault (McCaffrey et al., 2000; McCaffrey, 2002; McCaffrey, 2005; Scholz, 2007). The coupling fraction δ is defined as follows:

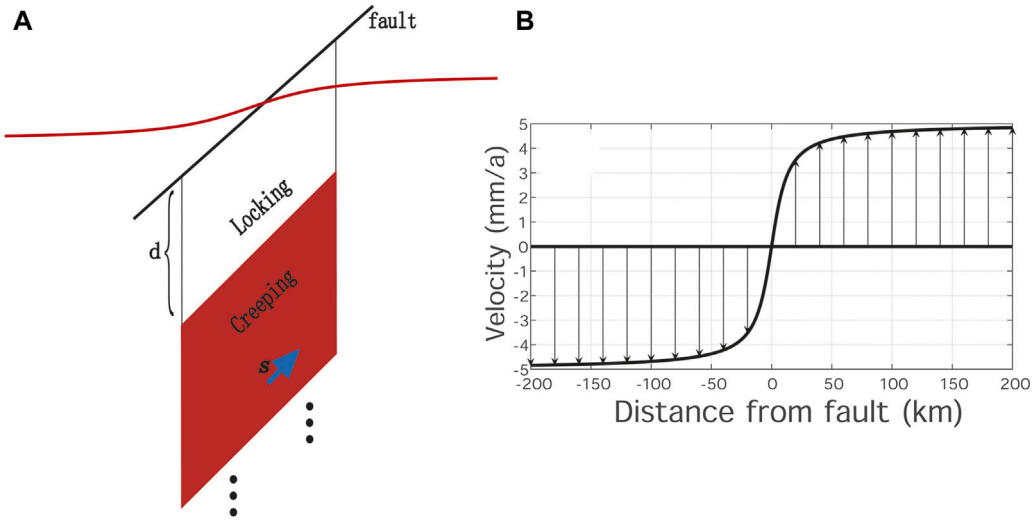

FIGURE 1
(A) Classic 2D strike-slip fault model and **(B)** produced surface deformation (redrawn according to Savage and Burford, 1973). A dextral strike-slip fault with a slip rate of 10 mm/a and a locking depth of 10 km was used as an example.

$$\delta = 1 - \frac{S_c}{S}, \tag{2}$$

where s is the free slip rate and s_c represents the creeping part of the non-fully coupled fault. Based on negative dislocation theory (Matsu'ura et al., 1986), the locking degrees of faults can be obtained by the inversion of surface deformation on each patch and used to estimate the seismic risk of the fault (Jiang et al., 2015; Zhao et al., 2020; Li et al., 2021a; Li et al., 2021b; Jian et al., 2022; Li et al., 2022).

Although the coupling fraction has been widely used in the interseismic period, questions remain regarding the coexistence of locking and creeping mechanisms, and the correlation between the coupling fraction and locking depth, because of the lack of a physical model. Why can the slip and lock happen at the same time during fault motion, and what is the physical meaning of the coupling fraction? In this study, an appropriate two-dimensional coupling fraction (CF) fault model is proposed for interpreting the motion of non-fully coupled strike-slip faults based on the SB73 model and the superposition principle. In addition, a varying decoupled fraction with depth (VDFD) model is established, based on the CF model, to expand the model's applications. Two models interpreting the motion of the non-fully coupled strike-slip fault can help us to understand why and how the faults can be creeping and locking at the same time.

2 Model with non-fully coupled strike-slip fault

In our discussion, a fault segment that is fully coupled or locked is called a *locking segment*, and a fault segment that is fully creeping or slipping is called a *creeping segment*. The length of the fault segment is called the *segment length*, and the function $Cf(d, L)$ represents the surface slip distribution by the fault segment, for which the vertical distance from the upper edge of the fault to the surface is d and the segment length is L (Figure 2A). Based on the superposition principle and the SB73 model, the CF and VDFD models are proposed in this study.

2.1 Model of the strike-slip fault with a finite locking segment length

The model for the slip distribution of the strike-slip fault with a finite locking segment length can be expressed as follows (Figure 2A):

$$Cf(d, L) = \frac{s}{\pi}\left(tan^{-1}\frac{x}{d} - tan^{-1}\frac{x}{d+L}\right). \tag{3}$$

It can be constructed based on the superposition principle and the SB73 model, or directly derived from screw dislocation (Savage and Burford, 1973; Savage, 1990; Segall, 2010).

2.2 Construction of the CF model

Based on the model mentioned previously, the locking segment is laid from the surface to depth d and the fault segment below d, where the segment length L is divided into n patches and the segment length of each patch is Δd, with $\Delta d = \frac{n}{L}$. The creeping segments with segment lengths of $\theta \cdot d$ are then laid on the random position of each patch (Figure 2B). Therefore, the total surface deformation $Cf(d, L)$ is the sum of the surface deformation of each creeping segment based on the superposition principle:

$$Cf(d, L) = \sum_{i=1}^{n} \frac{s}{\pi}\left[tan^{-1}\left(\frac{x}{d_{x_i}}\right) - tan^{-1}\left(\frac{x}{d_{x_i} + \theta\frac{n}{L}}\right)\right], \tag{4}$$

where $d \geq 0$, $0 < \theta \leq 1$, $i = 1, 2, \cdots n$, and d_{x_i} represents each of the upper edges of the creeping segment, which is a random value in the interval $[d + (i-1)\Delta d, d + i\Delta d - \theta\Delta d]$, $i = 1, 2, \cdots n$. When n is very

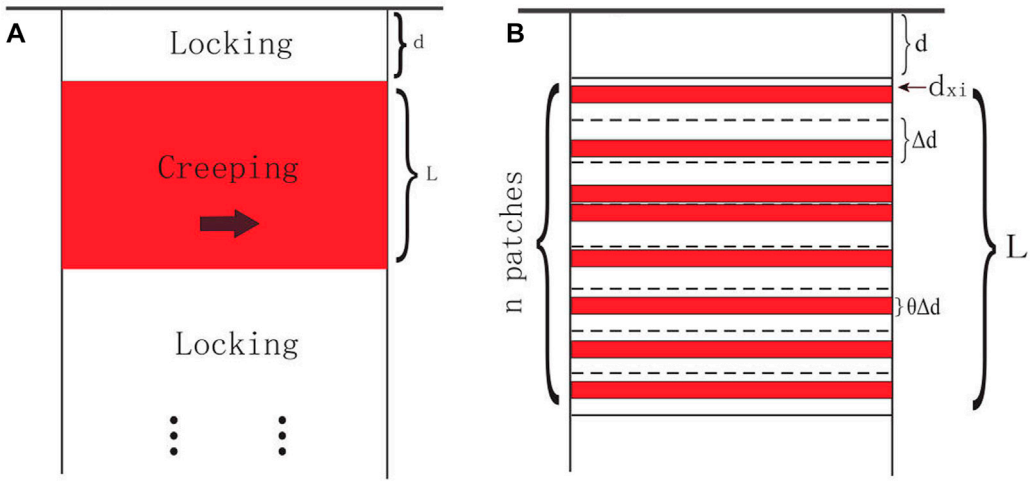

FIGURE 2
Red and white patches represent creeping and locking segments, respectively. **(A)** Model of the strike-slip fault with a finite locking segment length. Surface deformation is $\frac{s}{\pi}\left(tan^{-1}\frac{x}{d}-tan^{-1}\frac{x}{d+L}\right)$. **(B)** Schematic of the coupling fraction fault (CF) model construction.

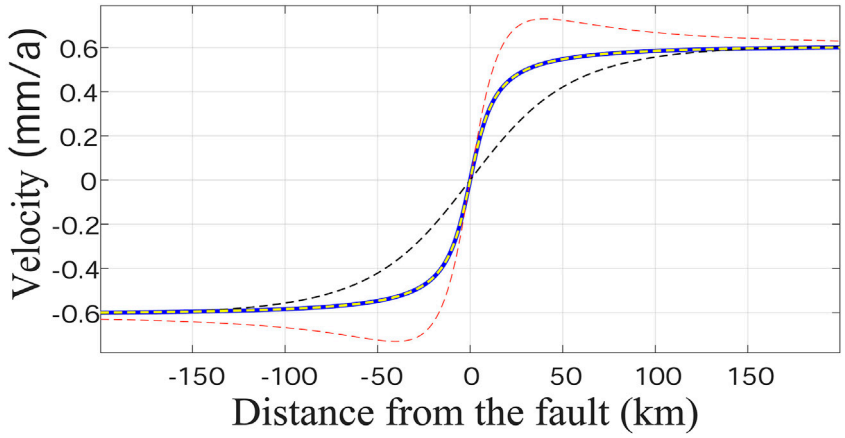

FIGURE 3
Curves obtained from the numerical simulation of $Cf(d, L)$. θ value is 0.4, d is 10 km, L is 10,000 km (without considering the actual situation, only for the validation of the model), s is π mm/a, and the thick blue line is $\theta\cdot\frac{s}{\pi}\left(tan^{-1}\frac{x}{d}-tan^{-1}\frac{x}{d+L}\right)$. Red and black dashed lines are the curves of $Cf(d, L)$ when $n = 100$. The curves are over- or underloaded because of the random positions of creeping segments in each patch; yellow dashed line ($n = 10{,}000$) and blue line overlap.

large, $Cf(d, L)$ approaches a result which is $\theta\cdot\frac{s}{\pi}\left(tan^{-1}\frac{x}{d}-tan^{-1}\frac{x}{d+L}\right)$ (Figure 3). Therefore, the CF model $\boldsymbol{Cf(d, L, \theta)}$ is expressed as follows:

$$\boldsymbol{Cf(d, L, \theta) = \lim_{n\to\infty}\sum_{i=1}^{n}\frac{s}{\pi}\left[tan^{-1}\left(\frac{x}{d_{x_i}}\right)-tan^{-1}\left(\frac{x}{d_{x_i}+\theta\Delta d}\right)\right]}. \tag{5}$$

This model represents the surface deformation caused by numerous tiny creeping segments that are separated by locking segments. As shown in Figure 2B, the creeping part of the fault segment with segment length L is discontinuous in depth when n is very large.

We applied the Lagrange mean value theorem, $\forall i$, as follows:

$$\boldsymbol{tan^{-1}\left(\frac{x}{d_{x_i}}\right)-tan^{-1}\left(\frac{x}{d_{x_i}+\theta\Delta d}\right)=-\frac{\theta L}{n}\cdot\left.\frac{d\left(tan^{-1}\frac{x}{\zeta}\right)}{d\zeta}\right|_{\zeta=\zeta_i}},$$

where $\zeta_i\in[d_{x_i}, d_{x_i}+\frac{n}{L}]$

$$\boldsymbol{\therefore Cf(d, L, \theta) = -\frac{\theta s}{\pi}\lim_{n\to\infty}\sum_{i=1}^{n}\frac{L}{n}\cdot\left.\frac{d\left(tan^{-1}\frac{x}{\zeta}\right)}{d\zeta}\right|_{\zeta=\zeta_i}}$$

$$\boldsymbol{=-\frac{\theta s}{\pi}\int_{d}^{d+L}\frac{d\left(tan^{-1}\frac{x}{\zeta}\right)}{d\zeta}d\zeta=\frac{\theta s}{\pi}\left(tan^{-1}\frac{x}{d}-tan^{-1}\frac{x}{d+L}\right)}, \tag{6}$$

where θ is called the "decoupled fraction" or "fault creeping" in Formula 6 (strict proof is provided in the Supplementary Material).

The CF model is derived from the superposition principle and the SB73 model, which ensure the correctness of the model in theory. The

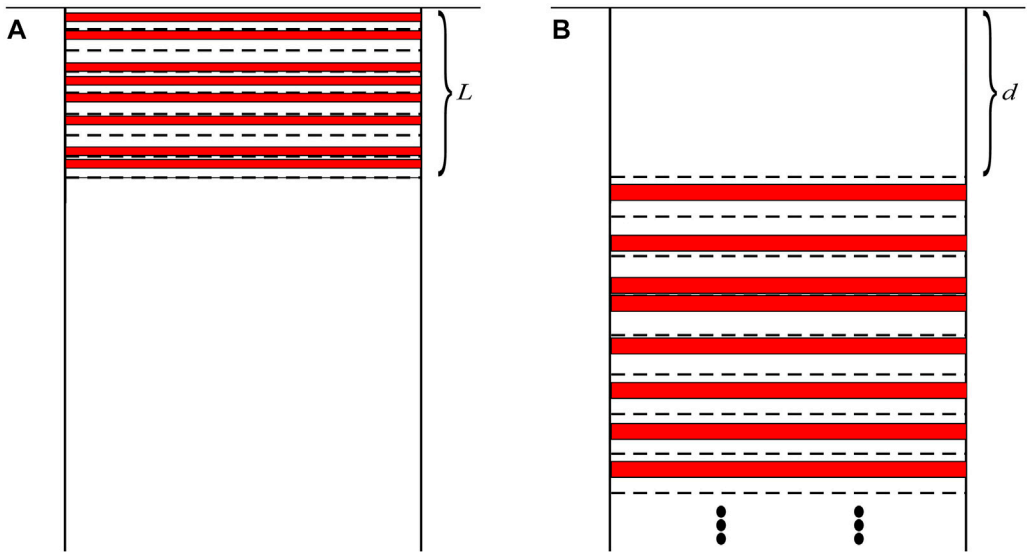

FIGURE 4
(A) $Cf(0, L, \theta)$ and **(B)** $Cf(d, \infty, \theta)$.

construction of the CF model shows that numerous, tiny creeping segments alternate with the locking segments. The results of the CF model illustrate that the sum of the deformation by these creeping segments is the same as the deformation by the large creeping segment in Figure 2A, except for the scale factor θ. Figure 3 shows the results of the comparison between $Cf(d, L, \theta)$ and $Cf(d, L)$. When n is not large enough, which also means that the creeping segments are not small enough, the curves are over- or underloaded because of the random positions of creeping segments in each patch. When n increases, $Cf(d, L)$ and $Cf(d, L, \theta)$ quickly coincide.

2.3 Correlation between θ and δ

The θ parameter in the CF model is derived from superposition and the SB73 model, whereas δ is defined by the equation (McCaffrey, 2002). In this study, the correlation between θ and δ is discussed. First, $Cf(0, L, \theta)$ and $Cf(d, \infty, \theta)$ must be derived using Formula 6 (Figure 4):

$$\begin{aligned} \boldsymbol{Cf}(\boldsymbol{0}, \boldsymbol{L}, \boldsymbol{\theta}) &= \boldsymbol{\lim_{d\to 0}} \boldsymbol{Cf}(\boldsymbol{d}, \boldsymbol{L}, \boldsymbol{\theta}) = \frac{\boldsymbol{\theta s}}{\boldsymbol{\pi}} \cdot \left(\frac{\boldsymbol{\pi}}{\boldsymbol{2}} \cdot \boldsymbol{sgn}(\boldsymbol{x}) - \boldsymbol{tan^{-1}} \frac{\boldsymbol{x}}{\boldsymbol{L}} \right) \\ &= \frac{\boldsymbol{\theta s}}{\boldsymbol{\pi}} \cdot \boldsymbol{tan^{-1}} \frac{\boldsymbol{L}}{\boldsymbol{x}}, \end{aligned} \tag{7}$$

$$\boldsymbol{Cf}(\boldsymbol{d}, \boldsymbol{\infty}, \boldsymbol{\theta}) = \boldsymbol{\lim_{L\to\infty}} \boldsymbol{Cf}(\boldsymbol{d}, \boldsymbol{L}, \boldsymbol{\theta}) = \frac{\boldsymbol{\theta s}}{\boldsymbol{\pi}} \cdot \boldsymbol{tan^{-1}} \frac{\boldsymbol{x}}{\boldsymbol{d}}, \tag{8}$$

where $sgn(x)$ is the signum function. Based on the negative dislocation (Matsu'ura et al., 1986), the slip distribution of the strike-slip fault with the coupling fraction δ can be expressed as follows:

$$\frac{\boldsymbol{s}}{\boldsymbol{2}} \boldsymbol{sgn}(\boldsymbol{x}) - \frac{\boldsymbol{\delta s}}{\boldsymbol{\pi}} \boldsymbol{tan^{-1}} \left(\frac{\boldsymbol{d}}{\boldsymbol{x}} \right),$$

where $\frac{s}{2} sgn(x)$ is the free slip rate and $\frac{\delta s}{\pi} tan^{-1}(\frac{d}{x})$ is the co-seismic deformation produced by δs.

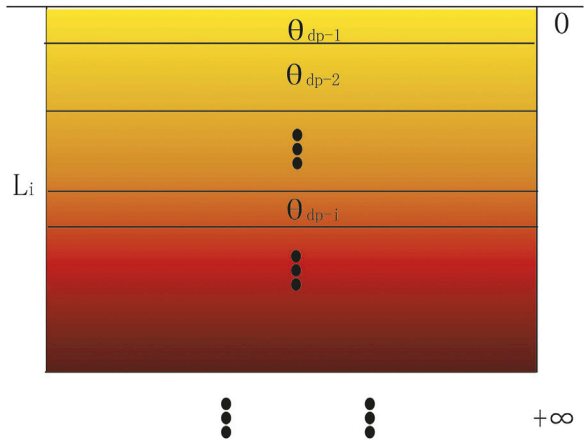

FIGURE 5
Model of the strike-slip fault with a depth-dependent θ value.

$$\begin{aligned} \Rightarrow \frac{\boldsymbol{s}}{\boldsymbol{2}} \boldsymbol{sgn}(\boldsymbol{x}) - \left[\frac{\boldsymbol{s}}{\boldsymbol{2}} \boldsymbol{tan^{-1}} \left(\frac{\boldsymbol{d}}{\boldsymbol{x}} \right) - \frac{(\boldsymbol{1}-\boldsymbol{\delta})\boldsymbol{s}}{\boldsymbol{\pi}} \boldsymbol{tan^{-1}} \left(\frac{\boldsymbol{d}}{\boldsymbol{x}} \right) \right] \\ = \frac{\boldsymbol{s}}{\boldsymbol{\pi}} \boldsymbol{tan^{-1}} \left(\frac{\boldsymbol{x}}{\boldsymbol{d}} \right) + \boldsymbol{Cf}(\boldsymbol{0}, \boldsymbol{d}, \boldsymbol{1}-\boldsymbol{\delta}). \end{aligned} \tag{9}$$

Formula 9 shows that the deformation produced by the coupling fraction is equal to the sum of the SB73 model and $Cf(0, d, 1-\delta)$. The equation $\theta = 1 - \delta = \frac{S_c}{S}$ illustrates that the CF model explains the coupling fraction well because θ represents the ratio of the creeping part of the fault segment. Therefore, based on the CF model, δ can be interpreted as the ratio of the total length of discontinuous locking parts in $Cf(d, L, \theta)$ to L (the correlation between θ and δ in layered faults is discussed in the Supplementary Material).

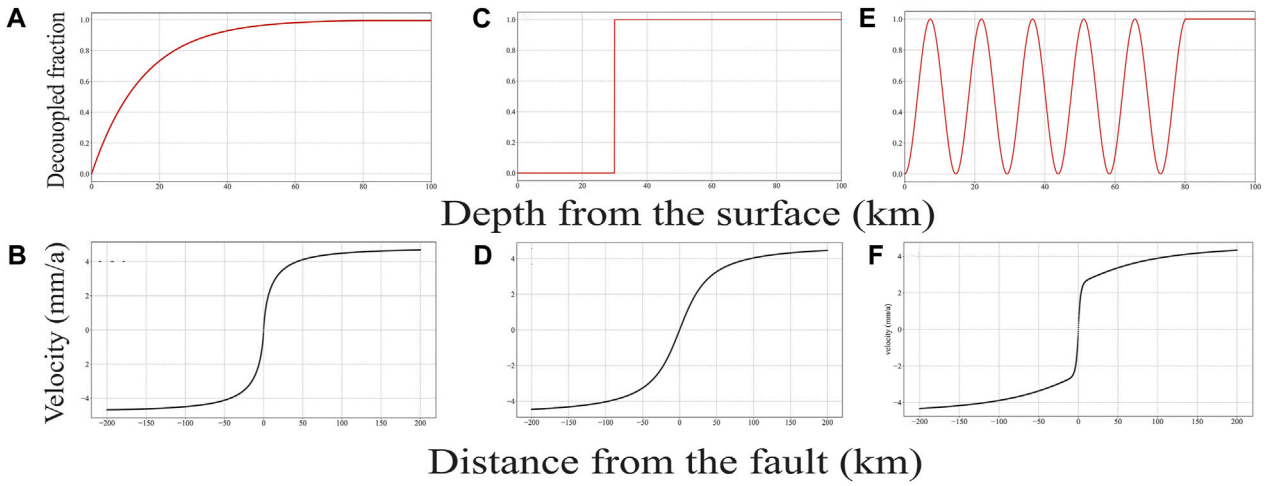

FIGURE 6
Examples of $\theta(l)$ values and the corresponding deformation. **(A)** $\theta(l)$ increases from the surface to underground 80 km; **(C)** $\theta(l)$ is 0 above 30 km and 1 below 30 km, which is the SB73 model; **(E)** $\theta(l)$ fluctuates from the surface to 80 km; **(B,D,F)** corresponding surface deformation. The shape of curve **(B)** is similar to the arctangent curve.

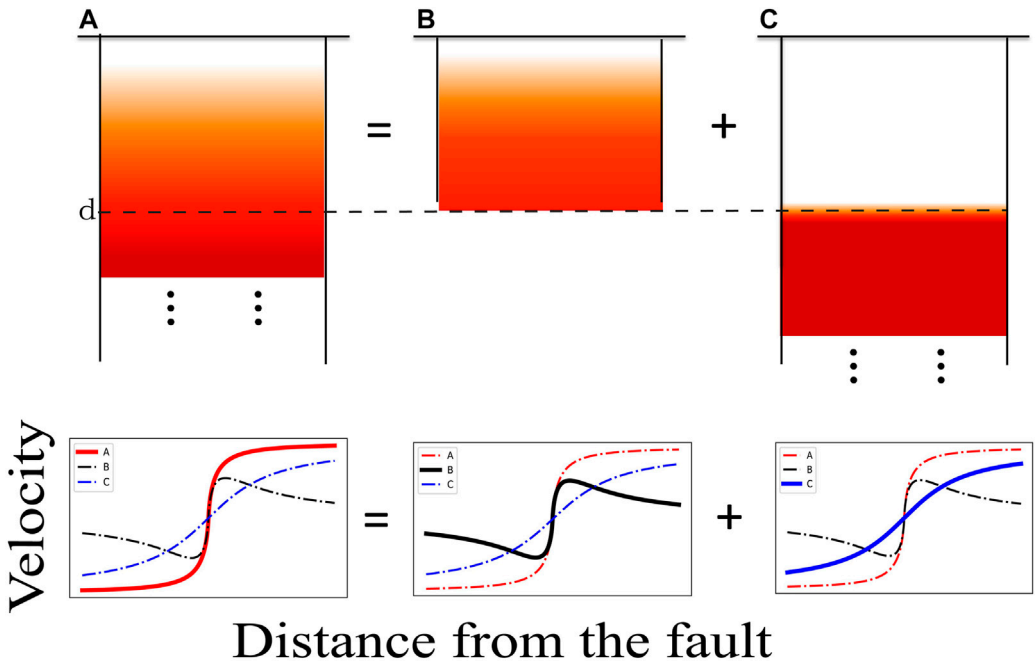

FIGURE 7
Schematic of the superposition of the decoupled fraction, which increases with depth; fault A = fault B + fault C. The corresponding deformation satisfies the equation. Red, black, and blue lines represent the deformation of faults **(A, B, and C,)** respectively.

2.4 Model with depth-dependent decoupled fraction

Based on the CF model, the model of the fault with a θ value varying in depth was studied (VDFD model). The model with θ varying in depth is shown in Figure 5. It can be divided into patches: $[L_0, L_1], [L_1, L_2], \cdots [L_{n-1}, L_n], \cdots. L_0 = 0$. The decoupled fraction is θ_{dp-i} in patch $[L_{i-1}, L_i]$, $i = 1, 2 \cdots n$. Based on the CF model, the total deformation generated by patches is presented as follows:

$$s_{total}(x) = \frac{s}{\pi} \cdot \sum_{i=1}^{n} \theta_{dp-i} \cdot \left[tan^{-1}\left(\frac{x}{L_{i-1}}\right) - tan^{-1}\left(\frac{x}{L_i}\right) \right].$$

We then applied the Lagrange mean value theorem, $\forall i$, as follows:

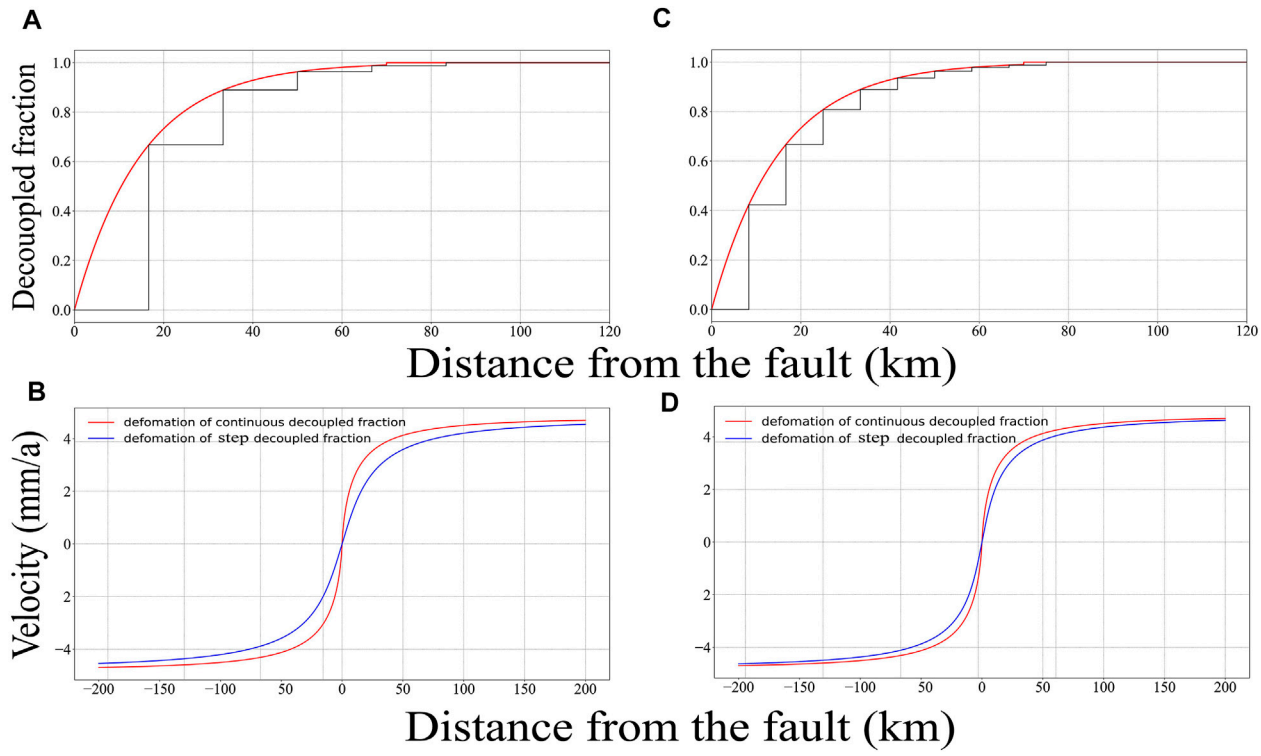

FIGURE 8
Deformation of step $\theta(l)$ approaching continuous $\theta(l)$. **(A,C)** Step $\theta(l)$ (black line) approaching continuous $\theta(l)$ (red line) with different steps. **(B,D)** corresponding deformation. Red and blue lines are based on continuous $\theta(l)$ and step $\theta(l)$, respectively.

$$s_{total}(x) = -\frac{s}{\pi} \cdot \sum_{i=1}^{n} \theta_{dp-i} \cdot \left. \frac{dtan^{-1}\left(\frac{x}{l}\right)}{dl} \right|_{l=l_{\xi_i}} \cdot (L_i - L_{i-1})\, l_{\xi_i} \epsilon [L_{i-1}, L_i].$$

When θ_{dp-i} continuously varies with depth, $\theta_{dp-i}(i = 1, 2 \cdots n) \Rightarrow \theta(l)$, the length of each patch is very small, that is, $n \to \infty$:

$$s_{total}(x) = \lim_{n\to\infty} -\frac{s}{\pi} \cdot \sum_{i=1}^{n} \theta_{dp-i} \cdot \left. \frac{dtan^{-1}\left(\frac{x}{l}\right)}{dl} \right|_{l=l_{\xi_i}} \cdot (L_i - L_{i-1}).$$

Therefore, the deformation of the VDFD model can be expressed as follows:

$$s_{total}(x) = \frac{s}{\pi} \int_0^{+\infty} \frac{\theta(l) \cdot x}{x^2 + l^2} dl, \tag{10}$$

where s is the free slip rate, x is the distance from the fault, and l is the vertical distance from a certain depth to the surface. The $\theta(l)$ represents the function of θ with respect to l, where $0 \le \theta(l) \le 1$. We defined the function of the coupling fraction with respect to l as $\delta(l) = 1 - \theta(l)$. The equation of $s_{total}(x)$ is similar to the distributed slip (Aki and Richards, 1980; Matthews and Segall, 1993). $s_{total}(x)$ is derived from the CF model, and $\theta(l)$ has a clear physical meaning. The critical function $\theta(l)$ controls the slip distribution of the fault. In this study, several examples of $\theta(l)$ and the corresponding deformation are provided (Figure 6). Figure 6A indicates that $\theta(l)$ gradually increases from the surface to the underground. Figure 6C indicates that $\theta(l)$ is fully locked above 30 km and fully creeping under 30 km, representing the SB73 model with a locking depth of 30 km. Figure 6E shows the fluctuation of $\theta(l)$ from the surface to the underground. Figures 6B, D, F show the corresponding curves. The VDFD model, which has a flexible $\theta(l)$, can produce more complex slip distributions than the SB73 and CF models.

3 Discussion

3.1 Why is the shape of the coupling fraction deformation curve, which decreases with depth, similar to that of the arctangent curve?

The decrease in the coupling fraction with depth means that the decoupled fraction increases with depth. This study discusses the reason for the similar shapes of the curves for the arctangent function and decoupled fraction, which increase with depth. As shown in Figure 7, the decoupled fraction increases from the surface to d and is fully creeping below d, which is equal to the sum of faults B and C (Figure 7). Fault C is the SB73 fault, which generates the arctangent curve. Based on the CF model, the fault segment near the surface, which should produce large deformation, generates small deformation because of the small decoupled fraction in fault B. Hence, fault C dominates the shape of the whole curve. Therefore, the curve of fault A is similar to the arctangent curve.

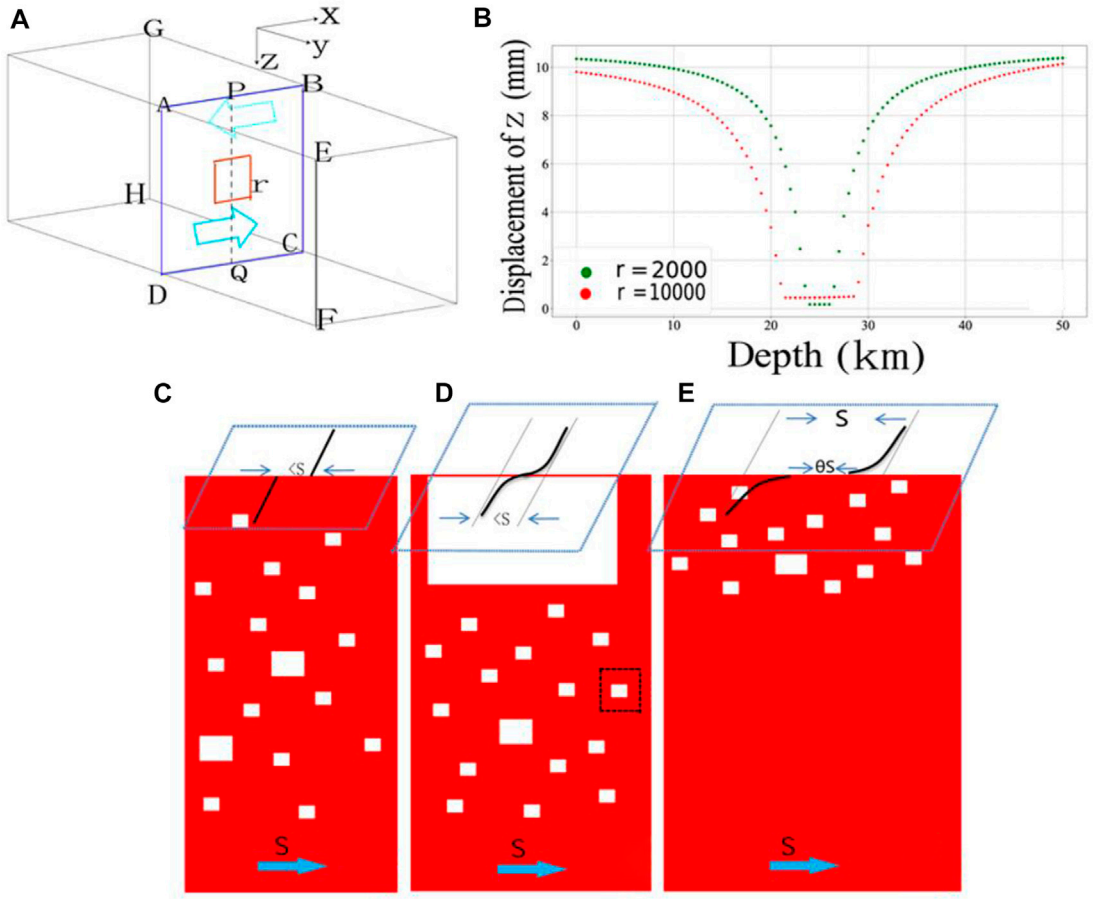

FIGURE 9
(A) Numerical simulation of the effect of asperity impediment using the three-dimensional (3D) numerical manifold method (NMM), which is useful for the simulation of discontinuous deformation as fault motion (Shi 2001; Wu et al., 2020). First, we set up a 3D research area and confining pressure. Subsequently, we pushed (two blue arrows) in opposite directions (AEFD inward and BGHC outward). The red-lined box represents an asperity; the side length is *r*. The displacement of the push is 10 mm. A row of measuring points PQ line was set up in ABCD. **(B)** Vertical deformation of the measuring points; the deformation for a side length of the asperity of 2000 m is represented by the green dashed line; the deformation for a side length of the asperity of 10,000 m is represented by the red dashed line. **(C)** *S* means the free slip rate. Small and numerous asperities without large asperities, <*s* means the value of creeping rate is smaller than the free slip rate *S*; **(D)** small and numerous asperities in the lower part and a huge asperity on the top part of the fault; **(E)** small and numerous asperities on the top part of the fault.

3.2 Correlation among the coupling fraction, locking depth, and value of the locking depth based on curve fitting

Locking depth is the parameter in the SB73 model, which considers full coupling above the depth and full creeping below the depth. The curve produced by the SB73 model is an arctangent function. The coupling fraction δ, which changes between 0 and 1, varies with depth. When δ is 1 above a certain depth d_0 and 0 below the d_0, then the d_0 can be considered the locking depth in the SB73 model. Sometimes the curves produced by the coupling fraction are similar to arctangent curves (Figure 7). By fitting curves that approximate the arctangent function with the SB73 model, we can obtain a value of the locking depth. The value reflects the average variation of the coupling fraction with depth. The quantitative correlation must be further studied.

3.3 Correlation between the deformation caused by step $\theta(\boldsymbol{l})$ and continuous $\theta(\boldsymbol{l})$

When inverting the coupling fraction on the fault, the fault plane is generally divided into many small patches, and the coupling fraction on each patch is a constant equivalent to replacing the continuous coupling fractions in practice with step ones. In this study, the correlation between the deformation caused by step $\theta(l)$ and continuous $\theta(l)$ in two dimensions is discussed based on the VDFD model. Based on Section 2.4, Formula 10 means the mapping from $\theta(l)$ to $s_{total}(x)$. The mapping is proven to have mathematical continuity and uniqueness (proof is provided in the Supplementary Material). Uniqueness means that there are no two different values of $\theta(l)$ that produce the same $s_{total}(x)$, which shows that there are no multiple solutions in theory. Continuity means that if $\theta_1(l)$ and $\theta_2(l)$ are similar, then $s_{total-1}(x)$ and $s_{total-2}(x)$ are also similar.

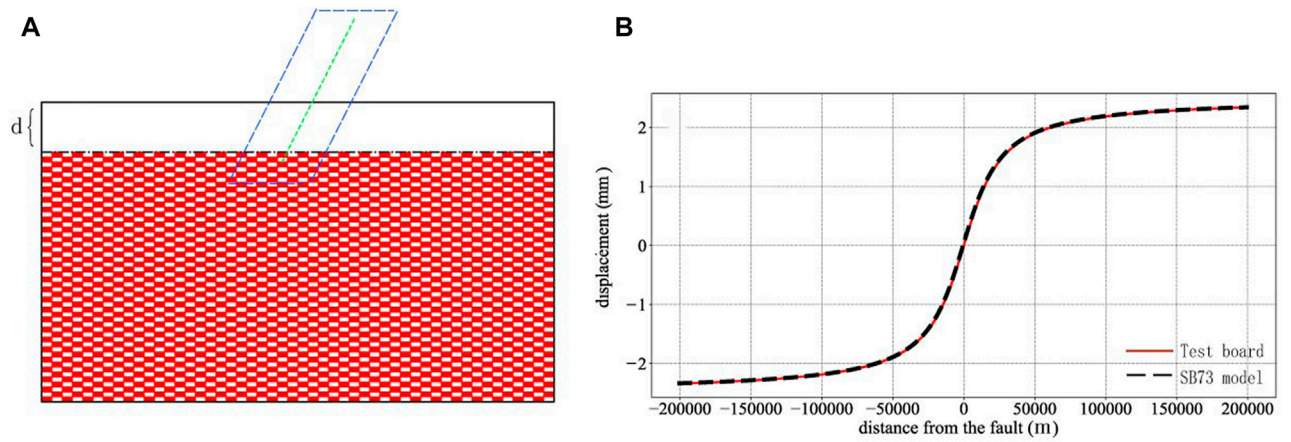

FIGURE 10
Results of test board fault. When the number of patches is 100 × 100 = 10000, the deformation curve is very close to the arctangent function. **(A)** Test board fault; green dash line means measurement points, s = 10mm/a and d = 20km; **(B)** curve made by the test board fault and the SB73 model with s = 5mm/a and d = 20km.

As shown in Figures 8A, C, the step $\theta(l)$ is used to replace the continuous $\theta(l)$. Figures 8B, D illustrate the difference between the deformations based on step $\theta(l)$ and continuous $\theta(l)$. The number of steps in Figure 8C is higher than that in Figure 8A, which is closer to the continuous $\theta(l)$. Therefore, the curve based on step $\theta(l)$ in Figure 8C is closer to that based on continuous $\theta(l)$, compared with that in Figure 8A. Thus, more steps yield results closer to the actual $\theta(l)$ but also indicate more unknown numbers with respect to the inversion. Therefore, the dense layout of global positioning system (GPS) stations can increase the data density of deformation, helping to improve the accuracy of the inversion of the coupling fraction, which may be hard to achieve at present because of the lack of sufficient GPS stations for some strike-slip faults. Three-dimensional models can be more complex because of lateral heterogeneity, which must be further studied.

3.4 Physical meaning of the coupling fraction

The CF model is obtained from the SB73 model and the superposition principle. Therefore, its mathematical correctness is guaranteed. One aim of this study was to explain the physical meaning of the coupling fraction. Based on the aforementioned discussion, we know that locking segments in the CF model could be tiny, numerous, and alternating with creeping segments. Based on microscopic and macroscopic views of the fault, fully coupled fault segments and non-fully coupled ones exist, respectively. The fault plane contains small and large asperities. Based on the magnitude–frequency correlation, it is known that the smaller the size, the greater is the number of asperities. Therefore, small asperities are widely distributed on the fault plane. The results of the numerical simulation show that the effect of an asperity impeding the creep of the fault diminishes by ~90% when the distance is larger than 3–5 times the size of the asperity (Figures 9A, B). The fault plane contains numerous small asperities, which are all at certain distances from each other and impede each other's motion. Although impediments lead to full coupling in local areas containing small asperities (e.g., black dashed box in Figure 9D), numerous impediments reduce the slip rate of the whole fault plane and the coupling fraction forms macroscopically. The test board results also show that when patches are very small, the alternate creeping and locking patches can also produce arctangent curves macroscopically (Figures 10A, B). Thus, the macroscopic fault slip rate should be less than that of the local area. Therefore, the fault slip rate obtained from repeating events (which may be closer to the free slip rate) is often greater than that based on the GPS velocity field (Li et al., 2011; Zhang et al., 2022). The physical meaning of the coupling fraction is the ratio of the total area of the small asperities to the fault area when the small asperities are distributed everywhere.

Based on Section 2.2, we know that $1-\theta$ represents the ratio of the total area of numerous small asperities on the fault plane to their surrounding areas. The creeping rate of the fault with s becomes smaller than s because of many small asperities. If the fault plane contains numerous small but no large asperities, the fault creeps at a rate smaller than s (Figure 9C). If the lower part of the fault contains many small asperities and the top part contains a giant asperity, the deformation is equivalent to that of the SB73 model with a slip rate smaller than s (Figure 9D). If the top of the fault contains a large number of small asperities and no asperity is observed in the lower part, the deformation is the sum of the SB73 model and $Cf(0, L, \theta)$, the step interval is θs, and the slip rate is s (Figure 9E). The large asperity and many small asperities determine the characteristics of surface deformation, but no matter how the small asperities are distributed, the far-field slip rate is often smaller than the free slip rate, s. The size of asperities is not infinitesimal, so the physical model is not the same as the mathematical model. The random positions of the asperities affect the shape of the deformation curve, which is similar but not identical to the arctangent curve (Figure 3). Therefore, it is possible that the surface deformation curve produced by a non-fully coupled strike-slip fault deviates from the arctangent curve. We can only approximate the shape of the arctangent curve because the distributions of a huge number of small asperities with certain sizes on the fault plane are unknown. In addition, limitations of this study exist due to the current models: 1) the models mentioned in this study are based on semi-infinite elastic bodies, so the transverse inhomogeneity

and the influence of viscoelastic bodies are not considered in the models, and 2) the positions of creeping segments are random but laid on a relatively small range (Figure 2B), and the segment length of creeping segments is equal. In practice, the segment length of the creeping segments should be unequal and the positions should be more random. These problems are closer to reality and must be further studied in the future. Based on the aforementioned discussion, we have known that the far-field slip rate of the fault (or the secular slip rate) could often be smaller than the free slip rate. We could only obtain the secular/far-field slip rate by GPS velocity. The terms "secular/far-field slip rate of fault" and "free slip rate" should be distinguished.

4 Conclusion

Based on the SB73 model and the superposition principle, a CF model of the motion of non-fully coupled strike-slip faults was constructed using numerous tiny, alternating creeping and locking segments. The slip rate of the deformation produced by the CF model is θs, where s is the free slip rate. The definition of the coupling fraction δ is interpreted by the CF model. A VDFD model is proposed based on the CF model. The models with non-fully coupled strike-slip faults provide insights into the complexity of the motion of strike-slip faults: 1) the surface deformation is generated by the fault slip rate s with numerous small asperities, but the shape is equal to that of the deformation based on a lower slip rate θs without asperities; 2) the meaning of the coupling fraction is the ratio of the total area of the small asperities to the fault area when the small asperities are widely distributed; and 3) according to the VDFD model, the curve generated by the non-SB73 model is sometimes similar to an arctangent curve. The CF and VDFD models provide deep cognition for understanding the deformation characteristics of non-fully coupled faults.

Data availability statement

The original contributions presented in the study are included in the article/Supplementary Material, further inquiries can be directed to the corresponding author.

Author contributions

Methodology, ZZ and ZJ; resources, ZZ; funding, ZZ, YW, and YC; test, ZZ; numerical simulation, ZZ and YW; visualization, ZZ; first draft preparation, ZZ and YC; editing, ZZ and YC; supervision, ZJ; proof, ZZ and HT.

Funding

This research was supported by the National Natural Science Foundation of China (41904092 and 41974011), the National Key Research and Development Program of China (2018YFE0109700 and 2019YFC1509203), and the Basic Research Project of the Institute of Earthquake Forecasting, China Earthquake Administration (2020IEF0506).

Acknowledgments

The authors express their gratitude to Tai Liu, Zhenyu Wang, and Yueyi Xu at the Institute of Earthquake Forecasting, China Earthquake Administration, and Long Zhang at the Institute of Geophysics, China Earthquake Administration, for their helpful discussions about the CF and VDFD models. The researcher YW in First Crust Monitoring and Application, China Earthquake Administration, provided the 3D-NMM calculation program. The authors also thank moderators Czhang271828, zhan-xun, kuing, and TSC999 on the online mathematics forum at http://kuing.infinityfreeapp.com/forum.php for their help with the core ideas of the proofs. Python and MATLAB software were used for numerical simulation and to prepare some of the figures.

Conflict of interest

The authors declare that the research was conducted in the absence of any commercial or financial relationships that could be construed as a potential conflict of interest.

Publisher's note

Supplementary material

The Supplementary Material for this article can be found online at: https://www.frontiersin.org/articles/10.3389/feart.2023.1059300/full#supplementary-material

References

Aki, K., and Richards, P. (1980). *Quantitative seismology*, 1. New York: W. H. Freeman.

Chinnery, M. (1963). The stress changes that accompany strike-slip faulting. *Bull. Seismol. Soc. Am.* 53, 921–932. doi:10.1785/bssa0530050921

Dong, J., Cheng, P., Wen, H., and Sun, W. (2021). Internal co-seismic displacement and strain changes inside a homogeneous spherical Earth. *Geophys. J. Int.* 225, 1378–1391. doi:10.1093/gji/ggab032

Jian, H., Gong, W., Li, Y., and Wang, L. (2022). Bayesian inference of fault slip and coupling along the tuosuo lake segment of the kunlun fault, China. *Geophys. Res. Lett.* 49, e2021GL096882. doi:10.1029/2021GL096882

Jiang, G., Xu, X., Chen, G., Liu, Y., Fukahata, Y., Wang, H., et al. (2015). Geodetic imaging of potential seismogenic asperities on the Xianshuihe-Anninghe-Zemuhe fault system, southwest China, with a new 3-D viscoelastic interseismic coupling model. *J. Geophys. Res. -sol Ea.* 120, 1855–1873. doi:10.1002/2014JB011492

Li, L., Chen, Q., Niu, F., and Su, J. (2011). Deep slip rates along the Longmen Shan fault zone estimated from repeating microearthquakes. *J. Geophys. Res. -sol Ea.* 116, B09310. doi:10.1029/2011JB008406

Li, L., Wu, Y., Li, Y., Zhan, W., and Liu, X. (2022). Dynamic deformation and fault locking of the xianshuihe fault zone, southeastern Tibetan plateau: Implications for seismic hazards. *Earth Planets Space* 74, 35. doi:10.1186/s40623-022-01591-9

Li, Y., Hao, M., Song, S., Zhu, L., Cui, D., Zhuang, W., et al. (2021a). Interseismic fault slip deficit and coupling distributions on the Anninghe-Zemuhe-Daliangshan-Xiaojiang fault zone, southeastern Tibetan Plateau, based on GPS measurements. *J. Asian Earth Sci.* 219, 104899. doi:10.1016/j.jseaes.2021.104899

Li, Y., Nocquet, J., Shan, X., and Jian, H. (2021b). Heterogeneous interseismic coupling along the xianshuihe-xiaojiang fault system, eastern tibet. *J. Geophys. Res. -sol Ea.* 126, e2020JB021187. doi:10.1029/2020JB021187

Matsu'ura, M., Jackson, D., and Cheng, A. (1986). Dislocation model for aseismic crustal deformation at Hollister, California. *J. Geophys. Res. -sol Ea.* 91, 12661–12674. doi:10.1029/JB091iB12p12661

Matthews, M., and Segall, P. (1993). Estimation of depth-dependent fault slip from measured surface deformation with application to the 1906 San Francisco Earthquake. *J. Geophys. Res.* 98, 12153–12163. doi:10.1029/93JB00440

McCaffrey, R. (2005). Block kinematics of the Pacific–North America plate boundary in the southwestern United States from inversion of GPS, seismological, and geologic data. *J. Geophys. Res.* 110, B07401. doi:10.1029/2004JB003307

McCaffrey, R. (2002). "Crustal block rotations and plate coupling," in *Plate boundary zones*. Editors S. Stein and J. T. Freymueller (Washington D.C.: Geodynamics Series), 101–122.

McCaffrey, R., Long, M., Goldfinger, C., Zwick, P., Nabelek, J., Johnson, C., et al. (2000). Rotation and plate locking at the southern cascadia subduction zone. *Geophys. Res. Lett.* 27, 3117–3120. doi:10.1029/2000GL011768

Okada, Y. (1992). Internal deformation due to shear and tensile faults in a half-space. *Bull. Seism. Soc. Am.* 82, 1 018–1040. doi:10.1785/BSSA0820021018

Okada, Y. (1985). Surface deformation due to shear and tensile faults in a half-space. *Bull. Seism. Soc. Am.* 75, 1135–1154. doi:10.1785/BSSA0750041135

Pan, E. (2019). Green's functions for geophysics: A review. *Rep. Prog. Phys.* 82, 106801. doi:10.1088/1361-6633/ab1877

Reid, H. (1910). "The machanism of the earthquake," in *The California Earthquake of april 18, 1906* (Washington, D.C: Report of the State Earthquake Investigation Commission), 2.

Savage, J., and Burford, R. (1973). Geodetic determination of relative plate motion in central California. *J. Geophys. Res.* 78, 832–845. doi:10.1029/JB078i005p00832

Savage, J. (1990). Equivalent strike-slip earthquake cycles in half-space and lithosphere-asthenosphere Earth models. *J. Geophys. Res. -sol Ea.* 95, 4873–4879. doi:10.1029/JB095iB04p04873

Scholz, C. H (2007). The mechanics of earthquakes and faulting. *Environ. Eng. Geoscience - ENVIRON ENG GEOSCI* 13, 81–83. doi:10.2113/gseegeosci.13.1.81

Segall, P. (2010). *Earthquake and volcano deformation*. New Jersey, United States: Princeton University Press. doi:10.1515/9781400833856

Shi, G. (2001). "Three dimensional discontinuous deformation analysis," in Proceedings of // International Conference on Analysis of Discontinuous Deformation, Glasgow, Scotland, UK, 6th - 8th June 2001, 1–21.

Steketee, J. (1958). On volterra"s dislocations in a semi-infinite elastic medium. *Can. J. Phys.* 36, 192–205. doi:10.1139/p58-024

Sun, W., and Okubo, S. (1998). Surface potential and gravity changes due to internal dislocations in a spherical Earth—ii. Application to a finite fault. *Geophys. J. Int.* 132, 79–88. doi:10.1046/j.1365-246x.1998.00400.x

Sun, W., and Okubo, S. (1993). Surface potential and gravity changes due to internal dislocations in a spherical Earth—I. Theory for a point dislocation. *Geophys. J. Int.* 114, 569–592. doi:10.1111/j.1365-246X.1993.tb06988.x

Wang, R., Martin, F., and Roth, F. (2003). Computation of deformation induced by earthquakes in a multi-layered elastic crust—FORTRAN programs EDGRN/EDCMP. *Comput. Geosci-Uk.* 29, 195–207. doi:10.1016/S0098-3004(02)00111-5

Wu, Y., Chen, G., Jiang, Z., Zhang, H., Zheng, L., Pang, Y., et al. (2020). Three dimensional numerical manifold method based on viscoelastic constitutive relation. *Int. J. Geomech.* 20. doi:10.1061/(ASCE)GM.1943-5622.0001798

Zhang, L., Su, J., Wang, W., Fang, L., and Wu, J. (2022). Deep fault slip characteristics in the Xianshuihe-Anninghe-Daliangshan Fault junction region (eastern Tibet) revealed by repeating micro-earthquakes. *J. Asian Earth Sci.* 227, 105115. doi:10.1016/j.jseaes.2022.105115

Zhao, J., Ren, J., Liu, J., Jiang, Z., Liu, X., Liang, H., et al. (2020). Coupling fraction and relocking process of the longmenshan fault zone following the 2008 Mw7.9 wenchuan earthquake. *J. Geodyn.* 137, 101730. doi:10.1016/j.jog.2020.101730

frontiers | Frontiers in Earth Science

TYPE Original Research
PUBLISHED 02 March 2023
DOI 10.3389/feart.2023.1060044

OPEN ACCESS

EDITED BY
Ziyadin Cakir,
Istanbul Technical University, Türkiye

REVIEWED BY
Zhangfeng Ma,
Hohai University, China
Guangcai Feng,
Central South University, China

*CORRESPONDENCE
Wenyu Gong,
gwenyu@ies.ac.cn
Xinjian Shan,
xjshan@163.com

SPECIALTY SECTION
This article was submitted to Structural Geology and Tectonics, a section of the journal Frontiers in Earth Science

RECEIVED 02 October 2022
ACCEPTED 13 February 2023
PUBLISHED 02 March 2023

CITATION
Hua J, Gong W, Shan X, Zhang G and Song X (2023), Three-dimensional coseismic displacements and slip distribution of the 2021 Mw 7.4 maduo earthquake: Synergy of SAR, InSAR and optical images.
Front. Earth Sci. 11:1060044.
doi: 10.3389/feart.2023.1060044

Three-dimensional coseismic displacements and slip distribution of the 2021 Mw 7.4 maduo earthquake: Synergy of SAR, InSAR and optical images

Jun Hua, Wenyu Gong*, Xinjian Shan*, Guohong Zhang and Xiaogang Song

State Key Laboratory of Earthquake Dynamics, Institute of Geology, Beijing, China

On 21 May 2021, an earthquake of moment magnitude (Mw) 7.4 occurred near Maduo county in Qinghai Province China. This is the first major earthquake that occurred in the interior of the Bayan Har block in the Tibetan Plateau over the past 70 decades. Focusing on this event, we conducted a study on three-dimensional (3D) coseismic displacement reconstruction and its tectonic implication. We acquired both Synthetic Aperture Radar (SAR) and optical imaging satellite imagery, including SAR images from Sentinel-1 and Advanced Land Observation Satellite-2 (ALOS-2) as well as the multi-spectrum images from the Sentinel-2 (S2) satellite. We applied the Interferometric SAR (InSAR) and pixel-offset tracking (POT) techniques to coseismic SAR data pairs and reconstructed two dimensional displacements. With the constructed displacement fields in multiple viewing directions, we resolved the 3D coseismic displacements (north-south, east-west, and up components) by integrating the regional strain model with variance components estimation (SM-VCE). We recommend using the standard deviation value at each grid cell, which can be calculated in the resampling, as the initial weight. Based on the resolved 3D coseismic displacements, we further estimated the dip angles for the two segments (F4 and F5) in the east of the rupture zone. The associated moment magnitude is about Mw7.4, which corresponds to the released energy of ~ 1.74×10^{20} Nm.

KEYWORDS

coseismic displacements, three-dimensional displacements, InSAR, pixel offset tracking, multi-source remote sensing

1 Introduction

On 21 May 2021, an earthquake of moment magnitude (Mw) 7.4 occurred near Maduo county in Qinghai Province China (Figure 1). The determined epicenter is located at 34.59°N, 98.34°E at a depth of ~17 km according to the China Seismological Network (CSN, https://ceic.ac.cn/). This Mw 7.4 earthquake occurred inside the Bayan Har block (Figure 1), which is one of the most active regions with strong earthquakes (Mw ≥ 7.0) in the Tibetan plateau (Jia et al., 2021). Most of these large earthquake events occurred along the boundaries of the Bayan Har block, e.g., the 1997 Mw7.5 Manyi earthquake (Wang et al., 2007), the 2001 Mw 7.8 Kokoxili earthquake (Vallée et al., 2008), the 2008 Mw7.9 Wenchuan earthquake (Diao et al., 2010), and the

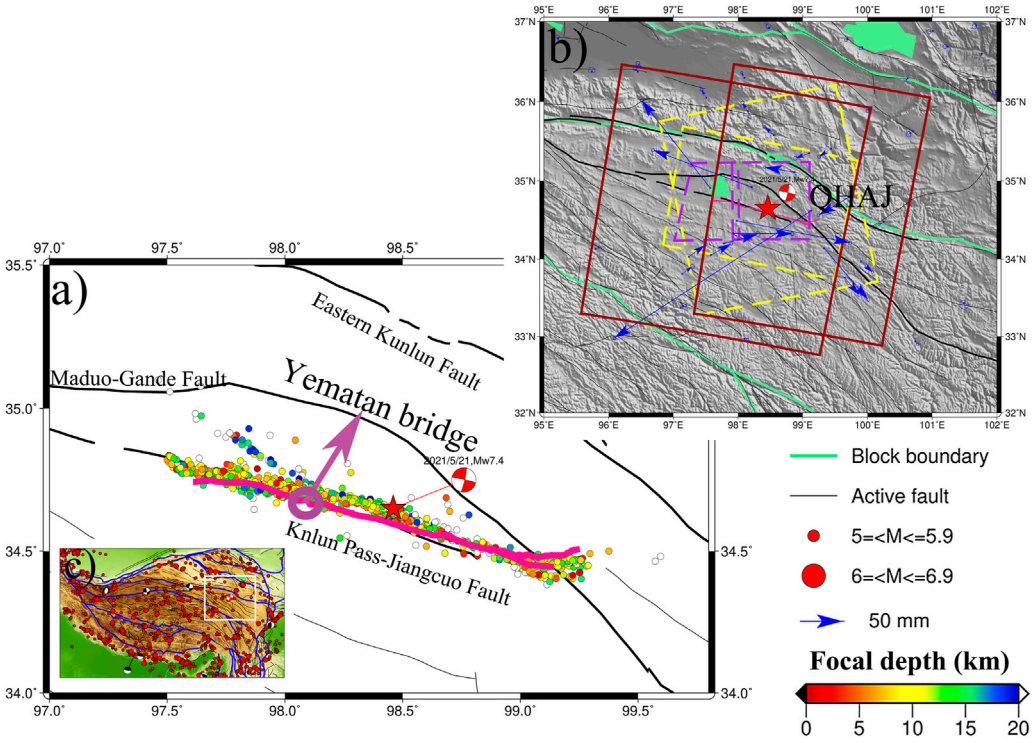

FIGURE 1
Tectonic setting of the 2021 Maduo earthquake. The red star denotes the epicenter location of the 2021 Maduo earthquake. Blue arrows in subplot **(B)** represent the coseismic horizontal GPS displacements (Wang et al., 2022). The pink line in **(A)** represents the surface rupture traces. In subplot **(A)**, the black lines are active faults from Deng et al. (2003) and the colored points represent the focal depth from aftershocks of the Maduo earthquake (Wang et al., 2021). The red boxes in subplot **(B)** are the coverages of ALOS-2 SAR data. The yellow dashed boxes represent the coverages of ascending and descending Sentinel-1 acquisitions. The purple dash boxes are denoted as coverages of Sentinel-2 data. The white box in subplot **(C)** is the region as shown in subplot **(B)**.

2008 Mw7.1 Yutian earthquake (Song et al., 2019). Whereas the Mw 7.4 Maduo earthquake is the first major earthquake to occur in the interior of the Bayan Har block since the 1947 Dari earthquake (Liu et al., 2022).

The overall length of the coseismic rupture zone is ~148 km (Yuan et al., 2022). It is located to the southeast of the big bend of the Kunlun fault (Zhao et al., 2021), which is seismically active and outlines the northern boundary of Bayan Har Block (See Figure 1). In the past year, there have been several geophysical studies (e.g. He et al., 2021; Zhao et al., 2021; Jin and Fialko, 2021; Chen et al., 2022; Liu et al., 2022; Tong et al., 2022) and geological studies (e.g., Ren et al., 2022; Yuan et al., 2022) to determine and investigate the characteristics of the seismogenic fault of the Mw7.4 Maduo earthquake. The geological studies were mostly focused on mapping fault geometry and coseismic surface ruptures. For example, Yuan *et al.* (2022a) surveyed the horizontal and vertical displacements in the field and *via* Unmanned Aerial Vehicle (UAV) imageries. They suggested that coseismic vertical displacements were generally small compared with the strike-slip displacements, except at a ~3 km zone to the west of the Yematan bridge (see Figure 1). According to the complex vertical displacement of surface ruptures, they also found a contrasting sense of fault dipping directions, especially in the west of the epicenter. Such complex geometry conditions are also supported by the study with relocated post-seismic sequences (Wang et al., 2022). Another feature worth noting is a ~5 km secondary fault rupture strand parallel to the main rupture strand towards the east section of the coseismic rupture (Xu et al., 2021; Liu et al., 2022). This secondary fault merges towards the northwest on the main earthquake fault at around 99 E ° through a blind fault segment (Yuan et al., 2022). According to the Global Positioning System (GPS) derived three-dimensional (3D) coseismic displacements, Wang *et al.* (2022) revealed a nearly vertical fault dipping (overall ~ 87°) to the north with two main slip areas above 15 km in depth. However, they have omitted the aforementioned secondary branch given the limited spatial resolution of GPS. Liu *et al.* (2022) reconstructed 3D displacements using imagery acquired by Synthetic Aperture Radar (SAR) satellites and suggested that the optimal solution of dip angle was 90° for both the main strand and secondary strand. Jiang *et al.* (2021) conducted a joint investigation with displacement resolved from both GPS and interferometric SAR (InSAR) and suggested the spatial diversity of the dip angle as well as an obvious segmental characteristic of the seismogenic fault. The previous studies mainly agree that the Mw 7.4 Maduo earthquake was dominated by the left lateral slip, but there may be some puzzles about other kinematic parameters of the seismogenic fault. Nevertheless, further studies of the Maduo earthquake, a rare large earthquake (Mw > 7) that occurred in the interior of a major tectonic block within the Tibetan plateau, would provide information to better understand the deformation style and earthquake potential of the Tibetan plateau.

TABLE 1 Basic information of SAR data used herein.

Sensors	Orbital type	Acquired time		Perpendicular baseline (m)	Wavelength (cm)	Incident angle (°)	Azimuth angle (°)	Imaging mode
		Master image	Slave image					
S1 A/B	Ascending	2021/5/20	2021/5/26	53	5.6	39	-13	TOPS
S1 A/B	Descending	2021/5/20	2021/5/26	117	5.6	39	-167	TOPS
ALOS-2	Descending	2020/11/1	2021/9/19	145	23.6	39	-170	ScanSAR
ALOS-2	Descending	2020/12/4	2021/6/4	197	23.6	39	-170	ScanSAR

In this study, we focused on the 3D coseismic displacement (north-south, east-west, and up components) reconstruction and its tectonic implication. The experiment employed both Sentinel-1 A/B (S1) and Advanced Land Observation Satellite-2 (ALOS-2) acquisitions and applied the Synthetic Aperture Radar Interferometry (InSAR) techniques, which are sensitive in estimating 3D earthquake location and magnitude (Lohman and Simons, 2005). Besides that, coseismic signals were retrieved *via* sub-pixel correlation from pre- and post-earthquake image pairs that were acquired by SAR and optical satellite sensors, respectively. The Sentinel-2 (S2) multi-band images are acquired in a view geometry differing from the side-looking SAR. It is therefore helpful in improving the constraint in 3D inversion (Zhang et al., 2017; Bacques et al., 2020; Lu et al., 2021). A strain model based on variance component estimation (SM-VCE) (Liu et al., 2019; Hu et al., 2021) was adopted in the reconstruction of 3D displacements. We also discovered the optimal weight scheme of the initial weight in SM-VCE to achieve robust and efficient 3D displacement estimations. Afterward, we further investigated the geometry and kinematic parameters of the seismogenic fault of the 2021 maduo earthquake based on the Okada model (Okada 1985) in an elastic half-space with the resolved 3D displacement field.

2 Dataset and methods

2.1 Data preparation

We acquired the S1 SAR imagery in both ascending and descending orbits, ALOS-2 SAR imagery in two adjacent descending orbits, and multi-band optical imagery acquired by the S2 satellite.

The acquisition dates of SAR coseismic pairs are listed in Table 1. The C-band S1 SAR imagery was acquired in Terrain Observation by Progressive Scans (TOPS) mode. The width of a standard swath is about 250 km. The L-band ALOS-2 SAR data has a longer wavelength of 23.6 cm, which is beneficial to resist decorrelation and measure displacements with a large gradient. The ALOS-2 ScanSAR mode imagery has a swath width of 350 km. The footprints of SAR and optical imagery are shown in Figure 1.

S2 is a high-resolution multispectral satellite with a standard granule size of $100 \times 100\,km^2$. Considering that the quality of optical images relies on cloud coverage, we selected coseismic pairs acquired on 12 October 2020 and 17 October 2021 based on the cloud amount criteria (<3%). Ortho-rectified Level-1C (L1C) products of S2 in two adjacent tracks were obtained to fully cover the coseismic rupture zone (Figure 1).

Additionally, GPS coseismic measurements published by Wang et al. (2022) were also used in the rest of the studies for validating the reconstructed 3D displacement field. They processed GPS time series ranging from 18 May 2021 to 24 May 2021 and resolved coseismic displacement at 58 continuous sites, which are located within a ~300 km radius of the epicenter. The GPS-derived coseismic displacement only has minor impacts from post-seismic deformation that are no more than 3 mm at the near-field sites (Wang et al., 2022). As shown in Figure 1, GPS site QHAJ shows a large horizontal displacement, which may be deteriorated by localized displacements (Jiang et al., 2022).

The Shuttle Radar Topographic Mission (SRTM) Digital Elevation Model (DEM) (Rodriguez et al., 2005) was used in the differential interferogram generation. We applied the 90 m SRTM DEM products to ALOS-2 pairs and 30 m SRTM DEM products to S1 pairs. This is because the reported spatial resolution of ALOS-2 ScanSAR data (~60 m resolution; JAXA, 2012) is lower than that for the S1 dataset (~22m; ESA, 2022b).

2.2 Extraction of 1D/2D displacement fields from multi-source remote sensing imagery

2.2.1 Sentinel-1 A/B pairs processing

We processed the S1 coseismic pairs in both ascending and descending orbits. Both differential InSAR and pixel offset tracking methods were applied to reconstruct the one-dimension (1D) displacement in Line-of-sight (LOS) direction as well as two-dimensional (2D) displacements in range/azimuth directions, respectively. In InSAR processes, the single look complex (SLC) SAR images were multi-looked by a factor of 10 in range and two in azimuth. The pixels with coherence (<0.6) were masked prior to the phase unwrapping. The Minimum Cost Flow algorithm (Werner and Wegm, 2002) was used to obtain a reliable unwrapped phase.

To conduct the pixel-offset tracking (POT) process (Michel et al., 1999), a window of 128 × 128 was adopted to estimate offsets with an oversampling factor of two between two SAR images, and the offsets were estimated from peaks of sub-pixel cross-correlation in range and azimuth direction respectively. This setup can guarantee a precise co-registration of the coseismic pair. The estimated local offsets were then

considered as the displacement signals caused by the earthquake. These 2D displacement fields include movements between satellite and ground targets (range direction), as well as those along the satellite flight direction (azimuth direction). Although the POT-derived range movement is in the same geometry as that in InSAR, POT can achieve complete displacements even if the displacement gradient is large (e.g., in the vicinity of the earthquake rupture zone).

2.2.2 ALOS-2 pairs processing

We processed ALOS-2 coseismic pairs in two adjacent descending orbits. The bandwidth of acquired SLCs in ScanSAR mode is 28 MHz with a swath width of 350 km, which is large enough to cover the entire rupture fault with a single standard frame. ALOS-2 SAR images were multi-looked by a factor of eight in range and 30 in azimuth. We applied the standard differential interferogram generation approach (Rosen et al., 2000) to each sub-swath of the ScanSAR data to then mosaic them in the geographic coordinate. Note that we did not apply the POT approach to ALOS-2 pairs. This is because: (1) ALOS-2 SAR data is in the L band which has better capability to measure a large displacement; and (2) the ionospheric artifact can largely affect the azimuth displacement estimation in the POT method (Brcic et al., 2010; Meyer, 2011). We used the same InSAR process scheme as that applied to S1 pairs to resolve the unwrapped phase of ALOS-2 pairs. A second-order polynomial was then applied to unwrapped interferograms to model and mitigate the ionospheric artifact.

2.2.3 Sentinel-2 pairs processing

The L1C product of the S2 satellite is an orthoimage product that is geometrically refined. The Sentinel Application Platform (SNAP) developed by ESA was used to conduct the atmospheric correction of L1C. Afterward, we used MicMac software (Rosu et al., 2015; Galland et al., 2016; Rupnik et al., 2017) to conduct sub-pixel correlation and reconstruct the lateral displacement between the pre-earthquake and post-earthquake images of each individual band. The MicMac software is developed to compute the correlation of image pairs in the spatial domain by using a regularization algorithm (Rosu et al., 2015; Galland et al., 2016). The derived displacement fields for visible bands (B2, B3, and B4 bands) and near-fared band (B8) were then stacked to reduce the overall noise level. The outcome is a two Dimensional (2D) ground deformation field in both East-West (EW) and North-South (NS) directions, given the orthographic projection of S2 products. However, the NS component was not included in the rest of the 3D reconstruction. This is because of the existence of large residuals and orbital errors in the NS measurements.

To sum up, the SAR coseismic products are limited to range displacement and azimuth displacement in the satellite side-looking geometry. Additionally, SAR measurements are largely ambiguous with regard to NS movement (Wright et al., 2004). This is related to the sun-synchronous orbit of SAR satellites, which would cause further difficulties in resolving 3D displacement given these SAR data shared a similar side-looking geometry. Therefore, we included the displacement products derived from S2 images in this study. The S2 coseismic pairs captured the displacement in another viewing direction that can introduce an extra constraint in the estimation of the 3D coseismic field.

2.3 Reconstruction of 3D coseismic displacements

Based on the above-generated 1D/2D displacement fields, we can reconstruct the 3D field of the Mw 7.4 Maduo earthquake. To begin the reconstruction, we first sampled the 1D/2D field into the same geographic grid. Each input coseismic displacement field was resampled into a $0.01^{\circ} \times 0.01^{\circ}$ grid size using uniform averaging. The associated standard deviation of each individual grid cell during this averaging process was also calculated and used as an initial weight in the rest of the 3D field estimation.

A strain model (SM) based 3D displacement reconstruction approach (Liu et al., 2018; Liu et al., 2019; Liu et al., 2022) was applied here. First of all, a design matrix (A) that connects observations in various viewing directions and unknown 3D displacement at each pixel was constructed. The mathematic expression of the inversion model at a single pixel is a simple linear equation that can be written as follows:

$$L = A \cdot d_{3d} \tag{1}$$

in which d_{3d} is the unknown 3D displacement components in the east-west (d_e), north-south (d_n), and up (d_u) direction and the unit is meter; L denotes the coseismic displacement components in different satellite viewing directions that were derived in the last sub-section.

$$L = \left[L^{A}_{s1-ra} \;\; L^{A}_{s1-azi} \;\; L^{A}_{s1-los} \;\; L^{D}_{s1-los} \;\; L^{D}_{s1-range} \;\; L^{41}_{a2-los} \;\; L^{42}_{a2-los} \;\; L^{EW}_{s2-ew} \right]^{T} \tag{2}$$

From left to right, L_{s1-ra} is the range offset of S1 data derived from offset-tracking; L_{s1-azi} is the azimuth offset of S1 data derived from offset-tracking; L_{s1-los} is the LOS displacement of S1; L^{41}_{a2-los} is the LOS displacement of ALOS-2 data in orbital 41. L^{42}_{a2-los} is the LOS displacement of ALOS-2 data in orbital 42. L_{s2-ew} is the east-west displacement of S2. Note that capital letters A and D denote ascending and descending orbits, respectively.

Given the SAR/optical remote sensing reconstructed coseismic components are the projection of 3D deformation components into a certain direction, the design matrix A can be generated from the satellite-looking vector of each component. The geometry vectors of each input displacement field were calculated according to corresponding satellite orientation parameters (e.g., heading angle or/and incidence angle). The basic expression of A can be written as $A = [-\sin(a)\sin(b) - \cos(a)\sin(b) \;\; \cos(b)]$, where a and b are calculated from incidence angle and satellite heading angle depending on the satellite viewing directions, as listed here:

$$\begin{cases} a_i = \alpha^{k}_{azi} - \dfrac{3\pi}{2}, \quad b_i = \theta^{k}_{inc} & \text{when LOS displacements} \\ a_i = \alpha^{k}_{azi} - \pi, \quad b_i = \dfrac{\pi}{2} & \text{when azimuth displacements} \\ a_i = \dfrac{3\pi}{2}, \quad b_i = \dfrac{\pi}{2} & \text{when east} - \text{west displacements} \end{cases}$$

in which $i\alpha^{k}_{azi}$ is the satellite direction of *kth* pixel. θ^{k}_{inc} is the incident angle of the *kth* pixel.

Afterward, we can further build the functional relationship between displacement observations and 3D surface displacements based on the SM model. The detailed steps of integrating a strain

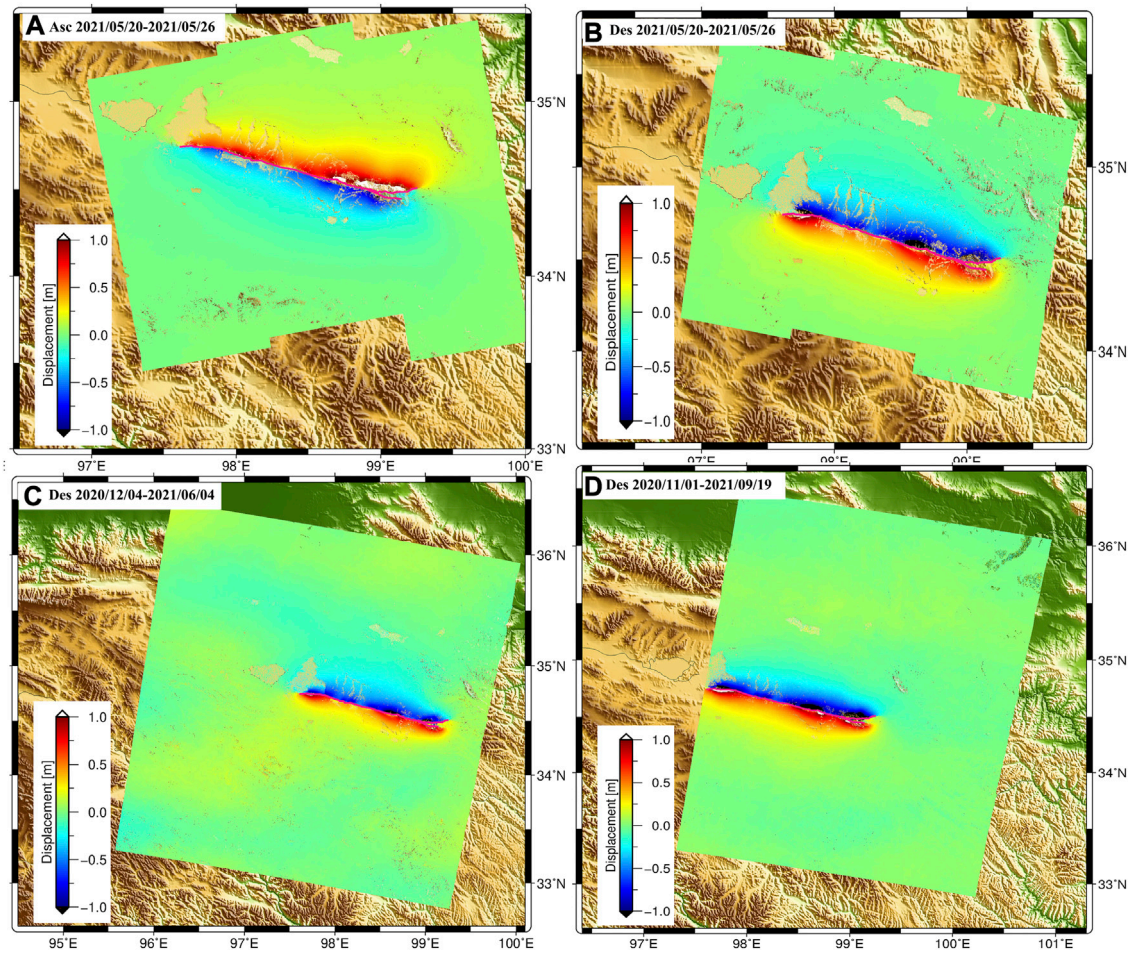

FIGURE 2
Satellite LOS displacement fields derived from ascending **(A)** and descending **(B)** of S1 data as well as track 41 **(C)** and track 42 **(D)** of ALOS-2 satellite in descending orbit.

model can be found in Liu *et al.* (2018) and Liu *et al.* (2019). Because the SM method is constrained by adjacent points, it is necessary to determine an optimal window to properly determine participating pixels (Shen and Liu, 2020; Wang and Wright, 2012). Taking into consideration that a large window may result in smooth but unrealistic 3D estimation, therefore, we determined an optimal value of window size *via* a trade-off curve. It was generated between misfit with metric of root mean square errors (RMSE) and different window sizes. Additionally, we took the aforementioned standard deviation calculated during the uniform averaging of each individual grid cell as their initial weight. Given that the input coseismic displacements were measured from multiple sources and techniques, it is necessary to determine a realistic weight for different input observations. Hence, a variance component estimation (Liu et al., 2018) was added to the strain model, as was the so-called SM-VCE method. We conducted an iterative process to determine the relative weight among the eight input observations (Eq. 2). The correction value of each iteration was calculated from the variance component estimation. Based on our experience, the number of iterations is limited to 35 to achieve an efficient convergence.

Note that the SM-VCM method is based on the assumption that the displacements are continuous and smooth in the space. The Maduo earthquake was mainly a strike-slip event, and the two sides of the seismogenic fault were moved relatively in different directions. Thus, the assumption is invalid for pixels in the near field of the rupture zone. Therefore, it is necessary to guarantee that the deformation signals of pixels within a certain window are spatially continuous when we used these surrounding pixels to form a strain model. To solve this issue, we set up a polyline barrier based on geologically mapped rupture information (Yuan et al., 2022). For each window, we then excluded the pixel from the other side of the barrier prior to the inversion 3D inversion.

3 Results

3.1 3D surface displacements

Based on the strategy described in Section 2.1, the coseismic displacement fields in the LOS direction *via* InSAR are demonstrated in Figure 2. The InSAR-derived range displacement

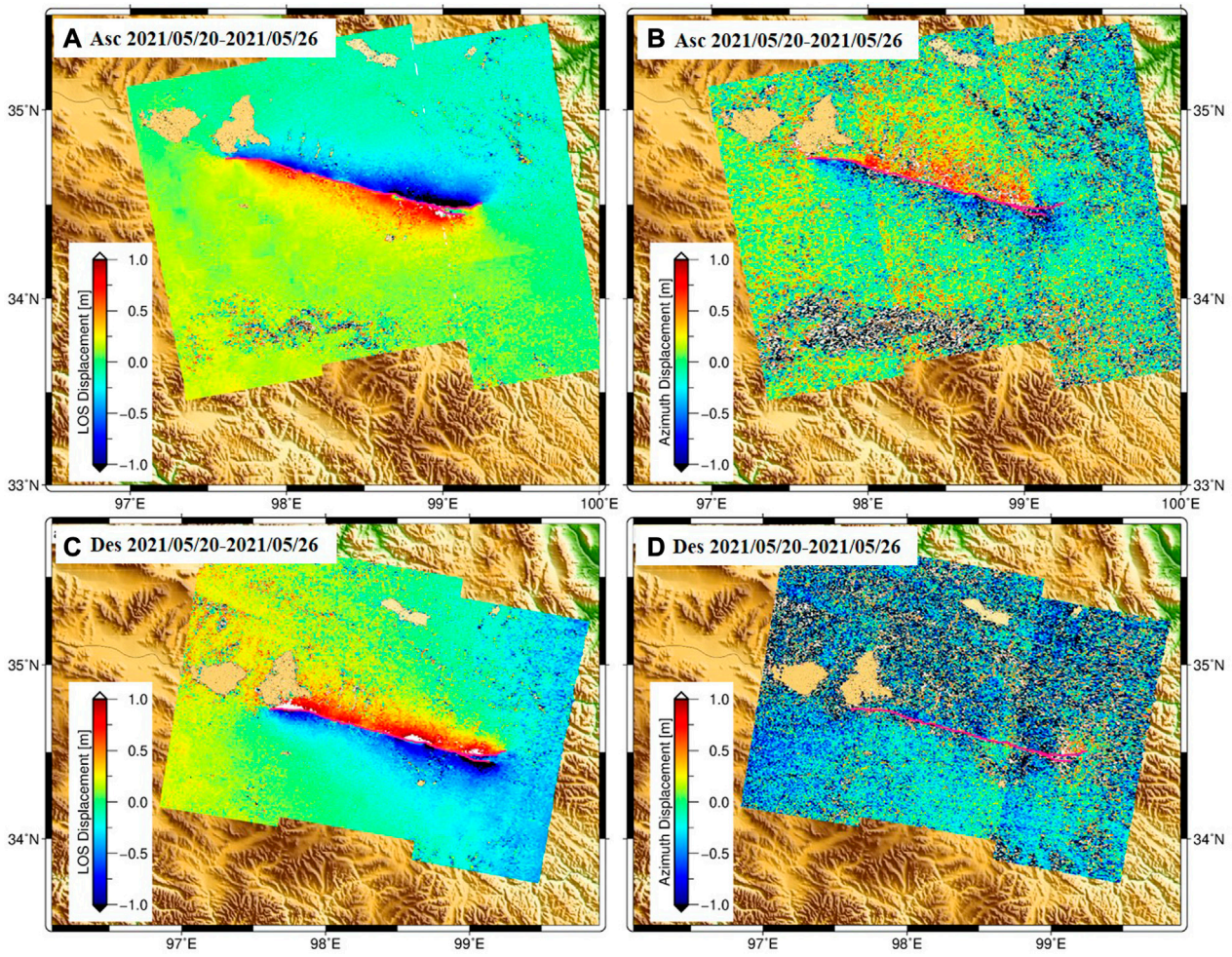

FIGURE 3
Range **(A–C)** and azimuth **(B–D)** displacement fields of Maduo earthquake calculated from the ascending and descending S1 pairs *via* POT approach.

fields show a similar spatial pattern. Their maximum displacements are both within 1 m. This is mainly because S1 and ALOS-2 have similar viewing geometries. However, the C-band S1 interferograms were decorrelated in the zone to the east of the epicenter, especially in the ascending orbit (Figure 2A). This decorrelation is related to the large displacement, as this zone is where the maximum coseismic deformation occurred (Wang et al., 2022). Benefiting from the longer wavelength, the L-band ALOS-2 results have achieved better coherence in the near field.

The coseismic displacements derived from the POT method are shown in Figure 3. The overall POT estimated displacement in range direction has similar patterns to that estimated from InSAR. The west part of the coseismic deformation field shows larger displacements than that in the east. As mentioned above, POT can measure offsets even when the displacement gradient is large regardless of data wavelength. Therefore, the coseismic movement near the fault rupture zone has been fully resolved. However, the azimuth displacement derived *via* POT shows a high noise level for both ascending and descending orbits. The sun-synchronous orbit and side-looking viewing geometry of SAR satellites, thus limits their ability in measuring NS movement. Additionally, the NS movement is relatively minor for the Mw 7.4 Maduo earthquake (Yuan et al., 2022). Both of these factors contribute to the high noise level of POT azimuth products (Figures 3B,D), which were therefore excluded in the rest of the 3D inversion.

The measured horizontal displacements from the multi-band optical remote sensing imagery are shown in Figure 4. The spatial pattern differs greatly from the range or LOS movement in Figure 2 and Figure 3, as NS displacements did not diminish towards the far field of the rupture zone (Figure 4A). This is likely because the displacements in the range direction are a combination of NS, EW, and UP components, while Figure 4B demonstrates only the NS component. Additionally, the spatial reference to EW movement in Figure 4 is also different from that of InSAR or POT. The measured coseismic displacement in the NS and EW directions range between ~2 m. This is reasonable for movement in the NS direction. However, it is too large for that in the EW direction. We considered that the EW estimation with the S2 pair was likely impacted by large residual orbital errors.

Finally, taking into consideration that the strike of the Maduo earthquake in the NW-SE direction is approximately perpendicular to the flight direction of the descending Sentinel-1 satellite, the

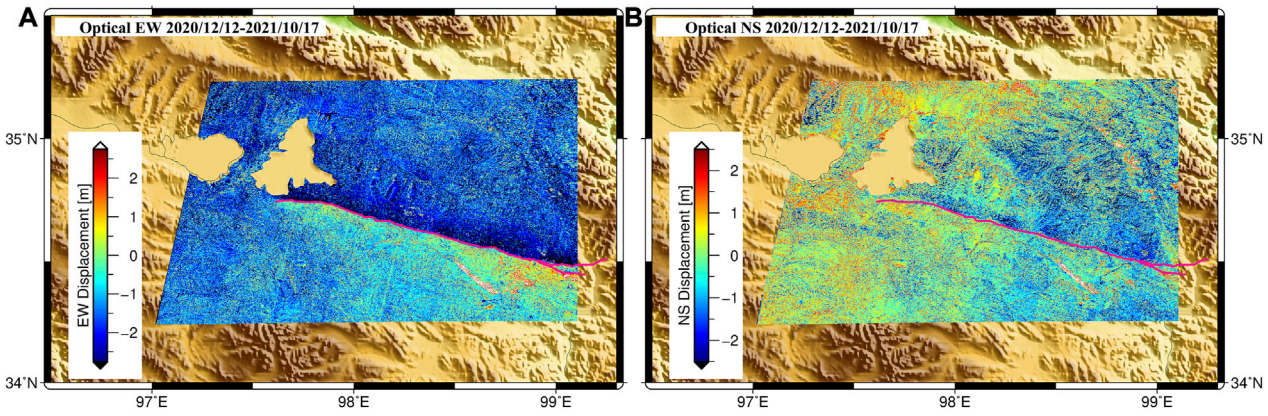

FIGURE 4
Horizontal coseismic displacements of Maduo earthquake based on MicMac software. **(A)** and **(B)** are the east-west and north-west components.

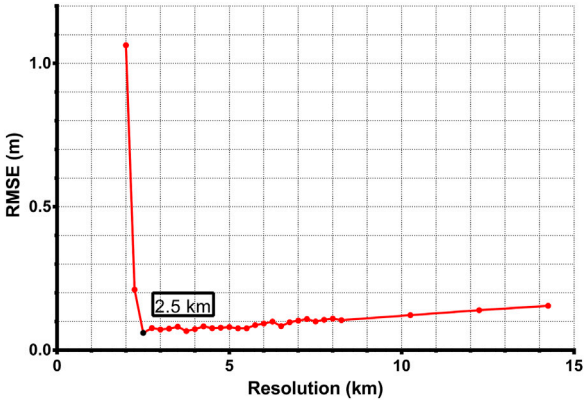

FIGURE 5
A trade-off curve between RMSE and window size in SM-VCE estimation.

azimuth displacement result from the descending S1 pairs shows large noises, so does the S2-derived NS displacement. Therefore, they were excluded in 3D inversion. Afterward, we conducted a joint estimation with the solution described in Section 2.3. Additionally, we tested the different sizes of windows (from ~2 km to ~14 km) in the SM-VCE inversion. As shown in Figure 5, the L curve was generated based on each tested window size and the associated global misfit. In the end, an optimal window of 2.5 km was determined and applied to solve the 3D displacement field.

The reconstructed 3D coseismic displacements are shown in Figure 6. Due to the limited spatial coverage of Sentinel-2 images, the resolved 3D displacements have a smaller spatial size that is nevertheless enough to cover approximately the entire rupture zone. Obviously, the ground surface movement of the 2021 Mw 7.4 Maduo earthquake is dominated by the EW displacements, which are in a range of -2m ~ 2 m. The NS displacement is much smaller (ranging from -0.8m–0.8 m), which also seems not continuous from east to west of the rupture zone. The UP component is in about -0.5m–0.5 m that is mainly concentrated in the near field of the rupture zone. The existence of a vertical movement field implies that this earthquake is also associated with some minor dip-slip movement, especially in the east and west sections of the rupture zone, where the strike direction starts changing.

We plotted four profiles across the coseismic zone (Figure 6A). As shown in Figure 7, there is a fast decaying on both sides of the Jiangcuo fault, which is the suggested seismogenic fault of the Maduo earthquake (Wang et al., 2022). The largest EW displacement is captured at profile DD'. Additionally, also along profile DD', there are two jumps in the UP component, which may be related to the eastern two branches of the rupture fault. The displacement signal for the UP component for these four profiles shows overall different patterns. It is likely because the dip angle varies from east to west as suggested by Yuan *et al.* (2022) and Wang *et al.* (2022).

3.2 Validation for 3D displacements

1) Validation with GPS

To validate the quality of reconstructed 3D displacement fields, we computed the difference between GPS-derived displacements (Wang et al., 2022) and above-derived 3D displacements. We determined pixels within a radius of 0.02° of each GPS station and averaged them to represent the SM-VCE-derived 3D displacement. We then further computed the RMSE of differences between SM-VCE and GPS measurements in three directions (Table 2). In the same table, we also listed the result from Liu *et al.* (2021), which reconstructed the 3D field with multi-source SAR imagery. The result indicates an improvement in the accuracy of the resolved NS and EW components. It indicates the advantages of adding displacement derived from S2 imagery and therefore highlights the importance of fusion SAR and optical products in 3D displacement reconstruction.

2) Validation with geological fieldwork

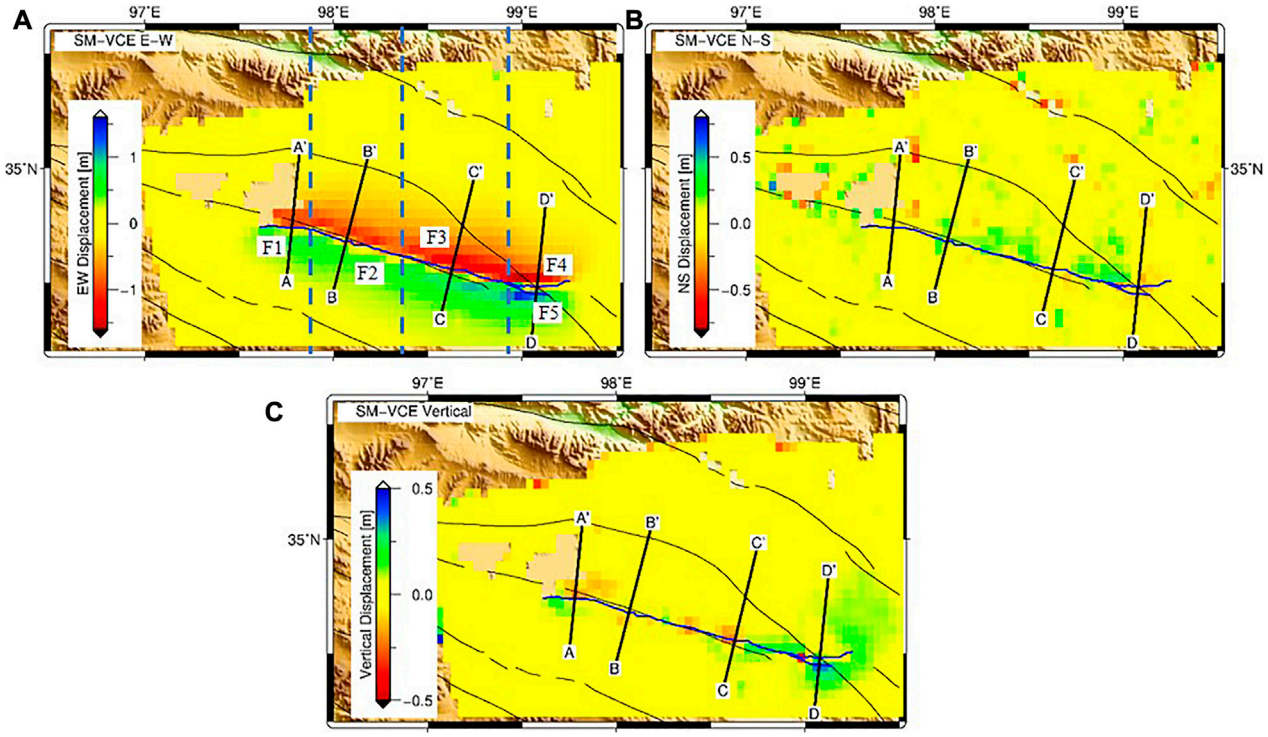

FIGURE 6
Derived 3D dimensional deformation fields of Maduo earthquake. **(A–C)** are the east-west, north-south and vertical components.

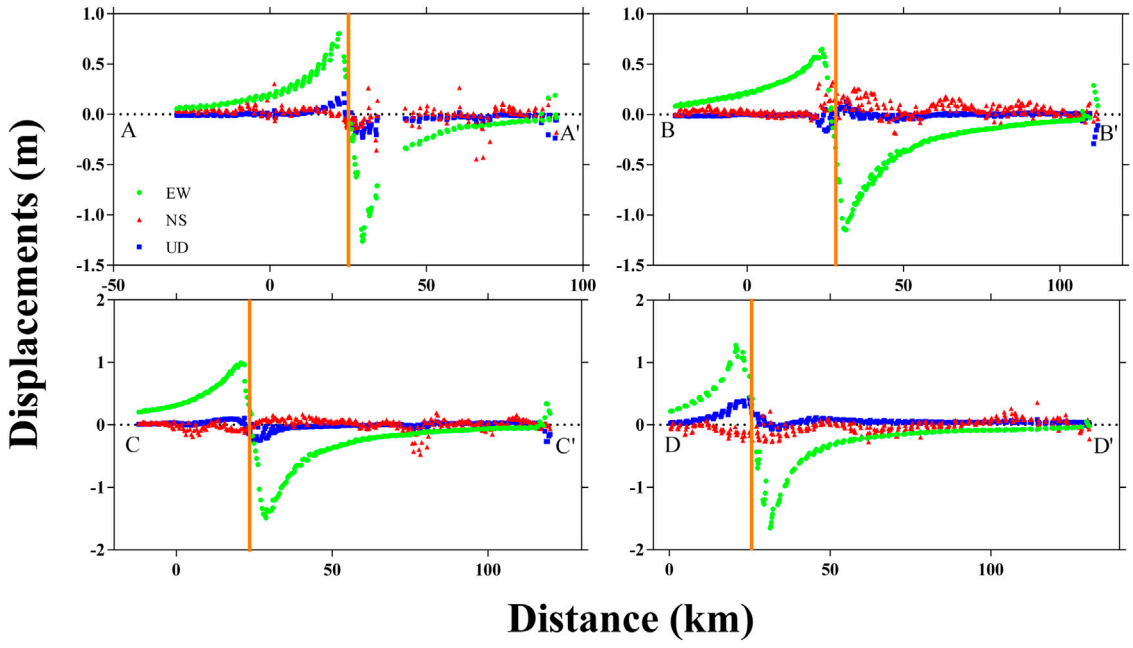

FIGURE 7
Cross section of 3D coseismic deformation fields. The EW (green circle), NS (red triangle), and UP (blue square) displacement components are corresponding to the four profiles. **(A)**, **(B)**, **(C)**, and **(D)** are associated with profiles AA′, BB′, CC′, and DD′ respectively. The orange line represents the Jiangcuo fault.

TABLE 2 RMSE of Maduo earthquake determined from different studies.

	RMSE (mm)		
	EW	NS	UP
Liu *et al.* (2021)	52	122	-
This study	10.29	89.03	30.00

Yuan *et al.* (2022) surveyed horizontal displacement at a total of 68 sites in the field. In this study, we compared reconstructed displacements with their measurements from the geological study. We adopted the same strategy used above to select pixels around each measurement site, while we took the maximum value from the selected pixel for the comparison. The result can be visualized in Figure 8. The horizontal displacements derived by the SM-VCE method are consistent with that surveyed in a field within a range of 0.5 m. We found that the SM-VCE result shows an overall underestimation in the west section, while an overestimation in the east section compared with the in-field measurements. This is likely related to the variation in the width of the coseismic rupture zone. The presented study measured overall displacement across the entire rupture zone, while the infield measurement surveys were offset at a fixed location with limited crossing fault distance (e.g., a few or tens of meters). Another impact could be the post-seismic deformation, given that the temporal resolution of remote sensing data was limited by the revisiting time of satellites. Their products therefore may contain some level of post-earthquake displacements. As suggested by He *et al.* (2021), the west section hosts larger post-seismic deformation compared with the other part of the fault.

4 Discussion

4.1 Optimal weight scheme of SM-VCE

During the study, we also found a strong dependence on reconstructed 3D displacements and initial weight at each input pixel in SM-VCE estimation. We tested a case run using equal weight as the initial weight scheme for each grid pixel. The corresponding result is presented in Figure 9, showing that the quality is obviously compromised with the equal initial weight. Moreover, the processing time for solving 3D displacements was nearly doubled, and it encountered more difficulties in reaching convergence. Therefore, we want to emphasize the importance of determining the proper initial weight of each input pixel when using the SM-VCE method. In Section 2.2, the applied initial weight was calculated from the standard deviation in the uniform averaging, which is recommended here. While any other weighting schemes that can properly represent the quality of the input dataset would also be applicable.

4.2 Coseismic slip distribution and structure of seismogenic fault

An elastic dislocation model (Okada 1985) with a Poisson's ratio of 0.25 was used here to discover the kinematic parameters of seismogenic fault as well as the coseismic slip distribution. The steepest decent method was applied to solve the parameter estimation (Wang et al., 2013). The relocated aftershock catalog (ranging from 22 May 2021 to 30 May 2021) and fault trace of remote sensing images were employed to constrain the fault strike, and we, therefore, construct a fault model with five segments (see Figure 6A). The average strike of F1, F2, F3, F4, and F5 are 272°, 285°, 285°, 89°, and 118°, respectively. The top and bottom of the fault depth are set at a value of 0 and 20 km, respectively. The fault plane is discretized into patches with a size of 2 × 2 km. The rake angles of slip vectors are applied to vary from -45° to 45°. A quad-tree algorithm (Simons et al., 2002) was applied to sub-sample 3D displacements. The down-sampled final dataset consists of 7548 points.

The coseismic slip distribution of the Mw 7.4 Maduo earthquake constrained by the resolved 3D displacements is shown in Figure 11. Note that the dip angles of F1, F2, and F3 which are pre-defined according to the result published by Xu *et al.* (2021) are 75°, 70°, and 80° respectively. While the fault dip was estimated for the rest of the two segments (F4 and F5). We set up a search space for dip angles that ranges from 85° to 115° for F4 and 50°–115° for F5 with a step of 5°. By changing the dip angle from 0° to 180°, the dipping direction changes from North to South. The optimal dip was then determined by minimizing the global misfit. In the end, the resulting dip angle of F4 and F5 are 85° and 80° towards the south direction, respectively

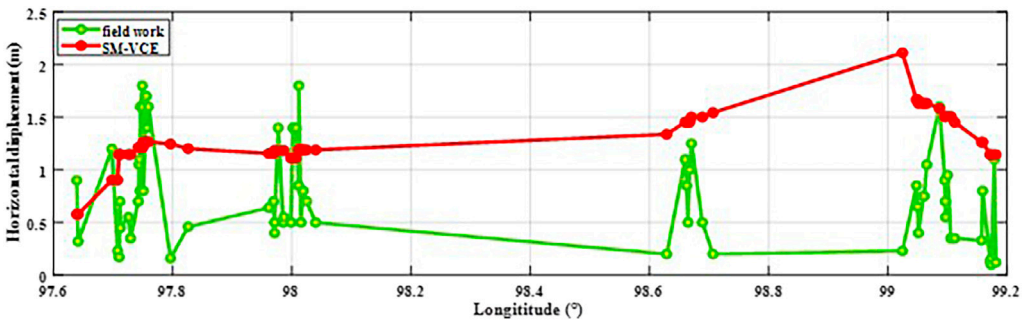

FIGURE 8
Comparison between the horizontal displacements based on SM-VCE method and infield measurement.

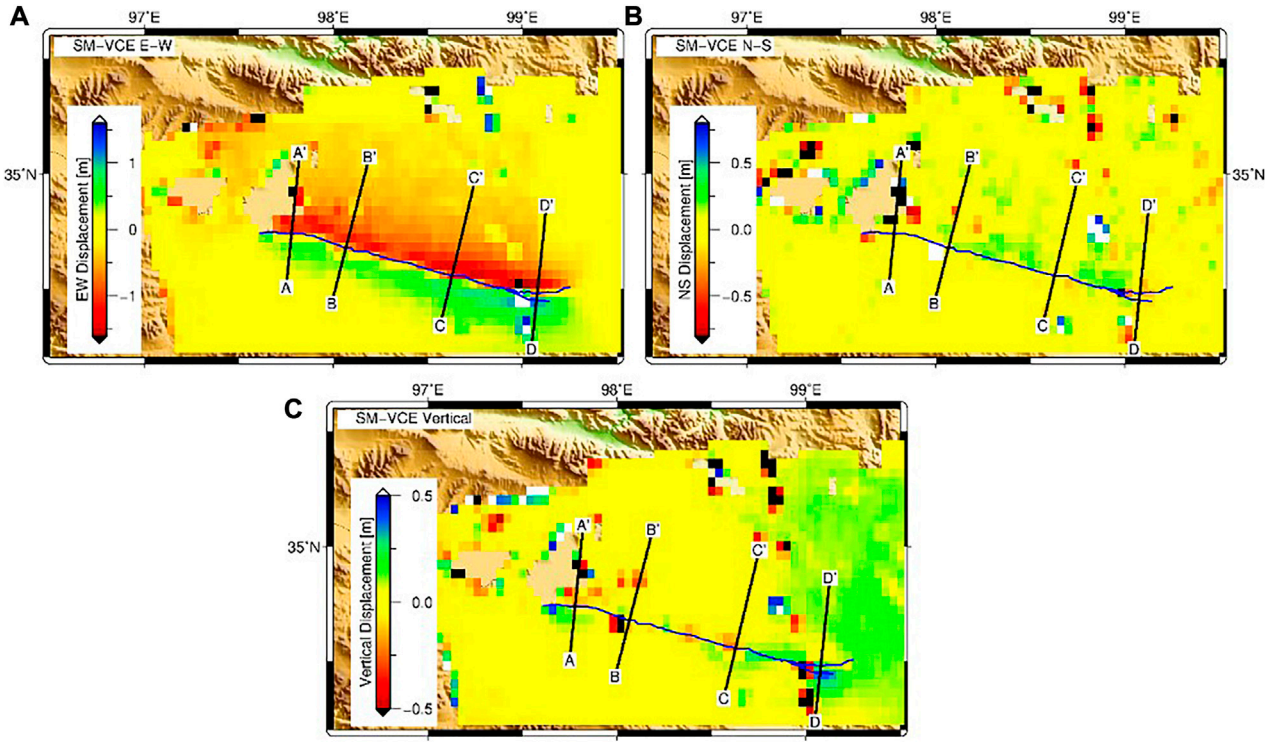

FIGURE 9
SM-VCE resolved 3D deformation of Maduo earthquake when using an equal initial weight of each input grid cell. **(A–C)** are the east-west, north-south and vertical components.

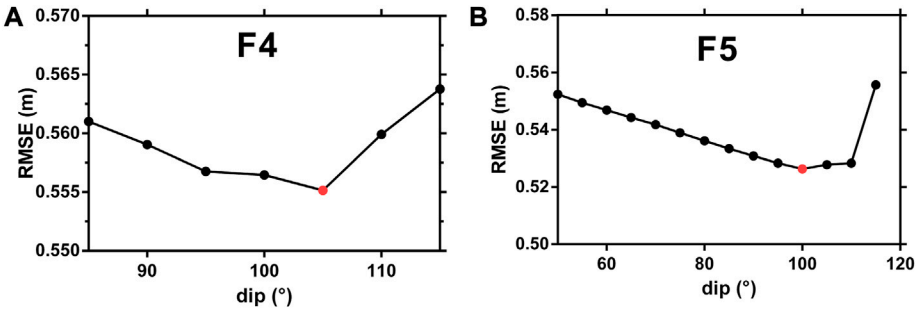

FIGURE 10
determination of optimal dip angle for segments F4 and F5.

(see Figure 10). The correlation between the observed and modeled dataset reached ~0.98.

The determined slip distribution is demonstrated in Figure 11. And the synthetic observation, simulation, and residual from the coseismic slip model inversion explains the rationality and reliability of the inversion result (Figure 12). The inversion result shows that the slip was mainly concentrated at a depth ≥15 km and the largest slip is approximately 6 m, which is located at the eastern section of the fault at a depth of 5 km. The moment magnitude obtained through inversion is about Mw 7.4 and the released energy is ~ 1.742×10^{20} Nm. The slip distribution also indicates that the slip at the top of the fault reaches ~3m, which is consistent with inverted 3D displacements. The maximum slip is in the east of the epicenter, e.g., the slip primarily ranged from 1.5 m to 6 m at a depth of 0 km–15 km in segment F3. Note that the western part of F3 lacks post-seismicities. This zone also corresponds to the area, where the continuous coseismic surface rupture was absent (Yuan et al., 2022). We, therefore, suspect the accumulation stress could be partially released during the main shock, making it far more below the fault strength (the maximum shear strain of the fault plane sustained). Wu *et al.* (2022) discussed the tectonic stress evaluation on the seismogenic fault of the Maduo earthquake with numerical simulation. They suggested that the low post-

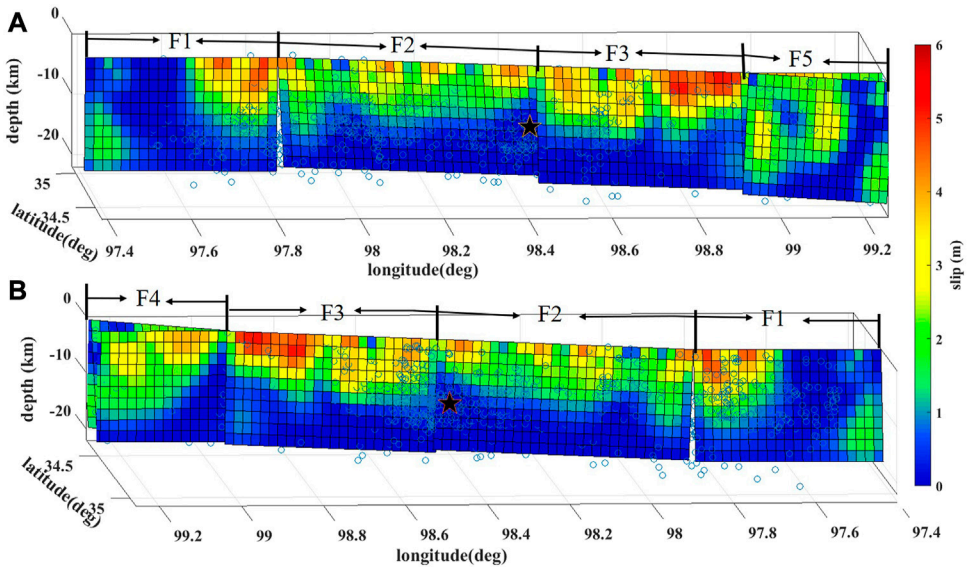

FIGURE 11
Fault-slip distribution of the Mw 7.4 mainshock. **(A)** is the front view of the slip distribution of two faults. **(B)** is the back view. The blue hollow is the result of relocated post-seismic sequence. Black stars represent the location of the hypocenter.

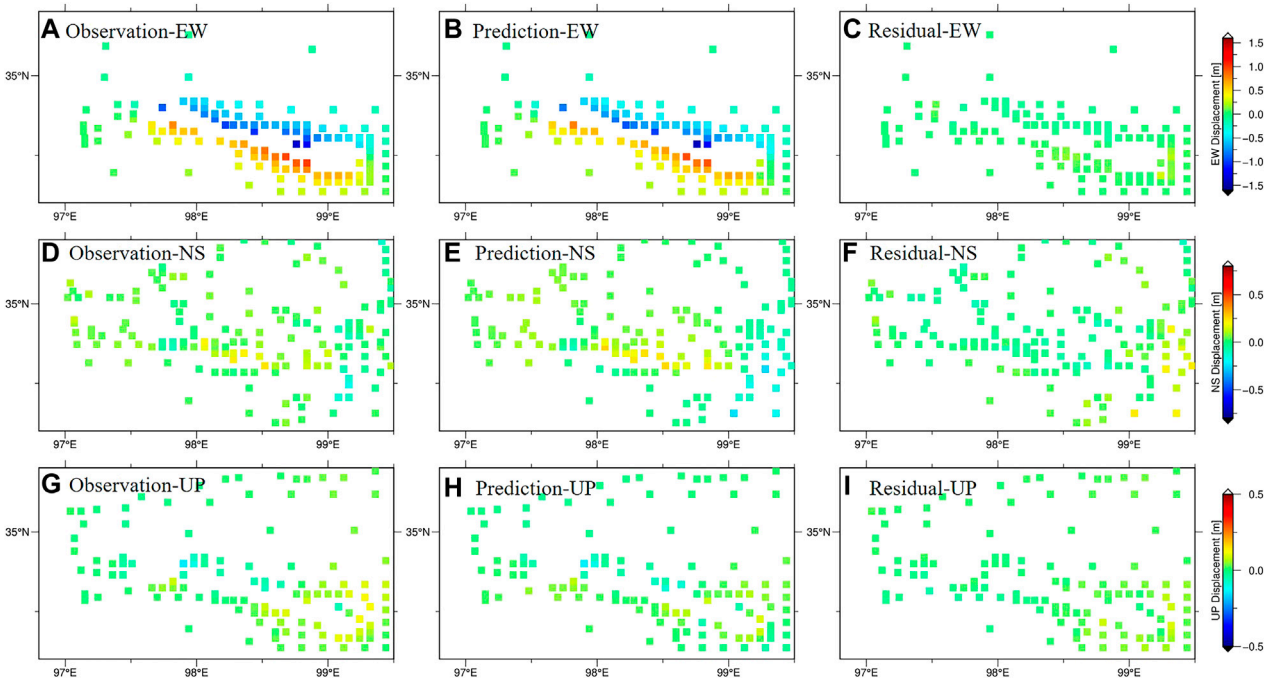

FIGURE 12
Synthetic observation, simulation, and residual from coseismic slip model inversion constrained by EW **(A–C)**, NS **(D–F)** and UP **(G–I)** displacements.

earthquake seismicity zone might relate to the low tectonic stress condition prior to the Maduo earthquake.

We also plotted the geodetic strain field for the 2021 Maduo earthquake (Figure 13). As the associated strain parameters were simultaneously calculated in SM-VCE when resolved from 3D deformation. According to Figure 13, the maximum shear strain is located at a zone around 99° E. This is where that fault extends to the east and orientation changes from NS to NW. Wu *et al.*

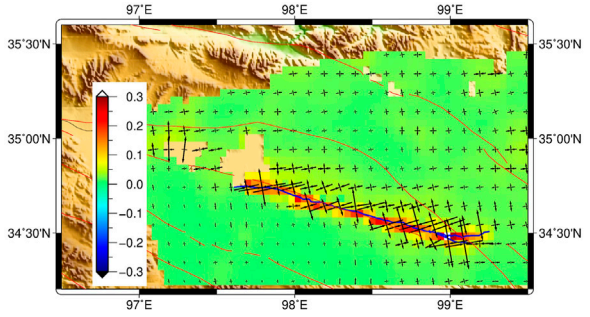

FIGURE 13
Maximum shear for the 2021 Maduo earthquake (Unit: × 10^{-4} rad).

(2022) suggest that the tectonic stress accumulated the most at this orientation-changing zone (around 99° E ~ 99.5° E) at the hypocenter depth. Although a large coseismic strain has been released here compared with the other segments along the fault (Figure 13), the stress condition of the east section of the rupture zone is questionable after the Maduo earthquake. This point is important in order to evaluate the seismic hazard potential in this area. Therefore, further study on post-seismic activities is needed in the future.

5 Conclusion

In this study, we focused on the 3D coseismic displacement reconstruction and its tectonic implication for Maduo Mw 7.4 earthquake. With derived displacement in range/offset directions from ALOS-2 and S1 pairs as well as NS direction from S2 pairs, we resolved the 3D coseismic displacement by using the SM-VCE method. We discovered the optimal weight scheme of the initial weight in SM-VCE to achieve robust and efficient 3D displacement estimations. We recommend using the standard deviation calculated in uniform averaging as the initial weight or other weighting schemes that can properly represent the quality of the input dataset. And adding displacement derived from S2 imagery can improve the accuracy of estimated NS and EW components. Based on the resolved 3D coseismic deformation fields, we further investigated the dip angles for the two segments (F4 and F5) to the east of the epicenter. The optimal dip angles were determined towards the south with values of 85° and 80° respectively. The moment magnitude obtained through inversion was about Mw7.4 corresponding to released energy of ~ 1.742×10^{20} Nm.

Data availability statement

The raw data supporting the conclusions of this article will be made available by the authors, without undue reservation.

Author contributions

All authors listed have made a substantial, direct, and intellectual contribution to the work and approved it for publication.

Funding

This work was supported by the National Key Research Development Program of China (Grant No. 2019YFC1509201).

Acknowledgments

We would like to thank Jihong Liu from Central South University in China for his helpful suggestions. The Sentinel Application Platform (SNAP) is a common architecture for all Sentinel Toolboxes and is distributed by ESA via the link https://earth.esa.int/eogateway/tools/snap. The Micmac software is open-source and developed by the Institute Geìographique National (IGN) in France, which could be downloaded via the link https://github.com/micmacIGN/Documentation. The Sentinel-1 A/B SAR data were provided by ESA via the distribution of the Alaska Satellite Facility (ASF) (https://search.asf.alaska.edu/). ALOS-2 PALSAR2 dataset was ordered via PASCO Corporation. And Generic Mapping Tools (GMT) were used for figure illustrations (https://gmt-china.org/).

Conflict of interest

The authors declare that the research was conducted in the absence of any commercial or financial relationships that could be construed as a potential conflict of interest.

Publisher's note

All claims expressed in this article are solely those of the authors and do not necessarily represent those of their affiliated organizations, or those of the publisher, the editors and the reviewers. Any product that may be evaluated in this article, or claim that may be made by its manufacturer, is not guaranteed or endorsed by the publisher.

References

Bacques, G., de Michele, M., Foumelis, M., Raucoules, D., Lemoine, A., and Briole, P. (2020). Sentinel optical and SAR data highlights multi-segment faulting during the 2018 Palu-Sulawesi earthquake (Mw 7.5). *Sci. Rep-Uk* 10, 9103. doi:10.1038/s41598-020-66032-7

Brcic, R., Parizzi, A., Eineder, M., Bamler, R., and Meyer, F. (2010). "Estimation and compensation of ionospheric delay for SAR interferometry," in Proceedings of the symposium at 2010 IEEE International Geoscience and Remote Sensing Symposium, Honolulu, HI, USA, 25-30 July 2010.

Chen, K., Avouac, J., Geng, J., Liang, C., Zhang, Z., Li, Z., et al. (2022). The 2021 Mw 7.4 madoi earthquake: An archetype bilateral slip-pulse rupture arrested at a splay fault. *Geophys Res. Lett.* 49, e2021G–e95243G. doi:10.1029/2021GL095243

Deng, Q., Zhang, P., Ran, Y., Yang, X., Min, W., and Chen, L. (2003). Active tectonics and earthquake activities in China. *Earth Sci. Front.* 10 (S1), 66–73.

Diao, G., Wang, X., Gao, G., Nie, X. H., and Feng, X. D. (2010). Tectonic block attribution of the wenchuan and yushu earthquakes distinguished by focal mechanism types. *Chin. J. Geophys.* 53, 849–854. doi:10.1002/cjg2.1554

ESA (2022b). *Level-1 single look complex*.

ESA (2022a). *Resolution and swath*. Available at: https://sentinel.esa.int/web/sentinel/missions/sentinel-2/instrument-payload/resolution-and-swath.

Galland, O., Bertelsen, H. S., Guldstrand, F., Girod, L., Johannessen, R. F., Bjugger, F., et al. (2016). Application of open-source photogrammetric software MicMac for monitoring surface deformation in laboratory models. *J. Geophys. Res. Solid Earth* 121, 2852–2872. doi:10.1002/2015jb012564

Gan, J., Hu, J., Li, Z., Yang, C., Liu, J., Sun, Q., et al. (2018). Mapping three-dimensional co-seismic surface deformations associated with the 2015 MW7.2 Murghab earthquake based on InSAR and characteristics of crustal strain. *Sci. China Earth Sci.* 61, 1451–1466. doi:10.1007/s11430-017-9235-4

He, L., Feng, G., Wu, X., Lu, H., Xu, W., Wang, Y., et al. (2021). Coseismic and early postseismic slip models of the 2021 Mw 7.4 Maduo earthquake (Western China) estimated by space-based deodetic data. *Geophys Res. Lett.* 48, e2021G–e95860G.

Hu, J., Liu, J., Li, Z., Zhu, J., Wu, L., Sun, Q., et al. (2021). Estimating three-dimensional coseismic deformations with the SM-VCE method based on heterogeneous SAR observations: Selection of homogeneous points and analysis of observation combinations. *Remote Sens. Environ.* 255, 112298. doi:10.1016/j.rse.2021.112298

JAXA (2012). *Satellite missions of ALOS-2*.

Jia, K., Zhou, S., Zhuang, J., and Jiang, C. (2021). Stress transfer along the western boundary of the bayan har block on the tibet plateau from the 2008 to 2020 yutian earthquake sequence in China. *Geophys Res. Lett.* 48, e2021G–e94125G. doi:10.1029/2021gl094125

Jiang, W., Xu, C., Li, Z., Wu, Y., Tan, K., Geng, J., et al. (2022). Using space observation techniques to study temporal and spatial characteristics of seismogenic process, occurrence and deformation of the Qinghai Madoi M_W7.4 earthquake. *Chin. J. Geophys.* 65, 495–508.

Liu, J., Hu, J., Li, Z., Ma, Z., Wu, L., Jiang, W., et al. (2022). Complete three-dimensional coseismic displacements related to the 2021 Maduo earthquake in Qinghai Province, China from Sentinel-1 and ALOS-2 SAR images[J]. *Sci. China Earth Sci.*

Liu, J., Hu, J., Li, Z., Zhu, J. J., Sun, Q., and Gan, J. (2018). A method for measuring 3-D surface deformations with InSAR based on strain model and variance component estimation. *IEEE Trans. Geoscience Remote Sens.* 56, 239–250. doi:10.1109/tgrs.2017.2745576

Liu, J., Hu, J., Xu, W., Li, Z., Zhu, J., Ding, X., et al. (2019). Complete three-dimensional coseismic deformation field of the 2016 central tottori earthquake by integrating left- and right-looking InSAR observations with the improved SM-VCE method. *J. Geophys. Res. Solid Earth* 124, 12099–12115. doi:10.1029/2018jb017159

Liu, L., Li, Y., Zhu, L., and Ji, L. (2021). Influence of the 1947 Dari M7.7 earthquake on stress evolution along the boundary fault of the bayan har block: Insights from numerical simulation. *Chin. J. Geophys.* 64, 2221–2231.

Liu, X., Chen, Q., Yang, Y., Xu, Q., Zhao, J., Xu, L., et al. (2022). The 2021 Mw7.4 Maduo earthquake: Coseismic slip model, triggering effect of historical earthquakes and implications for adjacent fault rupture potential. *J. Geodyn.* 151, 101920. doi:10.1016/j.jog.2022.101920

Lohman, R. B., and Simons, M. (2005). Some thoughts on the use of InSAR data to constrain models of surface deformation: Noise structure and data downsampling. *Geochem. Geophys. Geosystems* 6. doi:10.1029/2004gc000841

Lu, C., Lin, Y., and Chuang, R. Y. (2021). Pixel offset fusion of SAR and optical images for 3-D coseismic surface deformation. *Ieee Geosci. Remote S* 18, 1049–1053. doi:10.1109/lgrs.2020.2991758

Meyer, F. J. (2011). Performance requirements for ionospheric correction of low-frequency SAR data. *Ieee T Geosci. Remote* 49, 3694–3702. doi:10.1109/tgrs.2011.2146786

Michel, R., Avouac, J., and Taboury, J. (1999). Measuring ground displacements from SAR amplitude images: Application to the Landers Earthquake. *Geophys Res. Lett.* 26, 875–878. doi:10.1029/1999gl900138

Okada, Y. (1985). Surface deformation due to shear and tensile faults in a half-space. *B Seismol. Soc. Am.* 75, 1135–1154. doi:10.1785/bssa0750041135

Ren, J., Xu, X., Zhang, G., Wang, Q., Zhang, Z., Gai, H., et al. (2022). Coseismic surface ruptures, slip distribution, and 3D seismogenic fault for the 2021 Mw 7.3 Maduo earthquake, central Tibetan Plateau, and its tectonic implications. *Tectonophysics* 827, 229275. doi:10.1016/j.tecto.2022.229275

Rodriguez, E., Morris, C. S., Belz, J. E., Chapin, E. C., Martin, J. M., Daffer, W., et al. (2005). *An assessment of the SRTM topographic products. Technical Report JPL* **D-31639**.

Rosen, P. A., Hensley, S., Joughin, I. R., Li, F., Madsen, S., Rodriguez, E., et al. (2000). Synthetic aperture radar interferometry. *P Ieee* 88, 333–382. doi:10.1109/5.838084

Rosu, A., Pierrot-Deseilligny, M., Delorme, A., Binet, R., and Klinger, Y. (2015). Measurement of ground displacement from optical satellite image correlation using the free open-source software MicMac. *Isprs J. Photogramm.* 100, 48–59. doi:10.1016/j.isprsjprs.2014.03.002

Rupnik, E., Daakir, M., and Pierrot Deseilligny, M. (2017). MicMac – a free, open-source solution for photogrammetry. *Open geospatial data, Software and standards* **2**: 14.Shen Z and Liu Z. 2020. Integration of GPS and InSAR data for resolving 3-dimensional crustal deformation. *Earth Space Sci.* 7, e1036E–e2019E.

Simons, M., Fialko, Y., and Rivera, L. (2002). Coseismic deformation from the 1999 Mw 7.1 hector mine, California, earthquake as inferred from InSAR and GPS observations. *B Seismol. Soc. Am.* 92, 1390–1402. doi:10.1785/0120000933

Song, X., Han, N., Shan, X., Wang, C., Zhang, Y., Yin, H., et al. (2019). Three-dimensional fault geometry and kinematics of the 2008 M 7.1 Yutian earthquake revealed by very-high resolution satellite stereo imagery. *Remote Sens. Environ.* 232, 111300. doi:10.1016/j.rse.2019.111300

Tong, X., Xu, X., and Chen, S. (2022). Coseismic slip model of the 2021 maduo earthquake, China from sentinel-1 InSAR observation. *Remote Sens.* 14, 436. doi:10.3390/rs14030436

Vallée, M., Landès, M., Shapiro, N. M., and Klinger, Y. (2008). The 14 November 2001 Kokoxili (Tibet) earthquake: High-frequency seismic radiation originating from the transitions between sub-Rayleigh and supershear rupture velocity regimes. *J. Geophys. Res. Solid Earth* 113, B07305. doi:10.1029/2007jb005520

Wang, H., and Wright, T. J. (2012). Satellite geodetic imaging reveals internal deformation of Western Tibet. *Geophys Res. Lett.* 39. doi:10.1029/2012gl051222

Wang, H., Xu, C., and Ge, L. (2007). Coseismic deformation and slip distribution of the 1997 7.5 Manyi, Tibet, earthquake from InSAR measurements. *J. Geodyn.* 44, 200–212. doi:10.1016/j.jog.2007.03.003

Wang, M., Wang, F., Jiang, X., Tian, J., Li, Y., Sun, J., et al. (2022). GPS determined coseismic slip of the 2021Mw7.4 Maduo, China, earthquake and its tectonic implication. *Geophys J. Int.* 228, 2048–2055. doi:10.1093/gji/ggab460

Wang, R., Diao, F., and Hoechner, A. (2013). "Sdm - a geodetic inversion code incorporating with layered crust structure and curved fault geometry," in EGU General Assembly Conference Abstracts.

Wang, W., Fang, L., Wu, J., Tu, H., Chen, L., Lai, G., et al. (2021). Aftershock sequence relocation of the 2021 MS7.4 maduo earthquake, Qinghai, China. *Sci. China Earth Sci.* 64, 1371–1380. doi:10.1007/s11430-021-9803-3

Werner, C. L., and Wegm, U. (2002). "Processing strategies for phase unwrapping for InSAR applications," in Proceedings of the 4th European Conference on Synthetic Aperture Radar.

Wright, T. J., Parsons, B. E., and Lu, Z. (2004). Toward mapping surface deformation in three dimensions using InSAR. *Geophys Res. Lett.* 31, L01607. doi:10.1029/2003gl018827

Wu, L., Lu, J., Mao, W., Hu, J., Zhou, Z., Li, Z., et al. (2022). Sectional fault-inclination-change based numerical simulation of tectonic stress evolution on the seismogenic fault of Maduo earthquake. *Chin. J. Geophys.* 65, 3844–3857. doi:10.6038/cjg2022P0988

Xu, L., Chen, Q., Zhao, J., Liu, X. W., Xu, Q., and Yang, Y. H. (2021). An integrated approach for mapping three-dimensional CoSeismic displacement fields from sentinel-1 TOPS data based on DInSAR, POT, MAI and BOI techniques: Application to the 2021 Mw 7.4 maduo earthquake. *Remote Sens.* 13, 4847. doi:10.3390/rs13234847

Yuan, Z., Li, T., Su, P., Sun, H., Ha, G., Guo, P., et al. (2022). Large surface-rupture gaps and low surface fault slip of the 2021 Mw 7.4 maduo earthquake along a low-activity strike-slip fault, Tibetan plateau. *Geophys Res. Lett.* 49, e2021G–e96874G. doi:10.1029/2021gl096874

Zhang, L., Wu, J., and Feng, S. (2017). Measuring the coseismic displacements of 2010 Ms7.1 yushu earthquake by using SAR and high resolution optical satellite images. *ISPRS - Int. Archives Photogrammetry, Remote Sens. Spatial Inf. Sci.* XLII-2/W7, 665–670. doi:10.5194/isprs-archives-xlii-2-w7-665-2017

Zhao, D., Qu, C., Chen, H., Shan, X., Song, X., and Gong, W. (2021). Tectonic and geometric control on fault kinematics of the 2021 Mw7.3 maduo (China) earthquake inferred from interseismic, coseismic, and postseismic InSAR observations. *Geophys Res. Lett.* 48, e2021G–e95417G. doi:10.1029/2021gl095417

frontiers | Frontiers in Earth Science

TYPE Original Research
PUBLISHED 18 May 2023
DOI 10.3389/feart.2023.1083562

OPEN ACCESS

EDITED BY
Jeffrey Todd Freymueller,
Michigan State University, United States

REVIEWED BY
Xiwei Xu,
Ministry of Emergency Management, China
Lingyun Ji,
The Second Monitoring and Application Center, China Earthquake Administration, Xi'an, China

*CORRESPONDENCE
Jin Zhang,
zjgps@163.com

RECEIVED 29 October 2022
ACCEPTED 05 May 2023
PUBLISHED 18 May 2023

CITATION
Liu R, Zhang J, Guo W and Chen H (2023), Adaptive vertical-deformation field estimation and current tectonic deformation significance analysis in Shanxi rift valley.
Front. Earth Sci. 11:1083562.
doi: 10.3389/feart.2023.1083562

Adaptive vertical-deformation field estimation and current tectonic deformation significance analysis in Shanxi rift valley

Ruichun Liu[1,2,3], Jin Zhang[1]*, Wenfeng Guo[2,3] and Hui Chen[2,3]

[1]College of Mining Engineering, Taiyuan University of Technology, Taiyuan, China, [2]Shanxi Earthquake Administration, Taiyuan, China, [3]Continental Rift Valley Dynamics State Observatory of Taiyuan, Taiyuan, China

The Shanxi rift valley is a continental rift system that is characterized by mantle uplift, crustal thinning, and tectonic deformation. A continuous, vertical crustal-deformation field can elucidate the constraints for understanding the mechanisms currently driving the deformation of the rift. Accordingly, we acquired and processed data from 250 continuous and mobile GPS stations located in the Shanxi rift valley and its surrounding region. Accounting for the influence of fault activity, we established the vertical crustal-deformation field of the Shanxi rift valley as a continuous function of space, using an adaptive least-squares collocation method. The main research findings are stated as follows: 1) the adaptive least-squares model yielded a reliable interpolation prediction results with adequate robustness, even for relatively sparse actual observation data. 2) The current general deformation pattern of the Shanxi rift valley exhibits an uplift of the mountainous regions on both sides and subsidence of the central basin. The average uplift rate of the mountain area is 2–3 mm/a, and the subsidence rate of the basin is not uniform and is positively correlated with the spatial distribution of the Cenozoic sediment thickness. However, in certain areas, a high subsidence rate of 10–30 mm/a is associated with human activities such as groundwater exploitation. 3) In summary, the current vertical crustal deformation occurring in the Shanxi rift valley correlates with the pattern over a time scale of millions of years. Overall, it is controlled by regional geological structure pattern, and is influenced by nonstructural factors in the shallow crust, exhibiting both complex and orderly characteristics in its spatial distribution.

KEYWORDS

vertical deformation field, Helmert estimation, GPS, Shanxi rift valley, least-square collocation

1 Introduction

Continental rifting is an important global tectonic phenomenon and rift valleys are one of the most intense places of tectonic movement. Their formation and development are of great significance to the study of geodynamics (Zygouri et al., 2008; Zwaan et al., 2020), mineral exploration (Zou et al., 2015), and seismology (Crone and Haller, 1991; Roberts and Koukouvelas, 1996). The Shanxi rift valley is a distributed continental rift system that spans more than 1,000 km from north to south in a slanted "S" shape. The northeast-end strikes to the ENE, extending into Yuxian–Huailai Basin in Hebei province, and the southwest-end trends toward the WSW, extending into the Weihe Basin in Shaanxi Province (Zhang et al.,

1981; Liu et al., 1982; Xu and Ma, 1992). As a boundary zone between the Ordos and North China Plain, the Shanxi rift valley exhibits strong mantle upwelling, crustal thinning, and tectonic deformation (Xu et al., 1993). Strong earthquakes (Ms ≥ 5.0) have frequently occurred here, indicating frequent activity and ongoing development of the rift valley (Xu and Ma, 1992; Bai et al., 1994). The interior of the rift is not a single shear and tensile structure but is composed of five Cenozoic graben basins en echelon with NNE–and NE–trending strikes: Datong, Xinding, Taiyuan, Linfen, and Yuncheng. The non-uniformity of crust deformation in the rift is reflected by the significant variations in seismic activity of these faulted basins, and variable the Cenozoic sediment thickness (Xu et al., 1993) (Figure 1). The nonuniform deformation characteristics indicate that the intensity of fault activity and the risk of future strong earthquakes differ in each graben basin. To clearly reveal these nonuniform deformation characteristics, a reliable and accurate 3D-velocity field of the present crustal deformation is required.

Several research groups have comprehensively studied the deformation characteristics of its rift structures in depth. In terms of horizontal deformation, the Shanxi rift valley is consistent with the entire North China region. In other words, the maximum compressive stress axis of the tectonic stress field is aligned in the ENE–WSW direction, the maximum tensile stress axis is in NNW–SSE direction, and the elevation angle of principal stress axis is close to zero (Li, 1980; Li et al., 1982; Zhang et al., 1987; Zhuo et al., 2016). This tectonic deformation feature may be related to the far-field effect of subduction and the impact of the Indian and Eurasian plates (Li, 1997; Cen, 2015; Zhang et al., 2019). In terms of vertical deformation, the Shanxi rift valley displays characteristics of

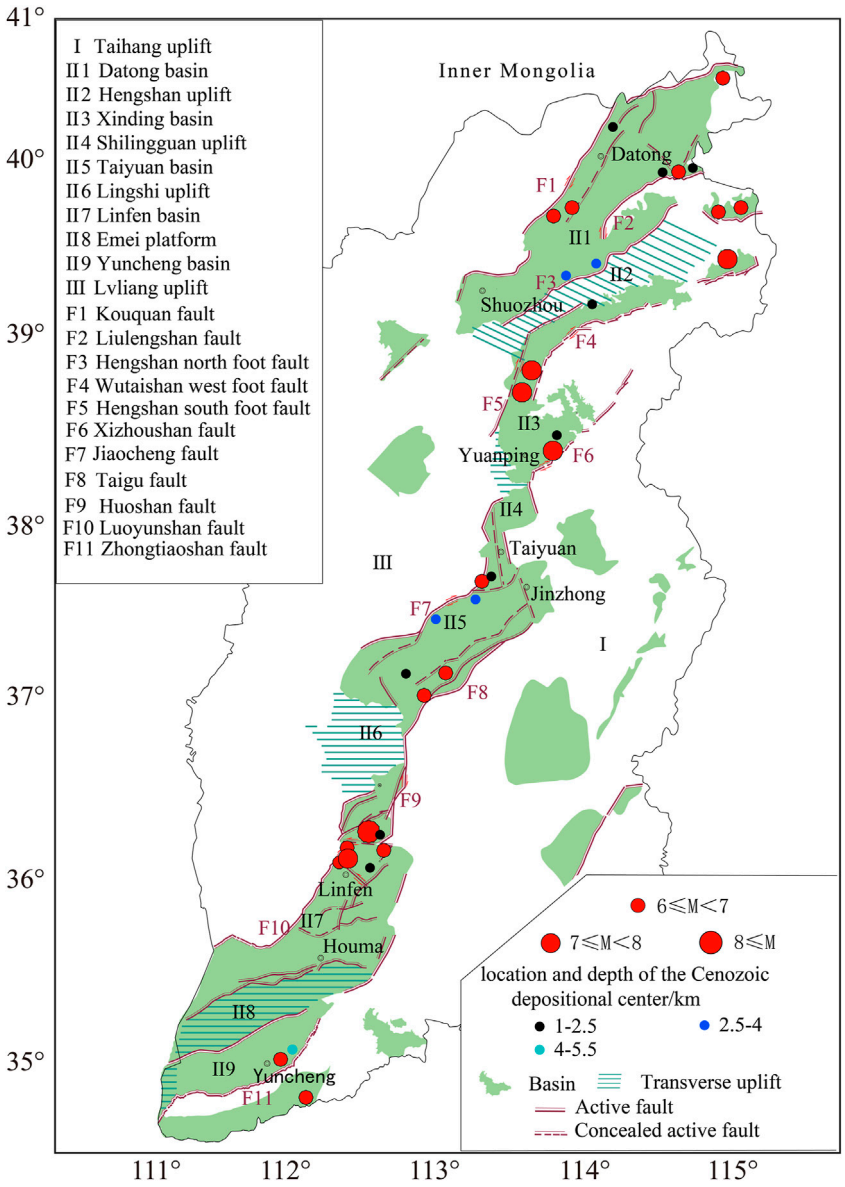

FIGURE 1
Seismic geological structure of the Shanxi rift valley.

inheritance and neogenesis, which may be related to the geological structure pattern (Hu et al., 1987; Zhang, 1993), regional stress-field variations (Hu et al., 1993), deep mantle material activity (Hao et al., 2016), and human activities, particularly groundwater extraction (Zhao et al., 2018; Yang et al., 2020; Liu et al., 2021).

Although Zhao et al. (2014) determined the GNSS vertical motion rate in North China, most measurement points were in campaign measurement mode and had a short observation periods and limited accuracy. Pan et al. (2021) used 260 continuously operating GNSS stations to demonstrate the vertical rate in mainland China. However, the obtained spatial resolution was low owing to the sparsely located cGNSS stations, and only the overall characteristics of a large range of vertical deformations were revealed. In general, the detailed characteristics of the current high-precision vertical deformation, along with its tectonic significance in the Shanxi rift valley, are still unclarified, mainly because of the following reasons: 1) The sparse spatial distribution of cGNSS observation data and the short observation period of the GNSS data in the campaign measurement mode failed to fulfill the high accuracy requirements of vertical deformation mapping. 2) The high-precision leveling points are primarily distributed along the roads; many of them are insufficient in the main structural units, and the crustal movement pattern as imaged by the measured points is incomplete.

Aiming at the need for studying vertical crustal deformation in the Shanxi rift valley, this study proposes a modeling method of crustal-deformation field based on an adaptive least-squares collocation method, considering regional fault activity. Subsequently, we acquired GNSS observation station data of 70 continuous measurement sites and 180 campaign sites for multiple period observations in the Shanxi rift valley and its surrounding areas. We computed regional GNSS vertical motion velocity field by refined processing and constructed the continuous distribution of the vertical crustal-deformation field of the Shanxi rift valley with the constraint of vertical motion velocity (Dong et al., 2008; Zhang et al., 2011; Liang, 2014). Furthermore, the fine features of the present vertical deformation and its tectonic significance were analyzed. The results provide reliable data constraints for the dynamic mechanism of current vertical deformations in the Shanxi rift valley.

2 Adaptive least-squares collocation method considering fault activity

2.1 Method of building vertical deformation field with least-squares collocation

Vertical crustal deformation includes both regional-scale tectonic deformation and local-scale nontectonic deformation. Regional-scale tectonic deformation exhibits appropriate stability over the geological time scale of millions of years, whereas local-scale nontectonic deformation exhibit randomness. In this paper, the least-square configuration method was employed to construct a vertical crustal-deformation model, which was segmented into two components: fixed effects and random effects, representing the background field and local motion signals of vertical crustal deformation obtained from the geodetic survey.

$$\boldsymbol{L} = \boldsymbol{AX} + \boldsymbol{BS} + \boldsymbol{r} \tag{1}$$

where L denotes the observation vector, representing the vertical deformation of the monitoring point; AX represents the fixed effect component; BS denotes the random effect component; X denotes a nonrandom undetermined parameter vector; A indicates the coefficient matrix, representing the influence of parameter X (coordinate information of observation station) on the observed value L; S denotes the signal vector, representing the current crustal-deformation signal of the monitoring point after subtracting the overall crustal background deformation; B indicates the coefficient matrix of S, considered to be the identity matrix. R indicates the random observation-error vector.

The first term accounts for the regional-scale tectonic deformation of the block. Herein, a two-dimensional surface with a second-order polynomial fit in latitude and longitude is used for fitting, and the coefficient matrix A can be expressed as

$$\boldsymbol{A} = \begin{bmatrix} 1 & \Delta\varphi_1 & \Delta\lambda_1 & \Delta\varphi_1^2 & \Delta\varphi_1\Delta\lambda_1 & \Delta\lambda_1^2 \\ \vdots & \vdots & \vdots & \vdots & \vdots & \vdots \\ 1 & \Delta\varphi_i & \Delta\lambda_i & \Delta\varphi_i^2 & \Delta\varphi_i\Delta\lambda_i & \Delta\lambda_i^2 \\ \vdots & \vdots & \vdots & \vdots & \vdots & \vdots \\ 1 & \Delta\varphi_n & \Delta\lambda_n & \Delta\varphi_n^2 & \Delta\varphi_n\Delta\lambda_n & \Delta\lambda_n^2 \end{bmatrix} \tag{2}$$

where (φ, λ) denotes the coordinate of the monitoring point, and $(\Delta\varphi, \Delta\lambda)$ represents the coordinate of the monitoring point relative to a central reference location.

The estimated and signal values of the least-square configuration can be derived as

$$\begin{cases} \hat{\boldsymbol{X}} = \left(\boldsymbol{A}^{\mathrm{T}}\boldsymbol{C}_{\boldsymbol{L}}^{-1}\boldsymbol{A}\right)^{-1}\boldsymbol{A}^{\mathrm{T}}\boldsymbol{C}_{\boldsymbol{L}}^{-1}\boldsymbol{L} \\ \hat{\boldsymbol{S}} = \boldsymbol{C}_{\boldsymbol{L}}^{-1}\boldsymbol{B}^{\boldsymbol{T}}\boldsymbol{C}_{\boldsymbol{L}}^{-1}(\boldsymbol{L} - \boldsymbol{AX}) \\ \hat{\boldsymbol{S}}' = \boldsymbol{C}_{\boldsymbol{S}'\boldsymbol{S}}\boldsymbol{C}_{\boldsymbol{L}}^{-1}\hat{\boldsymbol{S}} \end{cases} \tag{3}$$

In the Equation, $C_L = BC_SB^T + C_r$, C_S denotes the covariance matrix of the signals between measured points, which describes the spatial distribution correlation and dispersion of regional crustal deformation velocity groups. $C_{S'S}$ denotes the mutual covariance matrix of the measured point signal and the signal at the unmeasured point to be estimated. C_r represents the observation-noise covariance matrix, describing the discreteness of the deformation velocity of each point (reflecting the observation accuracy) and the correlation of errors between various stations.

To determine the optimal weighting between the covariance matrices of observation noise and signal, we employed the Helmert variance component method to estimate the posterior unit-weight variance of the observation noise and signal, respectively. Moreover, the adaptive factor of the variance component was constructed. After several iterations, the covariance matrix relationship was balanced. The adaptive factor is expressed as follows (Yang et al., 2008):

$$\alpha = \frac{\sigma_{0r}^{2(i)}}{\sigma_{0s}^{2(i)}}, \tag{4}$$

where $\sigma_{0r}^{2(i)}, \sigma_{0s}^{2(i)}$ denote the post-test unit-weight variance of the observation noise and the unit-weight variance of the signal after the i-th operation, respectively. According to the adaptive factor, the $(i+1)$-th observation-noise covariance matrix can be expressed as follows:

$$C_r^{(i+1)} = \frac{1}{\alpha} C_r^{(i)} \quad (5)$$

The adjusted observation-noise covariance matrix was used to adjust until the adaptive factor α approached 1.

2.2 Fitting of block tectonic movement

Quaternary active faults segment the Earth's crust into active blocks of multiple sizes, and the positions and dimensions of fault segments can be identified by analyzing spatial variation in fault displacements and fault kinematics (Roberts and Koukouvelas, 1996). Under the influence of tectonic stress, the crustal deformation is primarily characterized by the differential movement of each active block. Although the internal movement of the block remains consistent, the movement characteristics of the blocks vary. In particular, the fault and its adjacent crust show high displacement gradients (Zhang and Zhu, 2000; Deng et al., 2002; Li, 2003; Tan et al., 2009). To reduce the difference between observations, the values observed in each block are first centralized for establishing the function model, i.e., in Eq. 1, L is the velocity relative to a reference velocity, such as

$$L = V - \bar{V} \quad (6)$$

where $\bar{V}$ indicates the mean or median of the observed crustal movement of each block or the motion parameter determined using the relevant geological model. After applying the least squares collocation approach, $\bar{V}$ is added back in the velocities of the measured points and the unmeasured points to be estimated.

Principally, the Gaussian function is used to fit the covariance of the crustal movement rate (Jiang and Liu, 2010). First, the study area is segmented into multiple blocks, and the long-term background velocity of the corresponding block is deducted from the measured velocity field according to the block affiliation, i.e., the velocity after centralization is determined via Eq. 6 to evaluate the signal. Second, the correlation coefficient β ($0 \le \beta \le 1$) of the points on both sides of the main fault is defined with a weakened correlation to reflect the characteristics of regional crustal deformation (Zhang and Jiang, 2001; Chai et al., 2009). Accordingly, the covariance fitting formula is derived as follows:

$$F(d) = \beta C(0) e^{-K^2 d^2}. \quad (7)$$

The value of β is set as 1 when the two points are located on the same side of the main fracture, and that on the opposite side is less than 1, which is determined based on the actual situation, recommended at 0.5. In the case of using the determined covariance function to calculate $C_S, C_{S'S}$, the correlation between the points should also be considered according to the above rules.

2.3 Experiment on regional vertical-deformation field estimation

To evaluate the reliability of the crustal-deformation model along with the applicability of the method, we initially used an elastic dislocation model to simulate fault activity and forward the "theoretical deformation field." Thereafter, we compared and analyzed the deviation degree between the "calculated deformation field" and the "theoretical deformation field" simulated by various methods.

2.3.1 Simulation of the regional vertical-deformation field

A fault with a positive dip distributed in the study area (115°–120° E, 35°–40° N), with starting point (117.375° E, 39° N), end point (117.375° E, 36° N), dip angle (45°), and dip E. In particular, we assumed complete locking from the surface to 15 km underground, with 30 mm/a positive dip-slip and 20 mm/a right-lateral shear below 15 km. The homogeneous isotropic semi-infinite spatial dislocation model (Okada, 1985) is used to simulate the deformation field (0.25° × 0.25°) generated by the fault activity on the surface. As depicted in Figure 2A, the area with the high displacement gradient was primarily distributed in the vicinity of the fault. To simulate and analyze the influence of the discreteness and inhomogeneity of the measured points on the modeling, the measuring points in the range of the fault hanging wall (117.5°–118° E, 36.5°–38.5° N) were initially deleted. Subsequently, 30% of the remaining measuring points were randomly deleted. According to the above scheme, the velocities of 281 points in total can be used as constraints for fitting (Figure 2B), and those for 160 points can be used for result checking (Figure 2C).

The least-square collocation method was used to establish the overall crustal-deformation field with 0.25° × 0.25° resolution. Moreover, the Gaussian-type function with the decay of distance was adopted in the empirical covariance function fitting model. According to the distribution of the measurement points, we determine the covariance function model parameter K = 0.84 and the correlation distance d = 160 km (Zhang and Jiang, 1999). To evaluate the applicability of the method, modeling is performed according to the following four schemes:

Scheme 1: Using least-squares collocation modeling without considering fault activity;
Scheme 2: The variance factor for modeling was adjusted based on scheme 1;
Scheme 3: Considering the fault activity, the study area was segmented into two blocks along the fault. The average observed rate in the block was used to centralize the known observed values, and the covariance between the points on opposite sides of the fault was weakened. The point correlation coefficient on opposite sides of the fault was set as 0.5, and the least-squares collocation was used for modeling;
Scheme 4: The variance factor for modeling was adjusted based on scheme 3.

2.3.2 Analysis of experimental results

The crustal-deformation field obtained based on the four schemes is presented in Figures 3–6, depicting the (Figures 3A–6A) vertical-deformation field estimation result, (Figures 3B,C–6B,C) residuals of fitting points and checking points, respectively, and (Figures 3D,E–6D,E) residual frequency distributions of fitting points and checking points, respectively. As shown in Figure 3A, 6A, the deformation fields obtained from the four schemes exhibited similar overall characteristics. All of them revealed the crustal-deformation pattern of the falling on the

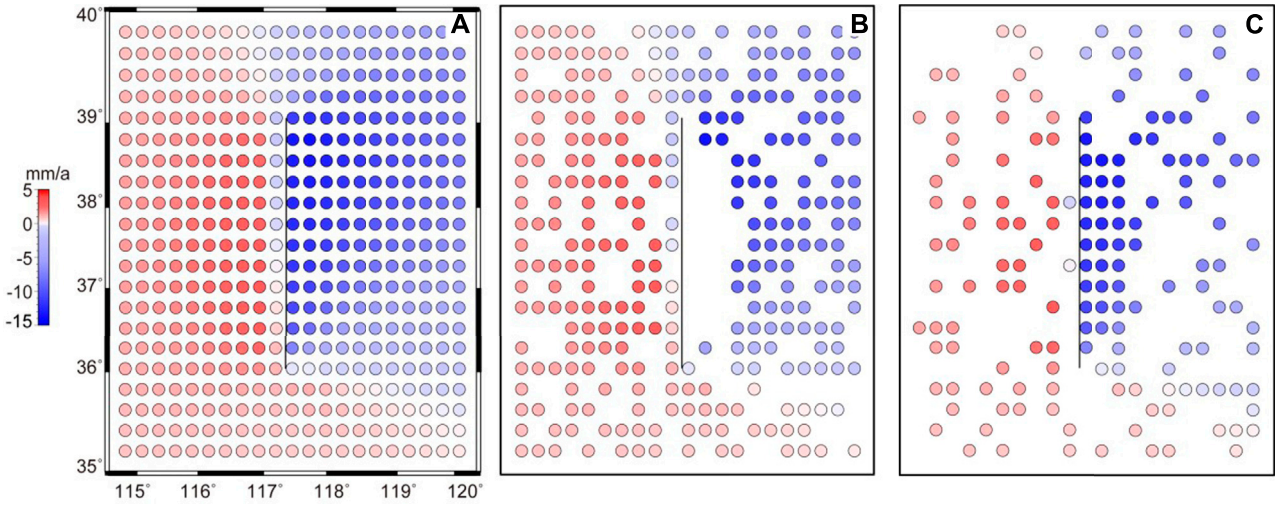

FIGURE 2
Vertical-deformation field derived from dislocation model.

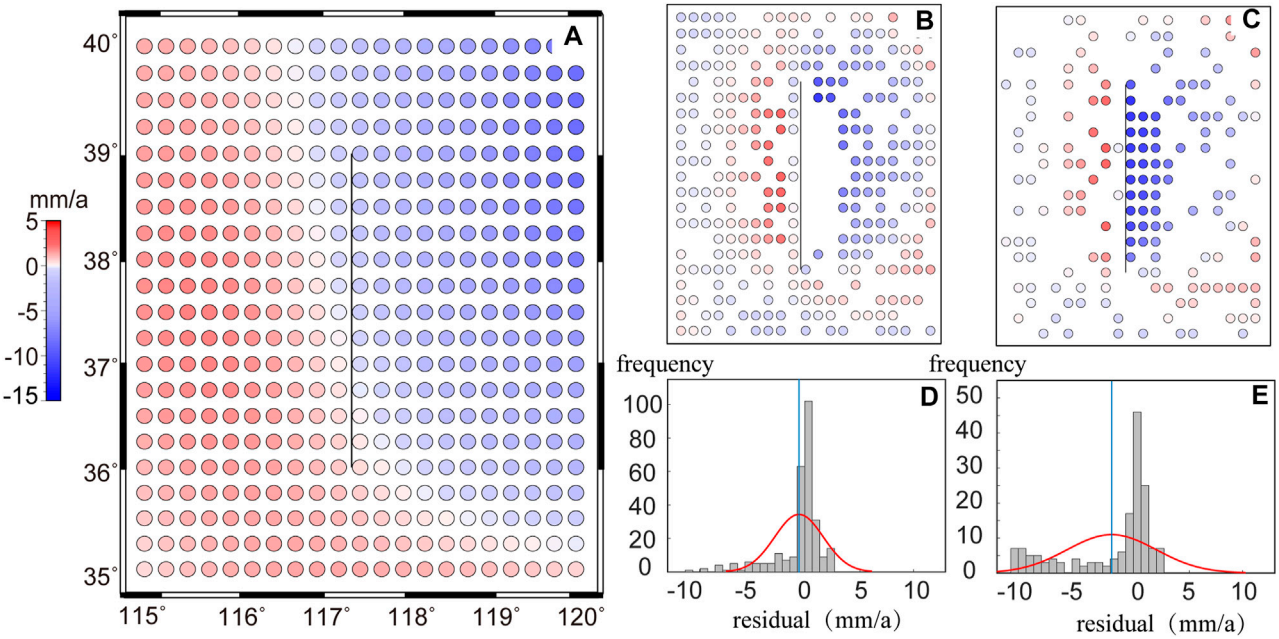

FIGURE 3
Deformation field model fitting based on Scheme 1.

hanging wall and the relatively rising on the footwall. In detail, the area with a large-displacement difference was distributed in the blank observation area of the hanging wall as well as the fault end. Influenced by the fault activity in these regions, the variations in the crustal-deformation velocity are susceptible to abrupt variability, and the interpolation accuracy of the model is poor. In particular, the velocity value in Figure 3A is evidently small in the fault hanging wall area, which differs from the original velocity field. Figure 4A, 5A, 6A are approximate to the original deformation field, but the details of the crustal deformation vary. To evaluate the accuracy and usability of the model, we employed qualitative and quantitative analysis methods to comprehensively evaluate the fitting and interpolation effects of the four stated methods. The RMS (Root Mean Square) values of the velocity residual between the actual observed values and the model values of fitting points and checkpoints obtained using the four methods are presented in Table 1. Among them, the near-field checkpoints of the fault included all the points within the range of 117.5°–118° and 36.5°–38.5°, and all the regional checkpoints incorporated the near-field checkpoints of the fault and the randomly deleted points.

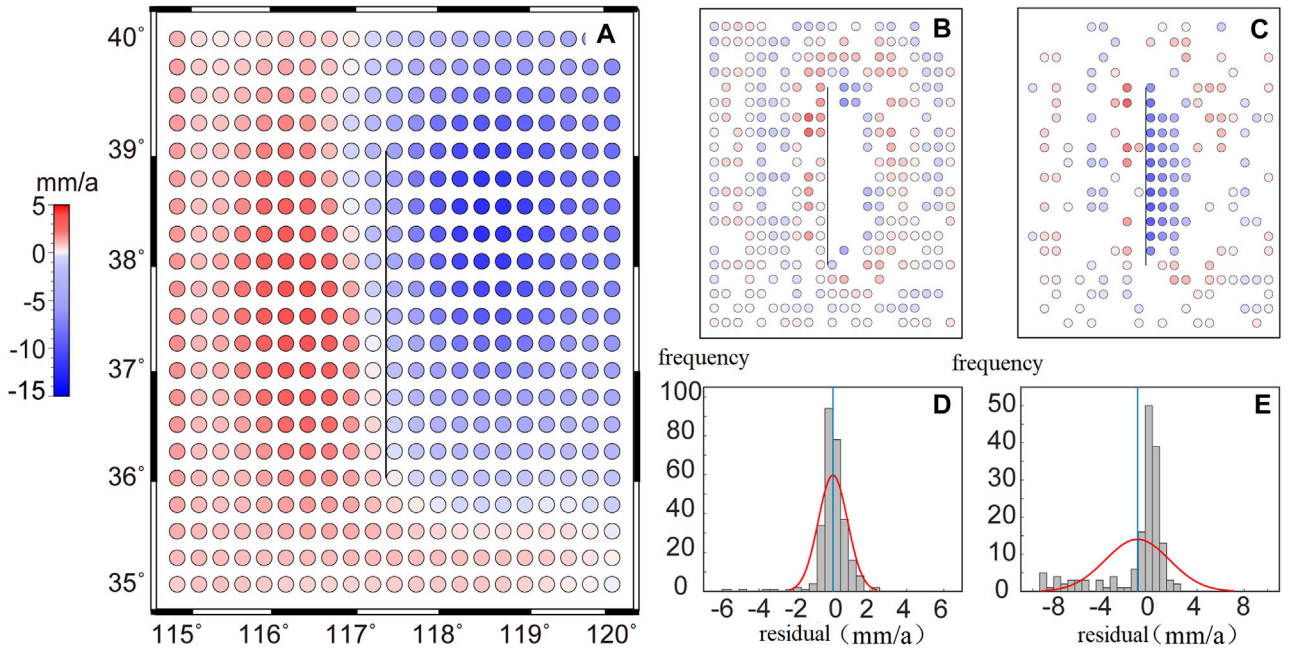

FIGURE 4
Deformation field model fitting based on Scheme 2.

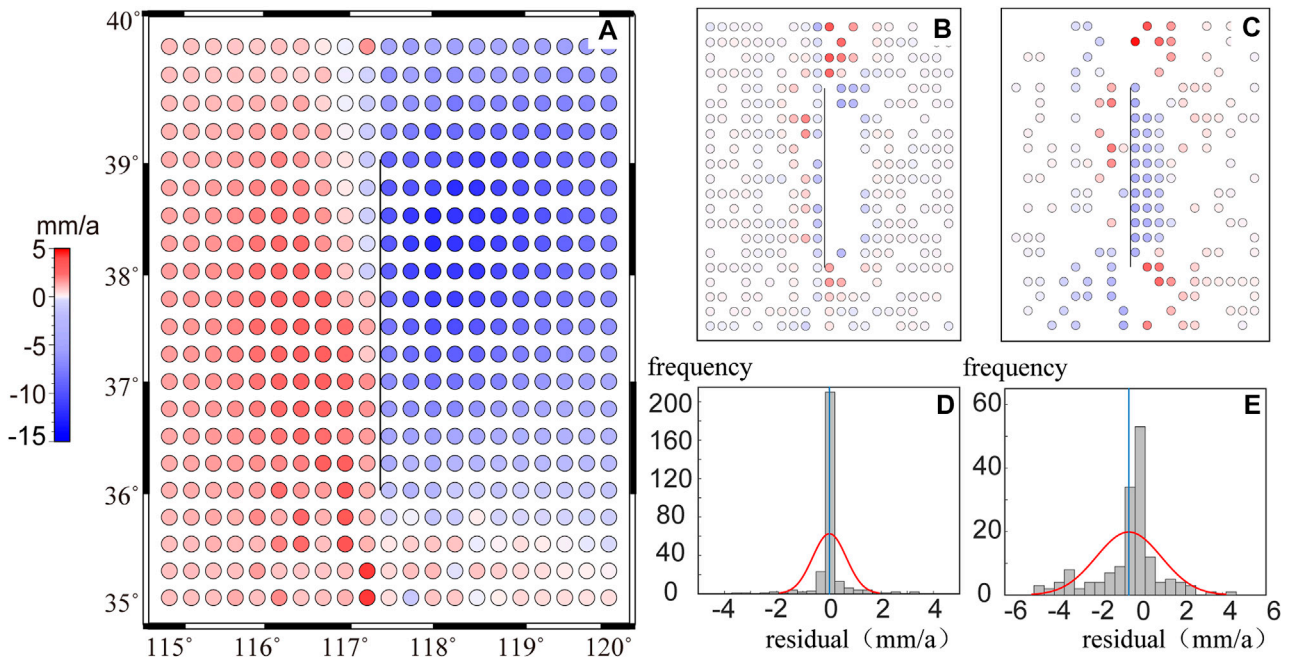

FIGURE 5
Deformation field model fitting based on Scheme 3.

In this example, Method 1 assumes continuous spatial variations of the crustal deformation. Consequently, the model exhibits inferior fitting accuracy, and the fitting residuals are skewed owing to the influence of abrupt variations caused by tectonic activities in the deformation field (Figures 3B, D). In comparison, Method 2 uses the Helmert variance component to estimate and construct the adaptive factor of the variance component. After several iterations, the balance of the covariance matrix

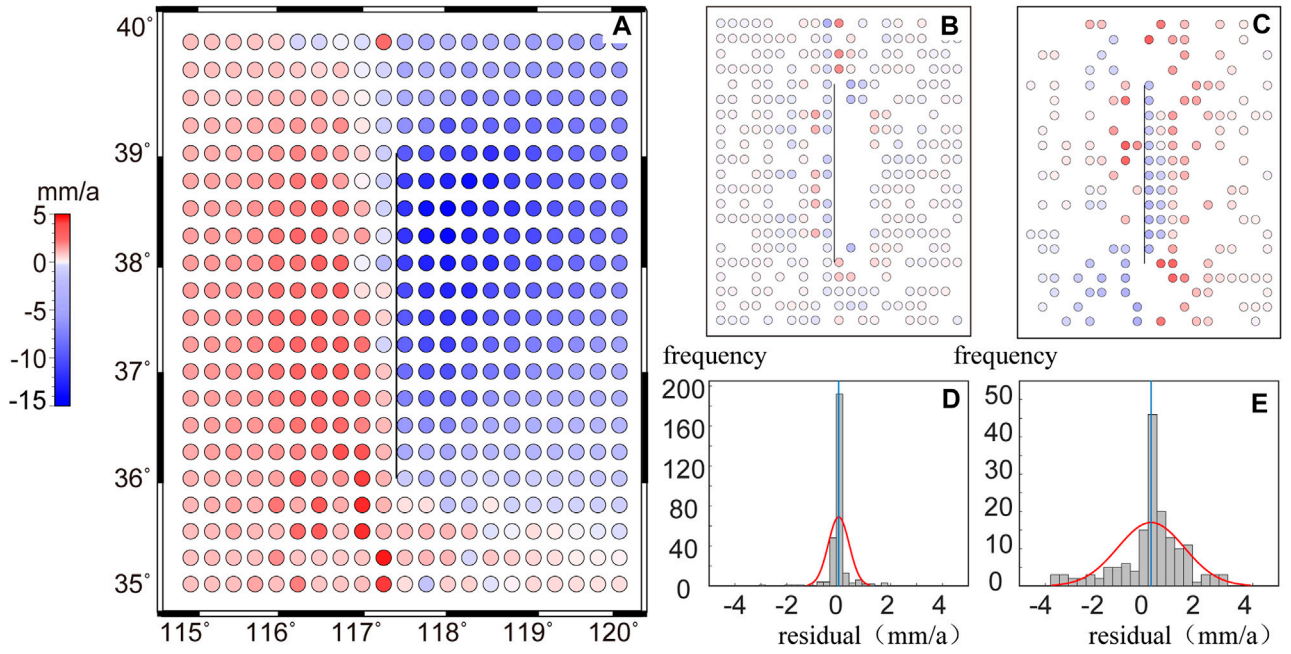

FIGURE 6
Deformation field model fitting based on Scheme 4.

TABLE 1 Comparison of different velocity field modeling methods.

Point type	Residual RMS (mm/a)			
	Scheme 1	Scheme 2	Scheme 3	Scheme 4
All fitting points	2.38	0.79	0.64	0.40
All checking points	4.73	2.93	1.51	1.28
Fault near-field checking points	9.95	6.55	2.72	1.56

relationship was achieved. Compared with the results of Method 1, the fitting accuracy of the model significantly improved with the application of Method 2, and the fitting residual approximated normal distribution with zero mean (Figure 4D). Method 3 considers the influence of geological structure and regards the regional faults as discontinuities in the continuum, which is a slight improvement compared to Method 2 in terms of fitting accuracy and statistical distribution of residuals. Method 4 combines the advantages of Methods 2 and 3 by simultaneously considering the balance of the covariance matrix relationship and the influence of geological structure. Consequently, the fitting accuracy of the model is the highest, and the residual approximates normal distribution with zero mean.

Based on the perspective of external coincidence accuracy, the interpolation accuracy of Method 4 is higher than that of Methods 1, 2, and 3, regardless of considering all regional checkpoints or fault near-field checkpoints for analysis. Based on the perspective of all checkpoints in the region, the interpolation accuracies of Methods 1 and 2 were greater than 2 mm/a, and the residuals displayed skewed distribution (Figures 3E, 4E). The velocity obtained via interpolation exhibited prominent systematic deviation in the observed blank area of the fault hanging wall (Figures 3C, 4C). Although the interpolation accuracy of Methods 3 and 4 is less than 2 mm/a, Method 4 delivers higher accuracy, more proximate residual to a normal distribution with zero mean (Figure 6E), and smaller residual in the blank area of near-field observations of fault (Figure 6C).

Owing to the influence of the velocity of points at the footwall of the fault, the interpolation results of Methods 1 and 2 were remarkably inferior and failed to accurately reflect the crustal-deformation status in the near-field area of the fault. In Method 3, the influence of fault activity was considered for constructing the covariance matrix, and the modeling accuracy and reliability in this area were significantly improved, which reflected the differential motion of the two blocks. This indicated that in areas with large local deformation, the least-squares collocation model, without considering fault activity, could not easily reflect these local variations without applying finer constraints. Based on the perspective of interpolation accuracy of fault near-field blanks, the results obtained by Method 4 were less than 2 mm/a. This

finding demonstrates the advantages of using Method 4, implying that the regional fault activity and determination of optimal weight of noise covariance and signal covariance matrix must be considered in practical application.

3 GPS model of vertical crustal-deformation field

3.1 GPS data and processing

The GPS data used in this paper were primarily acquired from the "Crustal Movement Observation Network of China," "Shanxi CORS network," and "Shanxi Earthquake GPS Monitoring Network," with 70 continuous stations and 180 campaign stations in the study area. Additionally, data processing was performed in four steps using GAMIT/GLOBK (Herring et al., 2010) and QOCA software. In particular, 1) GAMIT software was used to process the daily observation data for obtaining the single-day relaxation constraint solutions of the satellite orbit, station coordinates, antenna-phase offset, and zenith atmospheric delay parameters. 2) The regional single-day solutions were merged with the single-day solutions of approximately 80 IGS core stations produced by SOPAC. These IGS core stations were used as a "bridge" to transform the single-day relaxation constraint solutions into the ITRF2014 framework using seven parameters. 3) The annual motion amplitude of the GPS vertical time series can reach up to 5–10 mm owing to nontectonic factors such as atmospheric pressure, nontidal ocean loads, and hydrological loads (snow cover and soil water) (Mangiarotti et al., 2001; Dong et al., 2002; Dong et al., 2006; Wang, 2009; Jiang, 2013).The observation period of the campaign sites is small and the observation time is not fixed each year, it is significantly affected by the unestimated parameters when determining the vertical motion rate (Blewitt and Lavallée, 2002; Dong et al., 2002; Bos et al., 2010; Zhan et al., 2016). Considering that GPS vertical annual motion bears regional correlation (Wdowinski et al., 1997; Jiang, 2013; Sheng et al., 2014), this paper used the method of Liang (2014) to correct the vertical nonstructural load deformation of the GPS campaign station. First, 64 GPS continuous stations with long observational timespan were selected in the study area, and the annual term amplitude and initial equality parameters of the continuous station time series were fitted through the chord function. Thereafter, by eliminating the "abnormal" continuous stations inconsistent with the annual term amplitude and initial phase, 61 GPS continuous stations with adequate observation quality were ultimately selected to construct the Delaunay triangulation network. Using the harmonic function obtained by fitting the GPS vertical time series of the three endpoints of each triangle, the nonstructural deformation correction corresponding to the actual observation date of the campaign station in the network was evaluated based on the inverse-distance weighted-average algorithm. To ensure the accuracy and reliability of the vertical motion rate, only GPS campaign stations with observation timespan longer than 7 years were corrected (Blewitt and Lavallée, 2002; Bos et al., 2010; Li et al., 2015). 4) QOCA software was used to combinedly adjust the single-day relaxation constraint solutions of all GPS stations that completed the nonstructural deformation correction. Consequently, we obtained the present vertical motion velocity field of the Shanxi rift valley relative to the ITRF2014 reference frame.

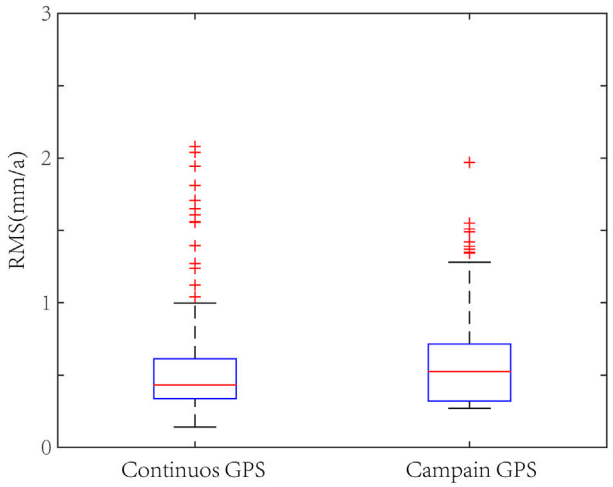

FIGURE 7
GPS measuring point vertical velocity RMS box diagram.

The RMS of vertical motion rates ranged between 0.1 and 1.0 mm/a at the GPS continuous station and between 0.3 and 1.3 mm/a at the GPS campaign station (Figure 7). Owing to the long observation period of the continuous station, the RMS of certain measuring points may be slightly larger than that of the campaign station because of the noise interference, but most of them did not exceed 2 mm/a. The observation timespan of certain GPS campaign stations was longer than that of the continuous stations. However, owing to the limitation of the observation mode, the campaign observation inevitably excluded a considerable amount of "noise" records, whereas the "signal" (velocity) retained the information as the observation period increased and, finally, obtained a statistically smaller RMS. Certain scholars believe that the RMS of the GPS campaign stations should be increased at least two times to correspond to the continuous station (Wang and Shen, 2020). However, the RMS of the vertical movement rates of the two kinds of GPS stations were comparable after the nonstructural load deformation correction applied in this study. For GPS vertical motion, the points whose uplift rate is inconsistent with the movement of most measuring points in the same block are removed, and the remaining 212 measuring points are used for subsequent analysis.

3.2 Continuous vertical-deformation model

The GPS-derived vertical-deformation field of the Shanxi rift valley relative to the ITRF2014 reference frame is presented in Figure 8, depicting that the GPS measuring points include both uplift and subsidence. However, the uplift rate is significantly lower than the subsidence rate, generally less than 3.0 mm/a. Primarily, the uplift measurement points are distributed in the Taihang Mountain area in the east and the Lvliang Mountain area in the west. In

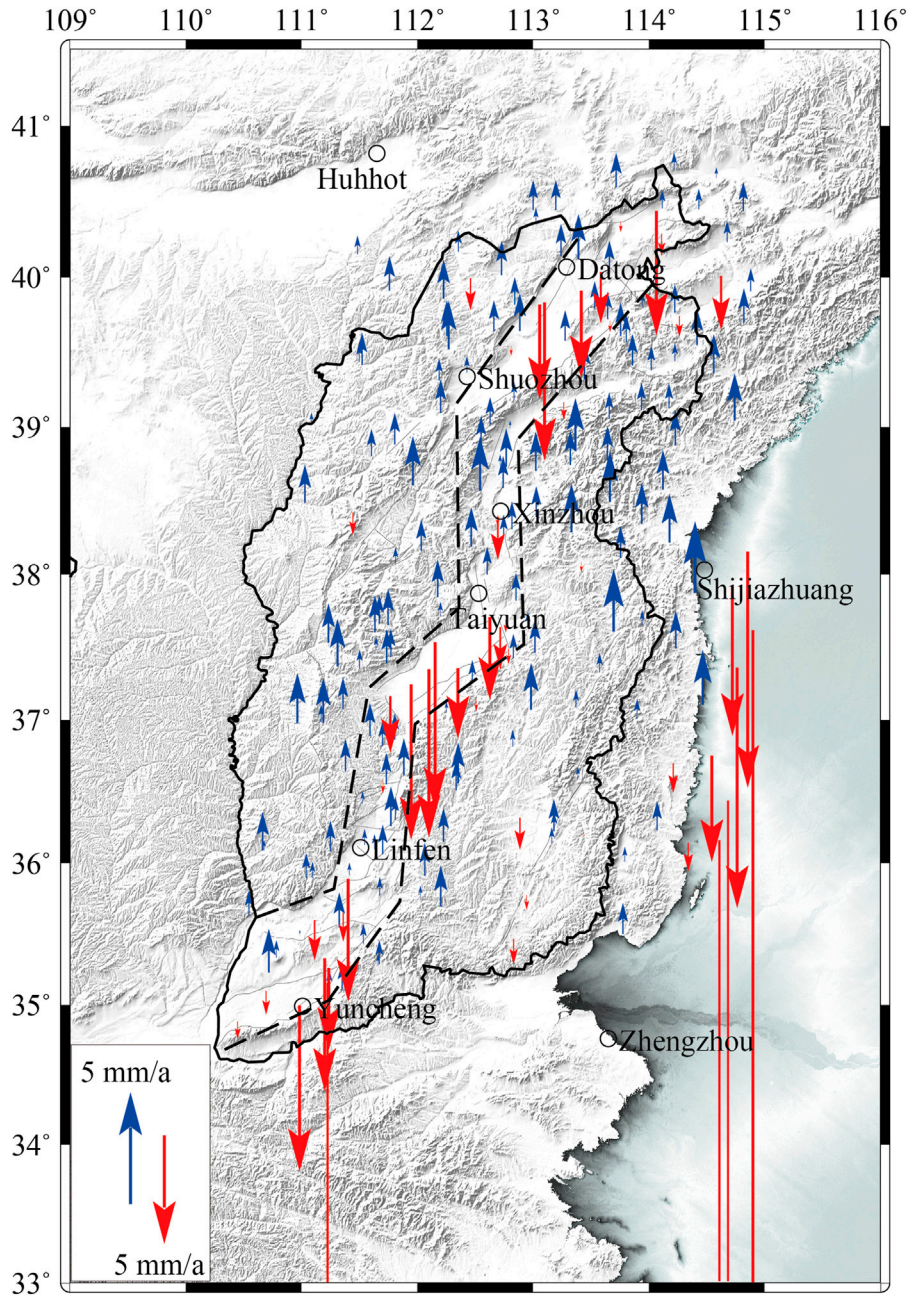

FIGURE 8
GPS vertical-deformation field in the Shanxi rift region (relative to ITRF2014 reference frame).

comparison, the settlement points are mainly distributed in two types of areas: first, the Hebei Plain in the east of the Shanxi rift valley, with a relatively dense distribution of subsidence points and the largest subsidence amount. The maximum subsidence rate of the measurement points is greater than 60 mm/a. Second, the Datong, Taiyuan, and Yuncheng basins in the Shanxi rift valley. The Datong Basin exhibits a small subsidence rate (maximum rate of ~10.0 mm/a), whereas the Taiyuan and Yuncheng basins display larger subsidence rates—maximum rates of −30.5 and −36.2 mm/a, respectively. To further analyze and study the current vertical deformation fine feature of the Shanxi rift valley, the continuous spatial distribution of vertical crustal deformation is deduced using the GPS velocity field of unified reference.

Due to the high gradient in crustal movement on both sides of the fault and uneven distribution of GPS measuring stations, the spatial information of regional crustal vertical deformation in the Shanxi Rift is unclear. Based on the information distribution of all observed data, spatially correlated models can be developed using traditional spatial statistical modeling methods, which yield singular values. In comparison, the adaptive least-squares collocation method considering fault activity can estimate the vertical-deformation velocity through the optimized empirical covariance

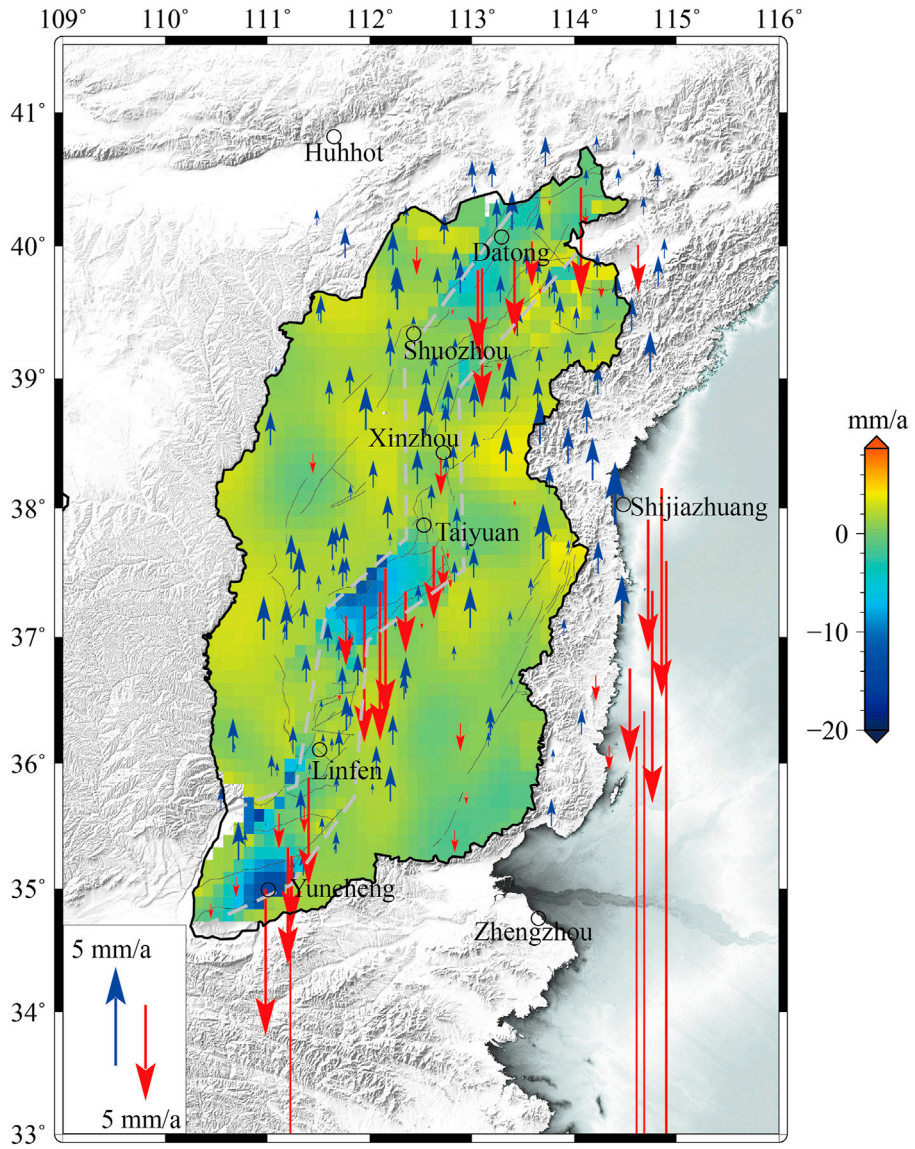

FIGURE 9
Model of vertical crustal-deformation field in the Shanxi region.

function, which enables appropriate modeling of regions with significant differential crustal deformation. Herein, we apply the least-squares collocation method to construct the continuous vertical-deformation model of the Shanxi rift valley.

The Shanxi rift valley and its surrounding areas can be segmented into three relatively independent blocks along the boundary faults of the five major graben basins, namely, the Lvliang Mountain in the west, the Taihang Mountains in the east, and the central graben basin belt. In Figure 9, the block boundaries are demarcated using gray-dashed lines. According to the determined block boundary, the known observed values in each block area were respectively centralized. According to the distribution of measurement points, the correlation distance of spatial signals d was determined as 158.7 km, and following inverse calculation, the covariance function model parameter K was obtained as 0.02 (Zhang and Jiang, 1999). Considering that the vertical motion of the mountainous region on both sides is completely opposite to that of the graben basin, the point correlation on both sides of the block boundary was defined as 0.5 when the prior covariance matrix is determined using the Gaussian-type empirical covariance function. Simultaneously, the Helmert variance component was introduced to estimate the *a posteriori* unit-weight variance of the noise and signal, which balanced the relationship between their covariance matrices.

The vertical crust-deformation image of the continuous distribution of the Shanxi rift valley established based on the GPS-measured data is illustrated in Figure 9, which indicates that the vertical deformation of the Shanxi rift valley is correlated with the overall tectonic landform. The orogenic belt and plateau area compose the uplift areas, primarily including the Taihang Mountains and Lvliang Mountains on both sides of the Shanxi rift valley, and the lateral uplift areas, such as Lingshi and Shiling

Pass, are situated between two graben basins. Moreover, the basins along the rift valley and plain area form the subsidence regions, including the central graben basin of the Shanxi rift valley and Hebei Plain, which is consistent with prior research results (Zhao et al., 2014). Furthermore, the average uplift rate of the Taihang and Lvliang mountains was approximately 2 mm/a, which is consistent with the InSAR monitoring results. The vertical crustal deformation in this region is unaffected by groundwater extraction, which may cause the background tectonic movement during the interseismic period (Zhao et al., 2018). Nonetheless, the subsidence of Datong, Taiyuan, and Yuncheng basins in the central rift valley is significantly large at a rate of 10–30 mm/a. Moreover, these regions experience severe groundwater extraction that causes hazardous geological disasters such as land subsidence and ground fractures (Yang et al., 2016, 2021; Peng et al., 2017; Liu et al., 2021). Although the Xinding Basin does not appear to subside, it exhibits a weak uplift that is consistent with the current horizontal extrusion deformation characteristics of the basin (Zhao et al., 2017).

The adaptive least-squares collocation method considering fault activity can adjust the empirical covariance matrix according to the structural characteristics of the Shanxi rift valley and the actual situation of the observed data, which can effectively improve the model fitting and interpolation accuracy. Specifically, in the blank observation area near the fault field, the interpolation results were obtained based on the observation results of the same structural area on same side of the fault. Overall, the interpolation results yielded no singular values, and the model results were consistent with the measured values. We believe that this method is suitable for studying the vertical-deformation characteristics of the Shanxi rift valley, and the interpolation results can represent the real deformation information of the region to a certain extent.

4 Discussion

4.1 Tectonic significance of current vertical deformation

The current subsidence rate in the central and southern regions of the Datong Basin increases up to 9.1 mm/a, which is the most significant subsidence region in the basin. This area is structurally located in the hanging wall of the Kouquan fault, with a Cenozoic sediment thickness of 1,800 m (Xu et al., 1993). More specifically, it encloses an industrial and agricultural activity area of Datong City, and the excessive groundwater exploitation by industrial and agricultural production resulted in the drainage of several aquifers and the continuous decline of underground water level, forming three large sedimentation funnels (Guo et al., 2002; Dong et al., 2008). The present vertical-deformation rate reported herein is consistent with the spatial distribution of the subsidence funnel, which indicates that groundwater exploitation is a vital reason for the present vertical deformation of the crust in the Datong Basin.

The current subsidence rate of the Taiyuan Basin reaches up to 10.5 mm/a and is primarily distributed along and near the Jiaocheng fault. In comparison, the Taigu fault along the eastern boundary exhibits a relatively small subsidence rate: 3–4 mm/a. Geological studies have reported that the deep-fault depression in the Taiyuan Basin is mainly distributed along the Jiaocheng fault in the west. The Cenozoic sediment thickness detected by artificial seismic is from 2,000 to 3,800 m, wherein the Quaternary sediment thickness ranges from 300 to 500 m (Xu et al., 1993). Although the Cenozoic sediment thickness along the Taigu fault in the east spans only hundreds of meters, the Quaternary sediment thickness ranges only within 100–150 m. The positive correlation between the current vertical-deformation rate and the Cenozoic sediment thickness of the basin suggests that the current vertical-deformation pattern of the Taiyuan Basin is consistent with the long-term deformation on geological time scales. However, the deformation of >10 mm/a in the western region of the basin is not entirely caused by the tectonic deformation, and it is closely related to groundwater exploitation (Sun, 2016).

The current subsidence rate of Yuncheng Basin is up to 36.2 mm/a, and the subsidence center region is located in the alluvial plain of the hanging wall on the north foot of the Zhongtiaoshan fault. In this region, the Cenozoic sediment thickness is up to 5,500 m at the deepest point, the largest Cenozoic sediment thickness in the Shanxi rift valley. The types of regional groundwater include pore water in loose rocks, and the phreatic aquifer, phreatic-confined aquifer, and confined aquifer as the major groundwater exploitation layers (Huang, 2007). The excessive groundwater exploitation has formed a permanent groundwater drop funnel that reduces the pore pressure of the aquifer, resulting in severe land subsidence (Yao, 2017). Compared with the Yuncheng Basin, the vertical-deformation range and amplitude of the Linfen Basin are relatively small. In this region, the maximum thickness of the Cenozoic sediment is approximately 2,200 m and pertains to the loess platform. Moreover, the groundwater content differs, and the correlation with land subsidence is weak (Yang et al., 2016).

The present vertical deformation of the Shanxi Rift Valley is controlled by the existing structural pattern and influenced by the shallow nonstructural factors as well as the physical properties of the crustal medium. Since the Quaternary age, the faulted basins have maintained a pattern of inherited decline, but the subsidence rate expresses prominent inhomogeneity, which is positively correlated with the Cenozoic sediment thickness of the basins. This type of deformation occurs only on the shallow surface of the Earth. Based on seismic geology, the deformation is much larger than the dip-slip rate of ~1 mm/a (Miao et al., 2014), and based on leveling, the vertical movement rate of 6–8 mm/a (Hao et al., 2016) is completely different from the fault activity mechanism driven by deep sliding (Qiao et al., 2019; Liu, 2021).

4.2 Dynamic mechanism of current vertical deformation

The subduction of the Indian plate to the Eurasian plate promoted the eastward expansion of the Tibetan Plateau along with the vertical uplift, and the eastward transmission of the tectonic stress generated the counterclockwise rotation of the Ordos block and the eastward extrusion escape of the Qinling Mountain (Deng and You, 1985; Xu et al., 1993; Zhang et al., 2019). The northwestern boundary of the Pacific plate subducted westward at the Japan Trench, and the westward progression of the flattened oceanic plate at a depth of 660 km possibly extended to the Shanxi rift valley (Huang and Zhao, 2006; Lei, 2012; Shao et al., 2016). Therefore, the far-field effect caused by the collision of the Indian and Eurasian plates and the mantle upwelling resulting from the subduction of the Pacific plate affected

the tectonic movement and deformation of the Shanxi rift valley through various mechanisms.

The regional vertical crustal-deformation images presented in this paper reflect the inherited deformation of the basin subsidence and mountain uplift since the neotectonic movement. However, as the vertical crustal deformation in the basin is gravely affected by nontectonic interference, the vertical tectonic differential deformation rate between the faulted basin and the mountainous regions on both sides cannot be accurately determined at present. Considering the Datong Basin in the north of the rift valley as an example, a vertical differential deformation rate of 2.5 mm/a was obtained from the observation data of ground fracture activity in the basin. After deducting the displacement caused by seasonal groundwater exploitation, the vertical differential deformation rate caused by tectonic activities ranged from 0.75 to 1.0 mm/a (Liu, 2021), which is approximate to the variation range of 0.12–1.48 mm/a of a normal fault-type vertical slip rate in the Datong Basin derived from geological data (Zhang et al., 1998; Deng, 2002). Therefore, the neotectonic movement and human activities, such as groundwater exploitation, combinedly affect the vertical crustal deformation in the Shanxi rift valley. In particular, neotectonic movement acts as the controlling factor, and under the compound influence of upper mantle uplift, regional tensile stress, and tectonic block movement, the fault system progress along the fault and forms a hidden fault system on its hanging wall (Wang et al., 2020). In certain regions of the basin, excessive groundwater exploitation has formed a permanent groundwater downward funnel, which consequently reduced the aquifer pore pressure and triggered severe land subsidence.

4.3 Application of crustal-deformation modeling method

The velocity variations occurring because of crustal deformation in regions with strong tectonic activity cannot be neglected, their estimation using accurate functional models is challenging (Diao and Xiong, 2008; Li et al., 2012; Wang et al., 2020). The least-squares collocation is a typical statistical method with theoretical rigor, which poses certain advantages when applied for estimating the signal in the spatial domain based on the crustal-deformation data of limited observation points. However, if the crustal-deformation field exhibits discontinuous variations caused by fault activity, the least-squares method can unreasonably estimate the correlation of point velocities on both sides of faults, which reduces the fitting accuracy of the velocity values in the near-fault region. Thus, the crustal deformation is artificially weakened or annihilated. The estimation of the variance component for adjusting the observation noise and signal in proportion to the covariance can yield a relationship that is more proximate to the real value. This improves the precision of the fitting and interpolation model to a certain extent. However, the interpolation accuracy of the deformation field remains inferior in the significant local-effect areas such as fault near-field. Thus, the model cannot facilely yield reliable fitting results in case of a wide range of measured data gaps for the above regions.

The empirical covariance matrix can be adjusted with the adaptive least-squares collocation considering the regional structural characteristics and the actual situation of the observed data, which effectively improves the accuracy of model fitting and interpolation in regions with fault activity. Specifically, the above-stated method delivers higher interpolation accuracy compared with the least-squares collocation method considering only the tectonic characteristics in the observation blank region near the fault field, which facilitates the current fulfillment of regional crustal deformation monitoring and research. In addition to providing an accurate description of the local deformation characteristics inside the basin, the vertical crustal-deformation field in the Shanxi rift valley based on the geological structure and GPS data can reveal the discontinuous deformation characteristics between the mountainous regions on both sides and the graben basin.

Notably, the interpolation method based on the mathematical model is insufficient in the physical sense. Regardless of the least-squares collocation method, the relationship between the interpolation point and the known point can be derived from the mathematical perspective. In fact, the movement and deformation of the Earth's crust are driven by certain dynamic mechanisms, such as the surface movement rate of an observation point is an external response under dynamic action. Thus, revealing the internal physical relationship between the motion of every point position can accurately evaluate the deformation rate. In addition, this study considered only a strike-slip and dip-slip fault activity, whereas fault movement, and tectonic deformation are extremely complex to be considered in practice. The extensive Late Quaternary active faults in the Chinese mainland segmented the Earth's crust into multiple levels of active blocks, thereby presenting extremely complex motion and deformation characteristics under the action of tectonic stress. Based on the variance among multiple observation data and geological structural environment, several algorithm models and parameter settings should be utilized according to the specific problems, which requires further in-depth research.

5 Conclusion

The adaptive least-squares collocation model considering fault activity effect can yield more reliable interpolation prediction results in case of relatively sparse actual observation data, and it exhibits appropriate robustness. These results revealed fine characteristics of vertical deformation in the Shanxi rift valley and provided reliable data to analyze the characteristics and tectonic implications of the present vertical deformation of the rift, thereby clarifying the mechanism of the present vertical deformation of the rift.

The current vertical crustal deformation in the rift valley follows the deformation pattern continuing for millions of years of geological history—generally characterized by continuous subsidence of the graben basin and relative uplift of the mountainous regions on both sides. The average uplift rate of the mountains on both sides was 2–3 mm/a, which may have been caused by the background tectonic deformation. Expectedly, the nonuniform subsidence rate of the graben basins was positively correlated with the Cenozoic sediment thickness in spatial distribution. However, the subsidence of 10–30 mm/a in certain regions was not entirely driven by tectonic deformation; it is closely associated with human production and life, such as groundwater exploitation.

Therefore, the complex yet orderly spatial distribution of the vertical deformation in the Shanxi rift valley and its surrounding regions reveals the control of regional geological structure pattern on its current vertical deformation and the influence of nontectonic factors on its shallow crust.

Data availability statement

The raw data supporting the conclusion of this article will be made available by the authors, without undue reservation.

Author contributions

RL performed data processing and modeling and drafted the manuscript; JZ revised the manuscript and analyzed the results; WG and HC illustrated the figures. All authors contributed to the article and approved the submitted version.

Funding

This research was funded jointly by the National Natural Science Foundation of China (42171424), the Basic Research Plan of Shanxi Province (202103021224438), the Science and Technology Research and Development Program of Shanxi Province (No. 20140313023-1), Earthquake Prediction Open Fund of China Earthquake Administration (XH22031D), Shanxi Taiyuan Continental Rift Dynamics National Observation and Research Station (Project Nos NORSTY20-09 and NORSTY20-01), Scientific Research Project of Shanxi Earthquake Administration (SBK-2121).

Acknowledgments

We would like to thank Associate Researcher Shiming Liang for his guidance in GPS data processing and senior engineer Yuebing Wang for providing GPS data.

Conflict of interest

The authors declare that the research was conducted in the absence of any commercial or financial relationships that could be construed as a potential conflict of interest.

The reviewer LJ declared a shared affiliation with the author(s) RL, WG, and HC to the handling editor at the time of review.

Publisher's note

References

Blewitt, G., and Lavallée, D. (2002). Effect of annual signals on geodetic velocity. *J. Geophys. Res. Solid Earth.* 107, ETG 9-1–ETG 9-11. doi:10.1029/2001JB000570

Bos, M. S., Bastos, L., and Fernandes, R. M. S. (2010). The influence of seasonal signals on the estimation of the tectonic motion in short continuous GPS time-series. *J. Geodyn.* 49, 205–209. doi:10.1016/j.jog.2009.10.005

Bai, L., and Hou, T. (1994). Deep Geophys. *Explor. Shaanxi Rift Syst. N. China Earthq. Sci.* 12, 27–35.

Cen, M. (2015). Structural analysis on the formation mechanism of Datong Basin. *Geol. Rev.* 61, 1235–1247. doi:10.16509/j.georeview.2015.06.004

Chai, H. Z., Cui, Y., and Ming, F. (2009). The determination of Chinese mainland crustal movement model using least-squares collocation. *Acta Geod. Cartogr. Sin.* 38, 61–65.

Crone, A. J., and Haller, K. M. (1991). Segmentation and the coseismic behavior of Basin and Range normal faults: examples from east-central Idaho and southwestern Montana, U.S.A. *U.S.A. J. Struct. Geol.* 13, 151–164. doi:10.1016/0191-8141(91)90063-O

Deng, Q., Zhang, P., Ran, Y., Yang, X., Min, W., and Chu, Q. (2002). Basic characteristics of active tectonics in China. *Sci. Sin. (Terrae).* 32, 1021–1030. doi:10.3321/j.issn:1006-9267.2002.12.007

Deng, Q., and You, H. (1985). *The characteristics of tectonic activity and its formation mechanism in the rifted basins around Ordos 1985*. Beijing: Institute of Geology, China Earthquake Administration Seismological Press, 58–78.

Diao, F., and Xiong, X. (2008). Interpolation Approach for Velocity Field of Crustal Movement. *Geom. Info. Sci.* 33, 627–630.

Dong, D., Fang, P., Bock, Y., Cheng, M. K., and Miyazaki, S. (2002). Anatomy of apparent seasonal variations from GPS-derived site position time series. *J. Geophys. Res. Solid Earth.* 107, ETG 9-1–ETG 9-16. doi:10.1029/2001jb000573

Dong, D., Fang, P., Bock, Y., Webb, F., Prawirodirdjo, L., Kedar, S., et al. (2006). Spatiotemporal filtering using principal component analysis and Karhunen–Loeve expansion approaches for regional GPS network analysis. *J. Geophys. Res. Solid Earth.* 111, 1–16. doi:10.1029/2005jb003806

Dong, S., Tang, Z., Liu, B., and Su, C. (2008). Numerical simulation of groundwater in Datong basin and evaluation of optimal allocation of water resources. *Geotech. Investig. Surv.* 3, 30–35.

Guo, H., Wang, Y., Wang, R., and Deng, A. (2002). Shallow groundwater environment evolution impacted by intensive anthropic activities in Datong city. *Bull. Geol. Sci. Technol.* 21, 65–72. doi:10.3969/j.issn.1000-7849.2002.04.014

Hao, M., Wang, Q., Cui, D., Liu, L., and Zhou, L. (2016). Present-day crustal vertical motion around the Ordos block constrained by precise leveling and GPS data. *Surv. Geophys.* 37, 923–936. doi:10.1007/s10712-016-9375-1

Herring, T. A., King, R. W., and McClusky, S. C. (2010). GAMIT Reference Manual, Release 10.4. Cambridge. *Mass. Inst.of Technol.*

Hu, H., Huang, L., and Wang, J. (1987). Recent structural activity in Linfen basin. *China Earthq. Eng. J.* 4, 90–92.

Hu, H., Huang, L., and Yang, G. (1993). Recent vertical crustal deformation in the coastal area of eastern. *Chin. J. Geol. Sci. Geol. Sin.* 3, 270–278.

Huang, J., and Zhao, D. (2006). High-resolution mantle tomography of China and surrounding regions. *J. Geophys. Res.* 111, B09305. doi:10.1029/2005JB004066

Huang, X., Dong, S., Tang, Z., and Hou, X. (2007). Groundwater numerical simulation and prediction of Yuncheng basin. *Resour. Environ. Eng.* 21, 402–406.

Jiang, W. (2013). Cause analysis of the non-linear variation of the IGS reference station coordinate time series inside China. *Chin. J. Geophys.* 56, 2228–2237. doi:10.1007/s11425-013-4584-2

Jiang, Z., and Liu, J. (2010). The method in establishing strain field and velocity field of crustal movement using least squares collocation. *Chin. J. Geophys.* 53, 1109–1117. doi:10.3969/j.issn.0001-5733.2010.05.011

Lei, J. (2012). Upper-mantle tomography and dynamics beneath the North China Craton. *J. Geophys. Res. Solid Earth* 117, 1–29. doi:10.1029/2012jb009212

Li, B., Atakan, K., Sørensen, M. B., and Havskov, J. (2015). Stress pattern of the Shanxi rift system, North China, inferred from the inversion of new focal mechanisms. *Geophys. J. Int.* 201, 505–527. doi:10.1093/gji/ggv025

Li, C., Li, J., and Qu, W. (2012). Establishing regional crustal movement velocity field with collocation model based on displacement principle. *J. Geod. Geodyn.* 32, 33–36.

Li, Q. (1980). General features of the stress field in the crust of north China. *Chin. J. Geophys.* 4, 376–388.

Li, Q., Jin, Y., and Yu, X. (1982). Focal mechanisms and crustal stress field in north China. *Acta Seismol. Sin.* 1, 55–61.

Li, S. (1997). The morphotectonics, seismicity, and origin of Shanxi Graben system, East China. *Acta Sci. Nat. Univ.* 04, 61–68.

Li, Y. (2003). Movement and strain state of active blocks in Chinese mainland. *Sci. Sin. (Terrae).* 33, 65–81. doi:10.3321/j.issn:1006-9267.2003.z1.008

Liang, S. (2014). *Three-dimensional velocity field of present-day crustal motion of the Tibetan plateau inferred from GPS measurement* (Beijing: Institute of Geology).

Liu, G., Ma, T., Huang, P., and Wang, S. (1982). Present-day tectonic movement along active faults in the east of China's mainland. *Seismol. Geol.* 4, 3–16.

Liu, R., Zhang, J., Guo, W., and Chen, H. (2021). Study on the recent deformation characteristic and structural deformation model of the south-eastern margin of Ordos block. *Seismol. Geol.* 43, 540–558. doi:10.3969/j.issn.0253-4967.2021.03.005

Liu, R., Yang, C., Wang, Q., and Ji, L. (2021). Possible mechanism of the formation of the Jichechang ground fissure in Datong, China, based on *in-situ* observations. *Environ. Earth Sci.* 80, 1–13. doi:10.1007/s12665-021-09715-2

Mangiarotti, S., Cazenave, A., Soudarin, L., and Crétaux, J. F. (2001). Annual vertical crustal motions predicted from surface mass redistribution and observed by space geodesy. *J. Geophys. Res.* 106, 4277–4291. doi:10.1029/2000JB900347

Miao, D., Li, Y., Lv, S., Tian, J., Wang, Y., and Si, S. (2014). Neotectonic activity in Xinxian segment of the North Zhongtiao Mountain fault zone, Shanxi. *Geol. Resour.* 33, 665–673.

Okada, Y. (1985). Surface deformation due to shear and tensile faults in a half-space. *Bull. Seismol. Soc. Am.* 75, 1135–1154. doi:10.1785/BSSA0750041135

Pan, Y., Hammond, W. C., Ding, H., Mallick, R., Jiang, W., Xu, X., et al. (2021). GPS imaging of vertical bedrock displacements: Quantification of two-dimensional vertical crustal deformation in China. *J. Geophys. Res. Solid Earth.* 126, JB020951. doi:10.1029/2020jb020951

Peng, J., Lu, Q., and Huang, Q. (2017). *Ground fissure disaster in fenwei basin*. Science Press, Beijing.

Qiao, X., Qu, C., Shan, X., Li, Y., and Zhu, C. (2019). Deformation characteristics and kinematic parameters inversion of Haiyuan fault zone based on time series, inSAR. *Seismol. Geol.* 41, 1481–1496.

Roberts, G. P., and Koukouvelas, I. K. (1996). Structural and seismological segmentation of the Gulf of Corinth fault system: Implications for models of fault growth. *Ann. Geofis.* 39, 618–646. doi:10.4401/ag-3996

Shao, Z., Wang, F., and Li, H. (2016). Review on researches associated with 2011 Mw9.0 Tohonku-Oki earthquake. *Earthquake* 36, 1–21. doi:10.3969/j.issn.1000-3274.2016.04.001

Sheng, C., Gan, W., Liang, S., Chen, W., and Xiao, G. (2014). Identification and elimination of non-tectonic caused by land water from time series in the Western Yunnan Province based on GRACE observations. *Chin. J. Geophys.* 57, 42–52. doi:10.6038/cjg20140105

Sun, X. (2016). Relationship between Ground Fissures, Groundwater Exploration and Land Subsidence in Taiyuan Basin. *Chin. J. Geol. Haz. Control.* 27, 91–98.

Tan, H., Shen, C., Li, H., and Li, J. (2009). Characteristics of Surface Deformation Caused by Fault Dislocation. *J. Geod. Geodyn.* 29, 42–49. doi:10.3969/j.issn.1671-5942.2009.03.008

Wang, F., Peng, J., Chen, Z., Wang, Q., Meng, Z., Qiao, J., et al. (2020). Development characteristics and mechanisms of damage-causing urban ground fissures in Datong City, China. *Eng. Geol.* 271, 105605. doi:10.1016/j.enggeo.2020.105605

Wang, H., Ren, Y., Lian, L., Wang, J., Cheng, Y., Wang, Y., et al. (2020). Research on an integrational scheme of large-scale GNSS network data processing and establishment of the horizontal grid velocity field model in Chinese Mainland. *J. Geod. Geodyn.* 40, 881–887 + 897.

Wang, M. (2009). *Analysis of GPS data with high precision & study on present-day crustal deformation in China*. Beijing: Institute of Geology.

Wang, M., and Shen, Z. K. (2020). Present-day crustal deformation of continental China derived from GPS and its tectonic implications. *J. Geophys. Res. Solid Earth.* 125, B018774. doi:10.1029/2019JB018774

Wdowinski, S., Bock, Y., Zhang, J., Fang, P., and Genrich, J. (1997). Southern California permanent GPS geodetic array: Spatial filtering of daily positions for estimating coseismic and postseismic displacements induced by the 1992 Landers earthquake. *J. Geophys. Res.* 102, 18057–18070. doi:10.1029/97JB01378

Xu, X., Ma, X., and Deng, Q. (1993). Neotectonic activity along the Shanxi rift system, China. *Tectonophysics* 219, 305–325. doi:10.1016/0040-1951(93)90180-R

Xu, X., and Ma, X. (1992). Geodynamics of the Shanxi rift system, China. *Tectonophysics* 208, 325–340. doi:10.1016/0040-1951(92)90353-8

Yang, C. S., Wei, Y., Xu, Q., Liu, R., and Liu, Y. (2021). Large-area ground deformation investigation over Taiyuan Basin, China 2007–2011 revealed by ALOS PALSAR imagery. *Arab. J. Geosci.* 14, 2055. doi:10.1007/s12517-021-08325-3

Yang, C. S., Zhang, F., Liu, R., Hou, J., Zhang, Q., and Zhao, C. (2020). Ground deformation and fissure activity of the Yuncheng Basin (China) revealed by multiband time series InSAR. *Adv. Space Res.* 66, 490–504. doi:10.1016/j.asr.2020.04.039

Yang, C. S., Zhang, Q., Xu, Q., Zhao, C., Peng, J., and Ji, L. (2016). Complex Deformation Monitoring over the Linfen–Yuncheng Basin (China) with Time Series InSAR Technology. *Remote Sens.* 8, 284–313. doi:10.3390/rs8040284

Yang, Y., Zhang, J., and Zhang, L. (2008). Variance component estimation based collocation and its application in GIS error fitting. *Acta Geod. Cartogr. Sin.* 37, 152–157. doi:10.3321/j.issn:1001-1595.2008.02.004

Yao, L. (2017). Analysis of the status quo and treatment measures of the groundwater funnel area in Yuncheng City. *Ground Water* 39, 57–59.

Zhan, W., Li, F., Zhu, S., and Zhang, J. (2016). Analysis and Test of Correction to Vertical Velocity Measured by GPS Mobile Observation with Continuous Observation. *Geom. Info. Sci.* 41, 963–968. doi:10.1002/gepi.22030

Zhang, C. (1993). Characteristics and origin of the vertical deformation in Shanxi Graben system, Shanxi Province. *Earthq. Res. China.* 9, 327–333.

Zhang, G., Yang, Z., Wang, Q., and Liu, T. (2011). Study on movement characteristic of Bayanhar Block in the Qinghai–Tibet Plateau based on least-squares collocation model. *J. Earth Sci. Environ.* 33, 213–216. doi:10.3969/j.issn.1672-6561.2011.02.018

Zhang, Q., and Zhu, W. (2000). Preliminary construction of motion models of tectonic blocks in China's crust. *Chin. Sci. Bull.* 45, 967–974. doi:10.1360/csb2000-45-9-967

Zhang, W., Li, Y., Ma, F., and Zhong, J. (1981). On the mechanical mechanism of the formation of graben. *Chin. J. Geol. (Sci. Geol. Sin.)* 1, 1–11.

Zhang, X., and Jiang, Z. (2001). Preliminary study on method of the least square collocation considering regional tectonic features. *Earthq. Res. China.* 17, 403–407.

Zhang, X., and Jiang, Z. (1999). Study on some questions of dynamic pictures of crustal deformation and strain fields obtained by the least square collocation. *J. Geod. Geodyn.* 19, 32–39. doi:10.3969/j.issn.1671-5942.1999.03.006

Zhang, Y. Q., Mercier, J. L., and Vergély, P. (1998). Extension in the graben systems around the Ordos (China), and its contribution to the extrusion tectonics of south China with respect to Gobi–Mongolia. *Tectonophysics* 285, 41–75. doi:10.1016/S0040-1951(97)00170-4

Zhang, Y., Shi, W., and Dong, S. (2019). Neotectonics of North China: Interplay between far-field effect of India–Eurasia collision and Pacific subduction related deep-seated mantle up welling. *Acta Geol. Sin.* 93, 971–1001. doi:10.3969/j.issn.0001-5717.2019.05.001

Zhang, Z., Fang, X., and Yan, H. (1987). A mechanical model of the formation mechanism of the Shanxi Graben zone and the characteristics of Shanxi earthquake zone. *Acta Seismol. Sin.* 1, 28–36.

Zhao, B., Nie, Z., Huang, Y., Wang, W., Zhang, C., and Tan, K. (2014). Vertical motion of north China inferred from dense GPS measurements. *J. Geod. Geodyn.* 34, 35–39.

Zhao, B., Zhang, C., Wang, D., Huang, Y., Tan, K., Du, R., et al. (2017). Contemporary kinematics of the Ordos block, North China and its adjacent rift systems constrained by dense GPS observations. *J. Asian Earth Sci.* 135, 257–267. doi:10.1016/j.jseaes.2016.12.045

Zhao, C. Y., Liu, C., Zhang, Q., Lu, Z., and Yang, C. (2018). Deformation of Linfen-Yuncheng Basin (China) and its mechanisms revealed by II-RATE, inSAR technique. *Remote Sens. Environ.* 218, 221–230. doi:10.1016/j.rse.2018.09.021

Zhuo, Y., S.A., Bornyakov., Guo, Y., Ma, J., and Sherman, S.I. (2016). Influences of obliquity angle difference on the evolution of Fen–Wei Rift: A study from segmented transtension clay model. *Seismol. Geol.* 38, 259–277.

Zou, C., Zhai, G., Zhang, G., Wang, H., Zhang, G., Li, J., et al. (2015). Formation, distribution, potential and prediction of global conventional and unconventional hydrocarbon resources. *Petrol Explor dev+* 42, 14–28. doi:10.1016/s1876-3804(15)60002-7

Zwaan, F., Corti, G., Keir, D., and Sani, F. (2020). A review of tectonic models for the rifted margin of Afar: Implications for continental break-up and passive margin formation. *J. Afr. Earth Sci.* 164, 103649. doi:10.1016/j.jafrearsci.2019.103649

Zygouri, V., Verroios, S., Kokkalas, S., Xypolias, P., and Koukouvelas, I. K. (2008). Scaling properties within the Gulf of Corinth, Greece; comparison between offshore and onshore active faults. *Tectonophysics* 453, 193–210. doi:10.1016/j.tecto.2007.06.011

Frontiers in Earth Science

Investigates the processes operating within the major spheres of our planet

Advances our understanding across the earth sciences, providing a theoretical background for better use of our planet's resources and equipping us to face major environmental challenges.

Discover the latest Research Topics

See more →

Frontiers

Avenue du Tribunal-Fédéral 34
1005 Lausanne, Switzerland
frontiersin.org

Contact us

+41 (0)21 510 17 00
frontiersin.org/about/contact